Protein stability at interfaces

Marianne Weidenhaupt

Communauté
UNIVERSITÉ Grenoble Alpes

Manuscrit

Pour obtenir le diplôme

Habilitation à Diriger des Recherches

DE LA COMMUNAUTE UNIVERSITE GRENOBLE ALPES

Spécialité : **Chimie et Sciences du Vivant**

Présenté par

Marianne WEIDENHAUPT

Laboratoire des Matériaux et du Génie Physique

École Doctorale Chimie et Sciences du Vivant (CSV)

Protein stability at interfaces

HDR soutenue publiquement le **22 janvier 2019**
devant le jury composé de :

Mme Séverine SIGRIST
CEO Defymed, Strasbourg (F), Rapporteure
M Alain ASTIER
Chef de Pôle Honoraire, PUI H. Mondor, Crétail (F), Rapporteur
M Jean-Luc LENORMAND
Professeur Université Grenoble Alpes, Grenoble (F), Rapporteur
Mme Lene Jørgensen
Associate Professor, University of Copenhagen (DK), Examinatrice
M Nicolas MOUZ
Chef Dépt. Antibody Discovery Sanofi, Vitry-sur-Seine (F), Examinateur
M Hans GEISELMANN
Professeur Université Grenoble Alpes, Grenoble (F), Président

Acknowledgements

I would like to express my deepest gratitude to all those who have contributed to the science that is presented in this manuscript: students, technicians, researchers and teaching colleagues and all those who do the jobs “behind the scene” that allow everyone to work in fine conditions. I am fortunate to have a workplace I enjoy going to every day.

En groussen Merci gëllt mengem Papp a mengem Brudder, déi mech ëmmer ënnerstetzt hun and déi houfrech sin op all dât wât ech a mengem Beruf errécht hun. Meng Mamm a meng Tat’Anny bleiwen ëmmer bei mer a léiwer Errënnerung.

I also want to thank Grandma and Granddad for their unconditional support since we first met 27 years ago.

My husband and my daughters are my best support. They are a continuous source of motivation, inspiration and dedication at work, at home and in our fantastic mountain adventures. Ta very much!

Table of contents

Part I

Curriculum vitae

1 A carrier overview

My scientific career started with a PhD thesis in microbial genetics and biochemistry at the Department of Microbiology of the ETH in Zurich (1996). I then went to Grenoble for my postdoctoral research and worked on the structure-function relationship of different proteins, learning to do science at the interface between physics, chemistry and biology (Figure 1-1). During those years I also worked in different settings, be it with industrial partners or on service platforms, which was enriching and valuable. In 2006, I obtained a permanent position as “Maître de Conférence” (Associate Professor) at Grenoble-INP Phelma and researcher at the Laboratory of Materials and Physical Engineering (LMGP). Below is a brief description of the various positions I held and the scientific projects I worked on.

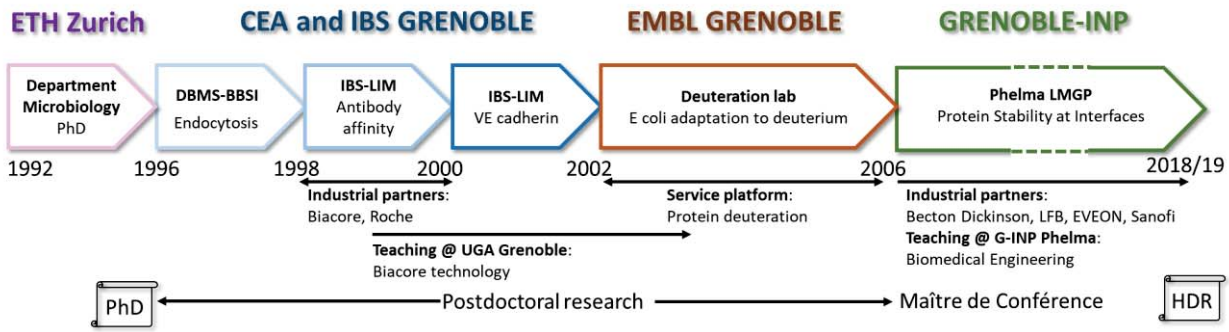

Figure 1-1: Timeline showing my positions and research projects since my PhD thesis
DBMS : Département de Biologie Moléculaire et Structurale
BBSI : Laboratoire de Biochimie et Biophysique des Systèmes Intégrés
IBS : Institut de Biologie Structurale
LIM : Laboratoire d’Ingénierie des Macromolécules
EMBL : European Molecular Biology Laboratory
Phelma : Physique Electronique et Sciences des Matériaux
LMGP : Laboratoire des Matériaux et du Génie Physique

***Endocytosis and membrane fusion in* Dictyostelium discoideum**

1996-1998
Laboratory: CEA-Grenoble, DBMS, Laboratoire de Biochimie et Biophysique des Systèmes Intégrés.
Head: Michel Satre
Funding: Postdoc grant of the Swiss National Research Foundation and "Contrat de Collaborateur Temporaire Etranger" (CTE) of the CEA-Grenoble

D. discoideum is a simple unicellular eucaryote, which is used as a model organism because of several distinct properties, among which high endocytic rates and a well-studied

intercompartmental traffic, based on vesicular fusion. The NSF-SNAP-SNARE machinery was discovered in the late 1980's as governing compartmental specificity of membrane fusion in eucaryots. Inter membrane docking complexes are mediated by the association of SNARE proteins, upon which cytosolic factors, like SNAP proteins and the ATPase NSF are recruited to form a fusion complex. Fusion is achieved by ATP hydrolysis mediated by NSF and the release of the complex. Small GTP-binding proteins of the Rab family govern the rate of the fusion events. Vesicular traffic and the molecular machinery involved have since been intensely studied in many organisms and diverse functional processes. The discoveries in these fields have led to numerous breakthroughs in cell biology and medicine and the Nobel Prize in Physiology or Medicine was awarded in 2013 to J Rothman, R Scheckman and TC Südhof for their ground breaking contributions.

In CEA Grenoble, we have identified, cloned, purified and characterized several proteins (NSF, SNAP isoforms) of the vesicular fusion machinery in *Dictyostelium*. These findings have been published in the following papers:

Weidenhaupt M., Bruckert F. and Satre M. (1998) Identification of the *Dictyostelium discoideum* homolog of the *N*-ethylmaleimide-sensitive fusion protein. *Gene*, 207, 53-60

Weidenhaupt M., Bruckert F., Louwagie M., Garin J. and Satre M. (2000) Functional and molecular identification of novel members of the ubiquitous membrane fusion protein α- and γ-SNAP (soluble NSF-attachment proteins) families in *Dictyostelium discoideum*. *Eur J Biochem*, 267, 2062-2070

Kinetic parameter modulation in antibody-antigen interactions

1998-2000
Laboratory: CEA-Grenoble, IBS, Laboratoire d'Ingénierie des Macromolécules
Head: Thierry Vernet
Funding: Postdoc grant of the EU 4th PCRD (BIO4-CT98-0502)

The engineering of antibody-antigen interaction parameters allows understanding the structure-function relationship governing the recognition and binding of an immun complex. We were particularly interested in the contribution of framework amino acids, which do not belong to the paratope, but can nevertheless contribute to binding affinity. In a comprehensive directed mutagenesis approach we replaced framework residues from the VH-

VL interface and studied their effect on association and dissociation rate constants by surface plasmon resonance (Biacore). Using several different antibody-antigen systems, we demonstrated that framework residues (especially charged ones) can affect kinetic interaction parameters, albeit only marginally and in an unpredictable manner. We identified position VL34 as a key amino acid linked to fast dissociation rates. These findings have been published in the following papers:

Ben Khalifa M., **Weidenhaupt M.**, Choulier L., Chatellier J., Rauffer-Bruyère N., Altschuh D. and Vernet T. (2000) Effects of mutations at the VH-VL interface of Fabs depends on the structural context. *J Mol Recogn* 13, 127-139

Weidenhaupt M., Ben Khalifa M., Hugo N., Choullier L., Altschuh D. and Vernet T. (2002) Functional mapping of conserved, surface-exposed charges of antibody variable domains, *J Mol Recogn* 15, 94-103

Hugo N and **Weidenhaupt M**, Beukes M, Xu B, Janson JC, Vernet T and Altschuh D. (2003) Identification of a key position for rational engineering of dissociation rates in antibodies, *Protein Eng.* 16, 381-386

VE-cadherin, an adhesive receptor affecting leucocyte and tumor cell migration

2000-2002
Laboratory: CEA-Grenoble, IBS, Laboratoire d'Ingénierie des Macromolécules
Head: Danielle Gulino-Debrac
Funding: Postdoc grant "Formation recherche" of the Luxembourgish government (BFR 00/011)

Cadherins are adhesion molecules that govern cell-cell interactions in tissues. Among different tissue-specific cadherins, vascular endothelial (VE) cadherin plays a major role in remodeling and maturation of the vascular endothelium. The extracellular part of VE cadherin consists of five homologous domains that self-associate in a Ca^{2+}-dependent hexamer in solution. Using recombinant proteins with different combinations of the extracellular domains of VE cadherin, we characterized the molecular assembly mechanism underlying hexamer formation. We showed that self-assembly as intermediate dimers is necessary to build homotypic interactions. We also investigated the functional role of VE cadherin in maintaining vascular endothelium integrity. This integrity is challenged by leucocyte transmigration and also during cancer metastasis. We have identified two metalloproteases, elastase and cathepsin G, which

cleave VE cadherin, thus allowing neutrophil transmigration from the blood towards underlying tissues. These findings have been published in the following papers:

Bibert S, Jaquinod M, Concord E, Ebel C, Hewatt E, Vanbelle C, Legrand P, **Weidenhaupt M**, Vernet T and Gulino-Debrac D. (2002) Synergy between extracellular modules of VE cadherin promotes homotypic hexameric interactions, *J Biol Chem*, 277, 12790-12801

Hermant B, Bibert S, Concord E, Dublet B, **Weidenhaupt M**, Vernet T, Gulino-Debrac D. (2003) Identification of proteases involved in the proteolysis of VE cadherin during neutrophil transmigration, *J Biol Chem,* 278, 14002-14012

Escherichia coli *response to deuterium*

2002-2006
Laboratory: EMBL-Grenoble, Deuteration laboratory
Head: Stephen Cusack
Funding: Postdoc grant of the EU (HPRI-CT-2001-50035 and NMI3, HII3-CT-2003-505925)

The deuteration isotope labeling lab at EMBL-ILL in Grenoble is a service facility to produce fully deuterated proteins for neutron protein crystallography studies. Indeed, key hydrogen atoms, that cannot be seen by X-ray analysis alone, can be located in molecular structures using the neutron Laue diffractometer LADI at ILL. The production of fully D-labelled macromolecules is done using bacterial expression systems. I was involved in the initial setup of this facility and worked particularly on the molecular response mechanism underlying bacterial adaptation to deuterated media. In order to understand and improve the adaptation process, we investigated the deuterium effect on *E. coli* in a comparative proteomic approach using 2D gel electrophoresis. Several interesting candidate proteins were identified. To my knowledge, this research project was not pursued after my leave. The following paper was published:

Dunne O, **Weidenhaupt M**, Callow P, Martel A, Moulin M, Perkins SJ, Haertlein M and Forsyth VT (2016) Matchout deuterium labelling of proteins for small-angle neutron scattering studies using prokaryotic and eukaryotic expression systems and high cell-density cultures. Eur Biophys J 46, 425–432

2 Current position

Since 2006, I work as a “Maître de Conférence“ (Associate professor) at G-INP Phelma and researcher at the Laboratory of Materials and Physical Engineering (LMGP). I am sharing the direction (since 2018) of the team “Interface between Materials and Biological Matter” (IMBM) which is headed by Catherine Picart. Our team is composed of 3 Professors/Associate Professors, 1 CR2 CNRS researcher, 2 research engineers (CNRS) and 1 assistant engineer (fixed-term contract, 50% LMGP, 50% CIME Nanotech).

Our common research area is the study of complex physico-chemical phenomena taking place at the interface between materials, biomolecules or cells and air. We develop both fundamental aspects in this field and applied research, often in collaboration with public (e.g. university hospitals) or private, industrial partners of the biomedical sector (e.g. pharma industry). Our research projects fall into two thematic groups:

1 Biomolecules at the interface and biomimetism
2 Tissue Engineering and cancer therapy

My research activities focus mainly on thematic 1 “Biomolecules at interfaces” and I collaborate, to a minor extent, in other research projects. The following chapter describes this in more detail.

2.1 Research activities

Since 2007, my research focuses mainly on the stability of therapeutic proteins at the interface with materials and air (see also Part II). This work is done in close collaboration with industrial partners who work in the sectors of production, marketing and delivery of drugs (Table 2-1). Major results of the research projects that I have lead together with Franz Bruckert (LMGP) between 2007 and 2018 in the field of therapeutic protein stability at interfaces, are presented in Part II of this manuscript.

Year	Secured funding	Research project	Collaborative Partners
2007-10	Cifre ANRT PhD grant + 90 k€	Protein stability at the material interface	Becton Dickinson (Mangiagalli)
2009-10	ANR (09-BIOT-11) 200 k€	Stability of therapeutic proteins	LFB (Huille) Becton Dickinson (Mangiagalli) CEA LCBM (Forge)
2009-12	Macodev PhD grant	Insulin amyloid fibre formation at material surfaces	
2013-16	Cifre ANRT PhD grant + 90 k€	Therapeutic protein aggregation at the triple interface solid-liquid-air	EVEON (Le Masne, Vomscheidt, Tempelaere)
2017-20	Cifre ANRT PhD grant + 90 k€	Stability study of therapeutic antibodies and surfactants for device ability	Sanofi (Huille, El Kechai, Filipe)
2018-21	Innovation grant ANR-15-IDEX-02 Technician 12 months + 35 k€	LabCom LMGP EVEON Preservation of therapeutic proteins in automated drug reconstitution and delivery devices	EVEON (Authesserre, Tempelaere)

Table 2-1: Research contracts in the field of therapeutic protein stability at interfaces

In the forthcoming years (funded up to 2021) we will take up the challenge of creating a **"Joint Laboratory" (LabCom)**, in the framework of the French National Research Agency's efforts to foster collaborations between public research and small or intermediate-sized enterprises. This project will unite EVEON (http://eveon.eu/) and the LMGP to optimize the compatibility of microfluidic protocols and device components of EVEON's automated reconstitution systems with different therapeutics.

Figure 2-1: Eveon's Intuity® mix platform. Credits to EVEON

The Intuity® mix platform (Figure 2-1) is an example of an automated preparation device developed by EVEON. It can solubilize, mix and distribute lyophilized therapeutic proteins. It consists of a disposable cartridge that holds 3 containers: a vial containing the lyophilized powder, a vial containing the solvent and an injection device (typically a syringe). First the solvent is pumped into the powder vial to dissolve the drug, which is finally filled into the syringe at the desired dose. The liquid handling protocols and the component materials within the device generate interfaces

between the protein solution, solid materials and air. The impact of these, often dynamic, interfaces has to be controlled in order to avoid or minimize interfacial adsorption and aggregation of the drug. Special attention will be given to the choice of materials in contact with the therapeutic solution and to fluidic parameters such as the impact of pressure, flow, volume and the presence of air. Our common objective is to develop a library of optimized combinations of component materials and reconstitution protocols adapted to different therapeutics.

Besides therapeutic protein stability at interfaces, I also collaborate in other research projects within LMGP and beyond (Table 2-2). In these collaborative projects my contribution is based on my expertise in protein biochemistry, molecular biology and biomedical applications. The following chart represents the current partitioning of my research time in different projects.

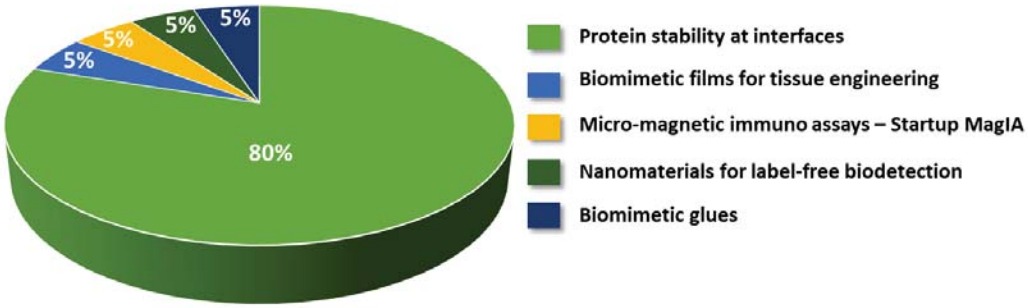

Figure 2-2: Chart showing the partitioning of my current research time in different ongoing projects

Over the years I have managed to collaborate in diverse research projects that are all centred on the common theme: Interactions between materials and biology. The materials part includes electrodes, micro or nanostructured materials, multi-layered polyelectrolyte thin films, liposomes and the biology part extended from proteins and nucleic acids to pro- and eukaryote cells. The following table gives an overview of these collaborative projects.

Year	Research Project	Collaborative Partners
2008-09	Microstructured materials for cell adhesion and directed migration	P Schiavone, T Tzvetkova (CEA LTM) A Stéfanou (TIMC-IMAG)
2007-10	Electrochemical synchronisation of cell spreading	D Delabouglise (SIMAP, LMGP IMBM team) and F Bruckert (LMGP IMBM team)

2009-12	Electrochemical analysis of anaerobic redox activity of *Escherichia coli*	V Stambouli and D Delabouglise (LMGP IMBM team)
Since 2014	Rapid diagnostic immune assays using micromagnets MagIA diagnostics (startup company)	P Kauffmann (MagIA), O Cugat (G2Elab), N Dempsey (Néel Institute), P Marche (IAB), F Bruckert and D Delabouglise (LMGP IMBM team)
Since 2015	Tissue engineering: delivery of bioactive molecules through polyelectrolyte films applied to cancer	C Picart (LMGP, IMBM team)
Since 2016	Protein interactions with lipid membranes	C Picart (LMGP, IMBM team)
Since 2016	Nature inspired biological glues (ANR-15-CE08-0003)	C Vendrely (ERRMECe, Univ Cergy-Pontoise, LMGP visitor)
Since 2018	Electrical detection of PCR-amplified DNA on Si nanonets	C Ternon, V Stambouli (LMGP FunSurf team)
Year	**Research & Education Project**	**Collaborative Partners**
2016-21	Research and Education in active coating technologies for the human habitat; ANR-PIRE-REACT, (https://react.seas.upenn.edu/)	CNRS DR11, ILL, CEA, CNRS Alsace, CNRS DR 16, GIANT, UPenn (US) Alabama Sate Univ (US)

Table 2-2: List of research projects I was or am involved in

2.2 Supervisions and Mentoring

During my postdoc studies, I mentored the PhD students Myriam Ben Khalifa-Cubizolles and Bastien Hermant at IBS Grenoble as well as several Master students. Since 2006, when I joined the LMGP, I yearly supervise 1-2 **Master I / II students** and have co-supervised the thesis of 6 **PhD students** (Table 2-3). I am currently the thesis Director of G Lefèbvre who does a Cifre PhD thesis in collaboration with Sanofi (Vitry, France) (see also Part II, 6 Monoclonal antibody adsorption at material surfaces). I was enrolled in 4 PhD thesis committees: L Altamura (PhD ED Phys, 2015), J Pansieri (PhD ED Phys, 2017), C Lu (PhD ED CSV, 2017), A Ho Shui Ling (PhD ED IMEP2, 2018).

Besides PhD students, I also supervise since 2010 an **assistant engineer** who works on research projects at LMGP and is in charge of the technical aspects of the Biotechnology facility which I head at CIME-Nanotech. My involvement in this facility is detailed hereafter (2.3 Teaching and related responsibilities). I have supervised **2 ATER fellows** (M Amari and M

Lourdin) for their teaching and research work and mentored the teaching activity (**Monitorat) of 3 PhD students** (A Arnaud, I Bouchnak and M Chieb).

A list of the Bachelor and Master students I supervised since 2010 is given in Annexe 1.

Year	PhD thesis	Supervision	Publications (MW co-author)	Current position
2006-09	Marius Socol ED Phys UGA Grenoble	D Delabouglise 50% F Bruckert 40% **M Weidenhaupt 10%**	Microel. Engin 2009, 86, 1485-1487. Bioelectrochemistry 2010,79, 198-210	Postdoc LAAS Toulouse
2009-12	Uyen Nguyen ED Phys UGA Grenoble	D Delabouglise 40%, V Stambouli 40% **M Weidenhaupt 10%**	Electrochimica Acta 2014, 130, 200–205	Postdoc PennState Univ., US
2007-10	Thomas Ballet ED Phys UGA Grenoble Cifre Becton Dickinson	F Bruckert 50% **M Weidenhaupt 50%**	Bulletin of the Polish Academy of Sciences 2010, 58, 303-315. Biochemistry 2012, 51, 2172−2180	Head of Chemical & Material Laboratories, Sanofi, Vitry
2009-12	Laurent Nault ED Phys UGA Grenoble	F Bruckert 50% **M Weidenhaupt 50%**	Acta Biomaterialia 2013, 9(2), 5070-5079. FEBS Letters 2013, 587, 1281–1286.	Scala development Engineer at Niji
2013-17	Karim Chouchane ED Phys UGA Grenoble	F Bruckert 50% **M Weidenhaupt 50%**	J Phys Chem B 2015, 119(30), 10543-10553 J Photochem Photobiol B: 181, 89-97	Looking for a postdoc position
2013-17	Thibaut Frachon ED Phys UGA Grenoble	F Bruckert 50% **M Weidenhaupt 50%**	Langmuir 2016, 32(49), 13009-13019	Formulation Engineer at Sanofi (Vitry)
2017-20	Guillaume Lefèbvre ED CSV UGA Grenoble Cifre Sanofi (Vitry)	**M Weidenhaupt 100%**		Thesis ongoing

Table 2-3: Summary of the PhD students I have supervised

2.3 Teaching and related responsibilities

I hold a position as an Associate Professor (Maître de Conférence, HC échelon 5) at the Engineer school for PHysics, ELectronics and MAterial sciences (Phelma) of Grenoble INP and teach at the Master's level I and II in Biomedical Engineering, in the International Master Nanotech and the Master Nanomedicine. At University Grenoble Alpes (UGA) I teach in the Master Nanobiosciences. My courses cover fundamental aspects in molecular biology, biochemistry, cell biology and immunology as well as engineering applications in biomedicine. I lecture and supervise practical labworks and project work of cohorts of 20-60 students per track. My courses are all given in English, except for a few hours of orientation courses in Biomedical Engineering at the bachelor level, which are given in French. I am also a regular teacher in the highschool programs of the campus GIANT, Nano@school and Inn.OTech. as well as in the European programs EduNano, Eurodots and ESONN.

At Phelma, I am part of the **managing team of the Biomedical Engineering** track and have been in charge of **international relations** of this track since 2008. As an international coordinator, I yearly welcome 10-20 international students in our programs (Erasmus exchanges and double degree students) and mentor the same number of Phelma students for their exchanges abroad. I am also **responsible for the Biotechnology training facility** at CIME Nanotech since 2006 (https://cime.grenoble-inp.fr/?q=fr/biotechnologies). This facility hosts yearly approximately 6000 student hours and it is currently also used by 3 research labs (LMGP, G2Elab, LTM) and hosts the research activities of 2 startup companies (MagIA diagnostics and Nanobiose). On 300m^2 it offers state of the art equipment to express, purify and analyse nucleic acids and proteins. It is equipped for bacterial and eukaryote cell culture (security level I), hosts a microscopy room (fluorescence microscopy) and state of the art equipment for biochemical and biophysical characterizations.

2.4 Other professionally relevant responsibilities

My career has allowed me to take part in the organisation of numerous science events, to participate in funding boards and in reviewing commissions. Table 2-4 gives an overview of these activities.

Year	Program	Task
2009	CNRS wokshop: Sciences de la Miniaturisation et Biologie (SMB), Grenoble	Organisation committee and scientific committee member
Since 2011	GIANT International Internship Program (GIIP) http://www.giant-grenoble.org/en/tag/giip-en/	Organisation committee member
Since 2011	French-American Workshop (FAW) Campus Giant, http://www.giant-grenoble.org/en/faw2018/	Organisation committee member
2010-15	Fonds National de la Recherche, Luxembourg (FNR)	Member of the funding board in Life Sciences and Medicine
Since 2016	Université Franco-Allemande (UFA) Saarbrücken Germany	Member of the funding board in Engineer Sciences, Natural Sciences, Informatics and Architecture
Since 2017	European school for Nanosciences and Nanotechnologies (ESONN) https://www.esonn.fr/	Organisation committee member
Since 2017	UFR Chemistry and Biology University Grenoble Alpes	Invited board member
2018	Workshop: Semi-conducting Nanomaterials for Health, Environment and Security Applications, Grenoble	Scientific committee member

Table 2-4: Participation in scientific organisation and reviewing committees

2.5 Publications

Hereafter is a list of all the peer-reviewed publications I co-authored (last update October 2018): 33 publications, 7 first author, 11 last and communicating author, 2 reviews.

Publications:

1. **Weidenhaupt M.**, Fischer H-M., Acuña G., Sanjuan J. and Hennecke H. (1993) Use of a promoter-probe vector system in the cloning of a new NifA-dependent promoter (*ndp*) from *Bradyrhizobium japonicum*. *Gene* **129**, 33-40
2. **Weidenhaupt M.**, Schmid-Appert M., Thöny B., Hennecke H. and Fischer H-M. (1995) A new *Bradyrhizobium japonicum* gene required for free-living growth and bacteroid development is conserved in other bacteria and in plants. *Mol Plant Microb Inter* **8**, 454-464
3. **Weidenhaupt M.**, Rossi P., Beck C., Fischer H-M. and Hennecke H. (1996) *Bradyrhizobium japonicum* possesses two discrete sets of electron transfer flavoprotein genes: *fixA*, *fixB* and *etfS*, *etfL*. *Arch Microbiol* **165**, 169-178

4. **Weidenhaupt M.**, Bruckert F. and Satre M. (1998) Identification of the *Dictyostelium discoideum* homolog of the *N*-ethylmaleimide-sensitive fusion protein. *Gene*, **207**, 53-60
5. **Weidenhaupt M.**, Bruckert F., Louwagie M., Garin J. and Satre M. (2000) Functional and molecular identification of novel members of the ubiquitous membrane fusion protein α- and γ-SNAP (soluble NSF-attachment proteins) families in *Dictyostelium discoideum*. *Eur J Biochem*, **267**, 2062-2070
6. Ben Khalifa M., **Weidenhaupt M.**, Choulier L., Chatellier J., Rauffer-Bruyère N., Altschuh D. and Vernet T. (2000) Effects of mutations at the VH-VL interface of Fabs depends on the structural context. *J Mol Recogn* **13**, 127-139
7. **Weidenhaupt M.**, Ben Khalifa M., Hugo N., Choullier L., Altschuh D. and Vernet T. (2002) Functional mapping of conserved, surface-exposed charges of antibody variable domains, *J Mol Recogn* **15**, 94-103
8. Gu Z., **Weidenhaupt M**., Ivanova N., Pavlov M., Xu B., Su ZG. and Janson J-C (2002) Chromatographic methods for the isolation and refolding of proteins from *E. coli* inclusion bodies, *Prot Expr and Purif*, 25, 174-179
9. Bibert S, Jaquinod M, Concord E, Ebel C, Hewatt E, Vanbelle C, Legrand P, **Weidenhaupt M**, Vernet T and Gulino-Debrac D. (2002) Synergy between extracellular modules of VE cadherin promotes homotypic hexameric interactions, *J Biol Chem*, 277, 12790-12801
10. Hugo N and **Weidenhaupt M**, Beukes M, Xu B, Janson JC, Vernet T and Altschuh D. (2003) Identification of a key position for rational engineering of dissociation rates in antibodies, *Protein Eng.* 16, 381-386
11. Hermant B, Bibert S, Concord E, Dublet B, **Weidenhaupt M**, Vernet T, Gulino-Debrac D. (2003) Identification of proteases involved in the proteolysis of VE cadherin during neutrophil transmigration, *J Biol Chem,* 278, 14002-14012
12. Delanoë-Ayari H., Lenz P., Brevier J., **Weidenhaupt M**., Vallade M., Gulino D., Joanny J.F. and Riveline D. (2004) Periodic adhesive fingers between contacting cells. *Phys Rev Lett*, 93, 108102 .
13. Tzvetkova-Chevolleau T., Yoxall E., Fuard D., Bruckert F., Schiavon P. and **Weidenhaupt M**. (2009) Microscale adhesion patterns for the precise localization of amoeba. Microel Engin 86, 1485-1487.
14. Socol M., Lefrou C., Bruckert F., Delabouglise D. and **Weidenhaupt M.** (2010) Synchronization of Dictyostelium discoideum adhesion and spreading using electrostatic forces. Bioelectrochemistry 79, 198-210.
15. Bruckert F. and **Weidenhaupt M**. (2010) Applications of micro- and nanotechnology to study cell adhesion to material surfaces (Review). J Adhesion Science and Technology 24, 2127-2140.
16. Ballet T., Boulangé L., Bréchet Y., Bruckert F. and **Weidenhaupt M.** (2010) Protein conformational changes induced by adsorption onto material surfaces: an important issue for biomedical applications of material science. Bulletin of the Polish Academy of Sciences – Technical Sciences 58, 303-315.
17. Ballet T., Bruckert F., Mangiagalli P., Bureau C, Boulangé L, Nault L., Perret T. and **Weidenhaupt M.** (2012) DnaK prevents human insulin amyloid fiber formation on hydrophobic surfaces. Biochemistry, 51, 2172−2180.
18. J M. Lackner, W Waldhauser, P Hartmann, F Bruckert, **M Weidenhaupt**, R Major, M Sanak, M Wiesinger and D Heim. (2012) Hemocompatibility of Inorganic Physical Vapor Deposition (PVD) Coatings on Thermoplastic Polyurethane Polymers. J. Funct. Biomater. 3, 283-297.
19. Pandey LM, Le Denmat S, Delabouglise D, Bruckert F, Pattanayek SK and **Weidenhaupt M**. (2012) Surface chemistry at the nanometer scale influences insulin aggregation. Colloids Surf B Biointerfaces, 100, 69-76.
20. Blaire G, Masse A, Zanini LF, Gaude V, Delshadi S, Honegger T, Peyrade D, **Weidenhaupt M**, Dumas-Bouchiat F, Bruckert F, Cugat O et Reyne G (2013) Hybrid Bio-Mag-MEMS combining magnetophoresis and dielectrophoresis Eur. Phys. J. B 86: 165
21. Nault L, Guo P, Jain B, Bréchet Y, Bruckert F and **Weidenhaupt M**. (2013) Human insulin adsorption kinetics, conformational changes and amyloidal aggregate formation on hydrophobic surfaces. Acta Biomaterialia 9(2), 5070-5079.
22. Nault L, Vendrely C, Bréchet Y, Bruckert F and **Weidenhaupt M**. (2013) Peptides that form β-sheets on hydrophobic surfaces accelerate surface-induced insulin amyloidal aggregation. FEBS Letters, 587, 1281–1286.
23. Nguyen U, Grekov D, Geiselmann J, Stambouli V, **Weidenhaupt M** and Delabouglise D (2014) Anodic deposit from respiration metabolic pathway of *Escherichia coli*. Electrochimica Acta 130, 200–205.
24. Dalonneau F, Liu XQ, Sadir R, Almodovar J, Mertani HC, Bruckert F, Albiges-Rizo C, **Weidenhaupt M**, Lortat-Jacob H, Picart C (2014) The effect of delivering the chemokine SDF-1α in a matrix-bound manner on myogenesis. Biomaterials 35(15), 4525-4535.

25. Serre P, Stambouli V, **Weidenhaupt M**, Baron T and Ternon C (2015) Silicon nanonets for biological sensing applications with enhanced optical detection ability. Biosens. Bioelectron. 68: 336-342.
26. Chouchane K, Vendrely C, Amari M, Moreaux K, Bruckert F and **Weidenhaupt M** (2015) Dual effect of (LK)nL peptides on the onset of insulin amyloid fiber formation at hydrophobic surfaces. J Phys Chem B 119(30), 10543-10553
27. Dunne O, **Weidenhaupt M**, Callow P, Martel A, Moulin M, Perkins SJ, Haertlein M and Forsyth VT (2016) Matchout deuterium labelling of proteins for small-angle neutron scattering studies using prokaryotic and eukaryotic expression systems and high cell-density cultures. Eur Biophys J 46(5), 425-432
28. Frachon T, Bruckert F, Le Masne Q, Monnin E and **Weidenhaupt M** (2016) Insulin aggregation at a dynamic solid-liquid-air interface. Langmuir 32(49), 13009-13019
29. Delshadi S, Blaire G, Kauffmann P, Fratzl M, Devillers, T, Delabouglise D, **Weidenhaupt M**, Dempsey N, Cugat O, Bruckert F and Marche P (2017) Rapide immunoassay exploiting nanoparticles and micromagnets: proof-of-concept using ovalbumin model. Bioanalysis 9(6), 517-526
30. Liu XQ, Fourel L, Dalonneau F, Sadir R, Leal S, Lortat-Jacob H, **Weidenhaupt M**, Albiges-Rizo C and Picart C (2017) Biomaterial-enabled delivery of SDF-1α at the ventral side of breast cancer cells reveals a crosstalk between cell receptors to promote the invasive phenotype. Biomaterials 127, 61-74
31. Lubart Q, Vitet H, Dalonneau F, Le Roy A, Kowlalski M, Lourdin M, Ebel C, **Weidenhaupt M** and Picart C (2018) Role of Phosphorylation in Moesin Interactions with PIP2-Containing Biomimetic Membranes. Biophys J 114(1), 98-112
32. Chouchane K, Pignot-Paintrand I, Bruckert F, **Weidenhaupt M** (2018) Visible light-induced insulin aggregation on surfaces via photoexcitation of bound thioflavin T. J Photochem Photobiol B: Biology, 181, 89-97
33. Migliorini E, **Weidenhaupt M** and Picart C (2018) A practical guide to characterize biomolecule adsorption on solid surfaces (Review) Biointerphases, 13 (6), in press.

Patents:

I am a co-author on 2 patents:

1. FR 3002536 A1: Use of peptide having alpha helix conformation to inhibit protein aggregation in contact with material surface
2. WO 2014111187 A1: Method for capturing, method for detecting and kit for capturing a molecule in a sample

A full list of oral and poster communications at conferences since 2010 is given in Annexe 2.

Part II

Protein stability at interfaces

1 Introductory words

This manuscript is meant to set the general scientific background in which I have developed my work on **Therapeutic Protein Stability at Interfaces**. Both fundamental aspects of protein biochemistry and the use of these molecules as an industrial product in the context of healthcare are treated. It was a challenge to shine light on both fundamental and applied protein science and to develop a fair measure for both.

I chose to start with a presentation of proteins, reviewing their structural stability and analysing the different functional and non-functional folds they can adopt (chapter 2 Proteins and their stability). In this chapter, the amyloid aggregate is highlighted because it took a central part in our work on insulin. I then switch to the use of proteins as therapeutics in today's medicine, highlighting specific constraints accompanying their development in the healthcare industry (chapter 3 Proteins as therapeutics). After a description of current production processes, I focus on stability issues of therapeutic proteins. Interfacial stress that proteins undergo during production and delivery is highlighted in particular. Chapter 4 (Proteins at interfaces) addresses the state of the art knowledge on protein activity at interfaces. Their adsorption, unfolding and aggregation at solid-liquid, liquid-liquid and liquid-air interfaces is described with a particular insight on the parameters that affect these processes. A summary of the most used techniques that allow to study protein interfacial activity at the solid-liquid boundary is also presented.

This general context prepares the reader to appreciate the motivation and impact of our work on the stability of insulin at hydrophobic interfaces (solid and air). In Chapter 5, I chose to present three aspects of our research:

- the role of hydrophobic surfaces in insulin amyloid aggregation
- the role of aggregative peptides in insulin aggregation at hydrophobic surfaces
- the role of a dynamic triple interface in insulin amyloid aggregation

The vast majority of the results presented in this chapter were obtained by four PhD students (Thomas Ballet, Laurent Nault, Karim Chouchane and Thibaut Frachon) which I supervised together with Franz Bruckert. I acknowledge also the contribution of Charlotte Vendrely (Associate Professor Univ Cergy-Pontoise, Errmece lab, visiting researcher at LMGP) and Ugo Hevin (technician) as well as numerous students who contributed during internships and

project work. The final chapter presents my current research project (Chapter 6) on the adsorption behaviour of monoclonal antibodies and surfactants at solid interfaces in the context of formulation optimisation. The experimental results of this work have been obtained by Guillaume Lefèbvre who is currently doing a Cifre PhD in collaboration with Sanofi. I conclude this manuscript with an outlook on the development of new approaches to image protein adsorption at interfaces and propose my view on future work in this area.

2 Proteins and their stability

Proteins are large molecules that are essential for the survival of the cells of all known living organisms. They consist of a linear arrangement of amino acids linked together by peptide bonds between the carboxy terminal group of one amino acid and the amino terminal group of the next one (Figure 2-1).

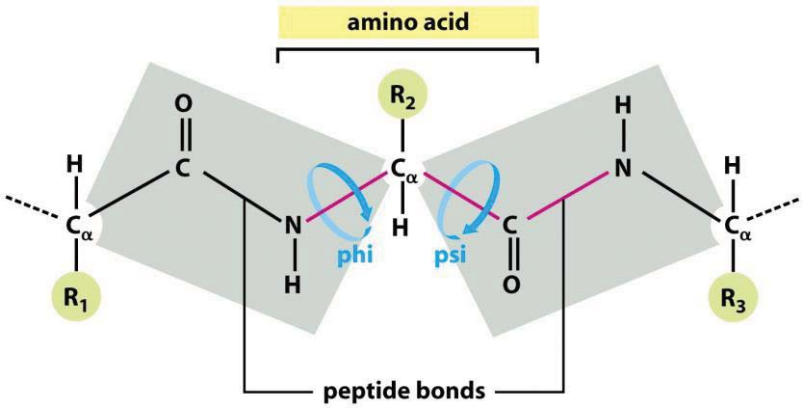

Figure 2-1: The tetrahedral carbon of each amino acid is denoted Cα, the side chains are represented by a numbered R (residue) in green. Peptide bonds are planar and do not allow rotation. Phi and psi angles, defining rotational orientation around the Cα. Figure credits to Molecular Biology of the Cell 5th ed. (© Garland Science 2008)

The sequence of amino acids in a protein is defined by the nucleotide sequence of its corresponding gene. The standard genetic code encrypts 20 amino acids that differ by their side chain and are used by most living species. A gene is transcribed on demand by RNA polymerase, which synthesizes an RNA molecule (transcription) that contains the information necessary to assemble the amino acids of the corresponding protein. This RNA transcript is used by the ribosome to manufacture the protein, catalysing the peptide bond formation between individual free amino acids (translation) and assembling them like beads on a string.

Proteins were identified and studied as early as the mid 19th century but the difficulty to purify them in large enough amounts hampered detailed scientific studies until the 20th century. Insulin became the first protein to be sequenced by Frederick Sanger in 1949 (Nobel prize 1958), thus establishing the linear arrangement of amino acids in proteins. This achievement was soon to be followed by the first structure determinations of hemoglobin and myoglobin in 1958 by Max Perutz and Sir John Kendrew (Nobel prize 1962). Today (Sept 2017) the protein data bank (PDB) has 133'277 entries of biological macromolecular structures including 41'843 distinct proteins and other biomolecules and the number of structural and functional data increases daily (Figure 2-2).

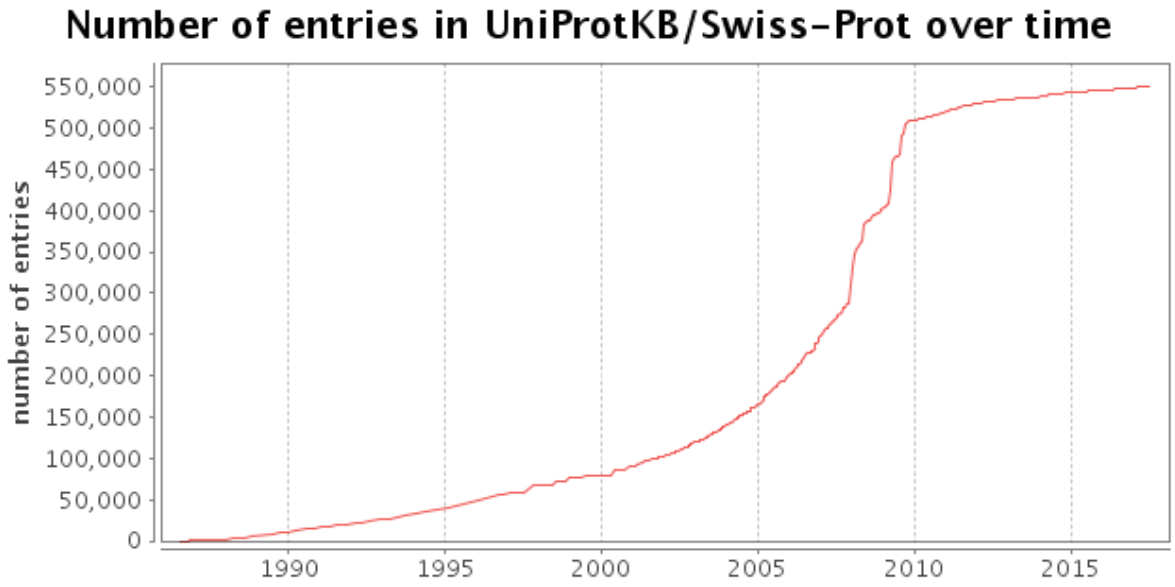

Figure 2-2: The reviewed protein sequence number in the Swiss-prot data base over the time. Note that in 2010, the data base was reorganized, which explains the lower entry number increase since 2010. Figure taken from http://www.uniprot.org/statistics/Swiss-Prot on Aug 30th 2017)

Proteins have been used by mankind long before they were identified as such, for nutritious purposes of course (plant and animal protein) but also for diverse manufacturing processes (fermentation, paper and leather fabrication). Nowadays their use bridges from the food industry to medicine, and they are omnipresent in our daily life in their natural or in a modified (recombinant) form to wash our cloths efficiently, transform our food or cure diseases.

2.1 Protein structure description

The linear arrangement of amino acids in a protein is described in its primary sequence. Many proteins enter a spontaneous folding process starting at their exit from the ribosome. This folding process is driven by thermodynamically favourable interactions between the atoms composing the amino acids and the water molecules surrounding the protein.

Four levels of folding are described starting from the primary sequence cited above. The secondary structure level is defined by characteristic local interactions between atoms of neighbouring amino acids (Figure 2-3). The most common secondary structure elements are alpha helices, parallel and antiparallel beta sheets and turns. They are stabilized by hydrogen bonds between the atoms (mainly N and O) of the peptide main chain. The constraints imposed by the planar nature of the peptide bond (Figure 2-1) and the steric limitations due to the L-isomer selectivity in naturally occurring amino acids, guide folding, together with the maximization of stabilizing interactions. The tertiary structure describes the global 3D arrangement of the protein amino acid chain and results in the so-called native or folded conformation (Figure 2-3). It is stabilized by interactions between distant amino acid atoms, such as electrostatic forces, van der Waals forces, hydrogen bonds and the exclusion of water molecules (hydrophobic interactions). Disulfide bonds between cysteine amino acids can stabilize the structure in oxidizing conditions. The tertiary structure is of critical importance because it generally ensures the biological activity of the protein. A loss of tertiary structure almost always leads to a loss of the protein function. The final structural level is the quaternary structure that describes the spatial arrangement of proteins composed of several polypeptide subunits (Figure 2-3).

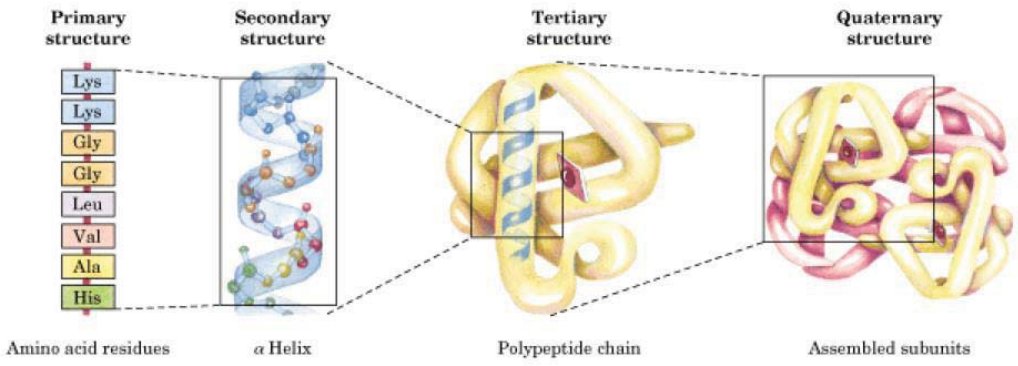

Figure 2-3: Levels of protein structure. Figure taken from Lehninger Principles of Biochemistry, 3rd ed. (© Worth Publishers Inc. 2000)

Protein folding occurs within milliseconds and is mostly spontaneous but takes place in a highly crowded, complex, cellular environment. Molecular chaperone proteins, some of which are associated to ribosomes, help the folding process. Being present in all cellular compartments, they are the warrants of proteostasis, regulating protein folding, unfolding and turnover[1,2].

2.2 Folding for function, yes and no

Protein folding is dictated by energetics and thermodynamics and they have the built-in capacity to fold spontaneously as evidenced by Christian Anfinsen in his groundbreaking work on folding/unfolding of ribonuclease[3]. Soluble proteins that fold in an aqueous environment therefore tend to form globular structures with non-polar, hydrophobic cores and hydrophilic shells, thus maximizing the interactions with the surrounding water molecules. Membrane proteins, like porins for example, adopt the reverse order, presenting hydrophilic centres and hydrophobic shells embedded within the lipid bilayer in the membrane. The main forces contributing to the interactions between protein and solvent atoms in the folded molecule are electrostatic, van der Waals and hydrophobic interactions as well as hydrogen bonding.

Proteins fold within milliseconds and this timescale does not allow a folding process based on a random exploration of all possible folds. It is believed today that folding efficiency is based on a limited ensemble of possible folding pathways that progressively narrows down like a funnel. The folding process starts at the top of the funnel from energetically disfavourable unfolded states and proceeds downwards via energetically more favourable intermediates towards a stable native fold at the end of the funnel (Figure 2-4).

The search for a free energy minimum depends on a multitude of weak interactions and thus, for every protein, there are several potential routes down the folding funnel involving different, partially folded intermediates with more or less native-like conformations. Stable key-residue interactions bias the population of all possible intermediate folding states, thereby paving the route to the final native state[4]. From the energetic point of view, stable folds are not limited to native (i.e. functionally active) states, but include different aggregated states (Figure 2-4), generally associated with a loss of function or even with disease (see 2.7

Amyloid aggregation and disease). In some cases, however, the aggregate can also be functional and this is especially true for the amyloid state[5].

In the ordered structure of the native conformation of a protein the atoms are not rigid but are more or less flexible according to their position. This small amplitude dynamics is associated with functional activity, for example in the active site of enzymes or in the paratope of an antibody. Despite such local movement, the overall integrity of the native conformation remains conserved and numerous proteins are therefore able to crystallize, allowing the determination of their 3D structure by X-ray scattering. The field of protein structure determination was largely guided by this approach for the first 50 years of its existence.

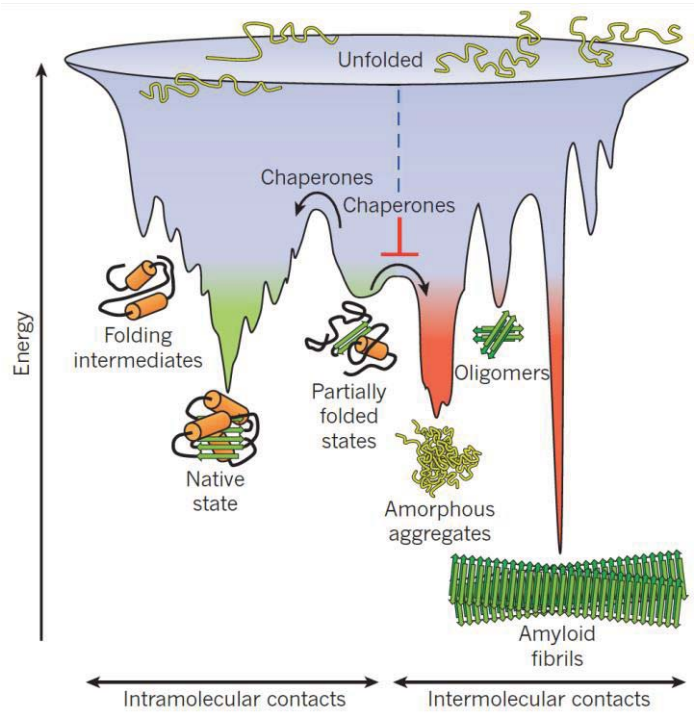

Figure 2-4: Scheme representing the funnel-shaped energy landscape that proteins traverse during their folding process. The native state and stable oligomer or aggregate states are represented as local energy minima. Chaperones are involved in folding or unfolding partially folded states. Figure credits to[1]

Yet, there is another class of proteins, described since the late 1990's as intrinsically disordered proteins (IDPs), which have no stable 3D conformation but they function as an ensemble of highly dynamic interchangeable conformational states[6]. Thus the "sequence-structure-function" paradigm, established 100 years earlier by Emil Fischer[7], has been largely reviewed in recent years. IDPs come in a variety of "formats" and can be completely unstructured or contain parts of varying lengths (loops, linkers, usually >50 residues) that do

not adopt a unique fold and are connected (or not) to folded domains. Disorder predicting algorithms estimate that around 30% of all eukaryotic proteins are at least partially disordered[8] and IDPs are involved in a plethora of biological functions serving as scaffolding hubs as well as in regulatory processes. A common feature of IDPs is that their binding to partner molecules (proteins or nucleic acids) is often accompanied by a transient folding of the corresponding binding region. The underlying mechanisms are still in debate but are likely to be based on conformational selection (folding before binding) or induced fit (folding after binding) or combinations/compromises of these two alternatives[9]. The lack of a unique stable structure can provide functional advantages that take all their biological sense in the high complexity environment of a eukaryotic cell. For example, coupling high specificity and low affinity may allow faster switching between on- and off-states in regulation processes[10].

Thus proteins are macromolecules that use the entire folding space from completely unfolded to highly compact to execute their functions.

2.3 Native state, amorphous or highly ordered aggregate states

The folding process of a protein includes many different conformational states before attaining its native (= functional) fold. The latter and those corresponding to intermediate folds represent local free energy minima separated by energy barriers (Figure 2-4). Different folding states coexist in the cell and the population of each of them is defined by the rates of converting one into the other (Figure 2-5). On top of their individual thermodynamic stability, chaperones, posttranslational modifications, as well as synthesis and degradation rates rule the existence and lifetime of different protein conformational states. In the crowded environment of the cell (average protein to protein distance < 100Å), protein folding/not folding can be unproductive and lead to off-pathway aggregates, which are generally unordered. These are taken care of by chaperones, which assist their refolding or by the protein degradation machinery (Figure 2-5).

Highly ordered structures, like the amyloid fibre, arise when intermolecular interactions become dominant. Because of its multimeric nature, the accumulation of the amyloid state is thermodynamically dependent on the protein concentration, whereas the free energy associated with the native state of a protein is concentration independent. Therefore, a critical

concentration can be defined beyond which the amyloid state is more stable than the native state of a protein. For Aβ42, involved in Alzheimer's disease, a critical amyloid concentration (cac) has been determined recently *in vitro* in physiological conditions[11]. At a cac of around 90 nM (concentration interval 60-120 nM), the fraction of aggregated Aβ42 (early oligomers) rises sharply. These concentrations are compatible with the physiological concentrations of Aβ, which are in the pico- to nanomolar range, taking into account their strong tendency to adsorb at interfaces inducing local accumulation[12].

Proteins thus exist in a so-called kinetically metastable native fold as long as the kinetic barrier existing between the native and amyloid states keeps them there[13]. Chaperones for example, have evolved to be the guardians of these kinetic barriers (Figure 2-4). In a pathological situation this kinetic barrier is broken and amyloid proteins accumulate.

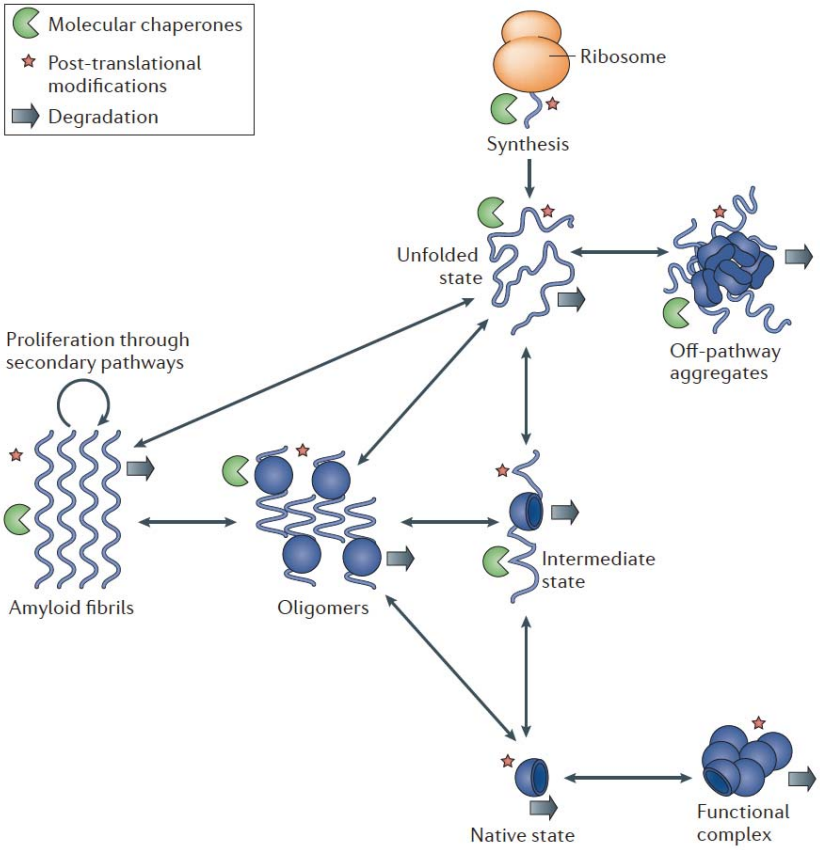

Figure 2-5: Different possible folding states of a protein are shown. Chaperones, posttranslational modifications, synthesis and degradation rates tune the inter-conversion rates between existing states. Figure adapted from[29].

2.4 The amyloid state

The amyloid state can in principle be adopted by any protein because it emanates from the tendency of polypeptides to form hydrogen bonds between backbone atoms and the fact that these can be most efficiently packed in extended beta sheets[14]. However, topological constraints make the packing into a fibril structure more difficult for polypeptide chains longer than 150 amino acids[13]. The average protein length is between 300-500 amino acids, which reflects the fact that evolution has limited the access to the amyloid state by adapting protein size (the other limitation being concentration). In this context it is also worth noticing that most amyloid proteins associated with disease are rather small peptides or proteins (Table 2-1).

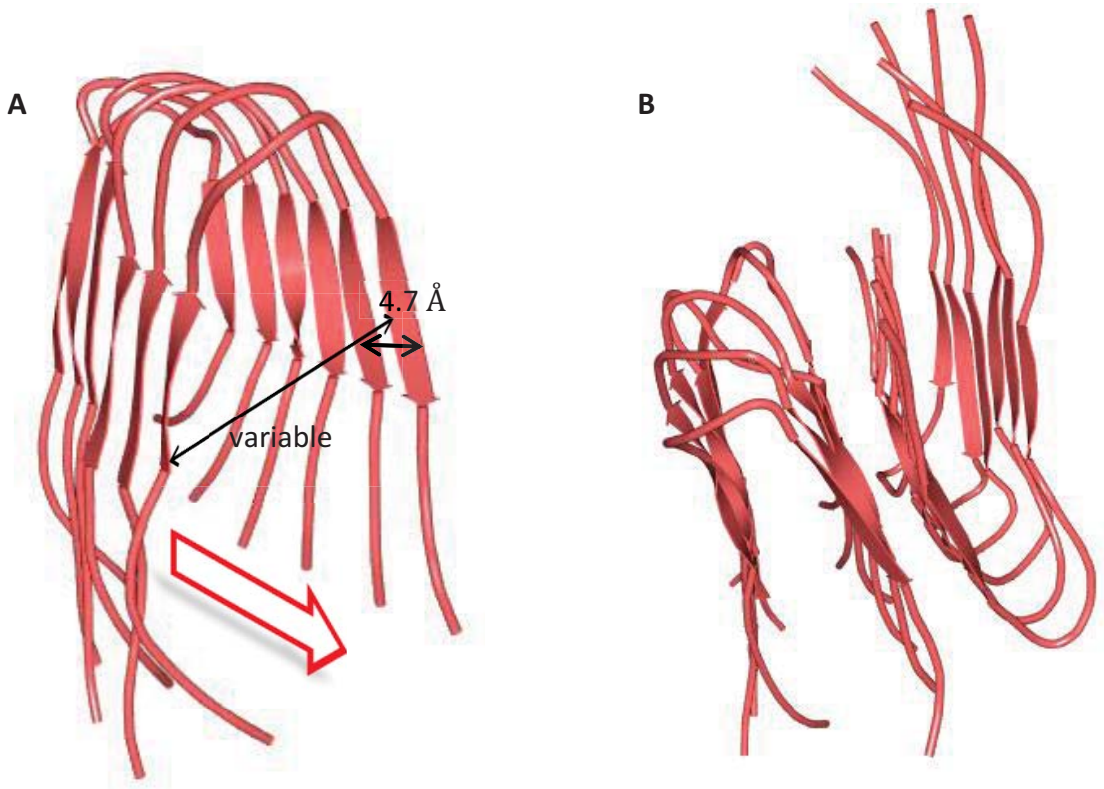

Figure 2-6: Structural model of the beta sheet spine of the 40-residue beta amyloid peptide (Abeta 1-40) fibril associated with Alzheimer's disease. A The red arrow indicates the fibre axis. The inter beta sheet distances in the fibre axis (4.7 Å) and in the perpendicular axis (variable) are indicated. B Lateral packing in the Abeta 1-40 fibre. Figure drawn with Protein Workshop from PDB entry 2LMN using 6 (A) and 12 (B) peptide chains.

The amyloid structure is highly ordered and defined by a continuous, repetitive stack of beta sheets, separated by 4.7 Å, that runs along the fibril axis (Figure 2-6). This inter beta sheet distance is common to all amyloid fibrils and independent of the protein sequence. The resulting twisted beta sheet stack, also known as the cross beta spine, has a distinguished X

ray diffraction pattern, first described in 1968[15]. Several such beta sheet stacks are then arranged side by side involving side chain interactions. The beta sheet spacing in the axis perpendicular to the fibril is variable, depending on the packing constraints of the side chains involved.

Beyond the cross beta diffraction pattern, amyloid fibrils share several common characteristics: binding of the dyes Congo Red and Thioflavin T, a characteristic green-yellow birefringence of Congo Red and unusual stability. Their formation follows a lag-dependent cooperative kinetics and they show self-seeding properties (see 2.5 Kinetics of amyloid fibre formation). Amyloid fibrils, also called protofibrils, appear as unbranched structures that are generally a few nanometers wide but several micrometers long (Figure 2-7A). They present a left-handed helical twist. Hydrogen bonding between backbone atoms of adjacent beta sheets give the fibre extreme stability, a high Young's modulus and remarkable tensile strength[16]. The mechanical properties of amyloid fibres are also a consequence of the association of several protofibrils that wind around each other to form twisted ribbons, tubes, tapes or ropes. This fibre diversity is mainly due to the sequence of the amino acid side chains which are involved in the lateral association of protofibrils[17]. The twist in the protofilaments can accompany the left-handed twist of the fiber such that the interactive sections between the protofilaments are constant. Such a "correlated twist" has been documented for insulin amyloid fibres[18] and fibres of other proteins (e.g. Sup35[19]). It has also been shown that fibres formed by the same protein (insulin, for example) contain different numbers of protofibrils (2, 4 or 6) and different spatial arrangements (Figure 2-7B). This polymorphism takes its roots at least in part in the assembly conditions that influence the lateral packing of protofilaments via protruding side chains.

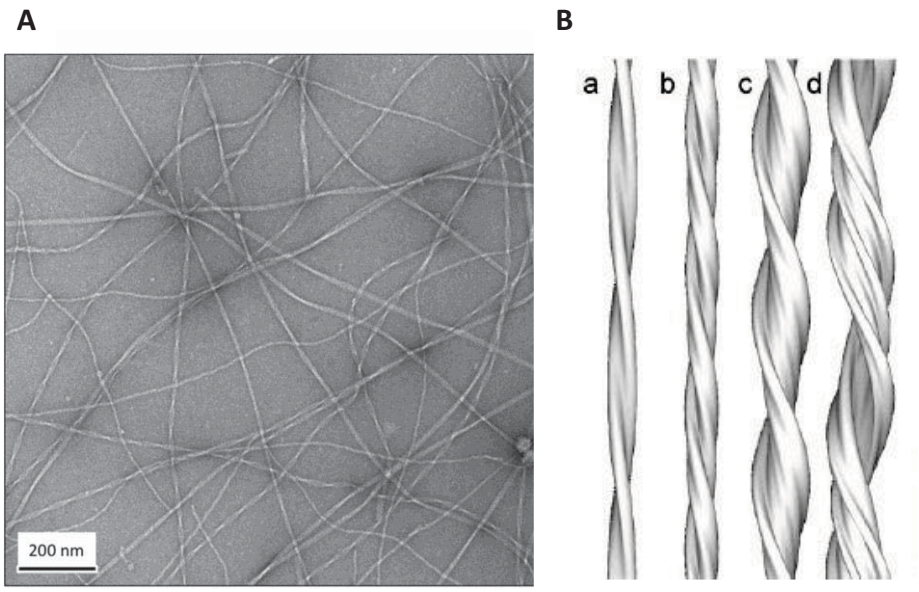

Figure 2-7: Representations of amyloid fibres. A Electron microscopy image of fibers of the islet amyloid polypeptide associated with type2 diabetes. B 3D reconstitution maps showing the polymorphism of insulin amyloid fibres with 2 (a), 4 (b) or 6 (c) protofibrils wound around each other and a twisted ribbon (d). Figure credits to[17] (A) and [18] (B).

2.5 Kinetics of amyloid fibre formation

The transition from the native to the amyloid state involves a conformational change leading to the establishment of the cross beta sheets, observed in the fibril spine. This conversion can be achieved through two mechanisms: nucleation or seeding.

The kinetics of amyloid fibre formation follows a typical sigmoidal reaction time course, characteristic of nucleated polymerization (Figure 2-8). At the molecular level, the lag phase translates the formation of different oligomeric states in the creation of an aggregative nucleus (primary nucleation). Such oligomers result from intermolecular interactions of at least partially unfolded monomers. This process is inherently very difficult to study because it is based on dynamic multi-component equilibria. Elegant microfluidic approaches have been developed to follow the elusive early stages of amyloid aggregation. In confined microdroplets single primary nucleation events can be detected and their subsequent spatial as well as temporal evolution monitored[20]. When a critical size is reached, soluble monomers are readily incorporated into the primary nuclei. During the elongation phase, fibrils start to form from primary nuclei by successive incorporation of soluble monomers. Seeding with preformed fibrils can bypass nucleation and directly lead to fibril elongation. Secondary nucleation events

drive the growth of the fibrils (Figure 2-8). Examples of well described secondary nucleation mechanisms include fibril fragmentation and fibril- or material surface-triggered nucleation. These contribute considerably to the kinetics of amyloid aggregation[21,22]. Fibril growth is limited by the availability of soluble monomers and typical kinetic curves thus present a plateau phase, when no free monomers remain in solution.

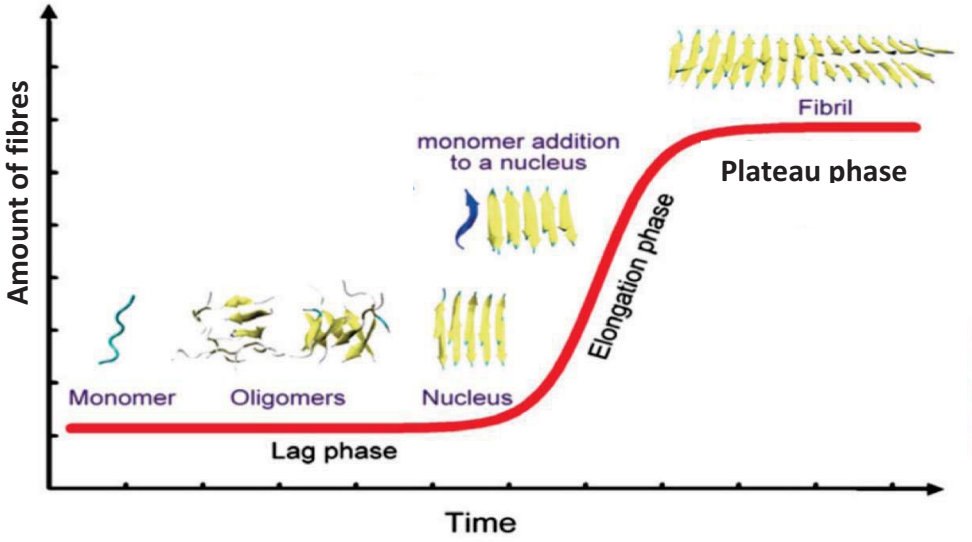

Figure 2-8: Typical nucleation-dependent polymerization model of amyloid fibril formation. During the lag phase, monomeric forms of the amyloid-forming protein self-aggregate into soluble oligomers which further transform into nuclei (nucleation). The nuclei are extended rapidly during the elongation phase, and fibrils grow. Fibrillation can reach a plateau phase when the soluble monomers have all been integrated into fibers. Figure adapted from[167].

2.6 Misfolding and Aggregation in vivo

A misfolded intermediate, occupying a local free energy minimum (Figure 2-4), can become a "trap" on the folding route of the protein. In general, misfolding exposes protein regions that are normally buried, to the solvent, where they can potentially interact with neighbouring molecules to which they normally would not bind. Such interactions give rise to the formation of aggregates, which can be unorganized (amorphous), or highly ordered, like the amyloid fibre (Figure 2-4).

The amino acid sequences of IDPs have evolved to avoid aggregation and stay soluble for function. Indeed they are intrinsically enriched in charged and polar amino acids, thus avoiding

intermolecular association[23]. Nevertheless many of the most common misfolding diseases involve peptides or proteins that are intrinsically disordered in their soluble state (Table 2-1).

In vivo, four conditions that are associated with the formation and accumulation of protein aggregates have been identified: mutations, translational errors, environmental stress and ageing, all of them resulting in a higher propensity for the protein to misfold[24]. The cell therefore deploys sophisticated strategies to maintain proteostasis and avoid an accumulation of protein aggregates: chaperones assist folding and keep misfolding under control and proteases together with the proteasome degrade incorrectly folded proteins[24]. Beyond this first line of defence, the cell is able to sequester accumulated protein aggregates in specific compartments, thereby minimizing possible toxic outcomes mediated by their interactions. Inclusion bodies in bacteria and the mammalian aggresome illustrate this strategy[25]. Autophagy has also been shown to participate in the clearance of accumulated protein aggregates[26].

The Panther geneontology software lists 172 hits in the chaperone class for *Homo sapiens* and 14 for *Escherichia coli* (http://pantherdb.org/ consulted on September 14th 2017). These findings illustrate that both pro- and eukaryotic cells deploy considerable efforts to overcome protein aggregation-related issues. It seems to be the price to pay for the intricately complex structure-function relationship that proteins have adopted to execute life. It also follows that when the cell protection is outrun and aggregates accumulate too much, the cell dies and disease follows for the affected organ.

In this context one should not forget that partial unfolding of a protein is not necessarily detrimental but sometimes necessary, for example during translocation across a membrane. Such programmed unfolding is often assisted by chaperones[27].

2.7 Amyloid aggregation and disease

The interest in amyloid aggregates has rapidly developed in recent years due to their association with a number of incurable diseases that challenge modern societies with ageing populations on a global basis[28]. Alzheimers's disease and Type II diabetes are among the most prevalent. The World Health Organization (WHO) has issued an action plan to tackle dementia, of which Alzheimers's disease accounts for 60-70% of the cases (http://www.who.int/mental_health/neurology/dementia/action_plan_consultation/en/). Today 45 million people have dementia and this number will increase as the number of people aged >60 years is predicted to rise from 900 million to 2 billion worldwide between 2015 and 2050 (http://www.who.int/features/factfiles/ageing/en/, consulted in Sept 2017). Type II diabetes is another amyloid-related disease (>400 million patients worldwide) linked to age and lifestyle in modern societies.

Disease	Aggregating protein or peptide	Polypeptide length (number of residues)	Structure of protein or peptide
Neurodegenerative diseases			
Alzheimer's disease	Amyloid-β peptide	37–43	Intrinsically disordered
Spongiform encephalopathies	Prion protein or its fragments	230	Intrinsically disordered and α-helical
Parkinson's disease	α-synuclein	140	Intrinsically disordered
Amyotrophic lateral sclerosis	Superoxide dismutase 1	153	β-sheet and Ig-like
Huntington's disease	Huntingtin fragments	Variable	Mostly intrinsically disordered
Familial amyloidotic polyneuropathy	Transthyretin mutants	127	β-sheet
Non-neuropathic systemic amyloidosis			
Amyloid light chain (AL) amyloidosis	Immunoglobulin (Ig) light chains or its fragments	~90	β-sheet and Ig-like
Amyloid A (AA) amyloidosis	Serum amyloid A1 protein fragments	76–104	α-helical and unknown fold
Senile systemic amyloidosis	Wild-type transthyretin	127	β-sheet
Haemodialysis-related amyloidosis	β_2-microglobulin	99	β-sheet and Ig-like
Lysozyme amyloidosis	Lysozyme mutants	130	α-helical and β-sheet
Non-neuropathic localized amyloidosis			
Apolipoprotein A1 (Apo A-1) amyloidosis	Apo A-1 fragments	80–93	Intrinsically disordered
Type II diabetes	Amylin	37	Intrinsically disordered
Injection-localized amyloidosis	Insulin	21 and 30	α-helical and insulin-like

Table 2-1: Selection of a number of human diseases associated with protein misfolding and amyloid aggregation. Credits to [29].

Today the list of amyloid-associated diseases comprises around 50 disorders, some systemic, some localized, associated with neurodegeneration or not (Table 2-1). The proteins associated with these show no particular sequence similarity, nor are they related by their native structure or function. Remarkably they all share the same, highly ordered, cross beta sheet structure, indicative of the amyloid fibril in their aggregated state (see 2.4 The amyloid state).

Why the accumulation of amyloid aggregates causes cell death is not clear. In systemic amyloidoses the sheer quantity of accumulated aggregates in vital organs causes organ failure but in neurodegenerative diseases, there is no particular correlation between the quantity of fibre deposits and the pathological stage of the disease[30]. Therefore it is likely that intermediate oligomers and not the final deposits interfere with vital functions in the cell. Many *in vitro* studies point to the toxicity of prefibrillar oligomeric intermediates, that lead to increased membrane permeability, collapsed ion homeostasis and oxidative stress[31]. It is likely that exposed hydrophobic stretches, mostly present in relatively disordered oligomers that precede fibril formation, lead to deleterious inappropriate interactions[32]. The term "protein metastasis" has been coined to describe the molecular mechanisms contributing to the conversion of a functional soluble proteome into self-propagating aggregates that trigger cytotoxicity[29]. Therapeutical strategies tackling the inter conversion rates of the different conformational states of the proteome -soluble, oligomeric intermediates, amyloid fibrils- are the most promising to maintain cellular proteostasis and cure amyloid diseases. A breakthrough in this direction has already been made with tafamidis, a transthyretrin tetramer kinetic stabilizer that slows disease progression in Transthyretin Type Familial Amyloid Polyneuropathy patients[33].

3 Proteins as therapeutics

In the last 50 years molecular and cell biology have allowed tremendous progress in our molecular understanding of disease. Together with genetic engineering and the industrial development of biotechnology, a new class of drugs, called biopharmaceuticals, has emerged. Synonyms for “biopharmaceuticals” are also “biotherapeutics,” “biologicals” or “biologics”. The production of these molecules through genetic recombination and cell expression has immensely improved their purity and overall quality over previous methods of extraction and purification from animal or plant tissues. Diagnosis and therapy have thus entered the age of target molecules with precise biological function that can be tuned to purpose.

Human insulin was the first biopharmaceutical to be produced from bacteria and marketed by Eli Lilly in 1982 (Eli Lilly acquired the licence from Genentech). Since then numerous other biomolecules are industrially manufactured from living cells, with proteins being the most

important class. Among the 10 most sold pharmaceuticals in 2016, so-called blockbusters, five are proteins and four of those are monoclonal antibodies (Table 3-1).

Product	Company	Therapeutical class	Protein/ mAb	Global market share in 2016 (%)
Humira	Abbvie	Rheumatoid arthritis	✓/✓	2.0
Harvoni	Gilead Sciences	Hepatitis C		1.8
Lantus	Sanofi	Diabetes	✓/✓	1.4
Enbrel*	Pfizer	Rheumatoid arthritis	✓/✓	1.1
Remicade	MSD	Rheumatoid arthritis	✓/✓	0.9
Seretide	GSK	Asthma		0.8
Xarelto	Bayer	Thrombosis		0.8
Mabthera	Roche	Lymphoma	✓/✓	0.7
Crestor	Astra Zeneca	Cholesterol		0.7
Lyrica	Pfizer	Epilepsis		0.7

Table 3-1: The 10 most sold biopharmaceuticals in 2016 as compiled by Quintiles IMS for "Les entreprises du médicament" (LEEM). Accessible at http://www.leem.org/article/marche-mondial-1; * note that Enbrel is a fusion protein containing only the Fc fragment of an IgG1.

The total annual sales of all monoclonal antibody products was around 75 billion USD in 2013[34] and the 2016 sales of Humira was estimated to 16 billion USD alone. This reveals today's trend for the development of therapies based on proteins and in particular on antibodies.

3.1 Unique assets and the price to pay

The first reason why proteins are valuable therapeutics is because of their unparalleled interaction specificity. Indeed, this has allowed new and more effective therapeutic solutions for instance in autoimmune diseases such as arthritis, which for decades could only be treated symptomatically. The mAb-based therapeutic Humira targets specifically the tumor necrosis factor alpha (TNFα), thus providing a directed, molecularly relevant therapeutic impact.

This specificity property is tightly linked to their three-dimensional structure, which is inherently labile and sensitive to the physico-chemical conditions of their environment (see 2 Proteins and their stability).

A second reason that makes proteins and in particular antibodies very attractive for therapy is the fact that they can be engineered to combine particular and multiple functions. Indeed, genetic recombination and molecular biochemistry allow to fuse protein domains with different functional properties. Examples of such constructs are antibody-fusion proteins, antibody-drug conjugates, bispecific antibodies and glyco-engineered antibody variants. A recent review on the state of the art of engineered antibodies can be found in reference [35].

Most traditional drugs are small organic compounds with structures based on covalent bonds between their atoms. Paracetamol for example has the general formula $C_8H_9NO_2$ and a molecular mass of 151g/Mole (Figure 3-1). They are therefore very stable and suitable for various production processes and administration formats. They are mostly produced by chemical synthesis from precursors and their production methods are based on decade-old robust protocols.

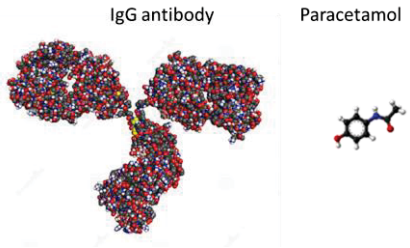

Figure 3-1: Comparison of an IgG antibody (150'000 g/mol) on the left and paracetamol (151 g/mol) on the right. Structures are not drawn to scale.

Proteins are made generally of several hundred amino acids (average molecular weight of an amino acid: 110 g/Mole), illustrating their inherent complexity. Beyond the number of atoms, the three-dimensional conformations that proteins adopt is based on a particular combination of weak forces, like van der Waals interactions, electrostatic interactions, hydrogen-bonding or the hydrophobic effect. Their stability is optimized for their *in vivo* activity and tolerates only small changes of the environmental conditions (see chapter 2 Proteins and their stability).

3.2 The challenges of protein production

The manufacturing process for therapeutic proteins is far more complicated than the chemical synthesis of organic compounds. They are expressed in and purified from live cells, once their genetic information has been cloned and introduced to a host cell. Bacteria, yeast, insect and mammalian expression systems are used, the latter being indispensable for the production of posttranslationally-modified proteins (e.g. glycolsylation) which cannot be achieved in bacteria. The majority of monoclonal antibodies for example is expressed in Chinese hamster ovary (CHO) cell systems. Transformed strains and cell lines are stored in frozen cell banks and transferred into nutrient medium for culturing. The following steps are necessary for the production of therapeutic proteins: sequential culture in increasing volumes (bioreactor fermentation), purification (low and high resolution), formulation and quality control (Figure 3-2).

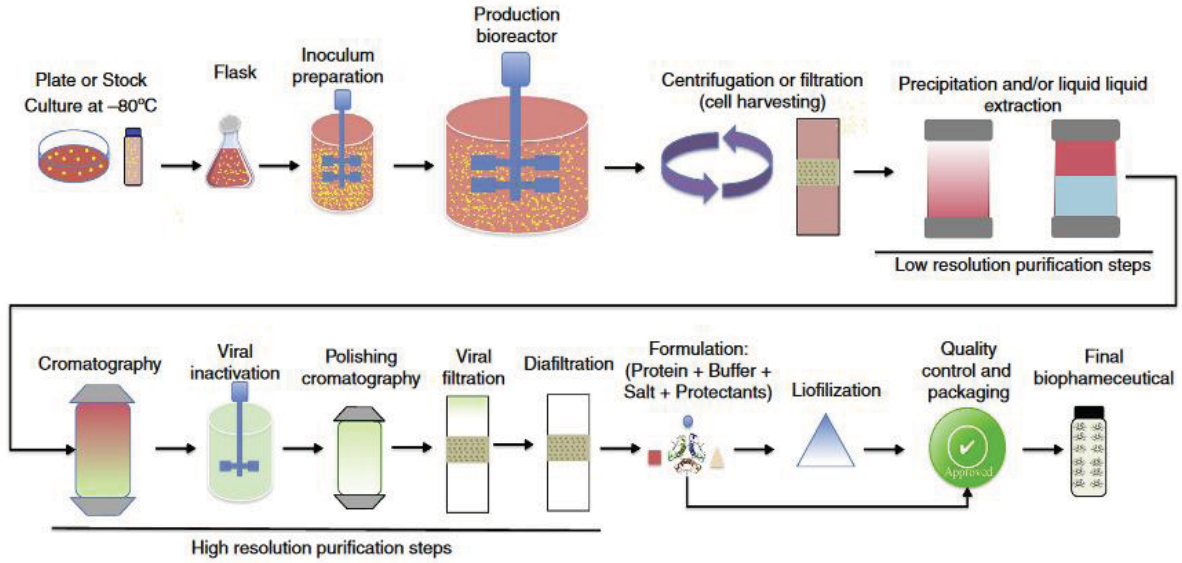

Figure 3-2: Flowchart of protein production manufacturing processes. Figure credits to [36]

In virtually every one of the above steps, efforts are made towards automated or even disposable platforms in order to optimize cost effectiveness and product quality. These two main goals also drive implementation efforts towards continuous culturing (as opposed to batch culturing) in the pharmaceutical industry. Because continuous processes are characterized by a high inherent reproducibility, they guarantee constant product quality[37].

Proteins being inherently not very stable, it is crucial to monitor the state of the molecules throughout the manufacturing process and to guarantee a final product quality. Indeed, during the production processes, proteins are exposed to many stress factors that can lead to quality losses:

- environmental factors such as pH, temperature, ionic strength or high concentration
- chemical modifications such as deamidation, hydrolysis or oxidation
- mechanical factors such as shear stress
- interfacial stress at the liquid-solid, liquid-liquid and liquid-air boundaries

Figure 3-3 below shows a compilation of the different factors that can impact protein quality along the manufacturing and delivery pipeline. It appears that many of these factors involve interfaces between the protein solution and either a solid material, the air or a second distinct liquid phase.

The processing steps, leading to the final drug product, contain several critical operations that are particularly prone to impact protein stability at interfaces. Here I briefly discuss the most prominent ones: freeze-thawing, filtration, filling and lyophilisation.

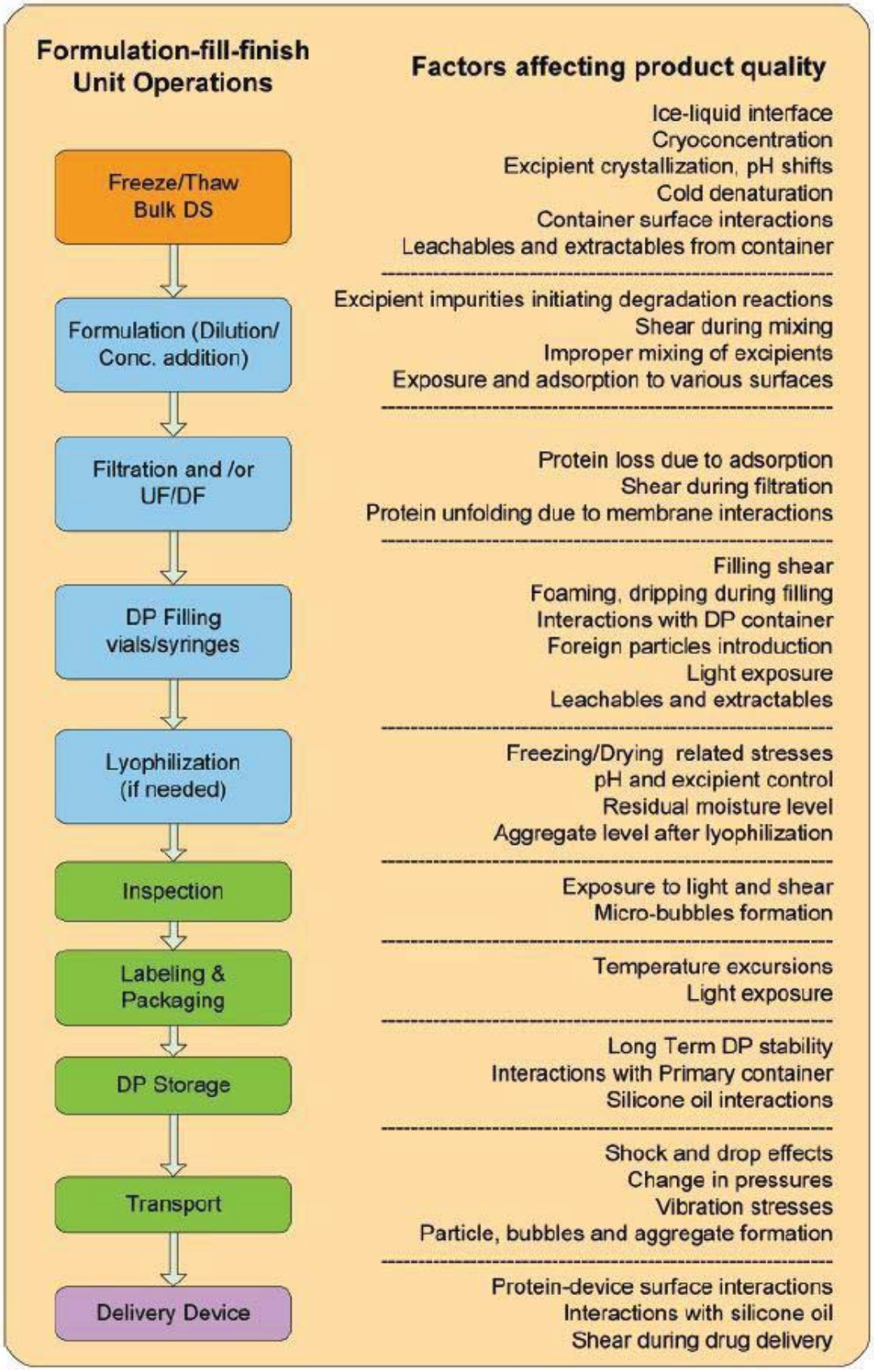

Figure 3-3: Chart presenting different production and delivery processes for therapeutic proteins and the factors that can affect product quality. Figure credits to [41]

3.3 Processes inducing interfacial stress during protein production

Protein freeze-thawing

Freezing a drug production bulk provides operational flexibility but can also lead to severe stability issues due to cryoconcentration. An uncontrolled movement of the freeze-front provokes exclusion of the solutes from the ice-liquid interface and thus leads to a concentration build-up in the liquid, yet to be frozen. This can affect protein stability directly or indirectly by buffer components that are also sensitive to this process[38]. The extent of cryoconcentration is especially high when the freeze front velocity is slow. Besides cryoconcentration, so called "cold denaturation", resulting from the decrease of water density and therefore the solvent-excluded volume effect at low temperatures, can unfold proteins locally and lead to aggregation[39]. Thawing of a bulk protein solution can further enhance protein stability issues initiated by cryoconcentration, and recrystallisation has to be minimized by appropriate mixing. Specific technologies have therefore been marketed (e.g. Celsius Pak) that allow controlling, and generally accelerating, the freeze-thawing rates in order to minimize protein stability issues[40].

Protein filtration

Filtration of a bulk protein solution through a 0.22 µm filter ensures that all viable microorganisms are eliminated. Besides the pressure stress applied to the solution to pass the filter pores, selective binding of the protein (or formulation components) to the filter membrane is often observed[41–43]. Typically, cellulose acetetate or polyvinylidene difluoride (PVDF) materials are used for their low protein binding properties combined with strong mechanic properties and/or chemical resistance. The adsorption loss but also the increased propensity of unfolding and aggregation upon binding to the filter membrane has to be considered during protein production.

Protein filling and storage in liquid state

The therapeutic protein formulations are filled into so called primary containers for storage, transportation and delivery. These containers are usually glass vials or syringes, with associated stoppers, plungers and closing devices. Leachables and extractables from container surfaces are known to impact protein stability[44]. Siliconized material parts are particularly prone to adsorb proteins and to release silicon oil droplets into the solution, on which proteins

adsorb and aggregate[45]. The filling protocols can introduce high shear rates, which affect the proteins particularly at the interfaces with the container materials, the silicon or the air[46].

Protein lyophilization

Due to chemical or physical instability, protein therapeutics are often lyophilized to increase their shelf life. This procedure consists in the removal of most of the water, in the absence of which many covalent degradation phenomena are impossible and diffusion-based aggregation is seriously limited. A lyophilization cycle consists in freezing, annealing, primary and secondary drying phases. The destabilizing effects discussed for the freezing of a protein solution also apply here. The ice is removed by sublimation during the primary drying and residual water is then removed by carefully increasing the temperature. This residual water is often essential for the structural integrity of the protein as hydrogen bonds between water molecules and protein amino acids stabilize the native structure. Therefore excipients are added (e.g. sucrose) to substitute for the loss of stabilizing hydrogen bonds.

3.4 Processes inducing interfacial stress during protein delivery

The vast majority of protein-based therapeutics has to be delivered through the blood or lymph system. They cannot be taken orally because of their degradation and inconsistent adsorption throughout the digestive system. This is the reason why they are usually administered either intravenously or subcutaneously using an injection device. The subcutaneous injection is favoured for chronic disease treatment (e.g. diabetes) because the patient can do it autonomously and at home. However, the volume that can be injected under the skin is limited to about 2 mL and thus a specific subcutaneous dosage, that takes this constraint into account, has to be developed. In general, intravenously injected therapeutics are efficient only at very high doses (several tens of $mg.mL^{-1}$). Indeed, in cancer therapy the tumor penetration of therapeutic mAbs is rather poor (0.01% of the applied dose)[47]. High therapeutic doses have two main drawbacks with immediate implications on their stability before and during delivery: an increased propensity for aggregation and high viscosity[48]. Both are a direct consequence of the small intermolecular distance that exists in highly concentrated formulations.

Before administration, lyophilised products have to be reconstituted which can add a number of stress factors such as interactions with surfaces in pumping devices, cavitation and shear stress[49]. Because of the elevated viscosity the glide force needed to inject the therapeutic solution subcutaneously is increased[50]. Injection devices such as prefilled syringes are therefore lubricated with silicon oil which has been shown to affect protein stability[51]. Indeed, silicone oil droplets that shed into solution present a liquid-liquid interface to which therapeutic proteins can adsorb. This adsorption has been shown to lead to aggregation in numerous cases [52–54].

4 Proteins at interfaces

Interfaces are defined as the boundaries between different matters or matters in different states, such as the solid-liquid, liquid-liquid and liquid-air interfaces. Protein interactions with these interfaces have been studied widely and have numerous practical applications and implications in different economic sectors (medicine, food industry, environment etc). For example, surface-adsorbed protein layers are used by cells to adhere, a process which can be either desired (e.g. cell colonization on scaffolds in tissue engineering) or not (e.g. biofouling of ship hulls). Due to the diversity of their chemical groups and their amphiphilic character, proteins are able to interact with a wide range of surfaces and interfaces. Here I focus on protein interfacial activity in the context of therapeutic protein production, storage and delivery as active molecules.

For therapeutic proteins, which are active in solution, the interfaces of interest are those that delimit this solution. In the majority of the cases, the interface with solid materials and the interface with air as well as the triple interface where solid, liquid and air meet are critical. They are almost always unavoidable and are present for example in a glass vial as represented on Figure 4-1.

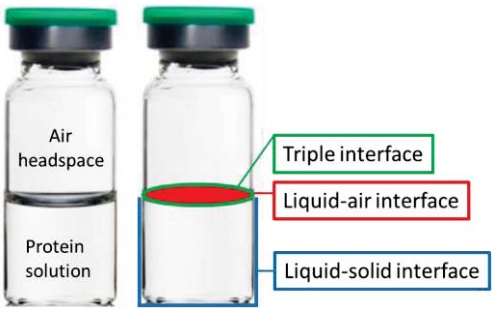

Figure 4-1: A glass vial containing a therapeutic protein solution and an air headspace is shown on the left. On the right, the liquid-solid interface is highlighted in blue, the liquid-air interface in red and the triple interface in green.

The liquid-liquid interface, which occurs when two immiscible liquids are in contact with each other, also plays a major role in the context of therapeutic proteins. Indeed, pharmaceutical emulsions of protein droplets in organic solvents or encapsulation within liposomes represent examples of novel delivery strategies in an effort to optimize pharmacokinetics[55]. On the other hand droplets of silicon oil, which is widely used as a lubricant in delivery devices, are known to act as a liquid-liquid interface, affecting protein stability [51,56].

The phenomena occurring at interfaces can be divided into 4 steps (Figure 4-2):

- Diffusion
- Adsorption/desorption
- Unfolding
- Rearrangements

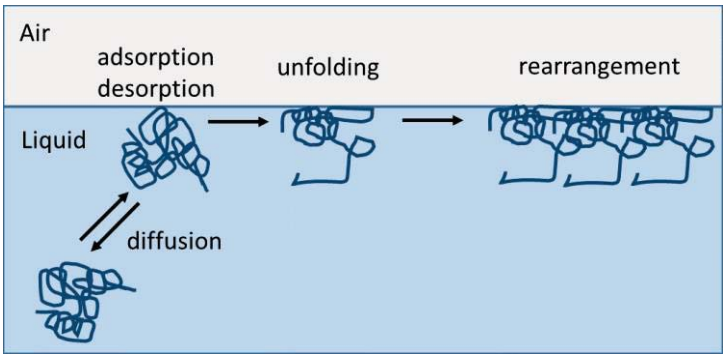

Figure 4-2: Schematic representation of the different steps in protein adsorption at the liquid-air interface.

Diffusion, adsorption/desorption and unfolding are observed for all interfaces, liquid-solid, liquid-liquid and liquid-air. Rearrangements (relaxation, reorientation) of proteins at solid interfaces can be triggered at high surface density[57]. By contrast with solid interfaces, liquid

and air interfaces are flexible and can be compressed and dilated. Such interfacial surface variations can promote aggregation and affect the local density of adsorbed proteins by lateral rearrangements in the interfacial protein network. In the following chapters protein adsorption and unfolding processes are presented with particular emphasis on solid interfaces, which are the most studied. Rearrangements of adsorbed protein networks are presented with their effects on protein aggregation. Finally particularities at liquid and air interfaces are discussed.

4.1 Protein adsorption, unfolding and rearrangements at solid interfaces

4.1.1 Parameters influencing protein interfacial activity

Protein adsorption is most studied at the solid-liquid interface. It is a very common phenomenon, in that most proteins are likely to adsorb on a solid surface whenever they meet one. The most important driving forces for protein adsorption on a surface are hydrophobic interactions, electrostatic interactions and internal structural rearrangements of the protein[58]. The following parameters, amongst others, are influencing interfacial protein adsorption and in particular surface adsorption (Table 4-1).

Solution	pH, ionic strength
Protein	size, shape, charge, pI, “hardness”
Surface	charge, hydrophobicity

Table 4-1: Selected parameters influencing protein adsorption. Table adapted from [59]

As the **pH** determines the overall charge of the protein, it can promote or inhibit their adsorption rate, on charged surfaces. Protein-protein interactions (repulsions or attractions) are also depending on their charges and can stabilize or destabilize adsorbed proteins, affect their packing density at the surface and facilitate or hamper the adsorption of new proteins in close proximity at the surface. At the pI, where the net charge of a protein is zero, the highest packing densities are generally observed[60].

The **ionic strength** of a solution defines the distance (Debye length) at which electrostatic interactions are effective in an electrolyte solution. It thus influences attractive or repulsive interactions between charged proteins and surfaces, affecting the adsorption kinetics. In the

same way as pH, the ionic concentration of the solution can also influence the way proteins interact with their neighbouring protein molecules during adsorption on a surface[61].

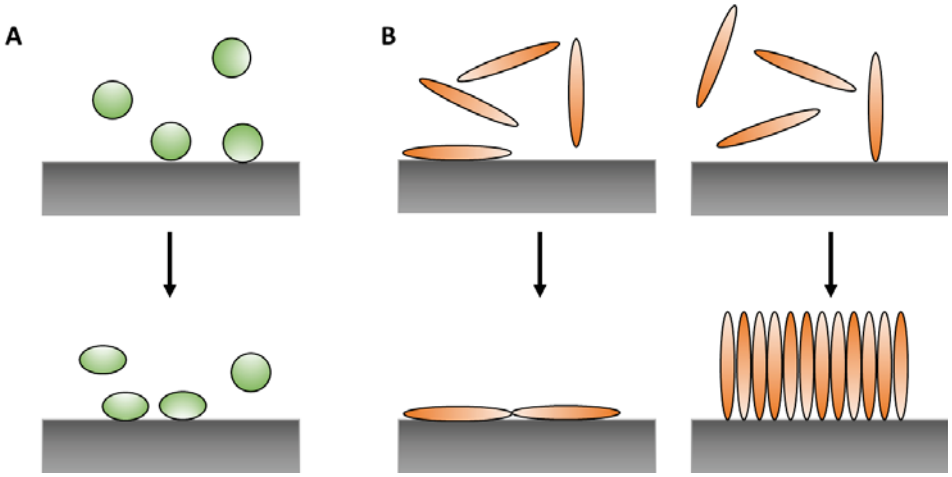

Figure 4-3: Schematic representation of the adsorption of a globular (A) and an elongated protein (B) on a solid surface. The elongated protein can adsorb in a flat (left) or upright (right) position, thereby influencing the packing density on the surface. Figure adapted from[168].

The **size and shape** of proteins influences their diffusion speed. Small proteins, which arrive quicker at the surface, usually dominate early adsorption steps. In protein mixtures, larger proteins can replace smaller proteins at the surface during later stages of adsorption because their interaction surface is typically bigger and they therefore bind stronger. This phenomenon, known as the Vroman effect[62], illustrates that protein adsorption at a solid surface can be competitive and pass through different phases with characteristic profiles of adsorbed species. The overall shape of a protein can be symmetric (globular proteins, e.g. albumin, insulin) or asymmetric (elongated, Y-shaped proteins, e.g. fibronectin, IgG) and they can both adsorb with different orientations on a surface. For asymmetric proteins in particular, their packing density at an interface is highly influenced by the orientation of the adsorbed proteins (Figure 4-3). Lateral rearrangements increasing protein-protein interactions can also change surface adsorption density.

Given the structural complexity of proteins, it is very difficult to find simple ways of predicting their adsorption behaviour at interfaces. An attempt to classify proteins into "**hard**" and "**soft**" ones, describing their propensity for structural modification upon surface binding was made by Arai and Norde[63]. "Hard" proteins tend to adsorb on surfaces undergoing none or only small conformational changes, whereas more extensive structural reorientations accompany

surface adsorption of “soft” proteins. Because of their low internal stability “soft“ proteins tend to adsorb well on both hydrophobic and hydrophilic surfaces, compensating the loss of hydration of the protein and the surface and electrostatic interactions by a gain in folding entropy. “Hard” proteins, on the other hand, tend to adsorb preferentially on hydrophobic surfaces and their adsorption is largely dominated by hydrophobic and electrostatic interactions.

Proteins tend to adsorb more strongly on hydrophobic than hydrophilic surfaces, on charged than on uncharged surfaces. In experimental studies **surface hydrophobicity and charge** are often tuned to reflect a given material of interest. This is commonly achieved by functionalisation using self-assembled monolayer thin films such as in silanisation of hydroxyl groups on glass or metal oxides. Functionalisations with polymers by dip- or spin-coating are also used. Protein adsorption behaviour is also studied on thicker polyelectrolyte multilayers, such as polyethylene-oxide or -glycol (PEO, PEG) brushes, for example. Such functionalisations have been shown to minimize protein adsorption through steric effects and excluded volume effects[64,65]. Finally, model lipid membranes can also be used to mimic protein adsorption at surfaces present in cells and tissues.

4.1.2 Adsorbed mass and surface coverage

Several techniques (see 4.4 Methods to characterize protein interfacial adsorption) are routinely used to measure adsorbed protein mass as a function of time or surface area. The results vary with the experimental setups (variable surface area, for example), the timescales and the sensitivities of the respective techniques and it remains challenging to compare different studies. In most cases, the irreversibly adsorbed surface coverage corresponds to a protein monolayer although stably adsorbed protein multilayers have also been documented[66]. Very often repulsion between adjacent adsorbed proteins entail monolayer formation. Multilayers are typically found in conditions that reduce protein-protein repulsion and promote aggregation. Different models have been used to describe the adsorption/desorption behaviour and the surface coverage of proteins at a solid interface[67]. The Langmuir model[68] (see Eq 1), initially developed for the adsorption of gas molecules,

considers adsorption, desorption and a limited surface area. Two important conditions underlying the Langmuir model however clash with protein adsorption at surfaces:

- first, the equilibrium hypothesis does not apply as desorption experiments generally lead to a residual, irreversibly bound protein fraction and desorbed proteins can potentially re-adsorb at the surface.
- second, the Langmuir model does not account for interactions between adsorbed molecules. The characteristics of proteins however clearly affect their interfacial activity such as the enormous variability of proteins in terms of size, structure and charge distribution, and their sensitivity to environmental conditions.

$$\theta\,(c) = c/\left(c + {}^{k_d}/_{k_a}\right) \quad \textbf{Eq.1}$$

Eq 1: Langmuir isotherm with θ (c), the protein surface coverage as a function of concentration, c, the protein concentration, k_a and k_d the first order adsorption and desorption rate constants, respectively.

Experimentally, at high protein concentrations ($c >> k_d/k_a$), surface coverage values are observed to be significantly lower than 1, which is accounted for by assuming randomly distributed surface binding sites. Indeed, in the random sequential adsorption model (RSA) protein binding sites present an irregular distribution on the surface such that, at saturation, proteins do not overlap and gaps are left which are too small to fit another protein. The maximum surface coverage predicted with RSA depends on the "footprint" of the protein (area covered by the adsorbed protein) and is assumed to be between 54 and 56%[69]. Again this model is limited in that it does not consider desorption or protein rearrangements on the surface (see 4.1.3 Unfolding and rearrangements upon adsorption) that lead to significantly higher observed surface coverages. The final surface coverage seems to be a fine balance between the time it takes for proteins to adsorb at the surface (hence depending on the bulk concentration) and the time and surface available for each protein to establish a stable footprint (relaxation) on the surface[70]. At high concentration, for example, when the surface is covered quickly, individual proteins do not have enough surrounding surface to maximize their footprint and the saturation level will therefore increase[58].

4.1.3 Unfolding and rearrangements upon adsorption

In solution, a protein is surrounded by a shell of water molecules that are associated with it and contribute to its stable conformation. Upon surface adsorption, proteins undergo rapid

conformational changes to increase the surface contact area and stabilize the adsorption by a maximisation of interaction forces with the surface (footprint)[58]. For example, a protein will re-orientate segments with a positive charge to a negatively charged surface, thus promoting attractive electrostatic forces. On a hydrophobic surface, protein adsorption is accompanied by an entropy gain resulting from the release of surface-adsorbed water molecules and ions and turning previously buried hydrophobic side chains towards the surface[58]. Such surface-induced re-orientations result in partial unfolding of the adsorbed proteins so that a stabilisation at the interface can be achieved. The protein-surface interactions that are created upon adsorption as well as the entropy gain from conformational relaxation contribute to a new free energy minimum of the adsorbed state of the protein. In general, structural changes in adsorbed proteins are more prominent on hydrophobic surfaces than on hydrophilic ones and vary according to the inherent stability of the protein. The consequence of this relaxation (unfolding and/or reorientation) is the establishment of an often irreversibly bound protein fraction (at least within the timeframe of most experimental approaches).

Beyond protein-surface interactions, protein-protein interactions also influence the final state of the adsorbed species[67]. Lateral interactions via electrostatic forces gain importance as adsorption proceeds and the distance between neighbouring adsorbed proteins decreases. The pH, which determines the net charge of proteins, thus influences the final packing density on the surface[60]. Moreover, lateral repulsion has been described as being the main cause for "desorption by adsorbed neighbours", a process in which desorption increases with surface coverage[71]. Lateral protein-protein interactions influence the conformational state of the adsorbed protein in such a way that the balance between protein-protein and protein-surface interactions changes, thus inducing an abrupt increase in desorption rates at a threshold surface coverage[72]. This has been documented for example for bovine serum albumin (pI 4.5) at pH 8[71].

The kinetics of surface adsorption is often sigmoidal pointing out that adsorption rates increase with surface coverage. Such positive cooperativity is based on protein self-assembly, either loosely, involving the electrostatic field around adsorbed proteins, or into inter-molecularly bound clusters (aggregates) at the surface (Figure 4-4)[61,73]. In general, at low surface coverage, Langmuir-type adsorption takes place which is subsequently, at higher surface coverage, replaced by a cooperative adsorption[61].

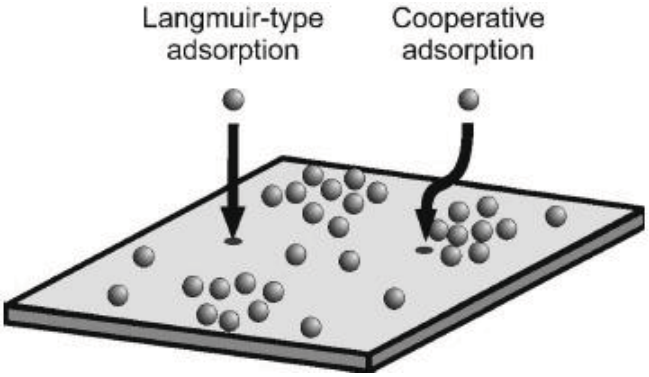

Figure 4-4: Langmuir-type adsorption: proteins adsorb at any available binding site. Cooperative adsorption: proteins adsorb in close proximity to pre-adsorbed proteins. Figure adapted from [61].

Surface adsorption can induce the formation of intermolecular protein aggregates. In general, protein aggregates are defined as irreversible complexes between two or more protein monomers, which present regions of extended, strong, non-covalent interactions between the monomers. Such surface-bound clusters (aggregates) can be formed either by lateral diffusion or by direct binding onto pre-adsorbed proteins[74]. The latter is the case for hydrophobic surface-induced amyloid fibrillation of insulin for example[75,76]. In this case, adsorbed proteins form clusters (nuclei) on the surface which, at a critical size, induce the growth of surface-bound amyloid fibres (see 5.3 Insulin amyloid aggregation at hydrophobic surfaces). Upon agitation, such protein aggregates can be released in solution which can trigger further surface aggregation and sometimes aggregate growth in solution. In the case of therapeutic proteins, surface-induced aggregate formation (and their release into solution) is considered as an important risk factor. The understanding of the underlying mechanisms, the design of more stable molecular variants and the control of the processes involved are all subject to intensive research efforts[77].

4.1.4 Reversibility of adsorption

Protein surface adsorption can be considered reversible (or irreversible) according to three different conditions: reversible upon dilution, reversible upon changing the physico-chemical conditions (pH, ionic concentration etc) and reversible upon exchange with other proteins (see for example "Vroman effect" 4.1.1 Parameters influencing protein interfacial activity). Adsorption to hydrophobic surfaces is usually irreversible with respect to dilution whereas adsorption on hydrophilic surfaces, which is dominated by electrostatic interactions, is subject to reversibility upon pH or ionic strength changes in the solution[78]. Homomolecular exchange at the surface has been documented for several proteins and surfaces[79,80], whereas other proteins do not undergo such exchanges[81] or change their behaviour depending on the surface[82]. More importantly, in the context of therapeutic proteins, is the question whether the protein released from the surface retains its conformational change or not. For bovine serum albumin it was found that the reversibility of the structural changes induced by adsorption was highly dependent on the surface properties[79] and the degree of relaxation during adsorption[80]. Identifying and quantifying the presence of surface-released protein aggregates and probing their conformational state represents a milestone in pharmaceutical quality control of protein therapeutics (see 4.4 Methods to characterize protein interfacial adsorption).

4.2 Protein adsorption and unfolding at liquid interfaces

The liquid-liquid interface is relevant for therapeutic proteins that are formulated as emulsions (water in oil) or those in which the proteins are present as (nano-) particles that are used as drug delivery systems. The latter are created using nanoprecipitation protocols based on desolvation from a water-organic solvent mixture[83]. While in emulsions the aqueous protein solution is in contact with a non-volatile oil, the organic solvents used in particle formation are usually volatile.

An undesired liquid-liquid interface in the form of silicon oil droplets in therapeutic solutions has been widely studied in the literature. Prefillable syringes, which have numerous advantages over vial packaging in terms of dosing accuracy, storage and disposal convenience, are classically made of glass and need lubrication for accurate gliding properties of the plunger

stopper. This is achieved by spraying a silicon oil film onto the glass body of the syringe or applying a silicon oil emulsion that can be stabilized by thermal fixation[84]. Depending on the process, the silicon film is more or less resistant and, upon storage and handling, silicon oil droplets can leak into solution. These droplets are not only undesired for injection but moreover affect protein stability as they trigger adsorption and aggregation. Thus novel lubrication methods and materials for prefilled syringes that do not need lubrication are currently researched. Krayukhina and coworkers have compared therapeutic mAb stability with respect to syringe material and silicon oil lubrication and clearly demonstrate that lubricated glass syringes take the highest toll on protein stability[85].

Similarly to solid interfaces, protein destabilization is generally increased with the hydrophobicity of the oil/solvent phase[86], although cases are reported where the opposite is true[87]. Thus experimental protocols can hardly be translated from one system to another and have to be optimized for each protein formulation. Protein adsorption at the liquid-liquid (or liquid-air) interface affects surface tension and rheology. These properties can be experimentally assessed to measure protein adsorption kinetics at these interfaces: the pendant drop technique for example measures the dynamics of interfacial surface tension using an optical contact angle measurement and contour analysis of a pendant drop of a protein solution inside an oil solution (or in air) (Figure 4-5).

The interfacial surface tension of the droplet decreases as a function of time as proteins accumulate at the liquid-liquid interface. Three regimes are generally described for a dilute protein solution: an induction regime (I on Figure 4-5), during which protein adsorption at the interface is diffusion-limited and too low to noticeably change the tension; as soon as enough proteins have adsorbed, interfacial tension decreases rapidly, reflecting the accumulation of stably adsorbed and relaxed proteins at the water-oil interface (regime II); the interfacial tension decrease eases out in regime III, when the layer of adsorbed proteins changes slowly conformation to seek for energetically favourable interactions. More and more proteins accumulate on the water side and a viscoelastic, gel-like network establishes.

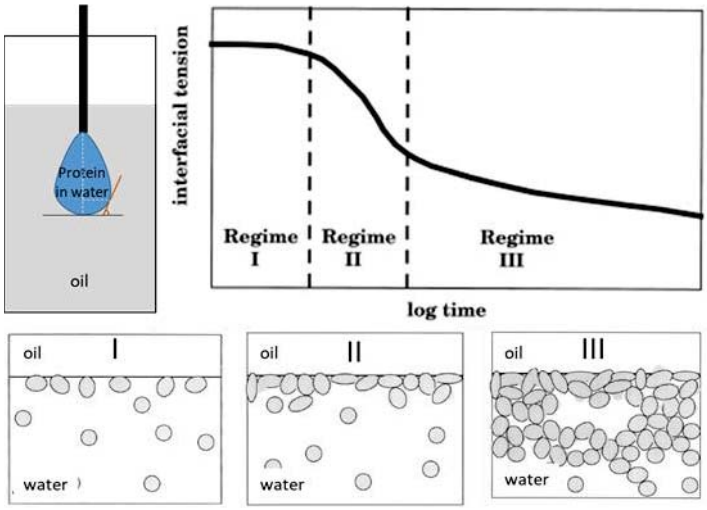

Figure 4-5: Schematic of the pendant drop technique (top left). Typical dynamic interfacial tension response of a dilute protein in an aqueous solution adsorbing to the oil-water interface (top right). The schematics below illustrate the adsorption of native proteins (circles) at the interface and their subsequent relaxation (ellipses) upon formation of an interfacial network. Figure adapted from[89].

It is interesting to mention that during the induction regime (I on Figure 4-5) proteins effectively accumulate at the interface but surface tension variations are measurable only beyond approximately 50% of surface coverage for proteins[88]. Indeed the surface pressure as a function of surface coverage is highly dependent on the molecular size of the adsorbed molecule, indicating that the number of surface contacts is prevailing in the surface pressure of a liquid phase. This is why diluted protein solutions usually show an extended induction regime[89]. Moreover the times of the induction regime observed for ovalbumin at the liquid-air and liquid-heptane interface vary by 2 orders of magnitude (1000 s vs. 10 s, respectively), although the entire surface pressure response is quite similar for both interfaces[89]. This illustrates that the characteristics of the hydrophobic phase affect the protein's interfacial activity and translates the difference in affinity and denaturation kinetics that the protein has for the two hydrophobic interfaces.

Although protein adsorption kinetics at the liquid-liquid interface can be studied in a relatively straightforward way, assessing the conformation of proteins at this interface is more challenging. Indeed, the light scattering properties of emulsions often prohibit techniques that allow assessing protein conformation in solution like for example circular dichroism (CD). Indirect measurements, like turbidity, are then usually used.

Due to the flexibility of liquid-liquid (and liquid-air) interfaces, compression, dilation or mechanical forces interrupting the interface can affect the stability of the adsorbed proteins. This has been studied in particular at the liquid-air interface (see 4.3 Protein adsorption and unfolding at air interfaces).

4.3 Protein adsorption and unfolding at air interfaces

The air constitutes a major hydrophobic interface in the context of therapeutic protein solutions because it is omnipresent and very often dynamic. Liquid-air interfaces exist as entrapped bubbles and headspaces in containers throughout manufacturing, storage and delivery processes of protein drugs. Although an overwhelming amount of studies addressing liquid-air interfacial stress on proteins are reported in the literature, the exact mechanism of how it affects protein stability is still not fully understood[90].

Similarly to the liquid-liquid interface, surface tension measurements are also routinely employed to follow protein adsorption at the air interface (see also 4.2 Protein adsorption and unfolding at liquid interfaces). A striking example of how lowering surface tension by protein adsorption at a liquid-air interface contributes to a vital function, is found in our lungs. Lung surfactant is a lipid-protein complex that forms a film delimiting the wet tissue from air in the alveoli. This interfacial film lowers the surface tension such that the pressure needed to maintain vital alveolar volume upon expiration is reduced, preventing their collapse. In the absence of surfactant, typically insufficiently developed in premature babies, rupture of the lung tissue occurs when their collapsed alveoli are forced open by breathing efforts[91,92].

In the context of therapeutic protein solutions, adsorption of proteins from the bulk at the air interface follows similar regimes than those described for the liquid-liquid interface. Some adsorbed proteins have been shown to change conformation at the air-liquid interface, while others are known to remain in their native state[93]. Agitation and air bubble coalescence are the main causes entailing variations in the surface area at the air-liquid interface. These dynamic increases and decreases of the interfacial surface impact directly on the density of adsorbed proteins and thereby exacerbate particle formation[53,94–96]. It has been shown that repeated compression and dilation cycles of the air-liquid interface causes the formation of IgG aggregates[97]. Bee and coworkers concluded that particles form during compression of the

interface, when the distance between interfacially adsorbed proteins is reduced, and are released into the bulk during dilation[97].

Synergistic effects on the stability of therapeutic proteins have been documented for different stresses at the air-liquid interface. Rudiuk and co-workers showed that, during agitation, a repetitive mechanical breaking of the air-liquid interface by a penetrating needle resulted in the formation of IgG aggregates[98]. In a recent study, Torisu and coworkers have shown that dropping a mAb solution vial, which causes cavitation, combined with agitation significantly enhances the formation of mAb aggregates[49].

Furthermore the triple interface line, where solid, liquid and air meet (see Figure 4-1), can move along the material surface during agitation, potentially exposing surface-adsorbed proteins to the air. A partial dehydration can then contribute to the unfolding and aggregation of adsorbed proteins. This phenomenon, highlighted by T Frachon during his PhD work[99], (see 5.5 Insulin aggregation at a dynamic triple interface), pinpoints to the complexity of the effects that can arise at interfaces and impact on protein stability.

Altogether, the combination of stresses that can entail protein loss or degradation at interfaces call for careful attention in the design of manufacturing, shipping, storage and delivery protocols for therapeutic proteins.

4.4 Methods to characterize protein interfacial adsorption

The characterization of molecular adsorption on a solid surface requires the use of analytical techniques, which are able to detect very low quantities of molecules, generally in a liquid environment, without modifying the adsorption process during acquisition.

Here I focus on the most used techniques for adsorption/desorption measurements on solid surfaces. A broad distinction can be done based on real time vs. equilibrium measurements concerning the adsorbed amount (expressed as Γ: adsorbed mass per surface area or d_A: adsorbed layer thickness) and the state of the adsorbed species (hydration, conformation) (Table 4-2). Real time measurements allow following adsorption and desorption processes with a decent time resolution (at best in the range of seconds) which is pertinent for processes that show distinct phases with characteristic and evolving parameters in time. A full

qualitative and quantitative description of protein adsorption at surfaces also needs to investigate adsorbed protein layers at “equilibrium”, or, more precisely, to do “endpoint measurements” at surface saturation.

The following parameters are commonly addressed in adsorption studies:

- Adsorption and desorption kinetics
- Number of adsorbed proteins per surface area
- Adsorbed layer thickness and hydration
- Conformation and arrangement (orientation) of adsorbed proteins

In Table 4-2 techniques to analyse different properties of proteins adsorbed on solid materials are compared in terms of sensitivity, penetration depth, ease of use and ability to perform parallel measurements. Techniques based on fluorescence (intrinsic or with labels) are not considered here nor are techniques that need large-scale facilities like neutron or X-ray scattering. This comparative table is extracted from a recent review[100] that I have co-authored with my colleagues Elisa Migliorini and Catherine Picart. For a full description of each of these techniques and references, the reader is referred to the reprint of the publication.

Method	Physical signal	Deduced parameters	Sensitivity Γ, d_A	Sensing depth (d_P, d_A)	Type of surface	Drawbacks	Advantages	Ease of use
ELISA	Colorimetry, Fluorescence, Luminescence	Amount Γeq (endpoint)	fM range		Multiwell plate (plastic); beads	Necessity for specific antibody Diffusion limited Long time (hours)	High specificity and sensitivity Automatization High throughput	++++
SPR	*Evanescent wave* Variation of resonance angle	Γ (time) Kinetic interaction parameters Affinity Concentration	1 pg/mm^2, Few tens of nm	d_P ~20 nm	Functionalizable Au-coated chips	Relatively small sensing depth Cost of sensors Limited parallelism	Very high sensitivity Real time analysis	++
SPRi	*Evanescent wave* Fixed angle; Δ of reflected light	Γ (time); Kinetic interaction parameters; Affinity	1 pg/mm^2	d_P ~20 nm	functionalizable Au-coated prism	Relatively small sensing depth and high cost of sensors	Very high sensitivity Real time analysis Parallel analysis of several hundred spots	++
OWLS	*Evanescent wave* Transverse electric and magnetic modes excited in the waveguide	n_A, d_A, Γ (time)	< 1 ng/cm^2, 0.1 nm	d_P~150 nm $d_A$max ~400 nm	SiO_2-TiO_2 sol gel waveguide layer	One provider (MicroVacuum) One measurement at a time n_A and d_A intrinsically linked (Γ being the invariant)	Real time analysis High sensitivity (< 1 ng/cm^2, 0.1 nm for d_A) Now available at high throughput in microplates	+
DPI	*Evanescent wave* Phase shift of TE and TM waves Analysis of interference pattern	n_A, d_A, density ρ_A Γ (time)	< 1 ng/cm^2, 0.1 Å n_A ~10^{-4}	unknown	Si oxynitride	Only relative parameters can be obtained Sensitive to wavelength instabilities Sensitive to mechanical vibrations n_A and d_A intrinsically linked (Γ being the invariant)	Very high sensitivity (0.001 for n_A; 0.01 nm for d_A) Interaction with the sample over several mm or cm	+++

ATR-FTIR	*Evanescent wave* IR light transmitted through a high *n* guiding crystal (Absorbance)	Secondary structure of proteins IR peaks of chemical groups	100 ng/cm^2, ~ 1 nm	$d_P \approx$ 900 to 1500 nm	Crystal of: ZnSe Si Ge	Need to work in D_20 Not highly sensitive Large volume required (mL) Peaks need to be deconvoluted	Sensing over long distance Specificity of IR bands Hydration state (H-bonds)	+
SE	Change in light phase or intensity: Ψ, Δ of reflected light	n_A, d_A	< 1 nm	From 1 nm (UV) to > 1 µm (IR)	Au or SiO_2	Complicated modeling to estimate n_A and d_A based on Ψ and Δ. One measurement at a time.	Measure of optical masses in real time with high sensitivity. No limitation in refractive index and film density High penetration depth.	+
QCM-D	Change in frequency shift of quartz crystal (Δf) and of dissipation (ΔD)	Hydrated mass, Viscoelastic modulus	1 ng/cm^2, 0.1 nm	~ 1 µm	Au, SiO_2, TiO_2, Zn, Mb	Measurement of the molecular mass adsorption always coupled with the solvent. Energy dissipation impacts mass calculation	Real time analysis Viscoelastic properties 4 measurements in parallel	+++
AFM	Tip–sample forces	x-y-z positions, Young's modulus, chemical mapping	~0.1 nm	Up to 100 nm	All surfaces	Very difficult to image very soft films. The resolution depends on the tip curve-radius Highly sensitive to working environment No high-throughput	Imaging molecules in their physiological environment. x-y-z information on surface distribution	+

Table 4-2: Comparison of the different surface-sensitive techniques used to characterize the adsorption of biomolecules on a surface: their physical principle, deduced parameters, sensing depth (d_P), type of surface, drawbacks, advantages and ease of use are compared. d_A: film thickness (nm); d_P: penetration depth; n_A: refractive index; Γ: adsorbed mass in mass per surface area (ng/cm^2 or µg/cm^2); SPR(i): surface plasmon resonance (imaging); OWLS: optical waveguide lightmode spectroscopy; DPI: dual polarization interferometry; ATR-FTIR: attenuated total reflection Fourier transform infrared spectroscopy ; SE: spectroscopic ellipsometry; QCM-D: quartz crystal microbalance with dissipation monitoring; AFM: atomic force microscopy

4.5 Formulation strategies

In order to guarantee product quality, a liquid formulation, based on an adequate mixture of various excipients, is generally developed to maintain the protein stable and active at the target concentration[101,102]. Liquid formulation science is anchored on three essential points: find the cause for aggregation, assess and quantify the types of aggregates and finally stabilize the active compound with the right combination of excipients. In order to design an efficacious formulation, a continuous interactive progression involving all three steps is necessary.

	Frequency of Inclusion in MAb Formulations (%)		
Excipients	All	Lyophilized	Liquid
Polysorbate 80	57	45	62
Polysorbate 20	19	36	12
Poloxamer 188	3	0	4
Mannitol	8	9	8
Sorbitol	3	9	0
Sucrose	35	82	15
Trehalose	14	18	12
Dextrose	3	9	0
Dextran 40	3	9	0
NaCl	49	18	62
Arginine	8	0	12
Glycine	8	0	12
Methionine	3	0	4
Acorbic acid	3	0	4
NaOAc	3	9	0
Phosphate	32	27	35
Citrate	11	9	12
Acetate	16	0	23
Tris	3	0	4
Succinate	3	9	0
Histidine	35	27	38

Table 4-3: Overview of excipients used in 37 commercial mAb formulations. Credits to [169]

The first step in formulation development is to determine the optimal pH. In general, therapeutic protein solutions are formulated at a pH that differs from the pI of the protein, in order to favour the correct ionization underlying the native fold of the protein. A slightly acidic pH is usually chosen because chemical degradation processes (e.g. deamidation) are enhanced at neutral or basic pH. The most used buffer components for mAb formulations are sodium phosphate- and histidine-based, the latter being well adapted for slightly acidic formulation conditions (pKa His ~ 6) (Table 4-3). Surfactants are usually included in formulations with the aim to reduce interfacial tension and stabilize the protein in solution. Their amphiphilic nature (which they share with proteins) is at the base of their surface activity. Their preferential accumulation at interfaces is assumed to prevent the protein from doing so and they thus would act as kinetic competitors in interfacial partitioning. Besides this kinetic stabilization mechanism, surfactants can also act via colloidal stabilisation in solution, thus covering the protein and preventing it in this way from interfacial adsorption[103]. The most used surfactants are polysorbates (PS 80 and PS20) as can be seen from the compilation in Table 4-3.

Formulations further contain stabilizers that are small molecules that can have anti-oxidant, chelating or cryoprotective properties. For the latter, sugars (e.g. sucrose and trehalose) and

polyols (e.g. mannitol and sorbitol) are widely used to stabilize the native conformation of proteins during freeze-thaw cycles and lyophilisation (Table 4-3).

To assess the efficacy of a liquid formulation, protein aggregative particles are quantified in solution. Such particles are classified according to their size into the following categories: submicron (<1μm), sub-visible (1-100μm) and visible (>100μm) particles. Different size-based detection techniques are used to assess the formation of protein aggregates in formulated solutions (see Figure 4-6)[104].

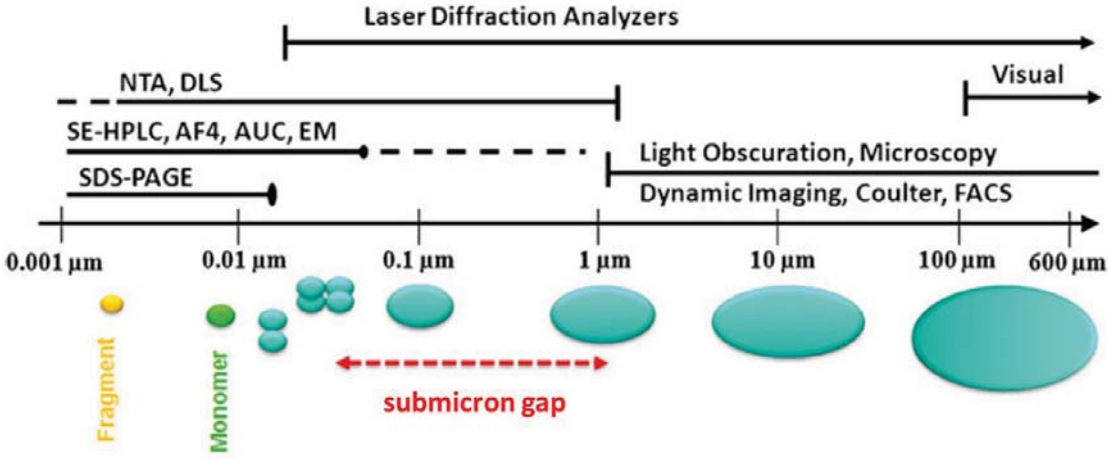

Figure 4-6: Techniques used to assess size and quantity of aggregates, plotted on a molecular size-line. Between 50-1000 nm, the availability of adequate characterization techniques is limited to laser diffraction, dynamic light scattering, and electron microscopy (submicron gap). NTA, nanoparticle tracking analysis; DLS, dynamic light scattering; SE-HPLC, size-exclusion high –performance liquid chromatography; AF4, asymmetric flow field flow fractionation; AUC, analytical ultracentrifugation; EM, electron microscopy, SDS-PAGE, sodium dodecyl sulphate polyacrylamide gel electrophoresis; FACS, fluorescence-activated cell sorting.
Figure credits to[104].

US and European pharmacopeia regulations aim at assessing the quality of a therapeutic protein solution by establishing an upper limit to the number of particles of a given size in a liquid formulation. Particles that are smaller than 10 μm are considered innocuous for patient safety. Bigger particles are analysed by light obscuration and microscopy techniques and the regulatory limit of their number is correlated to the injectable volume of the corresponding drug (Table 4-4). Visible particles are not tolerated and are assessed by visual inspection in front of white and black backgrounds (Ph. Eur.9.0, 2.9.20).

It should be noted that the origin of particles found in liquid formulations can also be non-proteinaceous. They can emanate from materials in contact with the solution (e.g. glass, rust,

silicon oil) or from the environment (e.g. dust, fibres). Excipients used in formulations can also represent a source of impurities and should therefore be of the highest purity. As they usually represent a major part of the components of a liquid formulation, their impact on the pharmacokinetic properties of the active drug has to be taken into account[105].

	Light obscuration	**Microscopy**
Number of replica	3	3
Small injectable volume (≤ 100 mL)		
Particles ≥ 10 μm	≤ 6000 per container	≤ 3000 per container
Particles ≥ 25 μm	≤ 600 per container	≤ 300 per container
Large injectable volume (> 100 mL)		
Particles ≥ 10 μm	≤ 25 per mL	≤ 12 per mL
Particles ≥ 25 μm	≤ 3 per mL	≤ 2 per mL

Table 4-4: Limits of particle numbers for quality assessment of liquid formulations (European pharmacopea 9.0, 2.9.19 Particulate contamination: sub-visible particles). Credits to G Lefebvre PhD in Pharmacy UCBL, 2017 N°38)

Beyond protective formulation additives, other strategies exist to stabilize therapeutic proteins in solution and optimize their pharmacokinetic properties. For example the protein can be chemically modified, either by mutation or recombination with other stabilizing protein domains (thus creating a protein analogue), or by acylation or PEGylation[106–108]. For example, rapid-acting insulin analogues have been obtained by mutating amino acids involved in self-association. These insulin analogues (Lispro (Eli Lilly); NovoRapid (Novo Nosrdisk)) are preferentially monomeric which accelerates their delivery into the bloodstream upon subcutaneous injection. The attachment of fatty acids (acylation) can increase circulation time by association with serum albumin, which has been successfully implemented with the insulin analogue Detemir (Novo Nordisk)[109].

5 Insulin adsorption and aggregation at hydrophobic interfaces: a case study

5.1 A tribute to PhD students and co-workers

In this chapter the research of 4 PhD students, whom I co-supervised with Franz Bruckert, and numerous other contributors is presented. Thomas Ballet (2010, Cifre PhD LMGP-Becton Dickinson) started the research project on the stability of insulin in contact with hydrophobic surfaces and developed invaluable tests based on 96-well microplates and functionalized beads to follow aggregation kinetics. He demonstrated that nucleation and fibre growth take place on the hydrophobic surface and not in solution[76]. Laurent Nault (2012) analysed the sequence of events at the surface and the conformational state of surface-adsorbed insulin using surface sensing techniques such as surface plasmon resonance and infrared spectroscopy[110]. He also developed aggregative peptides as a tool to study surface-induced aggregation[111]. Karim Chouchane (2017) completed the analysis of the effects of short peptides on surface-induced insulin aggregation and showed that these can either accelerate or inhibit the aggregation process depending on their concentration[112]. He demonstrated that they cooperatively accelerate nucleation at very low concentrations by binding to hydrophobic surfaces and inhibit aggregation in solution by binding to fibrillary insulin at higher concentrations. He also discovered that the energy of visible light can trigger the aggregation of surface-adsorbed insulin via bound ThT[113]. Thibaut Frachon (2017 Cifre PhD LMGP EVEON) shed new light on insulin stability at interfaces by analysing the effect of a dynamic triple line where hydrophobic surface, air and liquid meet. He combined a microfluidic setup with fluorescence and interference microscopy to document in real time the formation of insulin aggregates at a moving triple line where adsorbed proteins aggregate under the effect of local dehydration[99].

In the following the focus is on the highlights of our research on insulin stability at interfaces. For more detailed information the reader is referred to the reprints of the publications associated with this work[76,99,110–113], which are compiled at the end of this manuscript. The molecular tools, experimental protocols and the design of devices to produce these results are valuable achievements, at the same level as the actual data they have allowed to produce.

5.2 Human insulin

Insulin, the most produced therapeutic protein, is administered to diabetes patients by daily sub-cutaneous injections. It has been used for diabetes management for roughly 80 years and was the first therapeutic protein to be produced recombinantly in bacteria. Insulin is also used as a model protein in research including studies on protein stability at interfaces.

Human insulin is a small globular protein of 51 amino acids composed of two chains (A-chain: 21 aa and B-chain: 30 aa, Figure 5-1) linked by two interchain disulfide bridges (cysteines A20 and B19, A7 and B7 (Figure 5-1)). The A-chain is folded into two alpha helices (A1-A8 and A12-A20) and contains an internal disulfide bridge (between cysteines A6 and A11). The B-chain presents a central, hydrophobic alpha helix (B8-B19) surrounded by the two interchain disulfide bridges, and a turn (B20-B23) (PDB 3I3Z and 3I40 [114]).

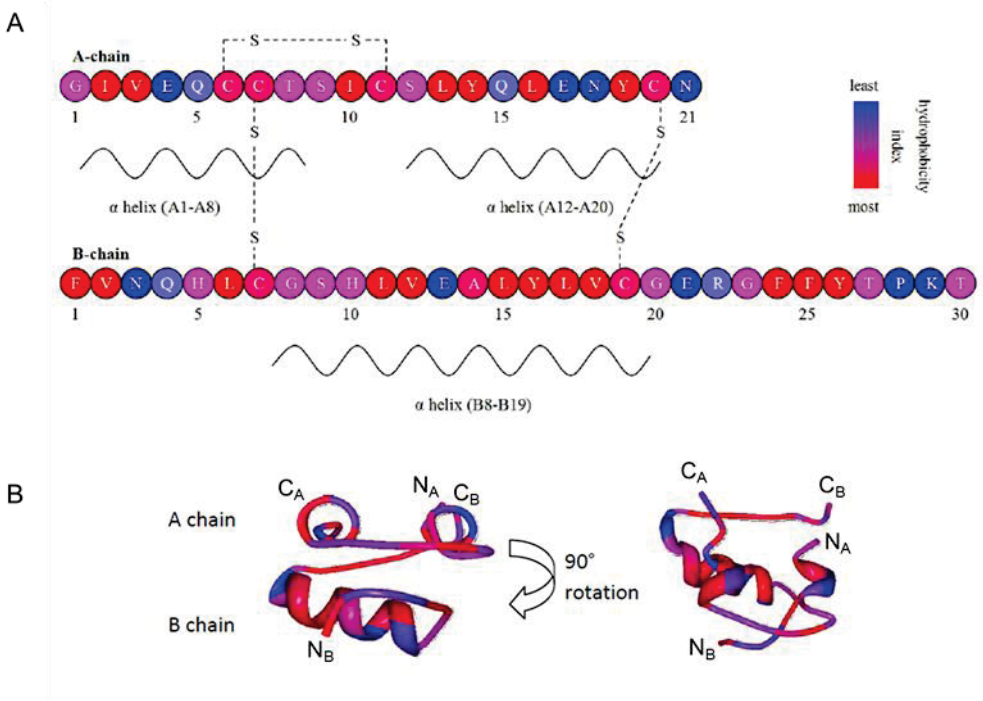

Figure 5-1: Human insulin primary, secondary and tertiary structure. A, Primary and secondary structure of human insulin. Disulfide bridges are represented by a dotted line and alpha helices by sinusoids. B, Monomeric tertiary structure. The color code represents the hydrophobicity of the amino acids from blue for most hydrophilic to red for most hydrophobic. N_A N_B and C_A C_B indicate N and C-termini of the A- and B-chain, respectively. Figure credits to T Ballet, PhD thesis, 2010, UJF, ED Phys.

In solution the quaternary structure of insulin is in equilibrium between the monomeric, dimeric and hexameric forms which coexist *in vivo* as well as *in vitro*. The monomer is the

biologically active form and the hexamer is the most stable one, used for insulin storage in granules. Insulin dimerization is stabilized by the formation of an antiparallel beta sheet between the C-termini of two B-chains and the packing of the B-chain alpha helices which increases the number of hydrophobic interactions in the dimer[115]. An insulin hexamer is composed of three dimers held together by two zinc ions that are conjugated by the imidazole ring of histidine B10 of each monomer[116]. Most of the hydrophobic side chains are located inside the hexameric structure, isolated from the solvent, resulting in an increased stability. The vast majority of our experiments are done at 0.5 $g.L^{-1}$ (86 μM) in a Zn-free buffer. Based on data obtained for bovine insulin [117,118], the monomer/dimer/hexamer distribution for a 0.5 $g.L^{-1}$ insulin solution at pH 7, 25 °C (in a 0.1 M TRIS-HCl and 0.1 M NaCl buffer), is estimated to be 5 %, 10 % and 85 %, respectively.

Recombinant human insulin produced in yeast (I2643 Sigma-Aldrich) is purchased as a powder and has to be solubilized before use. The solubilisation protocol involves a pH cycling between acidic and neutral pH in which the precision of the pH and the time the solution is kept at each pH impacts on the quality of the prepared solution. Hence, a meticulous preparation of insulin stock solutions is one of the corner stones in the reproducibility of the adsorption and aggregation experiments using this protein. Stock solutions (86 μM in 25 mM TRIS-HCl pH 7.4, 125 mM NaCl) are filtered and stored at 4°C.

Insulin amyloid aggregation is observed under two conditions:

- Acidic pH (pH 2) and high temperature (60°C)
- Neutral pH (pH 7), hydrophobic surfaces and agitation

In the latter case a temperature of 37°C is routinely used to speed up experimental protocols. Our work has been done exclusively in the latter condition and our standard insulin aggregation test consists in agitating (1200 rpm) an insulin solution (86 μM, 0.5 mg/mL) in a hydrophobic 96-well plate at pH 7.4. Thioflavin T (20 μM) is used as a conformational marker and its fluorescence properties in the fibre-bound state (λex ThT 450 nm; λem ThT 480 nm) are used to monitor insulin amyloid aggregation kinetics in time. A typical insulin aggregation kinetics is shown in Figure 5-2. The lagtime, during which aggregation nuclei are formed on

the hydrophobic surface, delimits the phase during which no ThT-positive aggregates can be recorded. It is followed by a growth phase during which insulin amyloid aggregates accumulate rapidly until no more monomeric insulin is available in solution (plateau phase). The lagtime is highly variable due to the stochastic nature of nuclei formation and is typically around 2-4h in our protocol. It should be noted that the reproducibility of the lag time also depends on the quality of the insulin solution during its preparation and storage.

The following subchapters describe insulin stability in the presence of hydrophobic interfaces, starting by rather macroscopic observations and then progressively revealing a more detailed molecular mechanistic view of the phenomena that produce insulin amyloid fibres at these interfaces.

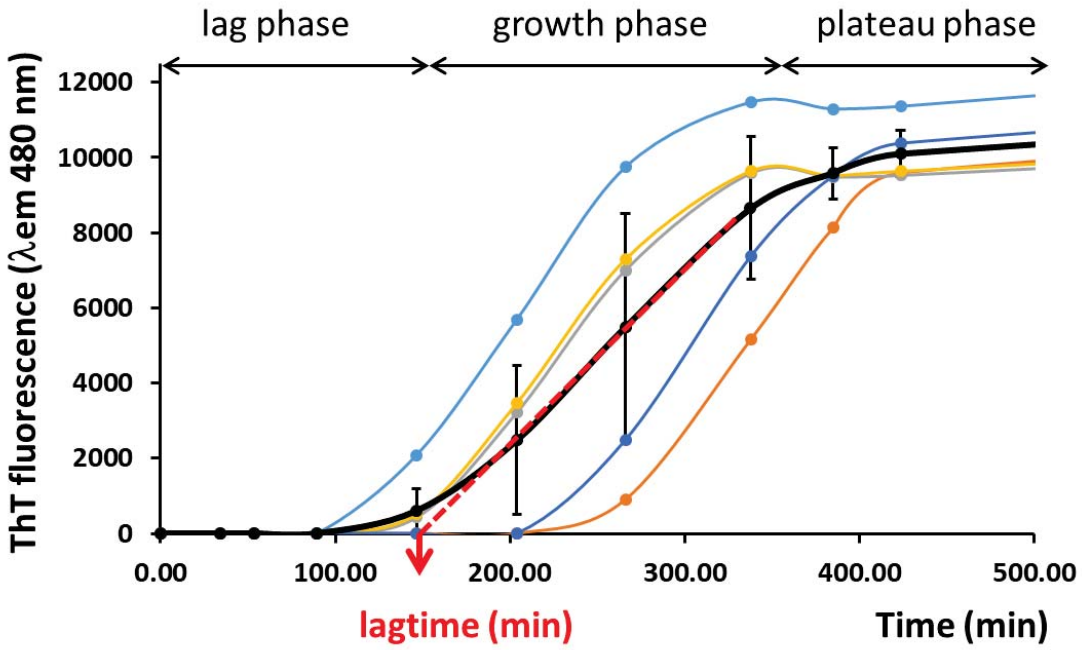

Figure 5-2: Insulin aggregation kinetics followed by ThT fluorescence in time. Coloured lines indicate kinetic data of individual replicates, the black line shows the mean curve with standard deviations. The lag phase is delimited by the lagtime (determined by the intercept of the slope (red dotted line) with the time axis). The growth phase and plateau phase are indicated. Figure credits to U Hevin.

5.3 Insulin amyloid aggregation at hydrophobic surfaces

As early as the 1940's Waugh described the "Fibrous modification of Insulin"[119] which he observed upon heating an acid insulin solution. At neutral pH, the aggregation of insulin into amyloid fibres was revealed when the first delivery systems involving pumps and syringes were introduced in the 1970s and 1980s[120]. Indeed, insulin deposits obstructing pumps and

catheters were regularly observed, and, when disposable syringes were introduced, silicone oil was identified as a major source for insulin aggregation[121,122]. It became apparent that insulin aggregation at neutral pH is mediated by its adsorption on hydrophobic surfaces and agitation was an important factor[123]. Sluzky analysed the effects of agitation rates, surface hydrophobicity, surface area and insulin concentration[75,124]. From these results, she proposed that insulin monomers could partially unfold upon reversible adsorption on hydrophobic surfaces. Such unfolded monomers could then either refold or interact *in solution* with other unfolded monomers to form aggregation nuclei, which eventually would lead to insulin amyloid aggregates in solution (Figure 5-3).

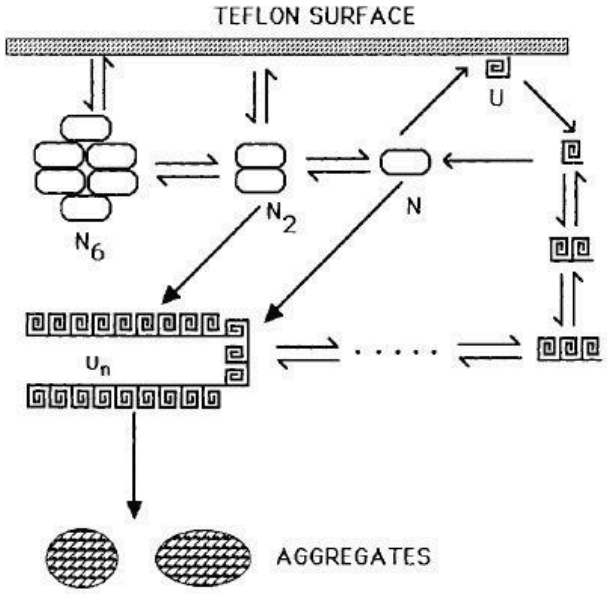

Figure 5-3: Model representing the mechanism of insulin aggregation at a hydrophobic interface as proposed by Sluzky[170].

In Thomas Ballet's PhD thesis, he developed a 96-well based assay to measure human insulin amyloid aggregation based on Thioflavin T (ThT) fluorescence[76,125]. This assay format allowed for multiple replicates and different solution conditions to be assayed simultaneously, thus enabling statistically sound experimental data to be produced in a relatively short time. He used functionalized beads and 96-well microplates with different hydrophobicities as solid interfaces and demonstrated that a hydrophobic surface pre-incubated with insulin could accelerate the formation of aggregation nuclei of a fresh insulin solution. On the other hand, the insulin solution from the pre-incubation experiment was not able to aggregate faster than a fresh insulin solution when put in contact with new hydrophobic surfaces. This

demonstrated that the aggregation nuclei are formed *on the hydrophobic surface* and remain strongly adsorbed on this surface (Figure 5-4).

Moreover, it was shown that fibril growth is a mechanism that takes place *on the hydrophobic surface*, before the fibres are shed into solution by agitation. Ballet also documented that hydrophobic surface-induced insulin amyloid aggregates have identical characteristics to those described in the literature that had been obtained in acid conditions and at high temperature[125]. Indeed cross-seeding experiments showed important lagtime accelerations and similar growth rates independently of the method used to generate insulin fibres[125].

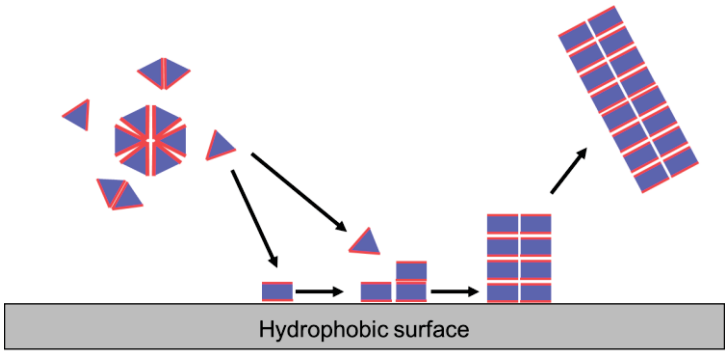

Figure 5-4: Model representing the mechanism of insulin aggregation at a hydrophobic interface as proposed by Ballet [125]. Triangles represent native (mono-, di- and hexameric) and rectangles represent partially unfolded insulin monomers. The red and blue colours represent a schematic distribution of hydrophobic (red) and hydrophilic (blue) parts of the protein. Figure adapted from Ballet [125].

In order to analyse insulin adsorption at hydrophobic surfaces *in situ* and in real time, to quantify adsorbed amounts, and to follow secondary structure changes of insulin accompanying its adsorption, surface-sensing techniques were used. Surface plasmon resonance (SPR) is sensitive to refractive index changes in the vicinity of a functionalized gold surface and one can therefore measure adsorption/desorption kinetics with an adequate time resolution (seconds)(Table 4-2). Using a dually functionalized gold prism, half hydrophobic, half hydrophilic (Figure 5-5 A), Laurent Nault studied insulin adsorption using SPR in the imaging mode (SPRi). It was demonstrated that insulin adsorbed exclusively on the hydrophobic surface, the signal on the hydrophilic surface being due to refractive index changes of the protein solution compared to buffer (Figure 5-5 B and C).

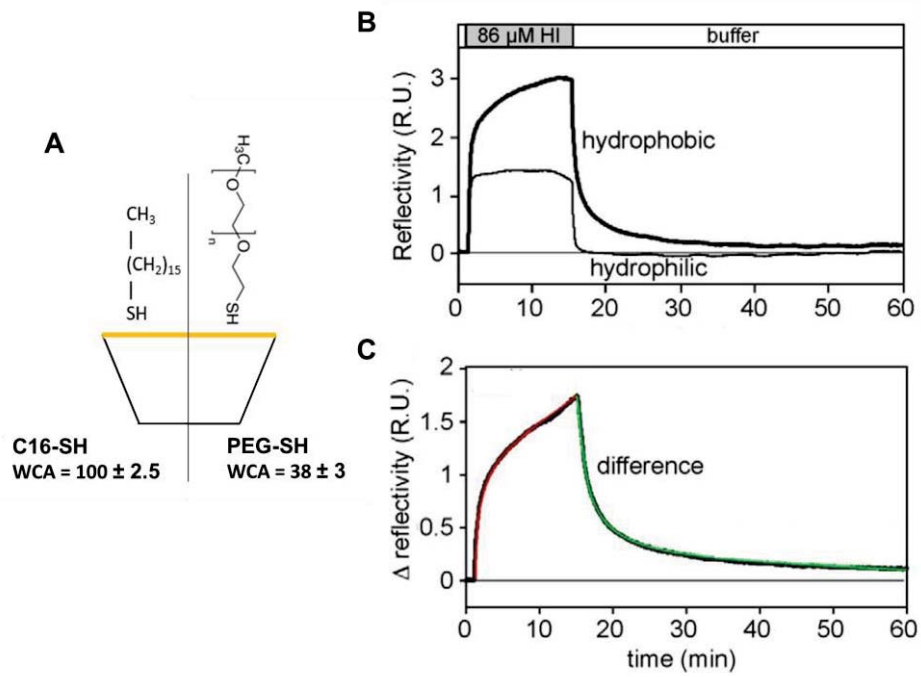

Figure 5-5: A Schematic representation of a dually functionalised gold prism with respective water contact angles (WCA) for the hydrophobic and hydrophilic sides. B SPRi reflectivity signal on the hydrophobic (bold line) and hydrophilic (thin line) sides obtained for a 86 µM insulin (HI) solution followed by a buffer wash. C HI association (red) and dissociation (green) kinetics on the hydrophobic surface as revealed by the difference signal (hydrophobic signal minus hydrophilic signal). Figure adapted from[110].

The adsorption of insulin on the hydrophobic surface rises sharply in about 1 minute followed by a slower almost linear adsorption phase. Similarly for desorption, a rapid and a slow decrease in the SPRi signal is observed. There is thus a defined sequence of adsorption events which starts with a very rapid monolayer formation on the surface followed by further binding of soluble insulin on top of the surface-adsorbed monolayer. The amplitude of the fast adsorbing insulin signal saturates with increasing concentrations of insulin in solution and a total amount of 260 ng.cm^{-2} is reached, when the entire hydrophobic surface is covered. Surface-adsorbed protein amounts reported in the literature are generally in the order of several hundred ng.cm^{-2} [126]. The dissociation kinetics corroborates the existence of two distinct pools of insulin at the surface: a strongly adsorbed layer, which desorbs very slowly, is covered by a more loosely adsorbed layer which dissociates rapidly upon dilution with buffer. With contact time the strongly adsorbed insulin pool becomes more important indicating that adsorbed insulin stabilizes further insulin binding at the surface.

To analyse the conformational state of insulin during the adsorption process on hydrophobic surfaces, attenuated total reflection Fourier transform infrared spectroscopy (ATR-FTIR) was used. It was confirmed that soluble and surface-aggregated insulin differed in their respective amide I band signatures, with a characteristic 1650 cm^{-1} band present in soluble insulin and two bands at 1660 and 1630 cm^{-1} for aggregated insulin[110,127]. Sequential acquisition of FTIR spectra in time showed that adsorbed insulin has a specific infrared signature, distinct from soluble or aggregated insulin. In the adsorbed protein, the amide A and amide II' bands are shifted to lower energies which goes in pair with an increase in hydrogen bonding. The amide I band of adsorbed insulin is compatible with the presence of intra and intermolecular beta-sheets (bands at 1635, 1687 and 1708 cm^{-1}). The evolution of the FTIR signatures with time corroborated the existence of different adsorbed insulin pools already characterized by their association and dissociation kinetics (SPRi). Other studies also point towards a decrease in alpha-helical structure upon adsorption to hydrophobic surfaces[128]. It should be noted however that in acidic conditions and at elevated temperature and longer incubation times adsorbed insulin was shown to remain in a close to native conformation on hydrophobic surfaces[129].

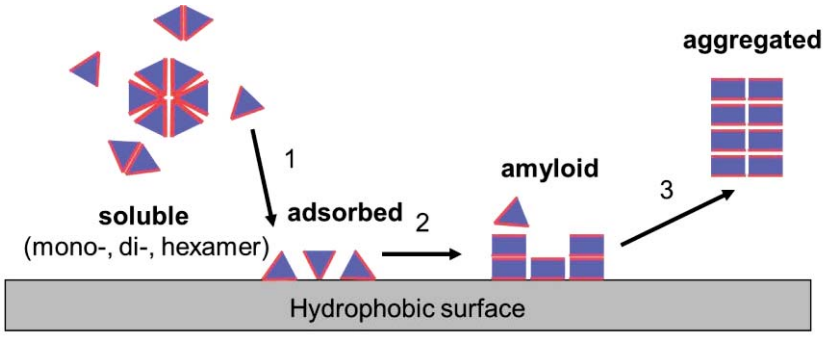

dissociation kinetics		fast	slow	
infrared signature	3420 cm^{-1} 1650 cm^{-1} 1450 cm^{-1}	3280 cm^{-1} 1655 cm^{-1} 1435 cm^{-1}	3280 cm^{-1} 1708 cm^{-1} 1435 cm^{-1}	3420 cm^{-1} 1630 cm^{-1} 1450 cm^{-1}
thioflavin T fluorescence	no	no	yes	yes

Figure 5-6: Sequence of insulin adsorption on hydrophobic surfaces. Schematic representation of the different conformational states of insulin (soluble, adsorbed, amyloid and aggregated). Triangles represent native and rectangles represent unfolded insulin monomers. The red and blue colours represent a schematic distribution of hydrophobic and hydrophilic parts of the protein, respectively. The characteristics in terms of dissociation kinetics, infrared signature and ThT fluorescence are given below for each state. Figure adapted from [110]

Using fluorescence microscopy to observe ThT fluorescence of adsorbed insulin flowing over a hrydrophobic glass surface in a flow chamber, the conformational state of the protein could be followed (Figure 5-6). (1) Monomeric insulin adsorbs rapidly on the hydrophobic surface, which is accompanied by a characteristic infrared signature (amide A and amide II' band shifts). At this stage aggregation nuclei are in formation on the surface but no ThT fluorescence can yet be measured. This adsorption is accompanied by alpha helix to beta sheet transitions in the protein and in this process the hydrophobic material surface (or air interface) are known to act as catalysts. Indeed they provide a platform for an accelerated formation of ThT-positive aggregation nuclei (2) [130–132]. Amyloid fibres then grow on the surface from these nuclei and are finally shed into solution (3).

Insulin adsorption and aggregation at hydrophobic surfaces is thus a complex, multistep phenomenon in which conformationally different protein populations exist and which results in the formation of amyloid fibres that are released from the surface upon agitation. Beyond surface hydrophobicity, surface roughness also influences insulin adsorption rates[133]. Several other recent studies using functionalized nanoparticles or quantum dots also confirm the importance of hydrophobicity in surface-induced amyloid insulin aggregation[134,135]. Insulin is stable when agitated in a hydrophilic 96-well microplate, indicating that the presence of a hydrophobic air interface alone is insufficient to trigger amyloid fibrillation[125].

5.4 Aggregative peptides and insulin aggregation at hydrophobic surfaces

In an attempt to elucidate the fibrillar structure of amyloids, the minimal amino acid sequence capable of producing these structures was analysed for diverse proteins. For insulin, Ivanova and coworkers showed that two peptides, SLYQLENY and LVEALYL, present in the A- and B-chain of insulin, respectively, formed amyloid fibrils on their own[136]. Analysing the structure of these fibrils they proposed a fibril model for insulin (Figure 5-7). The LVEALYL segments are stacked into tightly packed beta sheets, forming the dry steric zipper characteristic of the spine of amyloid fibres whereas the LYQLENY segments are on the periphery of the spine. The B-chain LVEALYL segment thus undergoes an alpha helix to beta sheet transition during insulin

amyloid aggregation. The disulfide bridge conservation between the A- and B-chain forces the A-chain segment to also adopt a beta sheet conformation, located at the edge of the fibril.

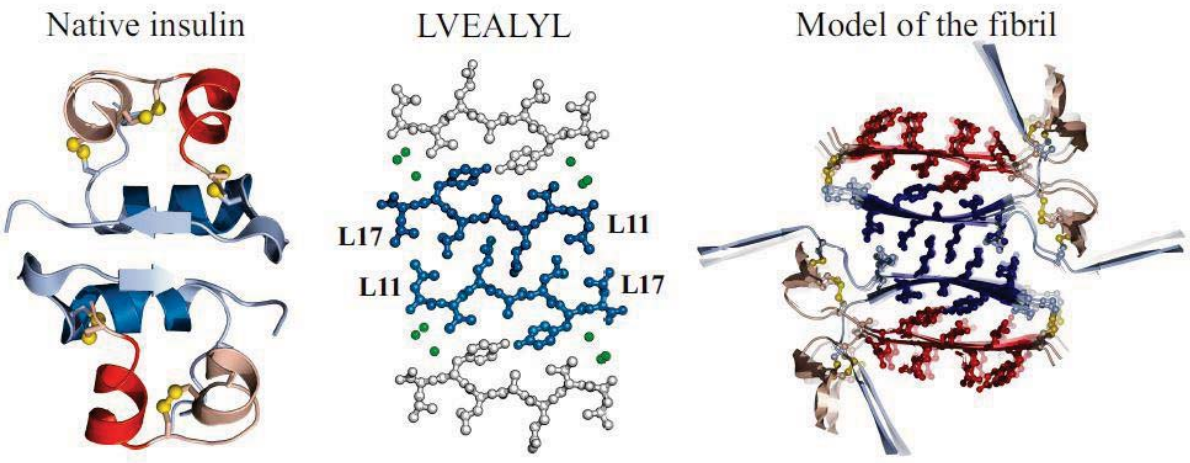

Figure 5-7: Fibril model of insulin. Left, Native structure of the insulin dimer (PDB 1GUJ), A chain in red, B chain in blue, LVEALYL segment in dark blue and SLYQLENY in dark red. Middle, View down the fibril axis of four beta-sheets in the crystal structure of B chain LVEALYL. The two sheets forming the dry steric zipper interface are in blue. Water molecules are shown as green spheres. Right, View of fibril model, looking down the fibril axis. Figure credits to [136]

While the SLYQLENY peptide had no significant effect on insulin aggregation kinetics, the LVEALYLV peptide was shown to accelerate the lagtime of insulin aggregation at sub stoichiometric concentrations (1:1/40) and to inhibit nucleation and fibril growth at equimolar concentrations in acidic conditions[136]. We showed that the acceleration of insulin amyloid aggregation in the presence of the LVEALYL peptide is also effective at neutral pH and is strictly dependent on the presence of hydrophobic surfaces[76] (Figure 5-8), which had not been examined by Ivanova.

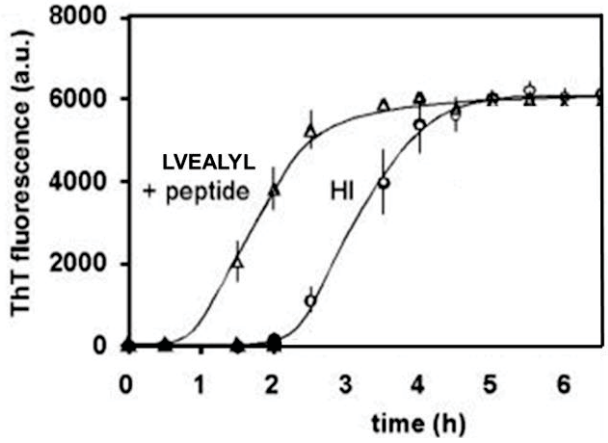

Figure 5-8: Human insulin (HI 86 μM) aggregation kinetics monitored by ThT fluorescence in the absence and presence of LVEALYL peptide (26 μM) during agitation in a multiwell plate at 37°C. Figure adapted from [76]

We showed that minute amounts of LVEALYL peptide remained stably adsorbed at hydrophobic surfaces and were responsible for the dramatic acceleration of insulin aggregation. A series of mutants of this peptide were also used to probe their effect on hydrophobic surface-mediated insulin aggregation[111]. Repetitive peptides alternating L and K residues were selected, because it was known from the literature that these would adsorb in beta sheet conformation on hydrophobic surfaces[137]. From SPRi studies and ATR-FTIR measurements, it was confirmed that peptides adopting a beta sheet structure when adsorbed on hydrophobic surfaces are capable to accelerate the formation of aggregative nuclei and therefore decrease the lagtime of insulin aggregation kinetics[110]. Moreover two other important characteristics were highlighted in this study:

-the accelerating effect could be obtained with amino acid sequences that are not present in the insulin primary sequence, like repetitive (LK) or (IS) sequences of various lengths. This confirmed that the adsorbed conformation of the peptide, namely beta sheet, was the dominating feature and not the primary sequence. Moreover the effect was correlated to the surface binding energy of the peptide on a hydrophobic surface.

-the accelerating effect was obtained at largely substoechiometric concentrations (with respect to the insulin concentration) which do not allow full surface coverage, indicating that aggregation nuclei form as discrete "islands" on the surface and not from a continuous peptide/protein layer (Figure 5-9).

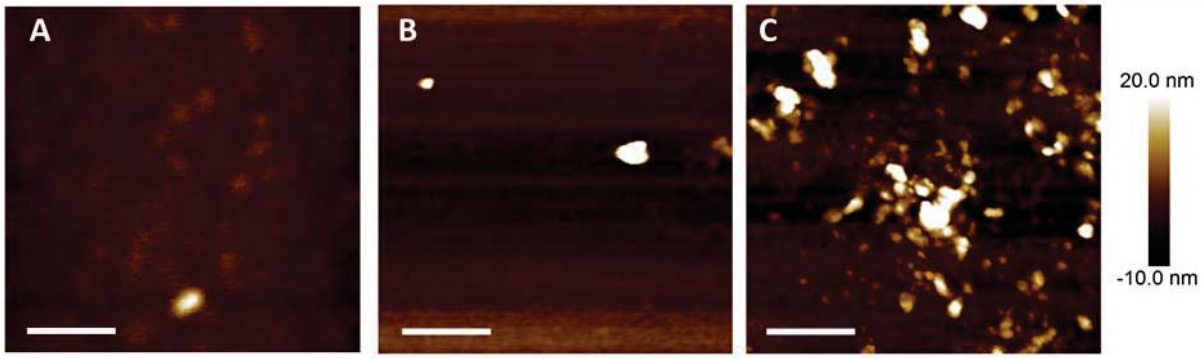

Figure 5-9: Observation of amyloid nuclei. AFM (tapping mode) images of silanized glass coverslips incubated at 37°C, 1200 rpm for 2h with peptide (LK)4L alone (A), for 1h with insulin solution (86 μM) without peptide (B) or with 0.2 μM of (LK)4L peptide (C). The scale bar represents 500 nm. Figure credits to [112]

The discovery of the properties of these aggregative (LK)nL peptides provided a tool to study the formation of surface-bound aggregation nuclei as the peptides could be employed simultaneously as aggregation inducers and tools to analyse the aggregates they triggered.

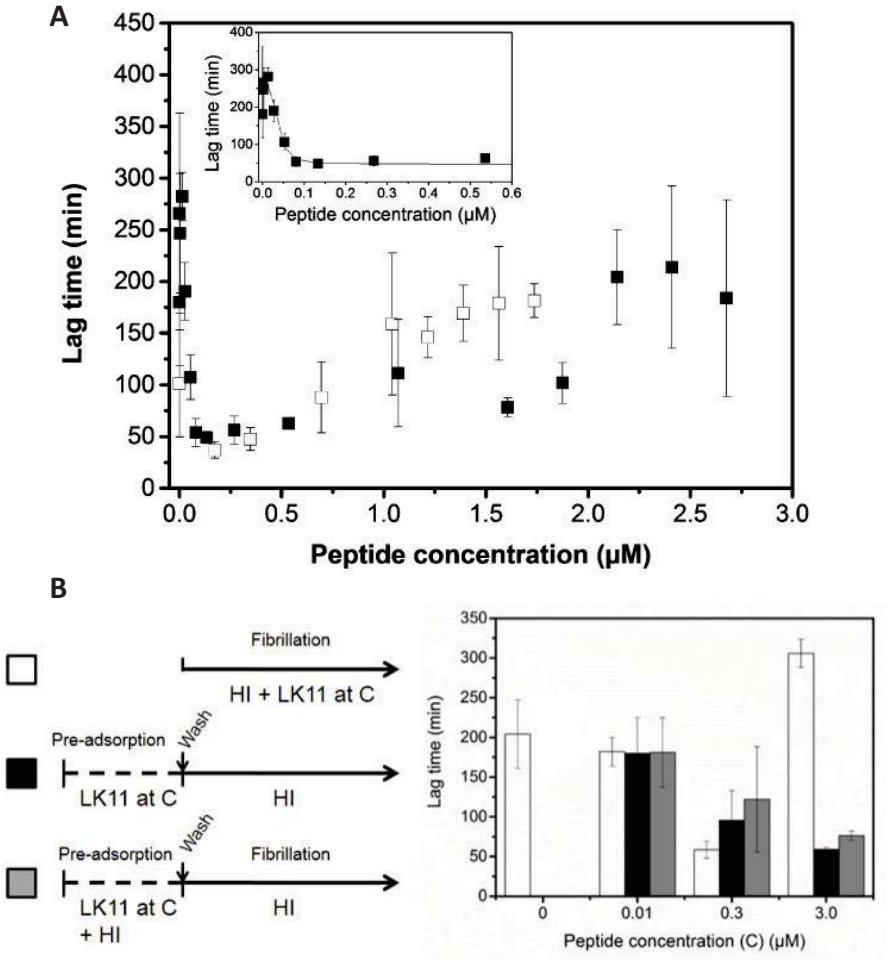

Figure 5-10: A Human insulin (86 μM) was incubated with $(LK)_4L$ (open squares) and $(LK)_5L$ (closed squares) at different concentrations in a hydrophobic 96 well plate at 37°C with agitation. The lagtime is represented as a function of concentration. B Pre-adsorption of $(LK)_5L$ (=LK11) at different concentrations and their influence on the aggregation lagtime. Figure credits to [112]

Using (LK)nL peptides of various length (2<n<5) we characterized their effects on insulin aggregation at hydrophobic surfaces as a function of their concentration[112]. For (LK)4L and (LK)5L, the aggregation lagtime is considerably shortened when these peptides are used in solution at 0.1 μM or lower concentrations. Above 0.3μM, the peptides have the opposite effect, i.e. delaying the lagtime (Figure 5-10 A). We have shown that these peptides cooperatively accelerate the formation of surface-bound aggregative nuclei through stable surface adsorption. The pre-adsorption of the peptides on the hydrophobic surface is

sufficient to trigger this acceleration effect (Figure 5-10 B) and the lagtime decrease goes in pair with a strong reduction in the variability associated with insulin amyloidal aggregation.

From these results, we concluded that surface-bound peptide patches facilitate the alpha helix to beta sheet transition in surface-adsorbing insulin by contact with lateral inter-peptide beta sheets (Figure 5-11). This mechanism drastically accelerates the formation of aggregative nuclei at the surface and alleviates the stochastic nature characterizing primary nucleation in amyloid aggregation kinetics.

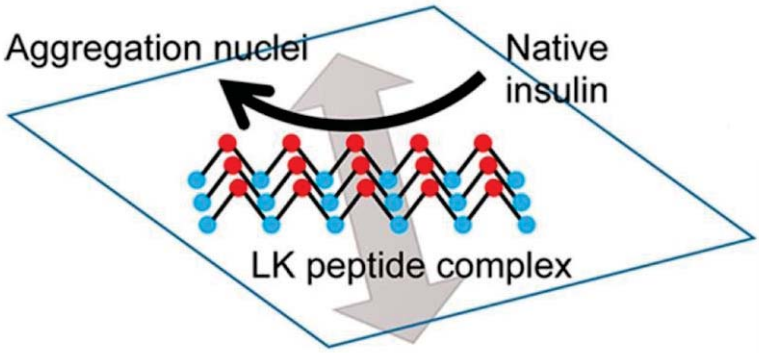

Figure 5-11: Scheme illustrating the accelerating effect of surface-adsorbed peptide patches on the formation of insulin aggregation nuclei. Surface-bound LK_5L peptide complexes (represented with blue leucine and red lysine residues) cooperatively and stably adsorb on the hydrophobic surface (square) in beta sheet conformation. The hydrogen-bonding axis is represented by a grey transparent double-headed arrow. Upon adsorption of native insulin, these peptides accelerate the formation of aggregation nuclei. Figure adapted from [112].

For $(LK)_4L$ and $(LK)_5L$ the accelerating effect on insulin aggregation kinetics is gradually lost at concentrations > 0.5 μM when an inhibitory effect is observed (Figure 5-10 A). We have demonstrated that this inhibition emanates from excess peptide in solution which prevents insulin from aggregating into growing amyloid fibres by stably binding to them. Electrostatic interactions between positively charged Lys (K) residues and negatively charged insulin (pI = 5.3) at pH7.5 play a role in this inhibition as shown by experiments using varying salt concentrations[112]. Co-precipitation experiments using a rhodamine labelled $(LK)_5L$ peptide, TAMRA-$(LK)_5L$, demonstrated that this peptide binds strongly to insulin aggregates, depleting the solution of the peptide with growing amounts of fibres[138]. This strong binding of the $(LK)_5L$ peptide to the growing fibre is responsible for the inhibition of insulin aggregation kinetics. By adding increasing concentrations of $(LK)_5L$ peptide in solution at different time points (60 and

120 min) during the insulin aggregation kinetics (Figure 5-12), we show that the growth rate is reduced as a function of concentration and tends towards a minimal growth rate. The aggregation can thus not be completely stopped, probably due to the generation of secondary nucleation sites. Such secondary nucleation sites are known to be induced by fibre breaking for example as a result of agitation[139]. The growth rate decrease is more pronounced when the peptide is introduced at 60 min, a time point in the kinetics, when insulin nuclei and fibres are less abundant. The minimal growth rate obtained after introducing the peptide at 120 min is twice as big as the one, when the peptide is introduced at 60 min. This is likely due to the amount of peptide remaining available in solution for inhibition, which is smaller at 120 min when the amount that can be bound to fibres is larger.

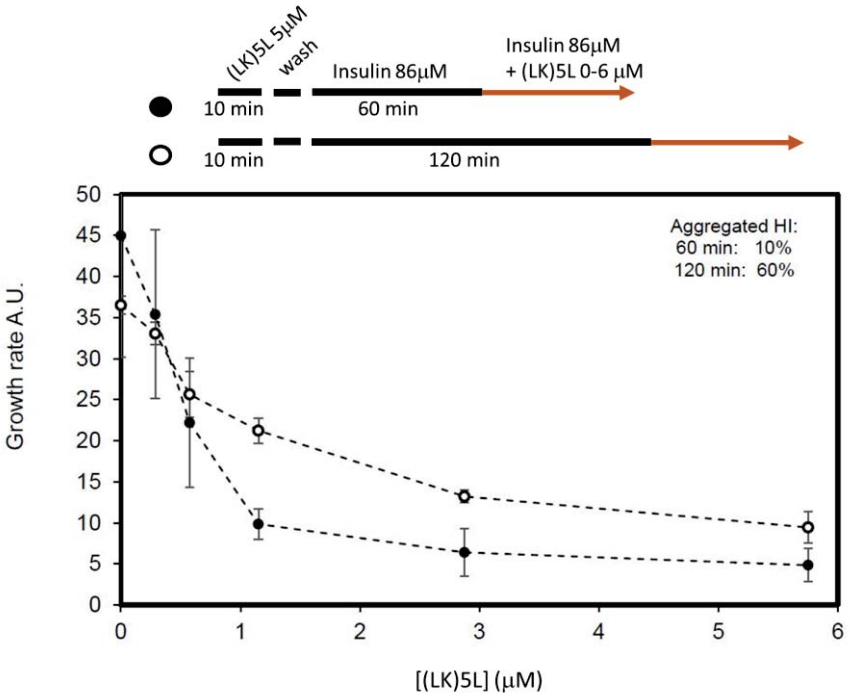

Figure 5-12: Plot showing the decrease of the insulin aggregation growth rate as a function of $(LK)_5L$ in solution. The wells of a hydrophobic multiwall plate are pre-incubated for 10 min with 5 μM $(LK)_5L$, they are washed, and insulin is added at 86 μM and incubated at 37°C with shaking. At timepoint 60 (closed circles) and 120 (open circles) minutes the indicated amount of $(LK)_5L$ peptide is added in solution and the growth rate is measured. Figure adapted from [138]

The inhibited growth rate recovers after several hours of incubation and the time needed to recover to the initial growth rate is shorter when larger amounts of fibrils are present at the addition of inhibiting concentrations of $(LK)_5L$ peptide (i.e. at later stages in the aggregation kinetics)[138]. Beyond binding to growing insulin amyloid fibres, excess $(LK)_5L$ peptides in

solution also interfere with the formation of effective aggregation nuclei. We therefore propose that the inhibiting effect of (LK)nL peptides in excess in solution is based on their strong binding to growing amyloid precursors and fibres.

From the ratio of bound peptide to amyloid insulin (1 peptide for 4-10 insulin molecules)[138], we predict that the peptide does not simply bind to the growing end of a fibre. The inhibition is thus more complex than a simple capping mechanism, preventing fibre elongation. There seems to be a distribution of peptide along the amyloid aggregate. This is also corroborated by preliminary results of fluorescence transfer experiments between fibre-bound thioflavinT and the TAMRA fluorophore of the peptide (Figure 5-13). Indeed the emission peak of fibre-bound ThT (centred at 480 nm) overlaps with the excitation peak of TAMRA (centred at 557 nm) between 450-550 nm, thus allowing fluorescence resonance energy transfer (FRET) between the two fluorophores if they are at close distance. When excited at 450nm (λex ThT), ThT bound to insulin fibres transmits the adsorbed energy to nearby bound TAMRA-$(LK)_5$L which in turn emits a fluorescence signal at 583 nm (λem TAMRA) (Figure 5-13, 0.5 μM (orange) and 1 μM (grey) TAMRA). With increasing amounts of TAMRA-labelled peptide, the fluorescence emission of TAMRA is self-quenched probably due to a local interference between closely bound fluorophores (Figure 5-13, TAMRA > 1 μM).

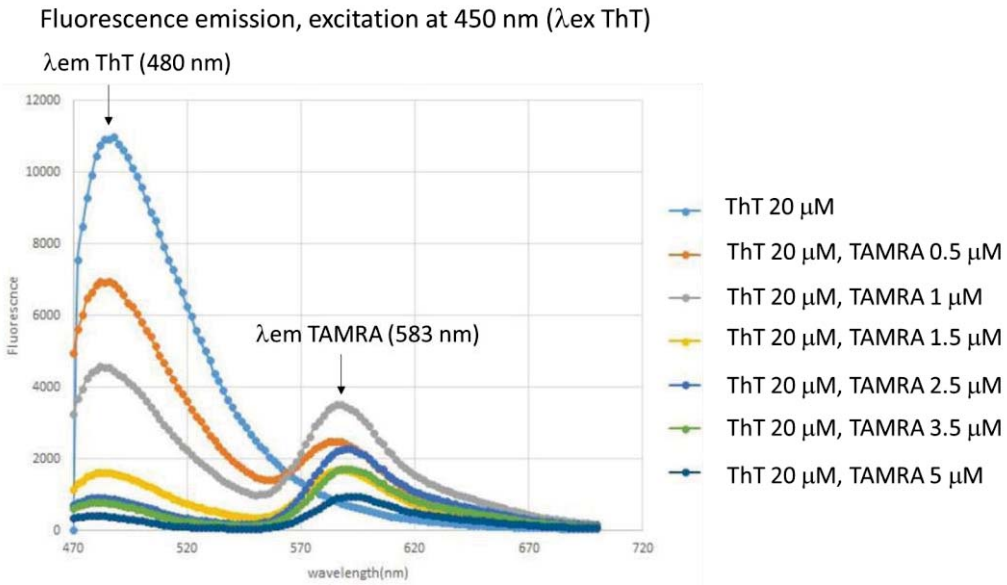

Figure 5-13: Fluorescence emission spectra of 86 μM insulin amyloid fibres incubated with thioflavin T (ThT) alone, or ThT with increasing amounts of TAMRA-$(LK)_5$L peptide. The excitation wavelength is 450 nm (λex ThT). Figure credits to W Labriji, N Yezza, C Lilliebjörn and A Gansmandel.

In conclusion, peptides, like (LK)nL peptides, adsorbing in beta-sheet conformation on hydrophobic surfaces accelerate the formation of aggregative nuclei that trigger insulin amyloid fibre growth on the surface. This effect is seen at low peptide concentrations (<< 1 μM), is strictly dependent on the presence of a hydrophobic surface and is based on a stable cooperative binding of the peptide at the surface. At higher concentrations (>3μM), when they stay in excess in solution, these peptides inhibit the insulin aggregation rate and bind to amyloid fibres and pre-aggregates. This binding is at least in part stabilized by electrostatic interactions and interferes with the effective incorporation of insulin monomers into growing fibrous aggregates.

Our study with peptides that interfere with insulin amyloid aggregation has allowed to shed light on the nucleation process at hydrophobic surfaces and on the growth mechanism of amyloid aggregates triggered by insulin surface adsorption. Beyond these fundamental results it has also allowed the development of fluorescent markers (TAMRA labelled peptides) that can be used to localize aggregates and to study their internal composition.

5.5 Insulin aggregation at a dynamic triple interface

Knowing that hydrophobic surfaces and agitation are both essential to trigger insulin amyloid aggregation at pH7, it is tempting to speculate that the movement of liquid over the hydrophobic surface is somehow involved in the trigger of the aggregation process. More precisely, the agitation of a solution in a container constantly moves the air-liquid interface up and down the container wall thus provoking a dynamic sweep of the triple line over the solid surface. The movement of the liquid generates a zone of intermittent wetting where liquid and air alternately recover the container wall (Figure 5-14).

Such dynamic triple interfaces are very frequently encountered in the handling of protein solutions. For therapeutic proteins, this is the case during production and storage, but also during reconstitution, when pumping of the solution can create bubbles that move and might cavitate or during administration protocols when the therapeutic solution is manipulated in perfusion bags with headspaces. Recent studies have documented the effect of a changing

liquid-air interface in the context of therapeutic protein aggregation without being able to fully describe the fate of proteins at a moving triple line[97,140–143].

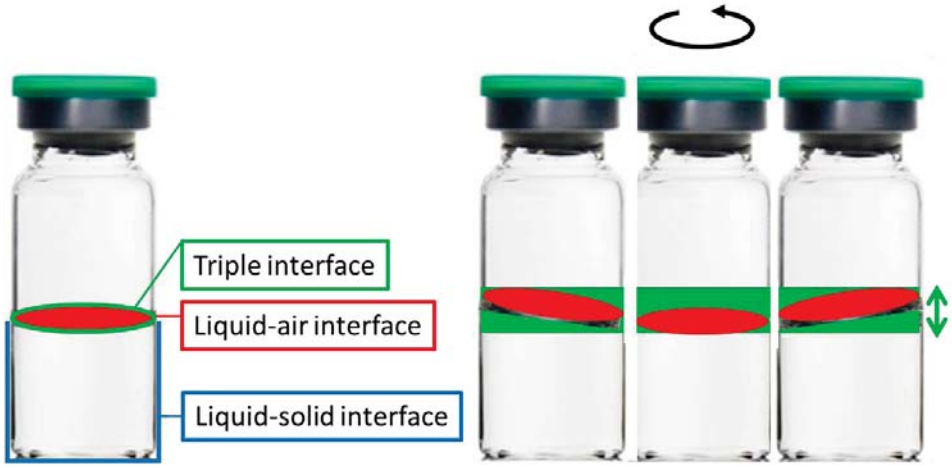

Figure 5-14: Moving triple interface upon agitation of a container with a liquid protein solution and an air headspace. The area swept by the triple interface is represented in green and its extension is indicated by a double-headed green arrow.

Karim Chouchane designed an experiment to precisely locate the formation of insulin amyloid aggregates at a hydrophobic surface, under solution agitation[138]. In a hydrophilic glass tube containing an insulin solution supplemented with ThT, a hydrophobic glass rod was introduced and rotated (1200 rpm for 2h) (Figure 5-15 A). ThT fluorescence was subsequently monitored along the glass rod (Figure 5-15 B) and it was shown that ThT-positive aggregates accumulate exclusively at the triple interface where the hydrophobic glass rod, the insulin solution and the air meet. The area covered by ThT-positive aggregates extends indeed over the surface that the inner meniscus of the solution sweeps when agitated by the hydrophobic glass rod.

No ThT-positive aggregates were observed on the hydrophilic glass tube and only a few fluorescent particles could be found on the permanently immerged surface of the hydrophobic glass rod. This shows that insulin preferentially unfolds and aggregates at the dynamic triple line due to the combination of two effects: a stable adsorption at the hydrophobic surface and a concomitant partial dehydration induced by intermittent wetting.

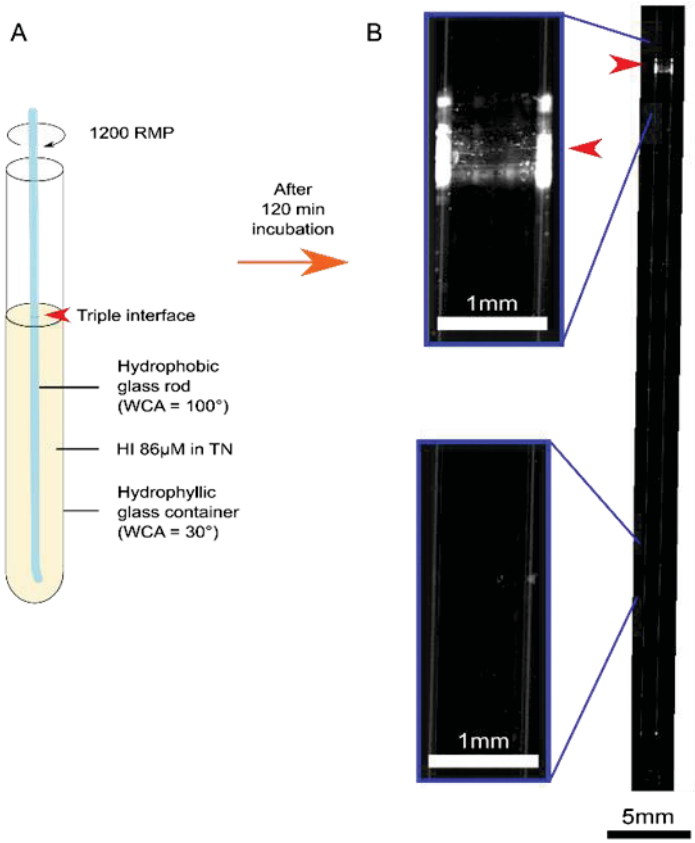

Figure 5-15: A Scheme of the experimental setup with a hydrophobic glass rod rotating in an insulin solution contained within a hydrophilic glass tube. B ThT fluorescence along the glass rod after 120 min incubation at 1200 rpm and 37°C. The red arrowheads indicate the triple interface.

In an effort to observe in real time what happens to proteins at a dynamic triple line, Thibaut Frachon designed a microfluidic setup allowing the movement of an insulin solution back and forth over a hydrophobic surface, thereby displacing the triple line locally and continuously in a controlled way (Figure 5-16). Combining reflection interference contrast (RICM) and fluorescence microscopy, the morphology of the liquid film and the formation of insulin amyloid deposits on the material surface was monitored, in real time and simultaneously.

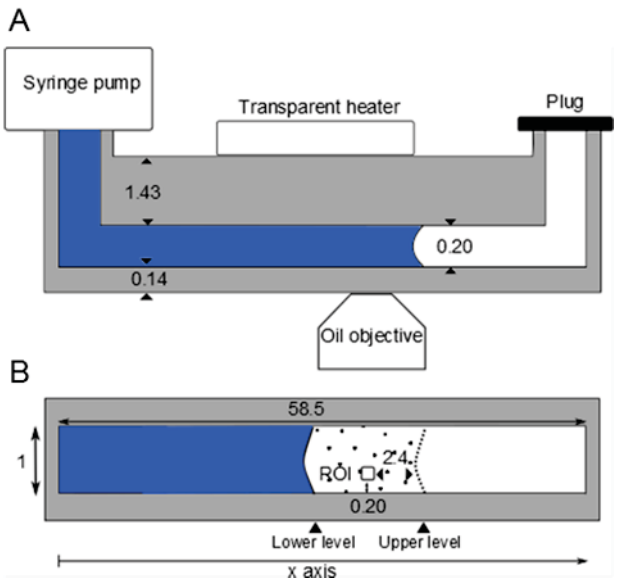

Figure 5-16: Microfluidic setup A, side view. B, top view. Blue colour represents the protein solution, white the air and grey the hydrophobic chip material. Dimensions are in mm. The x-axis represents the length of the channel and defines the position at which images are taken. Upper and lower levels correspond to the far left and far right meniscus positions during a hydration/dehydration cycle. ROI represents the microscope objective position and the field of view during image acquisition.

Inside the microfluidic channel, made of a hydrophobic plastic, three distinct areas can be identified: a zone (blue) that is constantly wet extends from the inlet until the lower level position of the solution meniscus, a zone (dotted) that is intermittently wet is bordered by the lower and upper levels of the solution meniscus, and a zone (white) that remains always dry is located beyond the upper level of the solution meniscus (Figure 5-16). Pumping an insulin solution back and forth in this channel, results in insulin aggregation with a nucleation-dependent kinetic, characteristic for amyloid aggregation (Figure 5-17A). The ThT-positive aggregate distribution within the channel was imaged at the plateau phase (Figure 5-17B). Amyloid aggregates grow only in the intermittently wet zone, where the triple interface is constantly moved over the hydrophobic surface. These aggregates are not desorbed and deposited elsewhere as the constantly wet and dry zones present very low levels of ThT fluorescence. The difference of the fluorescence signal between the always wet and intermittently wet regions shows that the presence of a triple interface is critical to induce insulin surface aggregation and that shear stress alone combined with a hydrophobic surface is not enough to trigger protein aggregation.

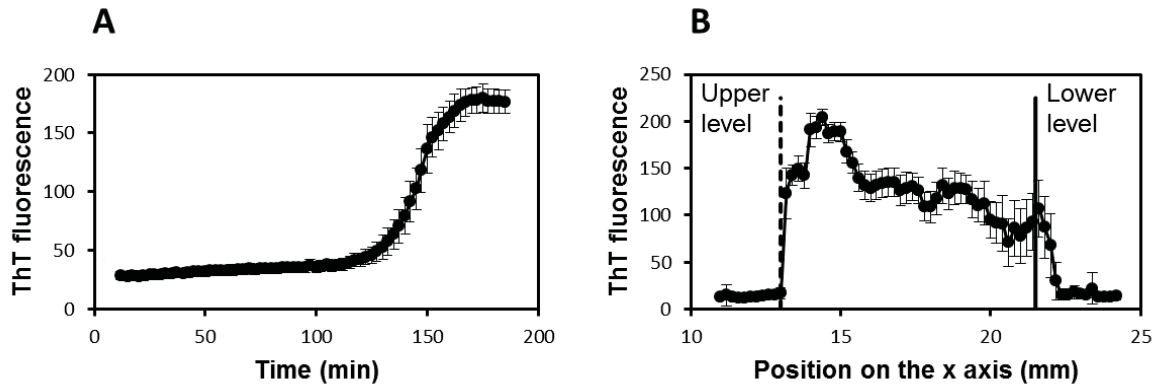

Figure 5-17: Insulin aggregation triggered by a moving triple interface. A Aggregation kinetics as a function of time (insulin 86 µM, displaced volume 2µL, cycling time 15s, 37°C). B ThT-positive aggregate distribution along the microchannel. The positions of the upper and lower level of the solution meniscus during cycling is indicated on the X axis.

RICM allows to observe the behaviour of the liquid film as it dewets the channel surface upon retraction of the insulin solution (Figure 5-18B, D and F). Liquid droplets are observed during dewetting and by analysing their position in time during wetting/dewetting cycles, it was shown that these droplets reform at identical positions on the dewetted surface during the lag and growth phase of the aggregation. At the plateau phase, a continuous liquid film covers the initially hydrophobic channel surface (Figure 5-18F). The identical repositioning of the droplets during the experiment is due to surface-adsorbed insulin that creates energetically favourable wetting zones, anchoring the liquid at the surface and thereby changing the water-retaining properties of the material. ThT fluorescence images (Figure 5-18A, C and E) indicate that insulin aggregates grow as circles that coincide with the border of the droplets (Figure 5-18C). These fluorescent rings grow eccentrically and expand on the surface until a continuous aggregate layer is formed (Figure 5-18E) that retains a thin water film during dewetting (Figure 5-18F). At each sweep of the triple line, a new layer of insulin aggregates is formed at the outer border of the already formed fluorescent aggregate ring (Figure 5-18G). No aggregates form at the centre of the droplet despite the fact that insulin is present in solution in this area.

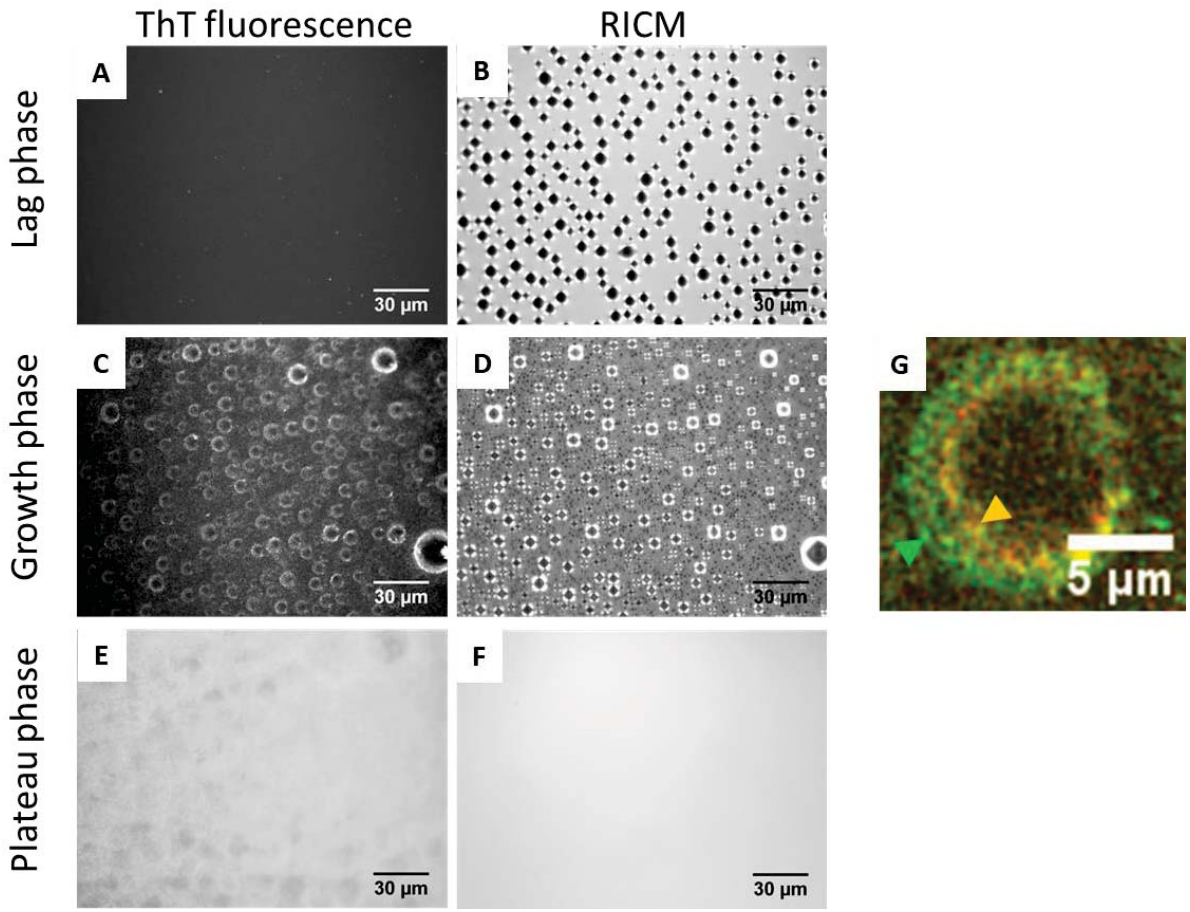

Figure 5-18: The position of ThT-positive insulin aggregates correlates with the position of droplets on the dewetted channel surface. A, C and E show ThT fluorescence images taken during the lag, growth and plateau phases, respectively, in the intermittently wet zone when the channel was filled with the insulin solution. B, D and F show RICM images taken at the same time points when the intermittently wet zone was exposed to the air. G Insulin amyloid aggregates grow eccentrically. Superimposition of a two THT fluorescence images taken at a 20 cycle interval. THT-positive amyloid aggregates are represented in red for the first image and in green for the following one. Overlapping fluorescent pixels between both images appear in yellow.

A thorough analysis of our results points towards the following detailed description of the parameters governing molecular aggregation at a dynamic triple interface (Figure 5-19):

Insulin stably adsorbs at hydrophobic surfaces and creates aggregation nuclei that act as surface anchoring points for the protein solution as the liquid sweeps over the surface. The droplets constitute the insulin supply and proteins adsorbed at the solid-liquid and air-liquid interfaces collide at the triple line inducing higher local concentrations and therefore intensifying intermolecular interactions. During dewetting, insulin from the air-liquid interface is incorporated into existing fibres. The partial dehydration induced by the receding liquid film favours intermolecular interactions between adsorbed proteins and protein fibrils, leading to amyloidal fibre growth. The driving force for the conformational change could in part be

provided by the release of solvation water around the insulin molecules concomitant with the formation of intermolecular hydrogen bonds. Our results imply that amyloid aggregates grow at the surface around the droplets rather than being formed elsewhere (e. g. at the liquid-air interface) and being deposited there. This is especially true when protein adsorption is strong enough to prevent their dissociation from the surface as the liquid is withdrawn.

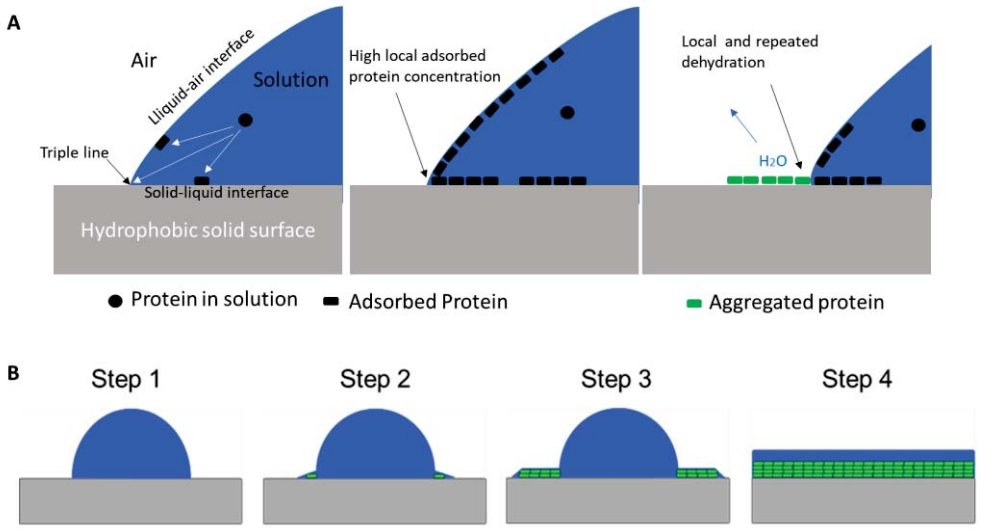

Figure 5-19: A Schematic representation of the parameters governing insulin aggregation at a dynamic triple interface. B : Schematic view of insulin aggregate growth at the triple interface.Step 1: liquid droplets are anchored at the surface by surface-adsorbed proteins. Step 2: ThT-positive insulin aggregates start to appear at the edge of the droplets. Step 3: the aggregates grow radially outwards of the droplets. Step 4: the microchannel surface is entirely covered by amyloid fibres retaining a continuous liquid film. Figure adapted from [99].

These experiments establish a predominant role of dynamic triple interfaces over hydrophobic solid or air interfaces alone for insulin aggregation. Indeed, it was shown earlier, that insulin is stable when agitated in a hydrophilic microwell plate, where a mobile liquid-air interface is present[125]. The liquid-air interface is thus less efficient at promoting insulin aggregation. We have shown that shear stress alone is not responsible for insulin aggregation as no ThT-positive aggregates accumulate in the permanently wet zone, where the same fluid movement is applied as in the intermittently wet zone. Aggregation is therefore mostly due to dehydration of surface-absorbed proteins at the triple line.

Looking back at the experimental setups used in the literature and in our own work to assess protein stability at interfaces, it appears that in the vast majority of the cases, a stable surface adsorption combined with a moving liquid-air interface is present when solutions are agitated

in one way or another in the presence of air. A partial dehydration of adsorbed proteins by intermittent wetting similar to the processes observed in our microchannel setup is therefore likely to occur. Unfortunately, it is difficult and most studies do not aim at analysing the triple interface but rather follow protein aggregates in the bulk solution or at a particular interface where they accumulate, without tracing their origin. Intermittent wetting zones are likely to represent the primary location for preferential protein aggregation, rather than liquid-air or solid-liquid interfaces alone.

Pharmaceutical processes involving both a hydrophobic solid surface to which proteins can strongly adsorb and a moving air interface due to voluntary mixing (reconstitution or administration protocols) or fortuitous shaking (transport), should therefore be carefully monitored for the risk of potential protein aggregation. It is noteworthy to mention that surfactants, like polysorbate 80, protect insulin from aggregation at a dynamic triple interface in our microchannel system[99]. This emphasizes the importance of the role that such formulation additives play and justifies a thorough inspection of the molecular mechanisms involved in this stabilization.

6 Monoclonal antibody adsorption at material surfaces

This chapter presents my current research activity in collaboration with the Department of Formulation in Sanofi (Vitry sur Seine, France). The results have been obtained by Guillaume Lefèbvre who is currently doing a Cifre PhD thesis (2017-2020) under the guidance of Vasco Filipe (Sanofi) and myself.

6.1 The need for early stability studies in formulation optimization

Our research on insulin stability at interfaces has highlighted the primary role that adsorption of proteins at hydrophobic interfaces plays in the formation of protein aggregates. Indeed, stable interfacial adsorption is the very trigger of stability issues. As long as it can be minimized or, even better, avoided, the protein is not submitted to interfacial stresses like, for example, dehydration in the case of intermittent wetting, and its stability will not be affected. Therefore it is important to investigate the interfacial activity of a protein with appropriate *in situ*

characterisation techniques and to propose protocols that can be implemented into the development pipeline to address this topic.

Therapeutic monoclonal antibody formulations often include surfactants that stabilize the protein in solution (Table 4-3). The choice of the surfactant type and concentration has to be led by the molecular characteristics of the drug, the aggregation mechanism that it should prevent and the nature of the interfaces that it encounters[144]. Nonionic polysorbates (PS), such as PS80 or PS20, are often used because of their pronounced surface activity and their low toxicity[145]. In theory, surfactants protect proteins in solution by a thermodynamic or a colloidal stabilization mechanism[103,145]. In the first case, their preferential adsorption to interfaces shields the surface and prevents access for the protein at the interface. Adsorption-induced aggregation can thus efficiently reduced. Colloidal stabilisation can be achieved by direct molecular interaction with the protein, thus lowering its surface activity and preventing homomolecular aggregation in solution. While direct PS-mAb interactions have been shown to be too weak to impact its colloidal stability[146], numerous studies document that interfaces (solid, liquid and gaseous) pre-adsorbed with PS, prevent protein binding (for recent examples see [147–149]). An orogenic displacement can also occur, whereby the surfactant adsorbs gradually, starting from nucleation sites until a critical surface pressure is attained at which previously adsorbed proteins desorb[150].

One could assume that the protective effect of surfactants is reflected by the surfactant:protein molar ratio in therapeutic formulations, at least in the case of colloidal stabilisation. Comparing more than 50 different commercial therapeutic mAb formulations for their PS content, it appears that there is no obvious correlation between the mAb dosage and the surfactant concentration (Figure 6-1). There are thus no easy-to-implement rational guidelines that could direct the choice and concentration of surfactants in formulation optimization.

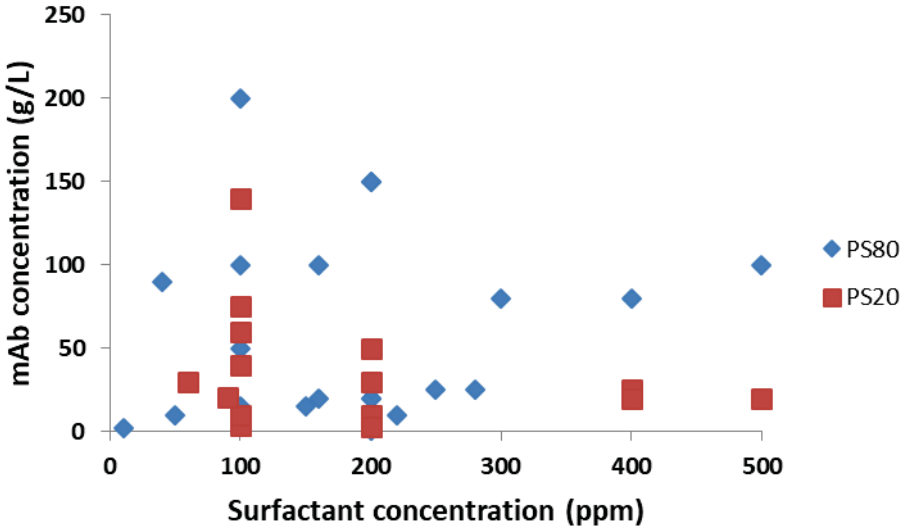

Figure 6-1: Plot showing the mAb concentration as a function of surfactant concentration for 53 different therapeutic mAb formulations (36 formulations with PS80 (blue diamonds), 17 formulations with PS20 (red squares)). PS80, polysorbate 80; PS20, polysorbate 20. Figure credits to G Lefèbvre.

The adsorption behaviour of a protein and surfactants at a given material surface can be used to guide drug candidate selection and formulation optimization. It is therefore our aim to develop biophysical characterization protocols that allow studying the adsorption and desorption properties of mAbs and surfactants at the solid-liquid interface. Our first approach is based on surface plasmon resonance imaging (SPRi) which allows to follow these events in real time and in parallel on different relevant surface chemistries. Chapters 6.2-6.4 summarize the kinetic SPRi studies that have been obtained so far for a given mAb and surfactant formulation. In chapter 6.5 I propose to use surface-enhanced ellipsometric contrast microscopy (SEEC) to image surface adsorption events with molecular resolution in order to provide a full picture of the interface activity of molecules in complex formulations. We focus in a first instance on the solid-liquid interface and will then analyse the liquid–air and triple interface. An overview of the experimental approaches is given in Table 6-1. Our research efforts aim at contributing to the development of tools and knowledge to understand molecular interface adsorption and guide formulation optimization. These contributions will help to anticipate device and container compatibility in early stability studies of drug candidates which has become an important topic. Indeed, the healthcare shift towards patient self-injection and homecare has initiated a rapid development of innovative drug storage, reconstitution and injection devices raising new challenges for biotherapeutic stability[151].

Experimental step	Technique used	Molecules	Parameters to be analysed	Output
Individual, sequential and concomittent adsorption studies	SPRi	mAbs Polysorbates Poloxamer	Surface chemistry Concentration Competitional binding	adsorption/desorption behaviour vs time adsorbed/desorbed amount
	SEEC			surface coverage/density vs time layer thickness
Kinetic adsorption studies	SPRi	mAbs Polysorbates Poloxamer	Surface chemistry	apparent k_{on} rates
Conformational adsorption studies	Fluorescence FTIR	mAbs Polysorbates Poloxamers	Surface chemistry Air interface	conformational signature

Table 6-1: Layout of the experimental approaches with parameters to be analysed and expected output.

6.2 Adsorption kinetics of mAbA at hydrophobic and hydrophilic surfaces

We have started working on the adsorption properties of a monoclonal antibody (termed mAbA) and different surfactants, supplied by Sanofi. The immunoglobulin is a glycosylated monoclonal IgG antibody of isotype 1, formulated at 30 $g.L^{-1}$ in a 20mM histidine buffer at pH6.0 containing 10% sucrose and 0.02 %w/v polysorbate 80. mAbA has been prepared without polysorbate for the experimental analysis. The following surfactants have been tested so far:

Surfactant	Supplier	CMC (%w/v)	N_{ag} (micelle aggregation number)	Micellar size (nm)
Polysorbate 80 (PS80)	Seppic	0.00332	280	10.7
Polysorbate 20 (PS20)	Seppic	0.00299	150	8.5

Table 6-2: Characteristics of polysorbates; the critical micellar concentration (CMC) is indicated for pure water.

We are performing the adsorption studies on a Horiba Scientific SPRi-Lab+™ instrument. A chemical functionalisation protocol was used to obtain a prism sensor surface that is covered with hydrophilic polyethyleneglycol-thiol (SH-PEG_8, water contact angle: 36° ± 3°) on one half and hydrophobic hexadecane-thiol (SH-C16, water contact angle: 103° ± 2°) on the other half[110]. This dual gold functionalisation allows to record the adsorption behaviour of mAbA and PS in parallel on the hydrophobic and hydrophilic surfaces. For this several analysis spots are defined on the surface, where the SPR signal is recorded. A sensogram is then plotted (Figure 6-2) which shows the average reflectivity measured on several spots as a function of time. The adsorption of mAbA is much more prominent on the hydrophobic surface than on the hydrophilic one (Figure 6-2A), with reflectivity difference maxima after rinsing on the hydrophobic surface ΔRH = 6 RU (mean ΔRH = 7.4 ± 1 RU, n=3) and on the hydrophilic surface ΔRh = 0.2 RU (mean ΔRh = 1.2 ± 1 RU, n=3), respectively.

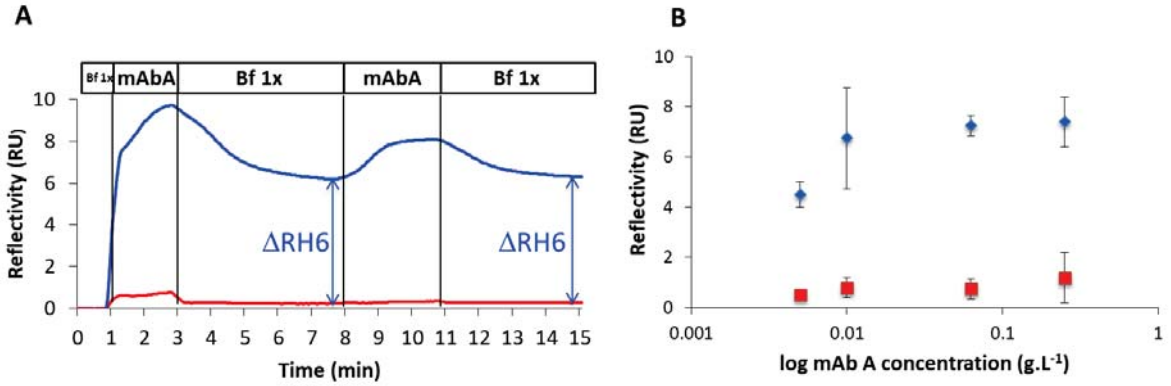

Figure 6-2: A: Sensograms representing the successive adsorption and desorption kinetics of two mAbA solutions (first injection 0.25 g.L-1, second injection 0.625 g.L-1) on the hydrophobic (blue) and hydrophilic (red) surfaces. Blue numbers indicate the ΔR measured on the hydrophobic surface at the indicated time points (double-headed arrow). Bf 1x represent buffer washes. B: ΔR values as a function of mAbA concentration measured on the hydrophobic (blue) and hydrophilic (red) surfaces. Sensograms display mean reflectivity signals obtained for at least three independent measurements at 4 different locations on the prism.

This preferential adsorption of mAbA on hydrophobic surfaces increases with the antibody bulk concentration (Figure 6-2B) and the surface contact time and is observed for all concentrations tested (0.005-0.25 $g.L^{-1}$) within the limit of the saturation of the SPR signal.

Successive injections of mAbA separated by a buffer wash indicate that the antibody can bind, albeit not stably, on previously adsorbed antibodies which therefore form a monolayer on the surface (Figure 6-2A). In our study, while mAbA has a net positive charge at pH6, the functionalized hydrophobic and hydrophilic surfaces are not charged. We therefore attribute

the surface activity of mAbA predominantly to hydrophobic interactions. Experimentally, we measured a maximal stable mAbA adsorption at 0.25 $g.L^{-1}$ of 0.9 ± 0.1 $ng.mm^{-2}$ (5 min contact time). Given the dimensions of the hydrophobic surface of the prism (71.25 mm^2), this corresponds to approximately 64 ± 7ng. This is slightly lower than the adsorbed amounts published for other IgGs[43,147], which are in the order of 10 $ng.mm^{-2}$. Differences on the amounts of surface-adsorbed mAbs should however be compared with care as they have been obtained on chemically different surfaces, with different protocols and techniques that have different sensitivities (TIRF, QCM-d, see also 4.4 Methods to characterize protein interfacial adsorption).

Bee and colleagues[152] have calculated the theoretical adsorption footprint and loading values for a mAb (IgG) monolayer according to different packing efficiencies. For the densest, end-on packing order and the least dense, side-on random sequential adsorption order, they found 0.26 and 1.04 $m^2.mg^{-1}$, (3.85 and 0.96 $ng.mm^{-2}$) respectively. Considering these surface packing orders, 68.5-274.0 ng mAbA could potentially bind on the hydrophobic contact surface of our SPRi prism (71.25 mm^2). Likewise a monolayer mass of 2 $ng.mm^{-2}$ was predicted for antibodies adopting a "flat-on" orientation on the surface by Buijs and colleagues[153]. We therefore conclude that the adsorbed mAbA amount, remaining after a buffer wash on the hydrophobic surface of the prism, is in accordance with a low density, side-on random packing order. Wiseman and Frank[154] analysed the orientation of an IgG1 antibody adsorbed on a hydrophobic surface as a function of its concentration by QCM-d. They conclude that up to a surface coverage of 2 $ng.mm^{-2}$, antibodies are adsorbed very rigidly in a "flat-on" orientation. Above this surface-coverage, antibodies approaching the hydrophobic surface bind in the remaining free interstices on the surface and adopt a more end-on orientation with a weaker coupling to the surface. Our sensogram, tracing the adsorption and desorption of mAbA on the C16-SH-coated surface (Figure 6-2A), shows an initial fast adsorption phase (first 30 s), followed by a slower adsorption phase (beyond 30 s). These distinct phases could potentially reflect the primary "flat-on" adsorption described by Wiseman and Frank[154], followed by a filling-up of free surface spaces between bound mAbA molecules. The subsequent flowing of buffer results in a partial desorption of bound mAbA, presumably dissociating weakly bound "end-on" antibodies. The remaining adsorbed mass (0.9 ± 0.1 $ng.mm^{-2}$ for mAbA at 0.25 $g.L^{-1}$

and 100µL.min^{-1}) is in accordance with the value of 2ng.mm^{-2}, determined by Wiseman and Frank[154]. Furthermore, a second injection of mAbA did not result in an increased reflectivity signal (Figure 6-2A), documenting that irreversible mAbA adsorption relies on available surface area and cannot be mediated by adsorption on previously adsorbed antibodies. This is consistent with results obtained by Bee and colleagues[155] who demonstrated monolayer coverage for a mAb interaction with a variety of hydrophilic nanoparticle surfaces. It is noteworthy that conformational changes in the Fab region of an IgG adsorbed on Teflon have been documented[156] as well as aggregation upon IgG adsorption to stainless steel[81]. In the latter case, antibody aggregation was occurring by successive layers of IgGs adsorbing on top of an irreversibly bound surface monolayer.

6.3 Polysorbates prevent adsorption but do not displace mAbA on hydrophobic and hydrophilic surfaces

In order to test whether polysorbates were able to protect mAbA from adsorption at surfaces we followed the SPRi signal during a sequential experiment using the polysorbates at 0.02% w/v: first polysorbates were put in contact with the functionalized prism surface followed by a washing step and then mAbA was flushed over the surface at 0.01 g.L^{-1}. As shown on Figure 6-3A, PS80 at 0.02% w/v adsorbs readily on the hydrophobic surface (ΔRH = 6 RU) while its adsorption on the hydrophilic surface remains very low (ΔRh = 0.5 RU). A subsequent injection of mAbA increases the SPRi signal very slightly but a buffer wash demonstrates that mAbA was not able to stably adsorb on any of the two surfaces. In a similar way, a pre-incubation of the prism surface with PS20 at 0.02% w/v prevents mAbA adsorption. A second injection of PS80 or PS20 shows that additional polysorbate molecules are able to bind on the pre-adsorbed hydrophobic surface, where mAbA molecules could not stably bind.

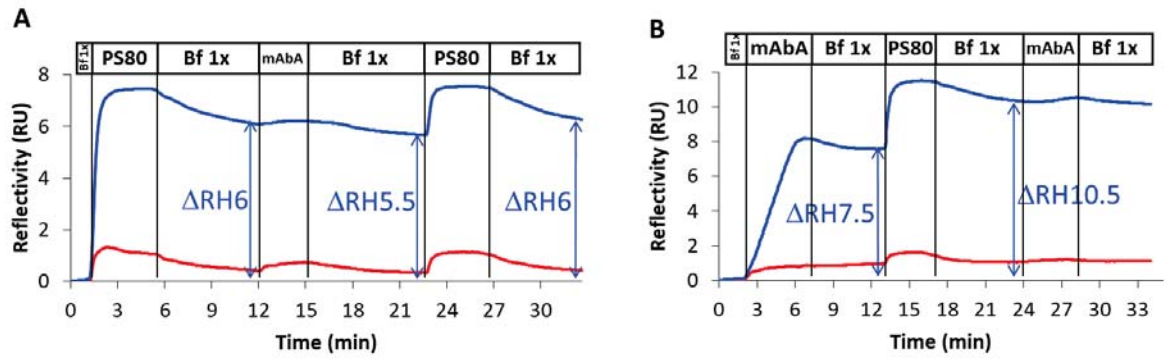

Figure 6-3: A: Sensograms representing the successive adsorption and desorption kinetics of a PS80 solution at 0.02% w/v followed by a mAbA solution at 0.01 g.L^{-1} and a second PS80 solution at 0.02% w/v on the hydrophobic (blue) and hydrophilic (red) surfaces. B Sensograms representing the successive adsorption and desorption kinetics of a mAbA solution at 0.01 g.L^{-1}, followed by a PS80 solution at 0.02% w/v and a second mAbA solution at 0.01 g.L^{-1} on the hydrophobic (blue) and hydrophilic (red) surfaces. Blue numbers indicate the ΔR measured on the hydrophobic surface at the indicated time points (double-headed arrow). Bf 1x represent buffer washes. Sensograms display mean reflectivity signals obtained for at least three independent measurements at 4 different locations on the prism.

We then performed the SPRi study in the reverse order and injected first the mAbA at 0.01 g.L^{-1}, followed by a buffer wash, before flushing the surface with the polysorbates at 0.02% w/v. As can be seen on Figure 6-3B, the mAbA binds preferentially to the hydrophobic surface and stays bound after rinsing with buffer (ΔRH = 7.5 RU). The increase of the SPRi signal after the subsequent injection of PS80 at 0.02% w/v (ΔRH = 10.5 RU) shows that an additional mass has been adsorbed at the hydrophobic surface, likely representing PS80 molecules that have been able to bind in between or on adsorbed mAbA molecules. This adsorbed mass desorbs extremely slowly upon buffer rinsing from the hydrophobic surface. An additional injection of mAbA at 0.01 g.L-1 does not change the SPRi signal anymore proving that no further molecular adsorption is possible. These results indicate that PS80 does not desorb previously bound mAbA from the hydrophobic surface. On the hydrophilic surface, the SPRi reflecticity signals measured upon contact with mAbA or PS80 do not allow concluding whether one molecular species remains adsorbed or is replaced by the other at the surface as both mAbA and PS80 bind very poorly to the hydrophilic surface. Similar results were obtained for PS20. The masses of PS20 and PS80, bound to a hydrophobic surface that is pre-adsorbed with mAbA, are very similar, indicating that both polysorbates are equally capable to fill in exposed free surface spaces or bind to adsorbed mAbA.

When polysorbates are adsorbed before mAbA injection, they completely prevent mAbA adsorption on the hydrophobic surface (Figure 6-3A). This is in agreement with the results of Kapp and colleagues[147] who have documented the same surface protection by a pre-adsorption of PS80 for two different IgG1 and IgG2 antibodies on a hydrophobic surface by TIRF and QCM-d. Joshi and colleagues[157] have shown a similar protective effect for a pre-coating with PS80 on lysozyme adsorption on a hydrophobic surface but a PS80 pre-coating could not prevent recombinant factor VIII adsorption[158]. A second injection of polysorbates shows that additional polysorbate can bind, where mAbA could not. This is likely due to the smaller size of polysorbates, which favours them for fitting into free surface spaces compared to the mAbA. The protective effect of a polysorbate precoating is likely to be dual: first, polysorbates occupy the hydrophobic interaction sites on the surface and mAbA cannot bind anymore and second, the hydrophilic heads of polysorbates sterically repulse mAbA molecules which cannot efficiently approach the surface.

When mAbA is adsorbed first to the hydrophobic surface, and polysorbates are injected subsequently after a buffer wash, the reflectivity signals show that additional polysorbate can bind in between or on surface-bound mAbA molecules (Figure 6-3B). There is no evidence for desorption and replacement of mAbA molecules by polysorbates on the hydrophobic surface. Indeed the reflectivity signal after the polysorbate injection (ΔRH=10.5 for PS80) is higher than the maximal ΔRH values obtained for polysorbate adsorption alone (not shown). We thus conclude that polysorbates are able to bind in addition to bound mAbA to the hydrophobic surface but do not displace mAbA while binding. A second injection of mAbA does not lead to an increase of the reflectivity signal (Figure 6-3B) that is observed for sequential injections of mAbA in Figure 6-2A. This indicates that the polysorbates bound in between or on adsorbed mAbs prevent further mAb adsorption efficiently. Kapp and colleagues show a drop in the intrinsic antibody fluorescence signal (TIRF) upon PS80 (2x CMC) rinsing of an IgG adsorbed on a hydrophobic surface[147]. They attribute this to a partial desorption of the antibody although the QCM-d signal of the same experimental sequence does not show a decrease in the adsorbed mass after the PS80 wash. PS80 does not desorb recombinant factor VIII from a hydrophobic surface as shown by ellipsometry[158]. Couston and colleagues, however, showed that polysorbates can desorb an adsorbed mAb from a hydrophobic silica surface with

efficiencies depending on the surface affinity of the polysorbate[159]. Similarly Serno and colleagues have shown efficient surface displacement of an IgG from the air-water interface by PS80[148]. In our case PS20 and PS80, at concentrations 10 times higher than their CMC, are incapable of displacing mAbA from the hydrophobic surface, despite their binding. It could be speculated that the surface orientation of the irreversibly adsorbed mAbA layer does not leave enough free space or is too strong for efficient polysorbate nucleation to establish a critical surface tension to displace mAbs. The extent of the orogenic effect depends strongly on the surfactant, the protein and the surface properties and can therefore not be generalized from one experimental system to another.

To conclude, these first experiments show that mAbA adsorbs preferentially as a monolayer on hydrophobic surfaces. Pre-adsorbed PS shields the surface from mAbA binding, so that the latter is no longer able to adsorb. However, once mAbA is bound, PS cannot displace it from the hydrophobic surface. These findings provide the first input into the molecular adsorption behaviour of the antibody and the surfactants, examined individually as a function of surface hydrophobicity.

In the therapeutic formulation mAbA is present at 30 $g.L^{-1}$ and PS80 at 0.02 %w/v. The competition for surface adsorption depends on the speed at which each molecule reaches the surface which is given by: $V_{ads} = k_{on}app \; . \; [C]$, in which $k_{on}app$ represents the apparent association rate constant of the molecule with the surface and [C] its respective concentration. Knowing the apparent association rate constants of formulation molecules for a given surface would thus allow predicting which molecule would adsorb first as a function of their respective concentrations.

It is known that the chosen formulation concentrations of mAbA and PS80 guarantee the stability of mAbA. This said, the molecular mechanism stabilising mAbA is not established and it is critical to understand protein-surfactant-surface interactions to guide formulation optimization. In order to investigate the competition between mAbA and PS80 for adsorption at a hydrophobic surface in the formulation conditions, we therefore set out to determine the apparent association rate constants of mAbA and PS for a bare hydrophobic surface.

6.4 Determination of apparent k_{on} rates for mAbA and polysorbates at a hydrophobic surface

SPR is widely used as a biosensing technique for the determination of association and dissociation rate constants in molecular interactions (Table 4-2). In the vast majority of the cases, one interacting species (ligand) is immobilized on the sensor surface while the second one (analyte) is flown over the surface in a controlled manner. The ligand is immobilized in such a way that the number of binding sites is very low compared to the concentration of the analyte in solution in order to avoid mass transport limitations[160]. In our case however, there is no immobilized ligand to which mAbA or PS bind, the surface-associated binding sites are unknown and they are potentially very abundant. It is therefore likely that rapid and massive binding of the analyte (mAbA or surfactant) in solution to the hydrophobic surface creates a depletion layer in the bulk analyte concentration near the surface, limiting its adsorption (Figure 6-4).

The formation of such a depletion layer implies that the diffusion of analyte from the bulk solution cannot match the removal of analyte by surface binding.

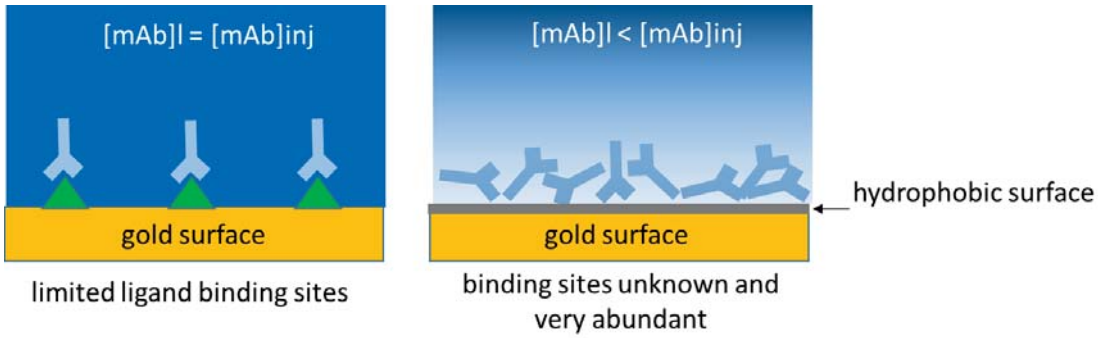

Figure 6-4: Schematic view of the prism surface in a common SPR binding study between a mAb and a limited number of surface-bound ligands (left) and our study with unknown and abundant surface binding sites (right). The blue shading represents the local concentration of mAb at the vicinity of the surface, [mAb]l, compared to the initial injected mAb concentration [mAb]inj.

For the determination of analyte association rate constants, however, it is assumed that the bulk concentration of analyte remains constant throughout the flow chamber at its initial injected value. Association rate constants commonly measured by SPR are in the range of 10^4-10^5 $M^{-1}.s^{-1}$, which is orders of magnitude below that for diffusion-limited reactions for proteins (10^9-10^{10} $M^{-1}.s^{-1}$)[161] and therefore depletion of the bulk analyte is usually not observed[162].

In our study, however, we demonstrate a striking dependence of the association of mAbA with the hydrophobic surface on the flow rate and the position on the surface inside the flow chamber with respect to the inlet (Figure 6-5).

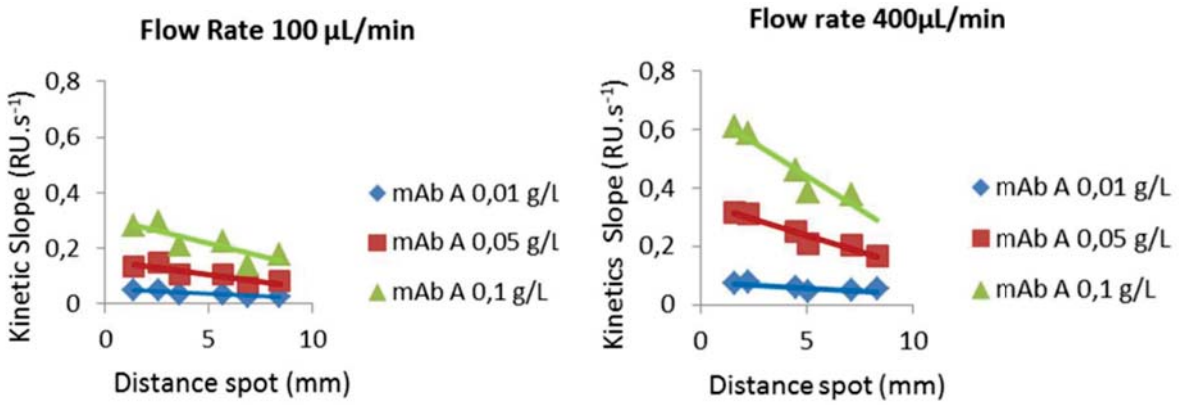

Figure 6-5: Plot showing the kinetic association slopes as a function of position in the flow chamber (distance definition, see Figure 6-6) at a flow rate of 100 µL/min (left) and 400 µL/min (right) for the indicated mAbA concentrations.

Therefore it is clear that a depletion layer forms, which places mAbA molecules too far from the surface for diffusion to allow them to approach the surface sufficiently in order to adsorb. This depletion layer increases, the further the solution flows over the hydrophobic surface (cf distance d in Figure 6-6) and hence the association rate becomes more and more underestimated with the distance along the flow chamber. This effect is especially pronounced at high mAbA concentrations and for high flow rates (Figure 6-5).

An efficient strategy to limit the creation of a depletion layer is to minimize the number of binding sites for mAbA on the surface. Knowing that mAbA does not bind to hydrophilic surfaces we chose to functionalize a gold prism such that the adsorption kinetics of mAbA could be studied at the smallest area possible when the antibody encounters the hydrophobic surface (Figure 6-6).

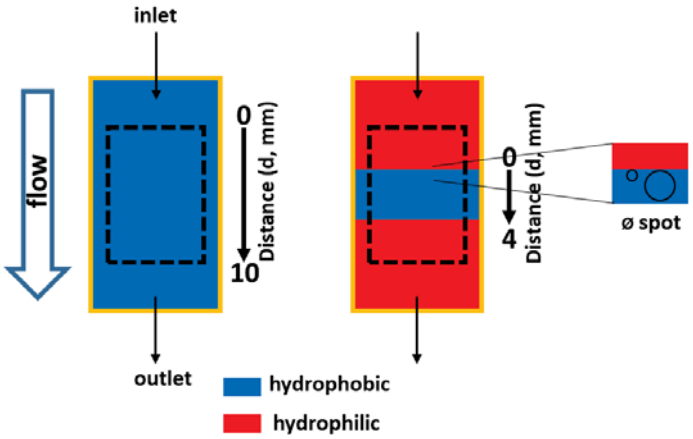

Figure 6-6: Schematic representation of the surface of a prism that is uniformly functionalized with hydrophobic hexadecane-thiol (blue, left) and one that is partly functionalized with polyethyleneglycol-thiol (red) and hexadecane-thiol (blue) (right). The study window is indicated by a dotted rectangle. The SPR signal is recorded at a spot that is positioned at the very border between the two surface chemistries and that has a minimal diameter (ø) (far right).

In this way it is possible to limit the depletion of the bulk mAbA concentration and to guarantee that the concentration of mAbA, in the vicinity of the surface position on which the binding kinetics is recorded, is approximately equal to the initial injected concentration.

We thus chose to record the mAbA binding kinetics for the hydrophobic surface right at the frontline between the hydrophilic and hydrophobic surface functionalisations and to limit the spot size to 33 µm (minimal spot size for our SPRi setup) (Figure 6-6). With these parameters we were able to estimate the apparent kon of mAbA for the hydrophobic surface to 1.4 ± 0.1 . 10^6 $M^{-1}.s^{-1}$. Our preliminary results (Figure 6-7) show that above a flow rate of 800 µL/min, the apparent k_{on} rate stabilizes. Unfortunately the spot size cannot be further decreased than 33 µm using the software associated with our SPRi apparatus but it is likely that even smaller spot sizes could provide a more accurate estimation. An extrapolation down to the minimal binding site area corresponding to the dimensions of a mAb size (3 x 10 nm), results in an estimated k_{on} app of 1.8-2.7 10^7 $M^{-1}.s^{-1}$.

So far no apparent molecular association rate constant for a bare surface without immobilized ligands has been described in the literature. This is certainly in part due to the experimental difficulty. Our SPRi setup allows to manually save images of the surface at a given spot position but this is only possible by stopping the experiment. If such images could be saved with a good time resolution, their analysis would allow to refine our data by minimizing the analysed surface area even further.

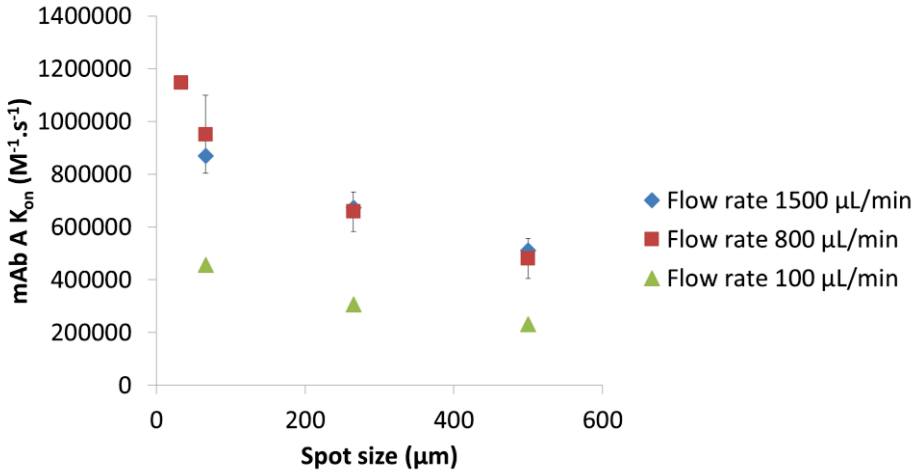

Figure 6-7: Apparent mAbA kon rates for a hydrophobic hexadecane-thiol surface as a function of spot diameter and flow rate. When data were obtained with multiple replicas (3 or more) the mean value is indicated and the error bars represent the standard deviation.

Once the apparent association rate constants for mAbA and PS are determined, one can theoretically predict which molecular species adsorbs first as a function of their respective formulation concentrations. It will then be necessary to verify that, at the proposed PS80 concentration (0.02 % w/v) used in the formulation of mAbA (30 g/L), the latter is effectively protected from surface adsorption by kinetic competition with PS80. For an injection of a mixture of mAbA and PS80, if mAbA adsorbs first at the hydrophobic surface, PS80 will not be able to desorb it (see results Figure 6-3B). However if the opposite is the case, mAbA will not be able to bind at the hydrophobic surface (see results Figure 6-3A). The presence of adsorbed mAbA can be tested using the SPRi signal of protein G or a secondary anti-IgG1 antibody that can bind to adsorbed mAbA. It might also be possible that the surface adsorption properties of the surfactants change in the presence of protein. Evidence for accelerated adsorption of PS in the presence of protein has been reported in the literature[163]. It is assumed that proteins can disrupt self-association of surfactants into micelles, thereby releasing monomers that will

bind to the surface. Surfactants that form stable complexes with proteins (e.g. poloxamers) and protect them by colloidal stabilization are not showing accelerated adsorption in the presence of protein.

6.5 Perspectives on molecular surface adsorption of mAbs and surfactants

In order to guide formulation optimization, it will be important to establish the underlying molecular protection mechanism in existing formulations. Considering the studied formulations, our approach will be the following:

- Determine apparent k_{on} rates for mAbs and surfactants from kinetic SPRi data
- Use k_{on} rates to predict if mAb or surfactant will bind first at the hydrophobic surface
- Demonstrate competitive binding of mAb or surfactant in formulation conditions
- Analyse stability of mAb under dehydration stress (air interface) with and without surfactants
- Establish molecular protection mechanism from the above results

We will analyse a series of mAb formulations with different types of immunoglobulins and surfactants on selected surface chemistries. The protocols for the kinetic analyses by SPRi are established and will be used to determine apparent k_{on} rates for the adsorption of the different molecules. The adsorption behaviour in formulation conditions can then be predicted and quantitatively verified. For this, we will develop an “ELISA-type” protocol using a secondary Ab or proteinA/G-based conjugate that allows to identify and quantify adsorbed mAb when a surface is incubated with the complete formulation, the formulation without mAb and the formulation without surfactant. This can be done using the SPRi signal of the binding secondary Ab or proteinA/G, or in a 96-well microplate protocol with an enzymatic readout.

The protection of the mAbs from dehydration stress at the air interface will also be analysed. As seen in chapter 5.5 (Insulin aggregation at a dynamic triple interface) the dehydration provoked by the movement of a sweeping solution meniscus over a hydrophobic surface with adsorbed proteins triggers their aggregation at the triple line. We will thus analyse the surface-adsorption state of mAbs in the presence or absence of surfactants, when they are transiently

exposed to air. SPRi allows to follow the adsorbed protein amount in these conditions and can therefore be used to study potential desorption. Conformational transitions induced by a transient exposure to air can be measured by infrared spectroscopy (ATR-FTIR) or with fluorescent conformational markers (e.g. ProteoStat). Obtaining images of adsorbed protein and surfactant layers in different conditions and on different surface chemistries is another useful complementary approach. Surface-enhanced ellipsometric contrast (SEEC) imaging is well suited for this. It is based on engineered glass coatings (commercialized by Nanolane), which allow to precisely control the surface reflection properties by multiple reflections and interferences such that the polarisation of the reflected light is not changed (Figure 6-8)[164]. In this way the contrast of nanometric objects deposited on them can be optimized. This is highly relevant for thin layers of translucent material that has very low optical contrast.

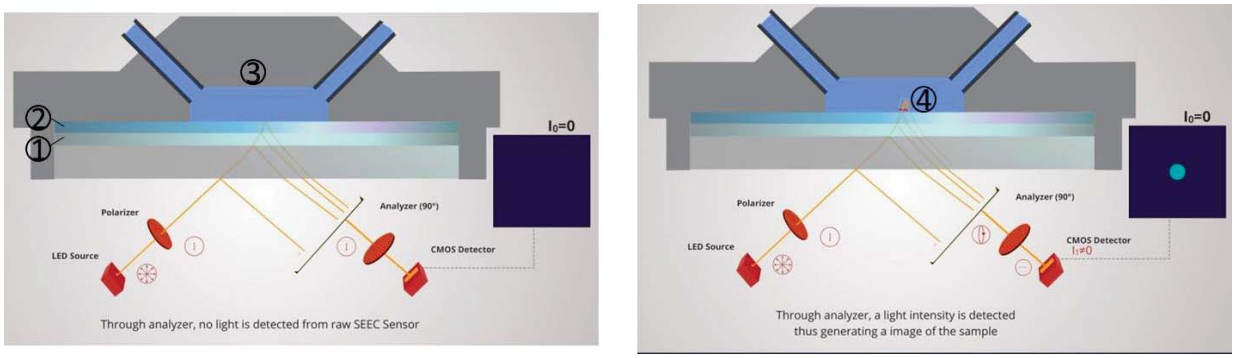

Figure 6-8: Principle of SEEC microscopy. Left A substrate (1) is covered by optical layers (2) providing a completely dark background (no change in the polarisation of the reflected light). Right When a small object binds to the surface (4), its presence is detected with nanometric axial sensitivity. Figure credits to Nanolane (http://www.nano-lane.com/seec-technology/principles/)

This interference microscopy technique can be used in liquid and in dry conditions (air) and is ideally suited to study protein adsorption at functionalized surfaces[165,166] as its axial (z) resolution is below 1 nm (Figure 6-9).

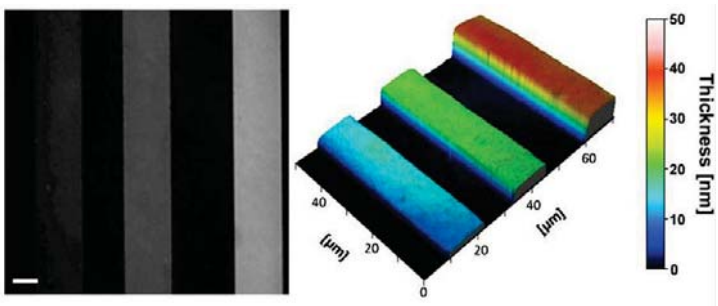

Figure 6-9: Wet-SEEC image (left) and Wet-SEEC topographic reconstruction (right) of calibrated resin steps, with thicknesses of 10, 18, and 40 nm. Scale bar, 10 µm. Figure adapted from[166].

In order to understand the molecular mechanisms underlying protein and surfactant surface adsorption it is important to obtain images of surface coverage and to measure surface-adsorbed molecular layer dimensions in real time. A detailed and more comprehensive picture of what happens to proteins and surfactants at liquid-solid and liquid-air interfaces can thus be obtained. Of special interest will be the SEEC analysis of the impact of dehydration. Measuring the variation of adsorbed layer thicknesses in response to dehydration can inform on the protection mechanism of surfactants which might help retaining water around adsorbed proteins (Figure 6-10). In this way, intermolecular protein aggregation triggered by the small distance between surface-adsorbed molecules and conformational changes due to variations in their hydration shell could be prevented.

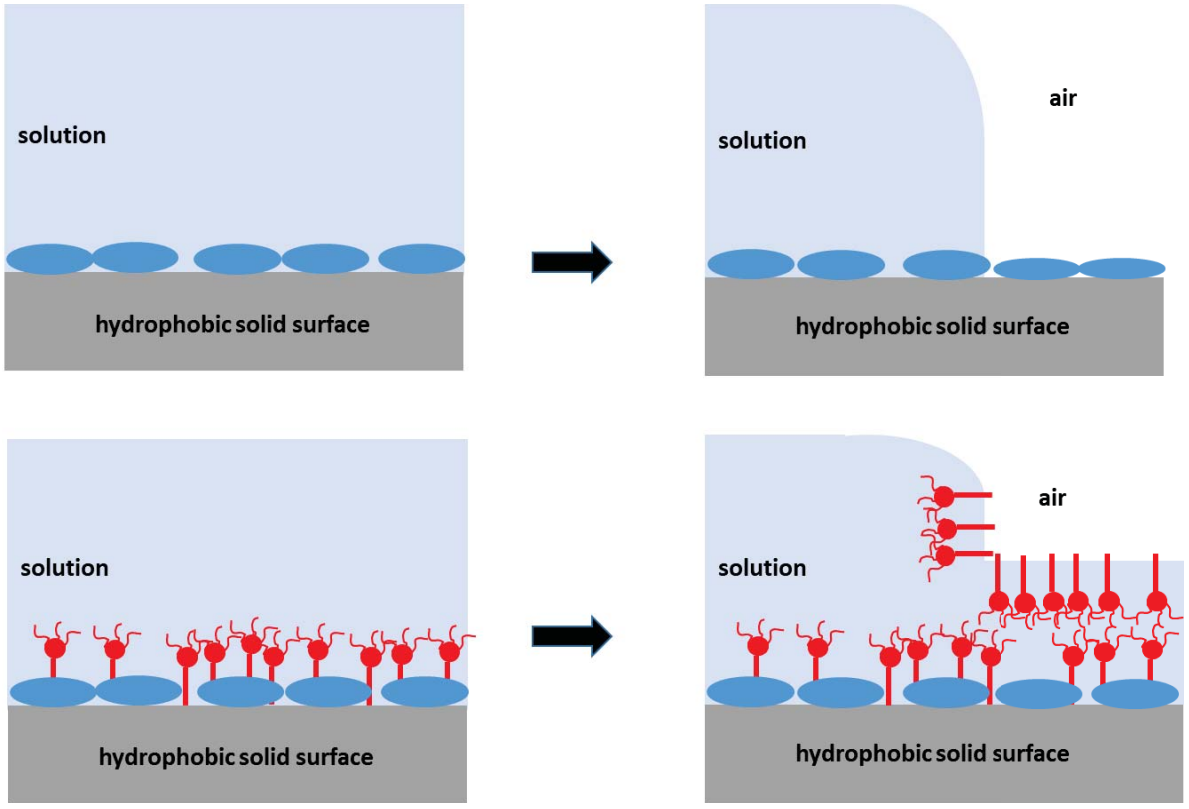

Figure 6-10: Scheme representing surface-adsorbed molecules (blue) which, when exposed to air, can be dehydrated (top). In the presence of surfactants (red) a protective water layer is retained (bottom).

The picture of how proteins and other molecules behave at interfaces is far from being completed. The infinite complexity of proteins and the simultaneous occurrence of different forces and phenomena at interfaces make this subject a rich and rewarding research area, abounding our fundamental knowledge in life sciences and applied research alike.

7 References

1. Hartl, F. U., Bracher, A. & Hayer-Hartl, M. Molecular chaperones in protein folding and proteostasis. *Nature* **475,** 324–332 (2011).
2. Saibil, H. Chaperone machines for protein folding, unfolding and disaggregation. *Nat Rev Mol Cell Biol* **14,** 630–642 (2013).
3. Anfinsen, C. B., Haber, E., Sela, M. & White, F. H. The kinetics of formation of native ribonuclease during oxidation of the reduced polypeptide chain. *Proc. Natl. Acad. Sci. U. S. A.* **47,** 1309–1314 (1961).
4. Jahn, T. R. & Radford, S. E. The Yin and Yang of protein folding. *FEBS J* **272,** 5962–5970 (2005).
5. Dragoš, A., Kovács, Á. T. & Claessen, D. The Role of Functional Amyloids in Multicellular Growth and Development of Gram-Positive Bacteria. *Biomolecules* **7,** 60 (2017).
6. Turoverov, K. K., Kuznetsova, I. M. & Uversky, V. N. The protein kingdom extended: ordered and intrinsically disordered proteins, their folding, supramolecular complex formation, and aggregation. *Prog Biophys Mol Biol* **102,** 73–84 (2010).
7. Fischer, E. Einfluss der Configuration auf die Wirkung der Enzyme. *Berichte der Dtsch. Chem. Gesellschaft* **27,** 2985–2993 (1894).
8. He, B. *et al.* Predicting intrinsic disorder in proteins: an overview. *Cell Res* **19,** 929–949 (2009).
9. Mollica, L. *et al.* Binding Mechanisms of Intrinsically Disordered Proteins: Theory, Simulation, and Experiment. *Front Mol Biosci* **3,** 52 (2016).
10. Zhou, H. X. Intrinsic disorder: signaling via highly specific but short-lived association. *Trends Biochem Sci* **37,** 43–48 (2012).
11. Novo, M., Freire, S. & Al-Soufi, W. Critical aggregation concentration for the formation of early Amyloid-β (1–42) oligomers. *Sci. Rep.* **8,** 1783 (2018).
12. Banerjee, S. *et al.* A novel pathway for amyloids self-assembly in aggregates at nanomolar concentration mediated by the interaction with surfaces. *Sci. Rep.* **7,** (2017).
13. Baldwin, A. J. *et al.* Metastability of native proteins and the phenomenon of amyloid formation. *J. Am. Chem. Soc.* **133,** 14160–14163 (2011).
14. Auer, S., Meersman, F., Dobson, C. M. & Vendruscolo, M. A generic mechanism of emergence of amyloid protofilaments from disordered oligomeric aggregates. *PLoS Comput. Biol.* **4,** (2008).
15. Eanes, E. D. & Glenner, G. G. X-ray diffraction studies on amyloid filaments. *J. Histochem. Cytochem.* **16,** 673–677 (1968).
16. Knowles, T. P. & Buehler, M. J. Nanomechanics of functional and pathological amyloid materials. *Nat Nanotechnol* **6,** 469–479 (2011).
17. Serpell, L. Amyloid structure. *Essays Biochem.* **56,** 1–10 (2014).
18. Jimenez, J. L. *et al.* The protofilament structure of insulin amyloid fibrils. *Proc Natl Acad Sci U S A* **99,** 9196–9201 (2002).
19. Glover, J. R. *et al.* Self-Seeded Fibers Formed by Sup35, the Protein Determinant of PSI+, a Heritable Prion-like Factor of S. cerevisiae. *Cell* **89,** 811–819 (1997).
20. Knowles, T. P. J. *et al.* Observation of spatial propagation of amyloid assembly from single nuclei. *Proc. Natl. Acad. Sci.* **108,** 14746–14751 (2011).

21. Fodera, V., Librizzi, F., Groenning, M., van de Weert, M. & Leone, M. Secondary nucleation and accessible surface in insulin amyloid fibril formation. *J Phys Chem B* **112,** 3853–3858 (2008).
22. Agrawal, S. G. & Paterson, A. H. J. Secondary Nucleation: Mechanisms and Models. *Chemical Engineering Communications* **202,** 698–706 (2015).
23. Forman-Kay, J. D. & Mittag, T. From sequence and forces to structure, function, and evolution of intrinsically disordered proteins. *Structure* **21,** 1492–1499 (2013).
24. Tyedmers, J., Mogk, A. & Bukau, B. Cellular strategies for controlling protein aggregation. *Nat Rev Mol Cell Biol* **11,** 777–788 (2010).
25. Scior, A., Juenemann, K. & Kirstein, J. Cellular strategies to cope with protein aggregation. *Essays Biochem.* **60,** 153–161 (2016).
26. Nakatogawa, H., Suzuki, K., Kamada, Y. & Ohsumi, Y. Dynamics and diversity in autophagy mechanisms: lessons from yeast. *Nat. Rev. Mol. Cell Biol.* **10,** 458–467 (2009).
27. Rapoport, T. A., Li, L. & Park, E. Structural and Mechanistic Insights into Protein Translocation. *Annu. Rev. Cell Dev. Biol.* **33,** annurev-cellbio-100616-060439 (2017).
28. Xu, J., Wang, J., Wimo, A. & Qiu, C. The economic burden of mental disorders in China, 2005-2013: implications for health policy. *BMC Psychiatry* **16,** 137 (2016).
29. Knowles, T. P. J., Vendruscolo, M. & Dobson, C. M. The amyloid state and its association with protein misfolding diseases. *Nat. Rev. Mol. Cell Biol.* **15,** 384–396 (2014).
30. Stefani, M. & Dobson, C. M. Protein aggregation and aggregate toxicity: new insights into protein folding, misfolding diseases and biological evolution. *J Mol Med* **81,** 678–699 (2003).
31. Baglioni, S. *et al.* Prefibrillar Amyloid Aggregates Could Be Generic Toxins in Higher Organisms. *J. Neurosci.* **26,** 8160–8167 (2006).
32. Olzscha, H. *et al.* Amyloid-like aggregates sequester numerous metastable proteins with essential cellular functions. *Cell* **144,** 67–78 (2011).
33. Bulawa, C. E. *et al.* Tafamidis, a potent and selective transthyretin kinetic stabilizer that inhibits the amyloid cascade. *Proc. Natl. Acad. Sci.* **109,** 9629–9634 (2012).
34. Ecker, D. M., Jones, S. D. & Levine, H. L. The therapeutic monoclonal antibody market. *MAbs* **7,** 9–14 (2015).
35. Strohl, W. R. Current progress in innovative engineered antibodies. *Protein and Cell* **9,** 86–120 (2018).
36. Jozala, A. F. *et al.* Biopharmaceuticals from microorganisms: from production to purification. *Brazilian J. Microbiol.* **47,** 51–63 (2016).
37. Karst, D. J., Steinebach, F. & Morbidelli, M. Continuous integrated manufacturing of therapeutic proteins. *Current Opinion in Biotechnology* **53,** 76–84 (2018).
38. Kolhe, P., Amend, E. & Singh, S. K. Impact of freezing on pH of buffered solutions and consequences for monoclonal antibody aggregation. *Biotechnol Prog* **26,** 727–733 (2010).
39. Privalov, P. L. Cold denaturation of proteins. *Crit Rev Biochem Mol Biol* **25,** 281–305 (1990).
40. Padala, C., Jameel, F., Rathore, N., Gupta, K. & Sethuraman, A. Impact of Uncontrolled vs Controlled Rate Freeze-Thaw Technologies on Process Performance and Product Quality. *PDA J Pharm Sci Technol* **64,** 290–298 (2010).

41. Rathore, N. & Rajan, R. S. Current Perspectives on Stability of Protein Drug Products during Formulation, Fill and Finish Operations. *Biotechnol Prog* **24,** 504–514 (2008).
42. Mahler, H.-C., Printz, M., Kopf, R., Schuller, R. & Müller, R. Behaviour of Polysorbate 20 During Dialysis, Concentration and Filtration Using Membrane Separation Techniques. *J Pharm Sci* **97,** 764–774
43. Mahler, H.-C. *et al.* Adsorption Behavior of a Surfactant and a Monoclonal Antibody to Sterilizing-Grade Filters. *J Pharm Sci* **99,** 2620–2627 (2010).
44. Bee, J. S., Randolph, T. W., Carpenter, J. F., Bishop, S. M. & Dimitrova, M. N. Effects of surfaces and leachables on the stability of biopharmaceuticals. *J Pharm Sci* **100,** 4158–4170 (2011).
45. Höger, K., Mathes, J. & Frieß, W. IgG1 adsorption to siliconized glass vials-influence of pH, ionic strength, and nonionic surfactants. *J Pharm Sci* **104,** 34–43 (2015).
46. Biddlecombe, J. G. *et al.* Determining antibody stability: creation of solid-liquid interfacial effects within a high shear environment. *Biotechnol Prog* **23,** 1218–1222 (2007).
47. Di Fede, G. *et al.* Monoclonal antibodies and antibody fragments: state of the art and future perspectives in the treatment of non-haematological tumors. *Expert Opin. Biol. Ther.* **11,** 1433–1445 (2011).
48. Saluja, A. & Kalonia, D. S. Nature and consequences of protein-protein interactions in high protein concentration solutions. *International Journal of Pharmaceutics* **358,** 1–15 (2008).
49. Torisu, T., Maruno, T., Hamaji, Y., Ohkubo, T. & Uchiyama, S. Synergistic Effect of Cavitation and Agitation on Protein Aggregation. *J. Pharm. Sci.* **106,** 521–529 (2017).
50. Rathore, N. *et al.* Characterization of protein rheology and delivery forces for combination products. *J. Pharm. Sci.* **101,** 4472–4480 (2012).
51. Ludwig, D. B., Carpenter, J. F., Hamel, J.-B. & Randolph, T. W. Protein adsorption and excipient effects on kinetic stability of silicone oil emulsions. *J Pharm Sci* **9999,** n/a (2009).
52. Basu, P., Blake-Haskins, A. W., O'Berry, K. B., Randolph, T. W. & Carpenter, J. F. Albinterferon α2b adsorption to silicone oil-water interfaces: Effects on protein conformation, aggregation, and subvisible particle formation. *J. Pharm. Sci.* **103,** 427–436 (2014).
53. Gerhardt, A. *et al.* Protein aggregation and particle formation in prefilled glass syringes. *J Pharm Sci* **103,** 1601–1612 (2014).
54. Thirumangalathu, R. *et al.* Silicone oil- and agitation-induced aggregation of a monoclonal antibody in aqueous solution. *J Pharm Sci* **98,** 3167–3181 (2009).
55. Kaur, K. Nanoemulsions as delivery vehicles for food and pharmaceuticals. in *Emulsions* 611–649 (Elsevier, 2016). doi:10.1016/B978-0-12-804306-6.00018-0
56. Gerhardt, A., Nguyen, B. H., Lewus, R., Carpenter, J. F. & Randolph, T. W. Effect of the siliconization method on particle generation in a monoclonal antibody formulation in pre-filled syringes. *J. Pharm. Sci.* **104,** 1601–1609 (2015).
57. Yano, Y. F. Kinetics of protein unfolding at interfaces. *Journal of Physics Condensed Matter* **24,** (2012).
58. Rabe, M., Verdes, D. & Seeger, S. Understanding protein adsorption phenomena at solid surfaces. *Adv Colloid Interface Sci* **162,** 87–106 (2011).

59. Pinholt, C., Hartvig, R. A., Medlicott, N. J. & Jorgensen, L. The importance of interfaces in protein drug delivery - why is protein adsorption of interest in pharmaceutical formulations? *Expert Opin Drug Deliv* **8,** 949–964 (2011).
60. Demanèche, S., Chapel, J. P., Monrozier, L. J. & Quiquampoix, H. Dissimilar pH-dependent adsorption features of bovine serum albumin and α-chymotrypsin on mica probed by AFM. *Colloids Surfaces B Biointerfaces* **70,** 226–231 (2009).
61. Rabe, M., Verdes, D., Zimmermann, J. & Seeger, S. Surface organization and cooperativity during nonspecific protein adsorption events. *J. Phys. Chem. B* **112,** 13971–13980 (2008).
62. Vroman, L. & Adams, A. L. Findings with the recording ellipsometer suggesting rapid exchange of specific plasma proteins at liquid/solid interfaces. *Surf. Sci.* **16,** 438–446 (1969).
63. Arai T, N. W. The behaviour of some model proteins at the solid-liquidinterface. *colloids surf* **51,** 1–15 (1990).
64. Jeon, S. I., Lee, J. H., Andrade, J. D. & De Gennes, P. G. Protein-surface interactions in the presence of polyethylene oxide. I. Simplified theory. *J. Colloid Interface Sci.* **142,** 149–158 (1991).
65. Jeon, S. I. & Andrade, J. D. Protein-surface interactions in the presence of polyethylene oxide. II. Effect of protein size. *J. Colloid Interface Sci.* **142,** 159–166 (1991).
66. Holmberg, M. & Hou, X. Competitive protein adsorption--multilayer adsorption and surface induced protein aggregation. *Langmuir* **25,** 2081–2089 (2009).
67. Kastantin, M., Langdon, B. B. & Schwartz, D. K. A Bottom-Up Approach to Understanding Protein Layer Formation at Solid-Liquid Interfaces. *Adv Colloid Interface Sci* **0,** 240–252 (2014).
68. Langmuir, I. Vapor pressures, evaporation, condensation and adsorption. *J. Am. Chem. Soc.* **54,** 2798–2832 (1932).
69. Cadilhe, A., Araújo, N. A. M. & Privman, V. Random sequential adsorption: From continuum to lattice and pre-patterned substrates. *J. Phys. Condens. Matter* **19,** (2007).
70. Norde, W. My voyage of discovery to proteins in flatland ...and beyond. *Colloids Surf B Biointerfaces* **61,** 1–9 (2008).
71. Kurrat, R., Ramsden, J. J. & Prenosil, J. E. Kinetic model for serum albumin adsorption: experimental verification. *J. Chem. Soc., Faraday Trans.* **90,** 587 (1994).
72. Tie, Y., Calonder, C. & Van Tassel, P. R. Protein adsorption: Kinetics and history dependence. *J Colloid Interface Sci* **268,** 1–11 (2003).
73. Chatelier, R. C. & Minton, A. P. Adsorption of globular proteins on locally planar surfaces: Models for the effect of excluded surface area and aggregation of adsorbed protein on adsorption equilibria. *Biophys. J.* **71,** 2367–2374 (1996).
74. Minton, A. Effects of excluded surface area and adsorbate clustering on surface adsorption of proteins. II. Kinetic models. *Biophys. J.* **80,** 1641–1648 (2001).
75. Sluzky, V., Tamada, J. A., Klibanov, A. M. & Langer, R. Kinetics of insulin aggregation in aqueous solutions upon agitation in the presence of hydrophobic surfaces. *Proc Natl Acad Sci U S A* **88,** 9377–9381 (1991).
76. Ballet, T. *et al.* DnaK prevents human insulin amyloid fiber formation on hydrophobic surfaces. *Biochemistry* **51,** 2172–2180 (2012).

77. Roberts, C. J. Therapeutic protein aggregation: Mechanisms, design, and control. *Trends in Biotechnology* **32,** 372–380 (2014).
78. Norde, W., MacRitchie, F., Nowicka, G. & Lyklema, J. Protein adsorption at solid-liquid interfaces: Reversibility and conformation aspects. *J. Colloid Interface Sci.* **112,** 447–456 (1986).
79. Norde, W. & Giacomelli, C. E. BSA structural changes during homomolecular exchange between the adsorbed and the dissolved states. in *Journal of Biotechnology* **79,** 259–268 (2000).
80. Vermonden, T., Giacomelli, C. E. & Norde, W. Reversibility of Structural Rearrangements in Bovine Serum Albumin during Homomolecular Exchange from AgI Particles. *Langmuir* **17,** 3734–3740 (2001).
81. Bee, J. S., Davis, M., Freund, E., Carpenter, J. F. & Randolph, T. W. Aggregation of a monoclonal antibody induced by adsorption to stainless steel. *Biotechnol. Bioeng.* **105,** 121–129 (2010).
82. Gurdak, E., Dupont-Gillain, C. C., Booth, J., Roberts, C. J. & Rouxhet, P. G. Resolution of the vertical and horizontal heterogeneity of adsorbed collagen layers by combination of QCM-D and AFM. *Langmuir* **21,** 10684–10692 (2005).
83. Herrera Estrada, L. P. & Champion, J. A. Protein nanoparticles for therapeutic protein delivery. *Biomater. Sci.* **3,** 787–799 (2015).
84. Reuter, B. & Petersen, C. Syringe siliconisation: Trends, methods, analysis procedures. *ONdrugDelivery* 16–19 (2013).
85. Krayukhina, E., Tsumoto, K., Uchiyama, S. & Fukui, K. Effects of syringe material and silicone oil lubrication on the stability of pharmaceutical proteins. *J. Pharm. Sci.* **104,** 527–535 (2015).
86. Hickel, A., Radke, C. J. & Blanch, H. W. Role of organic solvents on Pa-hydroxynitrile lyase interfacial activity and stability. *Biotechnol. Bioeng.* **74,** 18–28 (2001).
87. Zambaux, M. F., Bonneaux, F., Gref, R., Dellacherie, E. & Vigneron, C. Preparation and characterization of protein C-loaded PLA nanoparticles. *J. Control. Release* **60,** 179–188 (1999).
88. Gurkov, T. D., Russev, S. C., Danov, K. D., Ivanov, I. B. & Campbell, B. Monolayers of globular proteins on the air/water interface: Applicability of the volmer equation of state. *Langmuir* **19,** 7362–7369 (2003).
89. Beverung, C. J., Radke, C. J. & Blanch, H. W. Protein adsorption at the oil/water interface: Characterization of adsorption kinetics by dynamic interfacial tension measurements. *Biophys. Chem.* **81,** 59–80 (1999).
90. Koepf, E., Eisele, S., Schroeder, R., Brezesinski, G. & Friess, W. Notorious but not understood: How liquid-air interfacial stress triggers protein aggregation. *Int. J. Pharm.* **537,** 202–212 (2018).
91. Wrobel, S. Bubbles, Babies and Biology: The Story of Surfactant. *FASEB J.* **18,** 1624e–1624e (2004).
92. Pérez-Gil, J. Structure of pulmonary surfactant membranes and films: The role of proteins and lipid-protein interactions. *Biochim. Biophys. Acta - Biomembr.* **1778,** 1676–1695 (2008).

93. Lad, M. D., Birembaut, F., Matthew, J. M., Frazier, R. A. & Green, R. J. The adsorbed conformation of globular proteins at the air/water interface. *Phys. Chem. Chem. Phys.* **8,** 2179 (2006).
94. Jayaraman, M., Buck, P. M., Alphonse Ignatius, A., King, K. R. & Wang, W. Agitation-induced aggregation and subvisible particulate formation in model proteins. *Eur. J. Pharm. Biopharm.* **87,** 299–309 (2014).
95. Liu, L., Qi, W., Schwartz, D. K., Randolph, T. W. & Carpenter, J. F. The effects of excipients on protein aggregation during agitation: An interfacial shear rheology study. *J. Pharm. Sci.* **102,** 2460–2470 (2013).
96. Ghazvini, S., Kalonia, C., Volkin, D. B. & Dhar, P. Evaluating the Role of the Air-Solution Interface on the Mechanism of Subvisible Particle Formation Caused by Mechanical Agitation for an IgG1 mAb. *J. Pharm. Sci.* **105,** 1643–1656 (2016).
97. Bee, J. S., Schwartz, D. K., Trabelsi, S., Randolph, T. W. & Stevenson, J. L. Production of particles of therapeutic proteins at the air–water interface during compression/dilation cycles. *Soft Matter* **8,** 10329–10335 (2012).
98. Rudiuk, S., Huille, S., Tribet, C. & Cohen-Tannoudji, L. Importance of the dynamics of adsorption and of a transient interfacial stress on the formation of aggregates of IgG antibodies. *Soft Matter* **8,** 2651–2661 (2012).
99. Frachon, T., Bruckert, F., Le Masne, Q., Monnin, E. & Weidenhaupt, M. Insulin Aggregation at a Dynamic Solid-Liquid-Air Triple Interface. *Langmuir* **32,** 13009–13019 (2016).
100. Migliorini, E., Weidenhaupt, M. & Catherine, P. A practical guide to characterize biomolecule adsorption on solid surfaces. *Biointerphases* **13** (6), in press (2018)
101. Khan, T. A., Mahler, H.-C. & Kishore, R. S. K. Key interactions of surfactants in therapeutic protein formulations: A review. *Eur. J. Pharm. Biopharm.* **97,** 60–67 (2015).
102. Kamerzell, T. J., Esfandiary, R., Joshi, S. B., Middaugh, C. R. & Volkin, D. B. Protein-excipient interactions: Mechanisms and biophysical characterization applied to protein formulation development. *Advanced Drug Delivery Reviews* **63,** 1118–1159 (2011).
103. Lee, H. J., McAuley, A., Schilke, K. F. & McGuire, J. Molecular origins of surfactant-mediated stabilization of protein drugs. *Adv. Drug Deliv. Rev.* **63,** 1160–1171 (2011).
104. Das, T. K. Protein Particulate Detection Issues in Biotherapeutics Development—Current Status. *AAPS PharmSciTech* **13,** 732–746 (2012).
105. Elder, D. P., Kuentz, M. & Holm, R. Pharmaceutical excipients - Quality, regulatory and biopharmaceutical considerations. *Eur. J. Pharm. Sci.* **87,** 88–99 (2016).
106. Wang, W. Advanced protein formulations. *Protein Science* **24,** 1031–1039 (2015).
107. Frokjaer, S. & Otzen, D. E. Protein drug stability: a formulation challenge. *Nat Rev Drug Discov* **4,** 298–306 (2005).
108. Veronese, F. Peptide and protein PEGylation: a review of problems and solutions. *Biomaterials* **22,** 405–417 (2001).
109. Kurtzhals, P. Pharmacology of Insulin Detemir. *Endocrinol. Metab. Clin. North Am.* **36,** 14–20 (2007).
110. Nault, L. *et al.* Human insulin adsorption kinetics, conformational changes and amyloidal aggregate formation on hydrophobic surfaces. *Acta Biomater* **9,** 5070–5079 (2013).

111. Nault, L., Vendrely, C., Brechet, Y., Bruckert, F. & Weidenhaupt, M. Peptides that form beta-sheets on hydrophobic surfaces accelerate surface-induced insulin amyloidal aggregation. *FEBS Lett* **587,** 1281–1286 (2013).
112. Chouchane, K. *et al.* Dual Effect of (LK)nL Peptides on the Onset of Insulin Amyloid Fiber Formation at Hydrophobic Surfaces. *J Phys Chem B* **119,** 10543–10553 (2015).
113. Chouchane, K., Pignot-Paintrand, I., Bruckert, F. & Weidenhaupt, M. Visible light-induced insulin aggregation on surfaces via photoexcitation of bound thioflavin T. *J. Photochem. Photobiol. B Biol.* **181,** 89–97 (2018).
114. Timofeev, V. I. *et al.* X-ray investigation of gene-engineered human insulin crystallized from a solution containing polysialic acid. *Acta Crystallogr. Sect. F Struct. Biol. Cryst. Commun.* **66,** 259–263 (2010).
115. Murray-Rust, J., McLeod, A. N., Blundell, T. L. & Wood, S. P. Structure and evolution of insulins: Implications for receptor binding. *BioEssays* **14,** 325–331 (2018).
116. Huus, K., Havelund, S., Olsen, H. B., van de Weert, M. & Frokjaer, S. Thermal dissociation and unfolding of insulin. *Biochemistry* **44,** 11171–11177 (2005).
117. Jeffrey, P. D., Milthorpe, B. K. & Nichol, L. W. Polymerization pattern of insulin at pH 7.0. *Biochemistry* **15,** 4660–4665 (1976).
118. Milthorpe, B. K., Nichol, L. W. & Jeffrey, P. D. The polymerization pattern of zinc(II)-insulin at pH 7.0. *BBA - Protein Struct.* **495,** 195–202 (1977).
119. Waugh, D. F. A Fibrous Modification of Insulin. I. The Heat Precipitate of Insulin. *J. Am. Chem. Soc.* **68,** 247–250 (1946).
120. Irsigler, K. & Kritz, H. Long-term continuous intravenous insulin therapy with a portable insulin dosage-regulating apparatus. *Diabetes* **28,** 196–203 (1979).
121. Chantelau, E. A. & Berger, M. Pollution of insulin with silicone oil, a hazard of disposable plastic syringes. *Lancet* **1,** 1459 (1985).
122. Bernstein, R. K. Clouding and deactivation of clear (regular) human insulin: association with silicone oil from disposable syringes? *Diabetes Care* **10,** 786–787 (1987).
123. Thurow, H. & Geisen, K. Stabilisation of dissolved proteins against denaturation at hydrophobic interfaces. *Diabetologia* **27,** 212–218 (1984).
124. Sluzky, V., Klibanov, A. M. & Langer, R. Mechanism of insulin aggregation and stabilization in agitated aqueous solutions. *Biotechnol Bioeng* **40,** 895–903 (1992).
125. Ballet, T. Stability of therapeutic proteins in contact with materials: Surface-induced aggregation and detection of conformational changes by molecular chaperones. (2010).
126. Nakanishi, K., Sakiyama, T. & Imamura, K. On the adsorption of proteins on solid surfaces, a common but very complicated phenomenon. *J. Biosci. Bioeng.* **91,** 233–244 (2001).
127. Dzwolak, W., Smirnovas, V., Jansen, R. & Winter, R. Insulin forms amyloid in a strain-dependent manner: an FT-IR spectroscopic study. *Protein Sci* **13,** 1927–1932 (2004).
128. Jorgensen, L. *et al.* Adsorption of insulin with varying self-association profiles to a solid Teflon surface - Influence on protein structure, fibrillation tendency and thermal stability. *Eur. J. Pharm. Sci.* **42,** 509–516 (2011).
129. Mauri, S., Volk, M., Byard, S., Berchtold, H. & Arnolds, H. Stabilization of Insulin by Adsorption on a Hydrophobic Silane Self-Assembled Monolayer. *Langmuir* **31,** 8892–8900 (2015).

130. Sharp, J. S., Forrest, J. A. & Jones, R. A. Surface denaturation and amyloid fibril formation of insulin at model lipid-water interfaces. *Biochemistry* **41,** 15810–15819 (2002).
131. Smith, M. I., Sharp, J. S. & Roberts, C. J. Nucleation and growth of insulin fibrils in bulk solution and at hydrophobic polystyrene surfaces. *Biophys J* **93,** 2143–2151 (2007).
132. Jorgensen, L. *et al.* Adsorption of insulin with varying self-association profiles to a solid Teflon surface--influence on protein structure, fibrillation tendency and thermal stability. *Eur J Pharm Sci* **42,** 509–516 (2011).
133. Pandey, L. M. *et al.* Surface chemistry at the nanometer scale influences insulin aggregation. *Colloids Surf B Biointerfaces* **100,** 69–76 (2012).
134. Hosseinzadeh, G., Maghari, A., Farnia, S. M. F. & Moosavi-Movahedi, A. A. Interaction mechanism of insulin with ZnO nanoparticles by replica exchange molecular dynamics simulation. *J. Biomol. Struct. Dyn.* **1102,** 1–13 (2017).
135. Grigolato, F., Colombo, C., Ferrari, R., Rezabkova, L. & Arosio, P. Mechanistic Origin of the Combined Effect of Surfaces and Mechanical Agitation on Amyloid Formation. *ACS Nano* **11,** 11358–11367 (2017).
136. Ivanova, M. I., Sievers, S. A., Sawaya, M. R., Wall, J. S. & Eisenberg, D. Molecular basis for insulin fibril assembly. *Proc Natl Acad Sci U S A* **106,** 18990–18995 (2009).
137. DeGrado Lear JD, W. Induction of peptide conformation at apolar/water interfaces. 1. A study with model peptides of defined hydrophobic periodicity. *J. Am. Chem. Soc.* **107,** 7684–7689 (1985).
138. Chouchane, K. *Controlling surface mediated insulin aggregation by peptides and light*. (2017).
139. Cohen, S. I. A., Vendruscolo, M., Dobson, C. M. & Knowles, T. P. J. From macroscopic measurements to microscopic mechanisms of protein aggregation. *Journal of Molecular Biology* **421,** 160–171 (2012).
140. Gleason, C., Yee, C., Masatani, P., Middaugh, C. R. & Vance, A. Probing Shear Thinning Behaviors of IgG Molecules at the Air-Water Interface via Rheological Methods. *Langmuir* **32,** 496–504 (2016).
141. Wiesbauer, J., Prassl, R. & Nidetzky, B. Renewal of the air-water interface as a critical system parameter of protein stability: aggregation of the human growth hormone and its prevention by surface-active compounds. *Langmuir* **29,** 15240–15250 (2013).
142. Vieillard, V. *et al.* Pneumatic conveying systems and physical stability of monoclonal antibodies : example of Cetuximab. in *ECCO congress* poster (2013).
143. Sergii Rudiuk Sylvain Huille, Christophe Tribet, L. C.-T. Importance of the dynamics of adsorption and of a transient interfacial stress on the formation of aggregates of IgG antibodies. *Softmatter* **8,** 2651–2661 (2012).
144. Wang, S. *et al.* Stabilizing two IgG1 monoclonal antibodies by surfactants: Balance between aggregation prevention and structure perturbation. *Eur. J. Pharm. Biopharm.* **114,** 263–277 (2017).
145. Khan, T. A., Mahler, H.-C. & Kishore, R. S. K. Key interactions of surfactants in therapeutic protein formulations: A review. *Eur. J. Pharm. Biopharm.* **97, Part A,** 60–67 (2015).
146. Garidel, P., Hoffmann, C. & Blume, A. A thermodynamic analysis of the binding interaction between polysorbate 20 and 80 with human serum albumins and

immunoglobulins: A contribution to understand colloidal protein stabilisation. *Biophys. Chem.* **143,** 70–78 (2009).
147. Kapp, S. J., Larsson, I., Van De Weert, M., Cárdenas, M. & Jorgensen, L. Competitive Adsorption of Monoclonal Antibodies and Nonionic Surfactants at Solid Hydrophobic Surfaces. *J Pharm Sci* **104,** 593–601
148. Serno, T., Härtl, E., Besheer, A., Miller, R. & Winter, G. The Role of Polysorbate 80 and HPβCD at the Air-Water Interface of IgG Solutions. *Pharm Res* **30,** 117–130 (2013).
149. Gerhardt, A. *et al.* Surfactant Effects on Particle Generation in Antibody Formulations in Pre-filled Syringes. *J Pharm Sci* **104,** 4056–4064 (2015).
150. Mackie, A. R., Gunning, A. P., Wilde, P. J. & Morris, V. J. Orogenic Displacement of Protein from the Air/Water Interface by Competitive Adsorption. *J Colloid Interface Sci* **210,** 157–166 (1999).
151. Shortall, A. ADVANCED DELIVERY DEVICES - The Reconstitution Revolution - . *Drug Dev. Deliv.* (2013).
152. Bee, J. S. *et al.* Monoclonal antibody interactions with micro- and nanoparticles: adsorption, aggregation, and accelerated stress studies. *J Pharm Sci* **98,** 3218–3238 (2009).
153. Buijs, J., Lichtenbelt, J. W. T., Norde, W. & Lyklema, J. Adsorption of monoclonal IgGs and their F(ab')2 fragments onto polymeric surfaces. *Colloids Surfaces B Biointerfaces* **5,** 11–23 (1995).
154. Wiseman, M. E. & Frank, C. W. Antibody Adsorption and Orientation on Hydrophobic Surfaces. *Langmuir* **28,** 1765–1774 (2012).
155. Bee, J. S. *et al.* Monoclonal antibody interactions with micro- and nanoparticles: adsorption, aggregation, and accelerated stress studies. *J Pharm Sci* **98,** 3218–3238 (2009).
156. Vermeer, A. W. P., Giacomelli, C. E. & Norde, W. Adsorption of IgG onto hydrophobic teflon. Differences between the Fab and Fc domains. *Biochim. Biophys. Acta - Gen. Subj.* **1526,** 61–69 (2001).
157. Joshi, O. & McGuire, J. Adsorption behavior of lysozyme and Tween 80 at hydrophilic and hydrophobic silica-water interfaces. *Appl Biochem Biotechnol* **152,** 235–248 (2009).
158. Joshi, O., McGuire, J. & Wang, D. Q. Adsorption and function of recombinant factor VIII at solid–water interfaces in the presence of Tween-80. *J Pharm Sci* **97,** 4741–4755
159. Couston, R. G., Skoda, M. W., Uddin, S. & van der Walle, C. F. Adsorption behavior of a human monoclonal antibody at hydrophilic and hydrophobic surfaces. *MAbs* **5,** 126–139 (2013).
160. Schuck, P. & Zhao, H. The Role of Mass Transport Limitation and Surface Heterogeneity in the Biophysical Characterization of Macromolecular Binding Processes by SPR Biosensing. *Methods Mol. Biol.* **627,** 15–54 (2010).
161. Smoluchowski, M. v. Versuch einer mathematischen Theorie der Koagulationskinetik kolloiderLösnngen. *Kolloid-Zeitschrift* **21,** 98–104 (1917).
162. Hall, D. R., Cann, J. R. & Winzor, D. J. Demonstration of an upper limit to the range of association rate constants amenable to study by biosensor technology based on surface plasmon resonance. *Anal. Biochem.* **235,** 175–184 (1996).

163. Kim, H. L., Mcauley, A. & Mcguire, J. Protein Effects on Surfactant Adsorption Suggest the Dominant Mode of Surfactant-Mediated Stabilization of Protein. *J. Pharm. Sci.* **103,** 1337–1345 (2014).
164. Ausserré, D. & Valignat, M.-P. Surface enhanced ellipsometric contrast (SEEC) basic theory and lambda/4 multilayered solutions. *Opt. Express* **15,** 8329–8339 (2007).
165. Souplet, V., Desmet, R. & Melnyk, O. Imaging of protein layers with an optical microscope for the characterization of peptide microarrays. *J Pept Sci* **13,** 451–457 (2007).
166. Ducret, A., Valignat, M. P., Mouhamar, F., Mignot, T. & Theodoly, O. Wet-surface-enhanced ellipsometric contrast microscopy identifies slime as a major adhesion factor during bacterial surface motility. *Proc Natl Acad Sci U S A* **109,** 10036–10041 (2012).
167. Xi, W.-H. & Wei, G.-H. Amyloid- β peptide aggregation and the influence of carbon nanoparticles. *Chinese Phys. B* **25,** 18704 (2016).
168. Roach, P., Farrar, D. & Perry, C. C. Interpretation of protein adsorption: surface-induced conformational changes. *J Am Chem Soc* **127,** 8168–8173 (2005).
169. Jichao Kang Jason Penera, X. L. Rapid Formulation Development for Monoclonal Antibodies. *Bioprocess Int.* **14,** (2016).
170. Sluzky, V., Langer, R. & Klibanov, A. M. Insulin stability and aggregation in agitated aqueous solutions. *Department of Chemical Engineering* PhD, (Massachusetts Institue of Technology, 1992).

8 Annexe 1

List of students, other than PhD students, I supervised since 2010:

M2R Master Theses

2011

J. Bhagyashree. Master Nanobiology, UJF Grenoble; Protein aggregation on hydrophobic surfaces by SPRi

S. Menad. Master Nanobiology, UJF Grenoble; Capillary force assembly of DNA: deposition, stretching and AFM structure.

2012

G. Kaur Behrh, Master Nanobiology, UJF Grenoble; Adsorption kinetics of therapeutical proteins on material surfaces.

2013

K. Chouchane, Master Nanobiology, UJF Grenoble; Effect of peptides on insulin aggregation kinetics in contact with hydrophobic material surfaces.

2016

G Lefebvre, Master Sciences Pharmaceutiques "Nanomédecines", Univ Angers; Stability study of a therapeutic monoclonal antibody at the liquid-solid interface.

M1 internships

2010

C. Monnot (stage 2A Phelma SMPB); Etude de l'étalement de mutants de Disctyostelium discoideum sur des surfaces

2011

G. Bouchage (stage 2A Phelma SMPB); iGEM 2011: MercuroColi : a new way to quantify heavy metals

2012

A. Millet (stage M1 Biologie Moléculaire et Cellulaire UJF); iGEM 2012: sEnsiColi: A tunable and reliable ultra-sensitive detector

2013

A. Rapeaux (stage 2A Phelma SMPB); iGEM 2013: Talk E'coli

2014

A. Dolle (Stage ingénieur, Telecom Physique, Strasbourg); Agrégation de l'insuline en fibres amyloïdes sur des nanobilles fonctionnalisées

2017

S Cambronero (stage 2A Phelma Biomedical Engineering); Characterization of a drug in EVEON's fluidic technology

2018

X Gallard (stage 2A Phelma Biomedical Engineering); iGEM 2018 Phag'zer

BTS internships and international exchange students

2010

L. Lacroix, BTS AnaBiotech (analyses agricoles biologiques et biotechnologique), Lycée des Mandailles

V. Deroux , BTS AnaBiotech (analyses agricoles biologiques et biotechnologique), Lycée des Mandailles

2011

M. Norton, first year PhD student Summer Programm Minatec, UPenn, USA

P. Guo (Canada), third year bachelor student, Programme ORA Rhône-Alpes, Toronto University, Canada

2012

S. Fairley (Giant international internship program, Alabama State Univ, Montgommery, USA)

2013

K. Moreaux (Giant international internship program, Louisiana State Univ, Baton Rouge, USA)

2014

S. Humble (Giant international internship program, Louisiana State Univ, Baton Rouge, USA)

2017

B Weiner (Giant international internship program, UPenn, Philadelphia USA)

S Barrow (Giant international internship program, Alabama State Univ, Montgommery, USA)

T Niepa (Giant international internship program, UPenn, Philadelphia USA)

2018

K Rose (Giant international internship program, UPenn, Philadelphia USA)

S Barrow (Giant international internship program, Alabama State Univ, Montgommery, USA)

9 Annexe 2

List of oral and poster communications since 2010:

Oral Communications (*speaker in italics*)

2010, IBC's 10th Annual, Formulation Strategies for Protein Therapeutics, Providence (RI) US. F Bruckert, *T. Ballet*, P. Mangiagalli, C. Bureau, **M. Weidenhaupt**, Role of material surfaces in inducing protein aggregation.

2011, XXI International Symposium on Bioelectrochemistry and Bioenergetics, Krakow (Po), Nguyen U.H.P., Stambouli, V., **Weidenhaupt, M.**, *Delabouglise, D, Extracellular Redox Compounds produced by E. coli*

2011, Journées d'Electrochimie 2011, Grenoble (F), *Nguyen U.H.P.*, Stambouli, V., **Weidenhaupt, M.**, Delabouglise, D*, Extracellular Redox Compounds produced by E. coli*

2012, 13ème colloque du Groupe Français de Bioélectrochimie, Lacaneau (F), *Nguyen U.*, **Weidenhaupt, M.**, Geiselmann, H., Stambouli, V., D. Delabouglise, Electroactive deposit from Escherichia coli.

2013, Frontiers in BioMagnetic Particles, Telluride (Co) US, Zanini L.F., Blaire, G., Le Roy, D., Reyne, G., Cugat, O., **Weidenhaupt, M**., Bruckert, F., Dumas-Bouchiat, F., *Dempsey, N.M*. Development of hard magnetic micropatterns for biomedical applications.

2015, Biophysics of proteins at Surfaces, Madrid (E), *Chouchane K*, Amari, M, Vendrely C, Moreaux K, Bruckert F , **Weidenhaupt M,** Peptides forming beta-sheets on hydrophobic surfaces cooperatively promote insulin amyloidal aggregation.

2017, IMAPS, Lyon (F), T Frachon, F Bruckert, R Vomscheid, H Marko, E Monnin, Q LeMasne, ***M Weidenhaupt,*** Therapeutic protein aggregation at the triple interface air/liquid/solid: relevance to drug production, storage and delivery processes

Poster communications (student underlined)

2010 Workshop on Protein Aggregation and Immunogenicity, Breckenridge (Co), US. Mangiagalli F, Felsovalyi, T. Ballet, F. Bruckert, **M. Weidenhaupt**, S. Kumar, S. Banta, C. Bureau.

Development of pharmaceutically relevant model systems to study the role of solid surfaces in inducing protein aggregation and conformational changes.

2010 PEGS (Protein Aggregation in Biopharmaceutical Products), Boston (Ma) US. Mangiagalli T. Ballet, F. Felsovalyi, F. Bruckert, **M. Weidenhaupt**, S. Kumar, S. Banta, C. Bureau, P. Evaluating the role of solid surfaces in Inducing Aggregation and Conformational Changes in Model Proteins.

2010 4th annual seminar of the Cluster de Recherche Macodev, Annecy (F). Nault L. , Ballet, T. , **Weidenhaupt, M**. , Bruckert, F. , Brechet, Y. Mechanism of amyloïd fiber formation on material surfaces.

2010 The 61st annual meeting of the International Society of Electrochemistry, Nice (F), Nguyen U.H.P., Stambouli, V., Delabouglise, D., **Weidenhaupt, M**. , Douki, T. Electrochemistry of Bacterial Extracellular Redox Compounds.

2010, The Physical Cell, London(UK). Socol M., Lefrou, C. , Bruckert, F., Delabouglise, D., **Weidenhaupt, M**. Electrochemically-triggered, synchronized adhesion and spreading of Dictyostelium discoideum.

2010, WCARP IV, Arcachon (F). Socol M., Lefrou, C. , Bruckert, F., Delabouglise, D., **Weidenhaupt, M**. Electrochemically-triggered, synchronized adhesion and spreading of Dictyostelium discoideum.

2011, FEBS, Torino (I). Nault L., Ballet, T., Bruckert, F., Brechet, Y., **Weidenhaupt, M**. Protein stability upon contact with material surfaces.

2011, 5th annual seminar of the Cluster de Recherche Macodev, Annecy (F), L. Nault, T. Ballet, Y. Brechet, F. Bruckert, **M. Weidenhaupt** Mécanisme d'agrégation des protéines en contact avec les surfaces hydrophobes.

2012, 4th Workshop on Nano and Micro-Environments for Cell Biology, Grenoble (F) Blaire G., Masse, A., Zanini, L., Delshadi, S., Honegger, T., Bruckert, F., Peyrade, D., **Weidenhaupt, M**., Dempsey, N. M., Dumas-Bouchiat, F., Reyne, G., Cugat, O. Bio-Mag-MEMS combining magnetophoresis and dielectrophoris for cell sorting.

2012, JEMS, Parma (I), Blaire G., Masse, A., Zanini, L., Honegger, T., Bruckert, F., Peyrade, D., **Weidenhaupt, M**., Dempsey, N. M., Dumas-Bouchiat, F., Reyne, G., Cugat, O. Magnetic

microfluidic microsystems (Bio-Mag-MEMS) combining magnetophoresis and dielectrophoris for cell sorting.

2013, ERC Biomim, Grenoble (F), Nault L., Chouchane, K., Vendrely, C., Bruckert, F., **Weidenhaupt, M.** Peptides that form β-sheets on hydrophobic surfaces accelerate surface-induced insulin amyloidal aggregation

2013, SEP Conference, Paris (F), Zanini L.F., Blaire, G., Le Roy, D., Piveta, J., Osman, O., Tomba, C., Villard, C., Frénéa-Robin, M., Haddour, N., Reyne, G., Cugat, O., **Weidenhaupt, M**., Bruckert, F., Dumas-Bouchiat, F., Dempsey, N.M., Autonomous separation devices based on micro-magnets.

2015, Colloque ADEBiotech Stabilité et formulation des protéines et des peptides, Romainville (F), Chouchane K, Amari, M, Vendrely C, Moreaux K, Bruckert F , **Weidenhaupt M,** Peptides forming beta-sheets on hydrophobic surfaces cooperatively promote insulin amyloidal aggregation.

2015, Colloque ADEBiotech Stabilité et formulation des protéines et des peptides, Romainville (F), Frachon T, LeMasne Q, Bruckert F, **Weidenhaupt M**, Fast insulin amyloid aggregation at the air-liquid-solid triple interface.

10 Reprints of articles

The following articles are reprinted hereafter:

Ballet, T. et al. DnaK prevents human insulin amyloid fiber formation on hydrophobic surfaces. Biochemistry 51, 2172–2180 (2012).

Nault, L. et al. Human insulin adsorption kinetics, conformational changes and amyloidal aggregate formation on hydrophobic surfaces. Acta Biomater 9, 5070–5079 (2013).

Nault, L., et al. Peptides that form beta-sheets on hydrophobic surfaces accelerate surface-induced insulin amyloidal aggregation. FEBS Lett 587, 1281–1286 (2013).

Chouchane, K. et al. Dual Effect of (LK)nL Peptides on the Onset of Insulin Amyloid Fiber Formation at Hydrophobic Surfaces. J Phys Chem B 119, 10543–10553 (2015).

Frachon, T., et al. Insulin Aggregation at a Dynamic Solid-Liquid-Air Triple Interface. Langmuir 32, 13009–13019 (2016).

BIOCHEMISTRY
including biophysical chemistry & molecular biology

Article

pubs.acs.org/biochemistry

DnaK Prevents Human Insulin Amyloid Fiber Formation on Hydrophobic Surfaces

Thomas Ballet,[†,‡] Franz Brukert,[†] Paolo Mangiagalli,[‡] Christophe Bureau,[‡] Laurence Boulangé,[‡,§] Laurent Nault,[†] Thomas Perret,[†] and Marianne Weidenhaupt*[,†]

[†]Laboratoire des Matériaux et du Génie Physique, Grenoble Institute of Technology, 3 parvis Louis Néel, 38016 Grenoble Cedex 1, France

[‡]Becton-Dickinson Pharmaceutical Systems, 11, Rue Aristide Bergès, 38801 Le Pont de Claix, France

ABSTRACT: We have developed a multiwell-based protein aggregation assay to study the kinetics of insulin adsorption and aggregation on hydrophobic surfaces and to investigate the molecular mechanisms involved. Protein−surface interaction progresses in two phases: (1) a lag phase during which proteins adsorb and prefibrillar aggregates form on the material surface and (2) a growth phase during which amyloid fibers form and then are progressively released into solution. We studied the effect of three bacterial chaperones, DnaK, DnaJ, and ClpB, on insulin aggregation kinetics. In the presence of ATP, the simultaneous presence of DnaK, DnaJ, and ClpB allows good protection of insulin against aggregation. In the absence of ATP, DnaK alone is able to prevent insulin aggregation. Furthermore, DnaK binds to insulin adsorbed on hydrophobic surfaces. This process is slowed in the presence of ATP and can be enhanced by the cochaperone DnaJ. The peptide LVEALYL, derived from the insulin B chain, is known to promote fast aggregation in a concentration- and pH-dependent manner in solution. We show that it also shortens the lag phase for insulin aggregation on hydrophobic surfaces. As this peptide is also a known DnaK substrate, our data indicate that the peptide and the chaperone might compete for a common site during the process of insulin aggregation on hydrophobic surfaces.

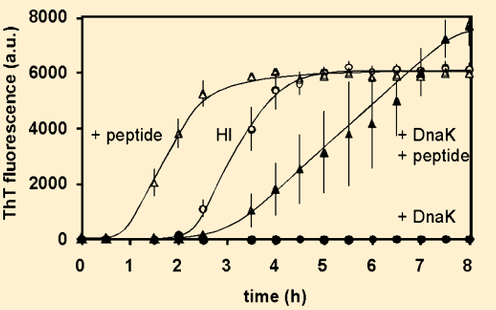

Adsorption of protein on material surfaces is of widespread importance in fields like cellular biology, pharmacology, and medicine. It can be quantitatively measured either biochemically after desorption or in situ by sensitive biophysical methods, like QCM-D or surface plasmon resonance (SPR). Protein adsorption is accompanied by conformational changes upon contact with the material surface, leading sometimes to protein aggregation. It is not easy to monitor these conformational changes on the material in a fast, convenient, and preferentially multiplexed assay. Albeit greatly sensitive, techniques like attenuated total reflectance Fourier transform infrared spectroscopy (ATR-FTIR) are not readily available and do not provide unambiguous information about the nature of the changes in protein folding.

Within cells, chaperones constitute a set of proteins whose function is to check the folding state of other proteins, and to refold them,[1−3] using ATP hydrolysis energy to drive protein disaggregation and renaturation. In *Escherichia coli*, Bukau and co-workers identified DnaK, DnaJ, and ClpB as the minimum set of bacterial chaperones needed to help the cell recover from a heat shock.[4] DnaK is an ATPase specific for unfolded hydrophobic amino acid stretches. DnaJ forms a complex with DnaK and stimulates DnaK ATPase activity.[5] ClpB is a hexameric ATPase that interacts with aggregated proteins and disaggregates them, in cooperation with DnaK and DnaJ.[4,6,7] Furthermore, in *E. coli*, ∼250 proteins are disaggregated and refolded when DnaK, DnaJ, and ClpB are present, which supports the broadness of their protein substrates.[4] Chaperones detect general conformational unfolding characteristics, rather than specific targets. In addition, many chaperones work in complexes; hence, chaperone combination is likely to enhance the recognition process. We therefore hypothesized that this protein family could provide new sensors for protein conformational changes at material surfaces.

We chose human insulin (HI) as a model because its aggregation has been studied under different physicochemical conditions.[8−10] It was shown that HI aggregation is formulation-dependent and that insulin undoubtedly changes its conformation upon binding to hydrophobic surfaces, leading to the formation and release of amyloid fiber aggregates.[11] From a concentration dependence study, Sluzky et al. deduced that the HI monomer was the molecular species leading to aggregation.[9] Using recombinant chaperones, we observe that different sets of them are able to prevent HI aggregation by binding preferentially to surface-bound insulin. Rüdiger et al.[12] have shown that DnaK binds to the insulin B chain peptide SHLVEALYLVCGER, and Ivanova et al.[13] demonstrated that the shorter LVEALYL peptide is the minimal sequence that can

Received: September 19, 2011
Revised: January 23, 2012
Published: February 21, 2012

accelerate the lag time of insulin fiber formation at acidic pH in a concentration-dependent manner. We show that this same peptide also accelerates the lag time of insulin aggregation on hydrophobic surfaces and that bacterial chaperones are able to counterbalance this effect.

EXPERIMENTAL PROCEDURES

If not otherwise stated, all chemicals were purchased from Sigma-Aldrich. Experiments were conducted in TBS [25 mM Tris-HCl (pH 7.4) and 125 mM NaCl]. HI (recombinant, expressed in yeast) solutions were prepared at 0.5 mg/mL (86 μM). All solutions were filtered (0.22 μm) before being used. The LVEALYL peptide was purchased from Genecust (Luxembourg) and dissolved in 20 mM NaOH at a concentration of 4.3 mM.

Bacterial Chaperone Preparation and Activity Assay. The bacterial strains used to produce DnaK (Hsp70), ClpB (Hsp100), and DnaJ (Hsp40) were kindly provided by B. Bukau and A. Mogk (Zentrum für Molekulare Biologie Heidelberg, Universität Heidelberg, Heidelberg, Germany). His-tagged ClpB and DnaJ were purified using nickel-nitrilotriacetic acid (Ni-NTA) metal affinity chromatography columns (Qiagen) according to the manufacturer's instructions. DnaK was purified as described by Cegielska and Georgopoulous[14] and McCarty and Walker,[15] with minor modifications by Buchberger et al.[16] The refolding activity of the purified proteins was controlled using the malate dehydrogenase (MDH) renaturation assay.[6,17] The three proteins and ATP were essential for the refolding activity (2 ± 0.3 nM min^{-1} at 1 μM DnaK, 0.2 μM DnaJ, and 1 μM ClpB).

Insulin Aggregation Assays. HI aggregation assays were conducted as eight replicates in plastic 96-well microplates. Polystyrene (Greiner Bio-One, contact angle of $85 \pm 4.7°$) or PEO-coated (Corning, contact angle of $3.5 \pm 5.8°$) microplates were used. In fluorescence assays, black polystyrene microplates were used (Nunc Nunclon Δ Surface). The plates were covered by plastic sheets, incubated at 37 °C, and shaken at 1200 rpm (Heidolph Titramax, 1.5 mm vibration orbit). At each time point, the solution was pipetted out of the microwells. Part of the solution was filtered to remove aggregated HI (100 nm cutoff). The wells were washed twice with 300 μL of TBS. The adsorbed HI fraction was desorbed with 100 μL of 5% SDS for a 1 h agitation at 37 °C. Negligible protein material remained on the surface thereafter. The total amounts of HI in solution (nonfiltered), soluble HI, and HI adsorbed in the wells were determined using the bicinchoninic acid (BCA) assay.[18−21] In addition, turbidity (λ = 600 nm) or thioflavin T (ThT, 20 or 50 μM) fluorescence was directly measured in the wells. Free and bound forms of ThT were measured at a λ_{ex} of 342 nm and a λ_{em} of 430 nm and at a λ_{ex} of 450 nm and a λ_{em} of 482 nm, respectively,[22] with a 5 nm excitation and emission slit (Tecan Infinite M1000).

Kinetic Analysis. The aggregation kinetics proceed in three phases: a lag phase, where the signal was not statistically different from the baseline (mean ± standard deviation), a linear growth phase, and a plateau phase. Experimentally, the lag time was defined by the intercept between the linear growth phase and the baseline. The growth rate was defined as the slope of the linear phase and the plateau as the maximal value attained. The parameters were calculated on individual kinetics corresponding to different samples, and the given statistics represent the average and standard deviation for each parameter.

Protection of Insulin Aggregation by Bacterial Chaperones. HI aggregation was monitored by turbidity or ThT fluorescence and confirmed by protein quantification after filtration at the end of the experiment. The TBS buffer solution was supplemented with 2 mM $MgCl_2$ (TBS-M), because Mg^{2+} ions are needed for the chaperone ATPase activity. Magnesium itself does not affect HI aggregation. All chaperones were stable in this buffer. The efficiency of chaperone protection was expressed as the lag time before the onset of HI aggregation. As Zn^{2+} influences the equilibrium of HI hexamer formation,[23] we tested the effect of Zn^{2+} addition (up to 10 μM) on HI aggregation: neither HI aggregation kinetics nor DnaK protection was modified.

Chaperone Binding Assays. Polystyrene microplates [96 wells, Greiner enzyme-linked immunosorbent assay (ELISA)] were incubated at 37 °C and 1200 rpm with insulin for various amounts of time and blocked with 10 mg/mL bovine serum albumin (BSA) in TBS-M (blocking buffer) for 30 min at room temperature (RT) with shaking (1000 rpm). DnaK, DnaJ, or both (diluted in blocking buffer) were then added for 30 min (RT) with shaking (1000 rpm). The plate was blocked again with BSA for 30 min (RT) with shaking (1000 rpm).

For DnaK detection, a mouse anti-DnaK (*E. coli*) monoclonal antibody (8E2/2; diluted 1:2500 in blocking buffer) was used, and for DnaJ detection, a mouse anti-penta-His antibody (diluted 1:1000 in blocking buffer) was added to each well and the mixture incubated for 15 min (RT) with shaking (1000 rpm). Finally, a goat horseradish peroxidase-conjugated anti-mouse antibody (diluted 1:2500 in blocking buffer) was added to each well and the mixture incubated for 15 min (RT) with shaking (1000 rpm). Wells were then washed three times with 200 μL of TBS, and 200 μL of ECL substrate solution was added per well. Chemiluminescence signals were immediately recorded using a TriStar LB 941 microplate multimode reader.

To relate luminescence values to the amount of DnaK adsorbed, a calibration experiment was conducted in parallel. Increasing amounts of DnaK were incubated in 96-well polystyrene microplates (Greiner ELISA). The amounts of adsorbed DnaK were determined using the NanoOrange assay, according to the manufacturer's instructions. An ELISA was performed on the adsorbed DnaK as described previously. A calibration curve was then obtained that related luminescence values to the amount of adsorbed DnaK.

RESULTS

HI Aggregation in the Presence of Hydrophobic Surfaces. To study the mechanisms of insulin aggregation on hydrophobic surfaces, we developed a HI aggregation assay using commercial hydrophilic or hydrophobic 96-well plates, to allow rapid screening of different experimental conditions. A HI solution was placed in the presence of hydrophilic or hydrophobic plastic surfaces and agitated at 37 °C. At the indicated times, the solution was recovered and filtered to separate the soluble and aggregated HI pools. The microwell surface was then washed, and adsorbed HI was desorbed with SDS. These three protein pools were then quantified using the BCA assay. In the presence of hydrophilic surfaces, HI remained soluble for several days and less than 1 μg of protein was adsorbed on the hydrophilic microwell surfaces (data not shown). In contrast, in the presence of hydrophobic surfaces, the concentration of soluble HI remained constant for ∼4 h (lag phase), after which the amount decreased

dx.doi.org/10.1021/bi201457u | *Biochemistry* 2012, 51, 2172−2180

sharply to trace amounts (Figure 1A). The amount of aggregated HI in solution increased in parallel at a similar rate.

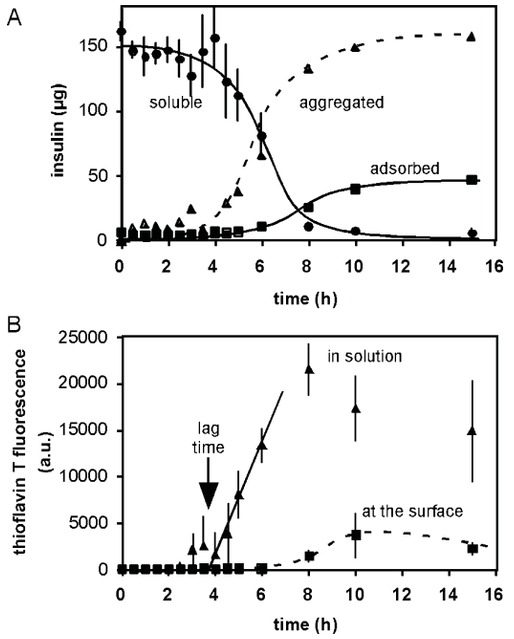

Figure 1. Kinetics of human insulin adsorption and aggregation in hydrophobic microplates. (A) Amount of soluble (●), aggregated (▲), and adsorbed (■) HI after the indicated incubation time. (B) Amyloid fiber-bound ThT fluorescence in solution (▲) and on the surface (■) plotted as a function of incubation time. The lag time as the intercept between the growth rate (—) and the baseline is denoted with an arrow. Other curves are hand-drawn and provided as a guide for the eye.

The amount of HI adsorbed on hydrophobic surfaces increased during the aggregation process, reaching a maximum amount of ~40 μg.

Amyloidal aggregates are characterized by the formation of intermolecular β-sheets, which can be probed by the binding of thioflavin T (ThT), resulting in a characteristic fluorescence signal. Both the aggregated and the adsorbed HI pools were stained with ThT, and the fluorescence intensity per microgram of protein was the same in both pools (Figure 1B). The ThT fluorescence is therefore a convenient method for monitoring the appearance of HI aggregates. In the following experiments, we defined the lag time as the intercept between the linear growth phase and the baseline of the ThT fluorescence kinetics. Depending on HI preparations, the lag time varied from 2 to 4 h. Within an experiment, using the same HI preparation in the same multiwell plate, the lag time was also variable from well to well, which explains the variation observed in the aggregation kinetics. HI aggregates exhibited elongated fiberlike rods with a diameter of 5−10 nm and a length of 50−100 nm when imaged using electron microscopy (data not shown). Their morphology and dimensions are similar to those of the fibers obtained after incubation of insulin at pH 2 and an elevated temperature.[24,25]

Effect of Bacterial Chaperones on Insulin Aggregation. We then studied whether bacterial chaperones could have an effect on the kinetics of HI aggregation. In the presence of 1 mM ATP, the simultaneous presence of the three chaperones delayed HI aggregation as shown by the 9-fold increase in the aggregation lag time (Figure 2A). DnaK alone slightly increased the lag time, whereas DnaJ was without effect. The combined

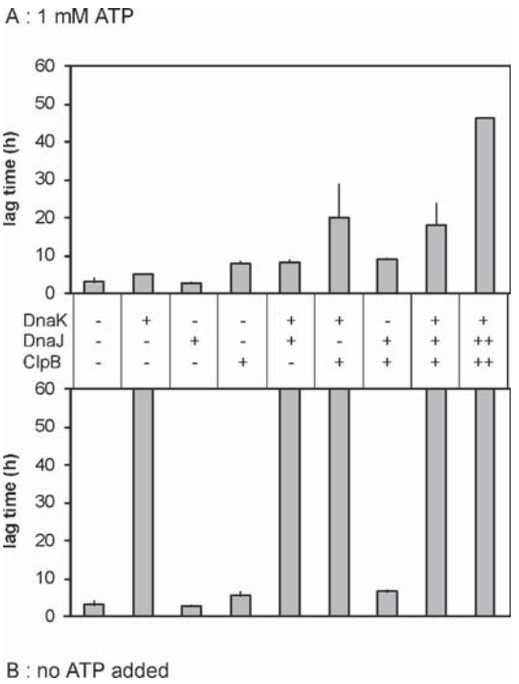

Figure 2. Effect of bacterial chaperones on human insulin aggregation. A HI solution was agitated in a hydrophobic microplate, in the presence of DnaK (0.3 μM), DnaJ [0.06 μM (+) and 0.3 μM (++)], and ClpB [0.3 μM (+) and 0.6 μM (++)] as indicated (A) in the presence of 1 mM ATP or (B) in the absence of ATP. The aggregation kinetics were monitored by turbidity, and the lag times were determined as explained in Experimental Procedures.

presence of DnaK and DnaJ significantly increased the lag time, to a level similar to that obtained in the presence of ClpB alone. Moreover, the combined presence of ClpB with DnaK, but not DnaJ, further delayed HI aggregation in the presence of 1 mM ATP. When the concentrations of DnaJ and ClpB were increased (++ vs +), the lag time further increased. These results show that HI undergoes conformational changes during the aggregation process that are recognized and could possibly be repaired by a minimal set of bacterial chaperones. Nevertheless, incubation of 150 μg of final amyloidal insulin aggregates with DnaK, DnaJ, and ClpB for 24 h does not allow recovery of more than 1 μg of soluble insulin (data not shown). This suggests that the three chaperones do not dissociate final aggregates but more likely block intermediate aggregation states.

Surprisingly, in the absence of ATP, no protein aggregation was observed whenever DnaK was present (Figure 2B). The effect was specific for DnaK because , in the absence of ATP, the presence of the other chaperones alone or in combination did not significantly change the HI aggregation kinetics. Addition of comparable and larger amounts of BSA, which is routinely used as a blocking agent to cover material surfaces and works by competitive adsorption, had no effect (data not shown). The peculiar role of DnaK is further investigated in the next section.

Prevention of Insulin Aggregation by DnaK in the Absence of ATP. In the presence of 1 mM ATPγS, a

dx.doi.org/10.1021/bi201457u | *Biochemistry* 2012, 51, 2172−2180

nonhydrolyzable form of ATP, DnaK did not prevent HI aggregation (Figure 3A), which showed that no ATP hydrolysis

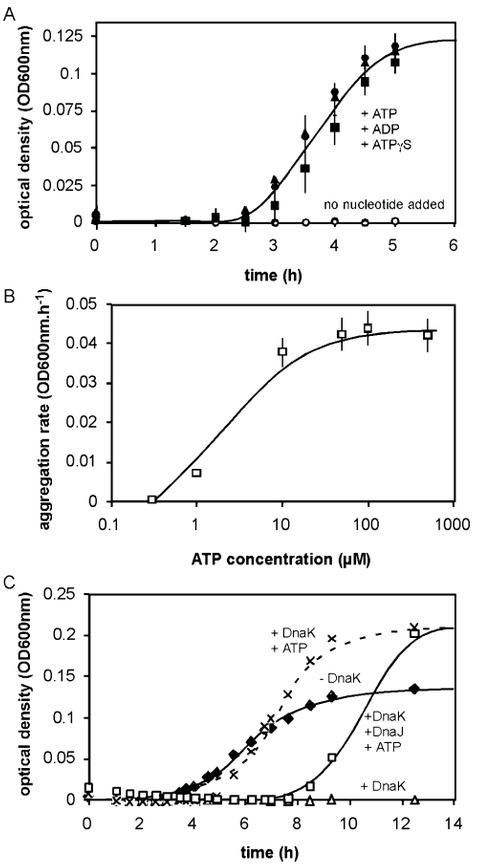

Figure 3. Nucleotide requirements for DnaK protection of human insulin aggregation on hydrophobic surfaces. A HI solution was agitated in a hydrophobic microplate in the presence of the indicated chaperones and nucleotides. HI aggregation was monitored by optical density measurements at 600 nm. (A) The HI solution was supplemented with 1 μM DnaK and either no nucleotide (○) or 1 mM ATP, ADP, or ATPγS (●, ▲, and ■, respectively). (B) The HI solution was supplemented with 0.3 μM DnaK, and the aggregation rate is plotted as a function of ATP concentration. (C) The HI solution was not supplemented with chaperones (◆), supplemented with 0.3 μM DnaK in the absence of ATP (△) or with 1 mM ATP (×), or supplemented with 0.3 μM DnaK and 0.06 μM DnaJ with 1 mM ATP (□).

took place on the HI substrate. Furthermore, addition of 1 mM ADP also abolished the protective effect of DnaK on HI aggregation. The similar effect obtained by the presence of ADP, ATP, or a nonhydrolyzable nucleotide suggested that the molecular species, active at preventing the formation of HI amyloidal fibers, was the nucleotide-free $DnaK_{empty}$–HI complex. This fits well with the biochemical properties of this protein because in the presence of ATP, DnaK indeed has a decreased affinity for its protein substrate[26,27] and hence could be less protective against aggregation. A series of HI aggregation experiments were performed in the presence of DnaK at different ATP concentrations ranging from 1 μM to 5 mM. The HI aggregation rate was used to measure the effect of added ATP on DnaK (Figure 3B). An apparent affinity of 2 μM was determined, which fits with the reported values of the affinity of DnaK for ATP.[28] Furthermore, in the presence of ATP, DnaJ increased the protective effect of DnaK on HI aggregation (Figure 3C). It is indeed known that the DnaK–DnaJ complex has a higher affinity for the protein substrate than DnaK alone.[29,30]

Several lines of evidence indicate that DnaK prevented early phases of HI aggregation. First, in the continuous presence of DnaK, the amount of HI that adsorbed on hydrophobic surfaces remained small (Figure 4A) and ThT did not stain the adsorbed HI (Figure 4B, vs Figure 1B). Second, in two-stage experiments, when the protective effect of DnaK was released after 5 h by addition of ATP, HI aggregation took place after the same lag time observed in the absence of DnaK (Figure 4C). Similarly, when DnaK was added after incubation for 1 h, the lag time was reduced by 1 h after the addition of ATP. This showed that, as long as it was present in a nucleotide-free form, DnaK prevented the formation of amyloid aggregates on hydrophobic surfaces. To confirm the early effect of DnaK, a constant amount of DnaK was added at different times after the beginning of the incubation. After a 1 h preincubation, DnaK considerably slowed HI aggregation kinetics, but after 2 h, it had no significant effect, although aggregation had not yet started (Figure 4D).

DnaK Binds to HI Adsorbed on Hydrophobic Surfaces.

We then determined the minimal amount of DnaK that should be added as a function of preincubation time to prevent HI aggregation for at least 18 h (Figure 5). This amount increased very rapidly without exceeding the amount of HI adsorbed on the surface, on a molar ratio basis.

Because insulin aggregates are present both on the plastic surface and in solution, we studied the binding of DnaK to the HI pool adsorbed on the surface and to HI aggregates in suspensions. BCA and sodium dodecyl sulfate–polyacrylamide gel electrophoresis (SDS–PAGE) analysis were combined to quantify the amount of DnaK and HI adsorbed on the surface or to aggregates in suspension (Table 1). For these experiments, we used an experimental setup similar to that of Sluzky et al.[8] SurfaSil-treated borosilicate beads were incubated with HI under agitation overnight. After the beads had been washed, 20 ± 2 μg of HI remained adsorbed to the beads. The HI solution fully aggregated, and 150 μg of HI aggregates was recovered by centrifugation and washed.

In a first set of experiments, the adsorbed HI pool was incubated with 8 μg of DnaK, or buffer alone, in the presence or absence of ATP, for 8 min, and the amount of insulin and DnaK adsorbed on the beads after the incubation was determined. The material released in solution after the incubation was also analyzed by centrifugation, to separate soluble and aggregated proteins, and the amount of DnaK associated with the aggregates was also quantified. In the absence of DnaK, 35% of the initially adsorbed HI detached from the bead surfaces (7 μg/20 μg), corresponding to the spontaneous detachment of HI aggregates from the surface. In the presence of DnaK, larger amounts of protein, which contained both DnaK and HI, were released from the surface (15.4 μg + 2.4 μg = 17.8 μg). Under these conditions, 77% of the initially adsorbed HI detached from the beads (15.4 μg/20 μg). This material could be recovered by centrifugation, showing that it contained only HI aggregates. Moreover, an ELISA confirmed that <0.1 μg of HI could be recovered in soluble form. No protein renaturation had thus taken place. A large fraction of DnaK (2.4 μg of 8 μg) cosedimented with the released HI material, and small but significant amounts of DnaK (0.2 μg) remained at the bead surface. This strongly suggested that

dx.doi.org/10.1021/bi201457u | *Biochemistry* 2012, 51, 2172–2180

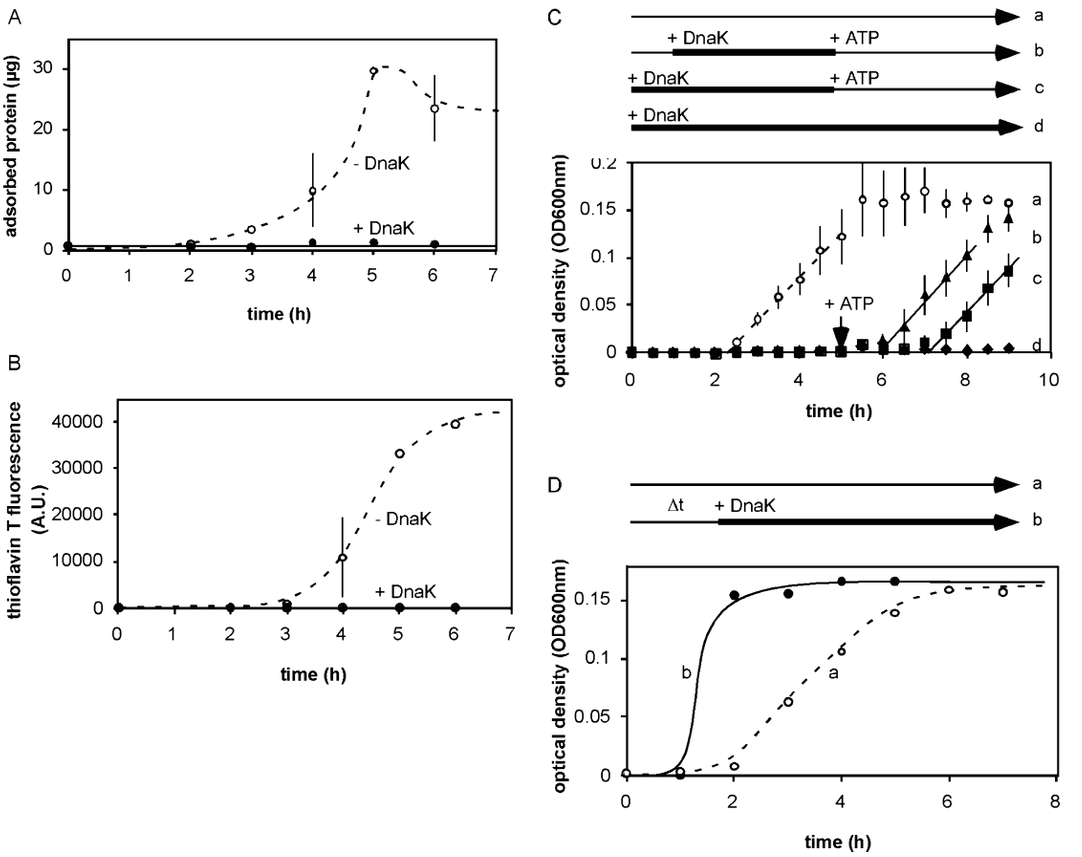

Figure 4. DnaK prevents the formation of prefibrillar insulin aggregates on hydrophobic surfaces. (A) Time course of adsorption of HI on hydrophobic surfaces in the presence of 0.3 μM DnaK without ATP (●) compared to the adsorption in the absence of DnaK (○). (B) Time course of amyloid fiber formation on hydrophobic surfaces in the presence of 0.3 μM DnaK without ATP (●) compared to the aggregation in the absence of DnaK (○). (C and D) Two-stage experiments. (C) A HI solution was incubated in the presence (filled symbols, b–d) or absence (○, a) of 0.3 μM DnaK. At the indicated time, 1 mM ATP was added to the DnaK-containing sample (b and c) and the HI solution was further incubated. Bold lines represent the time during which DnaK protects HI from aggregation. HI aggregation was monitored by turbidity. (D) DnaK (0.3 μM) was added at the indicated time (Δt) after the beginning of HI agitation in a hydrophobic microplate, and the incubation was further continued for 8 − Δt hours (●). In comparison, the kinetics of HI aggregation as measured in panel C (a) is shown (○). HI aggregation was monitored by turbidity after 8 h.

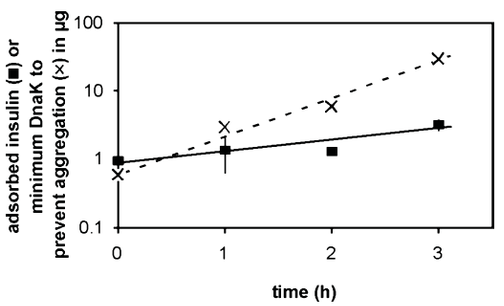

Figure 5. Stoichiometry of the interaction of DnaK with insulin adsorbed on hydrophobic surfaces. A HI solution was agitated in hydrophobic microplates for the indicated preincubation time. DnaK was then added at different concentrations, and the HI solution was further incubated for 18 h. The extent of HI aggregation was determined by ThT staining. A 2-fold increase in the level of ThT staining over background was used as a criterion for the onset of HI aggregation. The minimal amount of DnaK needed to prevent the onset of HI aggregation is represented as a function of preincubation time. The amount of adsorbed HI is also represented.

DnaK detached insulin aggregates from the bead surface, remaining associated to them. The time course of this process was ~20 min (data not shown). In contrast, no DnaK could be detected on hydrophilic surfaces where similar amounts of HI had been preadsorbed (data not shown). Qualitatively similar results were obtained in the presence and absence of ATP. However, less insulin was detached, and ~50% of the DnaK remained bound to insulin aggregates in the presence of 1 mM ATP.

In a second set of experiments, DnaK (8 μg) was incubated with HI aggregates that had already been released in solution. Under these conditions, ~0.5 μg of DnaK was bound to 150 μg of a HI aggregate suspension. This shows that DnaK does not bind efficiently to HI aggregates already present in solution. DnaK therefore binds specifically to HI adsorbed on hydrophobic surfaces.

Making use of the affinity of DnaK for insulin adsorbed on hydrophobic surfaces, we subsequently designed an assay for the sensitive detection of aggregated insulin on material surfaces. Insulin (or BSA as a control) was incubated in the presence of hydrophobic or hydrophilic surfaces for 1 h. The adsorbed protein (1–2 μg) was incubated with increasing amounts of DnaK, in the presence or absence of DnaJ and/or ATP. After the sample had been gently washed, DnaK was detected using anti-DnaK antibodies in a chemoluminescence

Table 1. DnaK Binding to HI-Covered Surfaces and HI Aggregates and LVEALYL Aggregates in Solution[a]

	fraction		
		released from beads	
	adsorbed	aggregates	soluble
Hydrophobic Surfaces, No DnaK Added			
human insulin (μg)	11 ± 2	7 ± 3	<0.1
Hydrophobic Surfaces, with DnaK (8 μg)			
human insulin (μg)	4.6 ± 1	15.4 ± 2.5	<0.1
DnaK (μg)	0.2 ± 0.1	2.4 ± 0.6	5.4 ± 0.7
DnaK:HI molar ratio	277	77	
Hydrophobic Surfaces, with DnaK (8 μg) and Aggregated Insulin in Solution			
human insulin (μg)		150 ± 10	
DnaK (μg)		0.5 ± 0.2	
Molar ratio (HI:DnaK)		4200	
Hydrophobic surfaces, with DnaK (1.5 μg)			
LVEALYL (μg)		25	
DnaK (μg)		0.5	
Molar ratio (peptide:DnaK)		4000	

[a]Acid-washed borosilicate glass beads (diameter of 1 mm) were siliconized by immersion in SurfaSil (Pierce, 10%, w/w) in acetone and stabilized by being cured at 100 °C for 1 h. The water contact angle was measured (DSA100 Krüss) (93.5 ± 3.5°). SurfaSil-treated beads were incubated with HI in TBS-M buffer overnight. The fully aggregated HI solution was removed, and the beads were washed three times with 500 μL of TBS-M. The initial amount of HI adsorbed on the beads was determined. DnaK was then added, in the presence or absence of ATP, and the beads were further incubated for 1 h at 37 °C under agitation. The total protein content and the amount of HI or DnaK were determined in three fractions: the one adsorbed on the beads, the aggregated one, and the soluble ones released from the beads and separated by centrifugation (5000*g* for 10 min). The total amount of protein was quantified by the BCA assay; the amount of soluble HI was quantified by an ELISA (I2018 mouse monoclonal anti-insulin antibody), and the amount of DnaK was determined using SDS–PAGE and Coomassie staining. Quantification was performed with ImageJ. For the interaction of DnaK with the aggregated LVEALYL peptide, the peptide solution was prepared at 1 mM glycine buffer (pH 2.5). This solution was incubated in hydrophobic 96-well plates overnight at 37 °C with agitation (1200 rpm). The resulting aggregates were centrifuged and washed three times in TBS-M buffer (pH 7.4) before being resuspended and incubated in TBS-M buffer containing 1.5 μg of DnaK over 30 min. The DnaK/peptide solution was then centrifuged and washed three times in TBS-M buffer before SDS–PAGE analysis.

assay (see Experimental Procedures). In Figure 6A, the amount of adsorbed DnaK is plotted as a function of the total amount of DnaK. In the absence of DnaJ, small but significant amounts of DnaK (26 ng) were bound to insulin adsorbed on hydrophobic surfaces compared to the amount of DnaK bound on adsorbed BSA (14 ng). In contrast, almost no DnaK was recovered when insulin was incubated with hydrophilic surfaces (data not shown). The amount of DnaK bound to adsorbed insulin was only slightly reduced in the presence of 1 mM ATP (23 ng). In the presence of DnaJ, much larger amounts of DnaK were bound to adsorbed HI (372 ng), but not on adsorbed BSA (27 ng). Addition of ATP reduced the amount of DnaK binding in the presence of DnaJ to 147 ng. To study the DnaJ requirement for DnaK binding, the amount of DnaK was kept constant at 2.5 μg (0.18 μM) and the DnaJ concentration was increased (Figure 6B). DnaK binding reached a maximum for amounts of DnaJ larger than 1.28 μg (0.16 μM), which corresponds to a 1:1 DnaJ:DnaK ratio. These

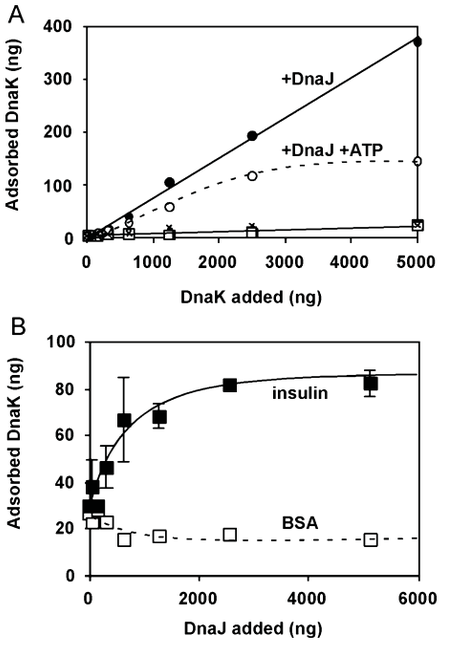

Figure 6. Amount of DnaK adsorbed on surface-bound HI. A 0.5 mg/mL insulin or 0.5 mg/mL BSA control solution (×) was agitated for 1 h in a hydrophobic microplate. After removal of the solution, a DnaK solution was added. (A) The DnaK solution was not supplemented with ATP (■), supplemented with 1 mM ATP (□), and supplemented with DnaJ (0.16 μM) in the presence of 1 mM ATP (○) or in the absence of ATP (●). The amount of adsorbed DnaK was measured using an ELISA as described in Experimental Procedures and is represented as a function of the total amount of DnaK added. (B) A 0.18 μM DnaK solution supplemented with different amounts of DnaJ was added to the adsorbed insulin (■) and the adsorbed BSA (□). The amount of adsorbed DnaK was measured using an ELISA as described in Experimental Procedures and is represented as a function of the total amount of DnaJ added. Lines are hand-drawn and provided as a guide for the eye.

data show that DnaK specifically interacts with HI adsorbed on hydrophobic surfaces and that the molecular cochaperone DnaJ reinforces this binding. The weak binding of DnaK in the presence of ATP is consistent with its lack of a protective effect against aggregation.

Competition between the LVEALYL Amyloidogenic Peptide and Bacterial Chaperones during HI Aggregation on Hydrophobic Surfaces. Recent studies by Ivanova et al.[13] pinpointed the role of two HI amino acid stretches that are likely to change extensively their conformation when HI spontaneously goes from a soluble form to amyloid aggregates at pH 2 and 60 °C. These sequences are SLYQLENY (A12–19) and LVEALYL (B11–17). Both contain hydrophobic residues and are mainly involved in α-helices in the HI monomer. In amyloid fibers, two LVEALYL stretches from two monomers are assumed to associate into antiparallel extended β sheets that tightly interact via their hydrophobic side chains. The SLYQLENY sequence shows similar properties and also contributes to the formation of fibrillar structures. In this model, the core of HI amyloid fibers is therefore provided by hydrophobic interactions between these polypeptides and stabilized by the stacking of extended β-sheets. To investigate whether hydrophobic surfaces drive similar conformational changes, we studied the effect of the LVEALYL and the SLYQLENY peptides on HI aggregation kinetics. The SLYQLENY peptide

dx.doi.org/10.1021/bi201457u | *Biochemistry* 2012, 51, 2172–2180

had no effect on HI aggregation kinetics, whereas the LVEALYL peptide strongly reduced the lag time in HI aggregation kinetics at substoichiometric concentrations relative to HI (Figure 7A). At higher concentrations, the

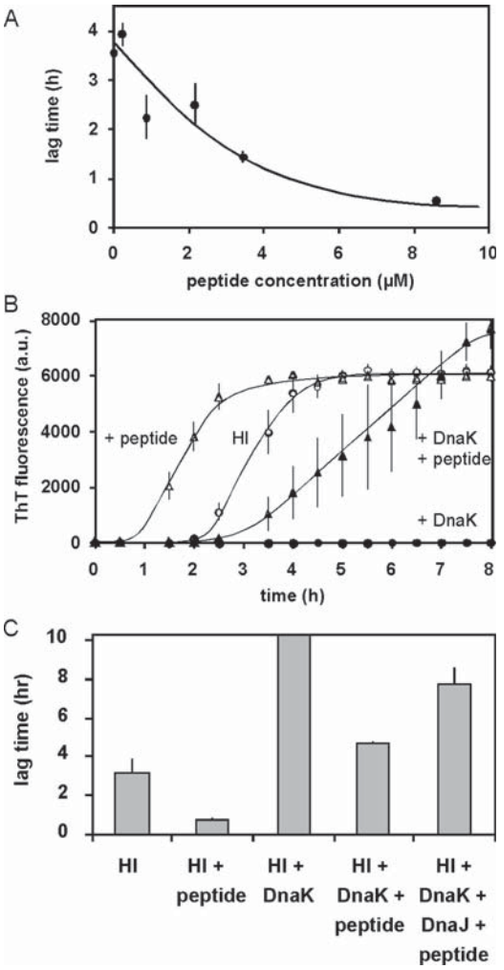

Figure 7. Effect of the LVEALYL peptide on HI aggregation kinetics. (A) A HI solution was agitated in a hydrophobic microplate in the presence of different amounts of the LVEALYL peptide, and aggregation was monitored using ThT fluorescence. The lag time (as defined in Experimental Procedures) is represented as a function of peptide concentration. (B) Aggregation kinetics of HI alone (○) or HI supplemented with 26 μM LVEALYL peptide (△), with 0.3 μM DnaK (●), or with both peptide and DnaK (▲). Aggregation was assessed using ThT fluorescence. Lines are hand-drawn and provided as a guide for the eye. (C) A HI solution was agitated in a hydrophobic microplate in the presence of the LVEALYL peptide (8 μM), DnaK (0.3 μM), and DnaJ (0.16 μM), as indicated. Aggregation was monitored using ThT fluorescence, and the lag time was determined. In the presence of DnaK, the lag time extended beyond 10 h.

LVEALYL peptide inhibited the growth of HI amyloidal aggregates, as reported previously at pH 2.[13] The effect of the LVEALYL peptide was observed only in the presence of hydrophobic surfaces, the HI solution remaining perfectly stable in hydrophilic multiwell plates, whatever the peptide concentration. It should be noted that none of the peptides alone aggregate in hydrophobic or hydrophilic plates under the same pH, temperature, and concentration conditions.

Rüdiger et al. showed that the SHLVEALYLVCGER and CTSICSLYQLENYCN sequences in insulin bind DnaK.[12] Both encompass the aforementioned peptides involved in amyloid fiber formation (underlined). The same portions of insulin sequence are likely to be recognized by DnaJ, because it shares its substrates with DnaK.[5] It follows that DnaK should antagonize the aggregation promoting effects of the LVEALYL peptide. As shown in Figure 7B, adding 26 μM LVEALYL peptide reduced the HI aggregation lag time from 2.5 ± 0.2 to 1.1 ± 0.2 h. The addition of 0.3 μM DnaK antagonized the effect of the LVEALYL peptide, extending the HI aggregation lag time up to 4.2 ± 0.7 h and slowing aggregation (Figure 7B). The presence of DnaJ enhanced the effect of DnaK [lag time of 7.8 ± 0.9 h (Figure 7C)]. More DnaK was needed to block HI aggregation for longer times. Conversely, ~60 μM LVEALYL peptide was needed to reduce the lag time to the value obtained in the absence of DnaK. Moreover, DnaK binds to amyloid aggregates formed by the LVEALYL peptide alone. Table 1 shows that 0.5 μg of DnaK binds to 25 μg of LVEALYL peptide aggregates.

DISCUSSION

DnaK Recognizes a Conformational Change Occurring on HI Adsorbed on Hydrophobic Surfaces. During aggregation, three pools of insulin were evidenced in this study: the soluble insulin pool, the final amyloidal aggregates, and insulin adsorbed on hydrophobic surfaces. In another article, we show that the latter pool contains prefibrillar insulin aggregates that are essential intermediates in the pathway(s) leading to insulin aggregation. The amount of DnaK needed to block insulin aggregation supports the view that DnaK binds to a minor portion of insulin present in the adsorbed insulin pool. The DnaK concentration (0.3−3 μM) is indeed much lower than the HI concentration in solution. Thus, DnaK cannot significantly displace the monomer−dimer−hexamer equilibria and therefore cannot significantly reduce the HI monomer concentration, which is the form of HI in solution that aggregates in the presence of hydrophobic surfaces.[9] Because DnaK weakly interacts with preformed amyloidal aggregates released in solution, the binding of DnaK to the end product of the aggregation reaction cannot explain its inhibitory effect (Table 1). The target of DnaK is therefore to be found at the material surface. Because the amount of DnaK needed to block HI aggregation increases during the lag time (Figure 5), we rule out competitive adsorption at the material surface as the reason for DnaK inhibition. Moreover, we show that DnaK directly binds to HI adsorbed on hydrophobic surfaces and to HI aggregates released from the surface (Figure 6 and Table 1). We therefore propose that DnaK blocks the formation of HI amyloid fibers on hydrophobic surfaces, by selective binding to target sequences in adsorbed HI. One of these targets is likely to be the hydrophobic LVEALYL peptide, aggregates of which also bind DnaK (see Table 1 and below).

There is kinetic competition between amyloid fiber growth and protection by DnaK, which is illustrated well by the effect of ATP and DnaJ. ATP-loaded DnaK is known to have a lower affinity for its protein substrate than ADP-loaded DnaK[5] and DnaJ, which stimulates ATP hydrolysis on DnaK and reinforces its interaction with its substrate. Our results suggest that in the absence of nucleotides, DnaK binds strongly to adsorbed HI and DnaJ further stabilizes DnaK binding. When the mean residence time of DnaK on exposed hydrophobic HI stretches is sufficiently long, the formation of amyloid fibers is inhibited

(Figure 4). On the other hand, when the residence time of DnaK is reduced by addition of ATP, aggregates can form rapidly because of the liberation of previously occupied hydrophobic growing fiber ends (Figures 3 and 4). Thus, the absence of ATP, through a substrate affinity increase, allows DnaK to win the competition between adding a blocking DnaK to a growing fiber end and an additional HI molecule, which would promote fiber growth. The competition can also be promoted by a sufficiently high concentration of the LVEALYL peptide, which accelerates HI aggregation so that it overcomes DnaK protection (Figure 7). Although significant amounts of DnaK are released from the surface (Table 1), together with the HI amyloid aggregates, it is the surface-bound DnaK fraction that sets the pace for fiber growth. In the ATP-free state, this latter DnaK fraction exhibits an affinity for growing fiber ends that is sufficiently high to block fiber formation. The inhibitory effect of DnaK on HI aggregation is therefore linked to its presence on the material surfaces.

The Amyloidogenic LVEALYL Peptide Is Exposed on HI during Its Aggregation on Hydrophobic Surfaces. The results of this work and others show that insulin aggregates are able to form and grow on hydrophobic surfaces. What is the likely mechanism of this self-assembly process? Up to 40 μg of HI accumulates on the 2 cm^2 surface area of a single microwell during aggregation (Figure 1A). This high surface concentration (0.2 g/m^2) corresponds to 50 protein layers, assuming a uniform coverage of the surface. A consequence of this observation is that insulin does not merely adsorb on the plain hydrophobic surface, but on insulin already bound to the surface. The effect of the hydrophobic surface should therefore be transmitted from the bottom to the top HI layers, where incoming HI binds. This implies the existence of global conformational changes that relay the effect of the hydrophobic surface. Adsorption of HI molecules on a hydrophobic surface will itself trigger the exposure of a hydrophobic stretch at the surface of adsorbed HI. Although we did not evidence these conformational changes directly, several results support this hypothesis. (i) DnaK binds to HI adsorbed on hydrophobic surfaces, which shows that the structure of the HI protein has changed, exposing one of the two hydrophobic peptides known to bind DnaK: SLYQLENY and LVEALYL. (ii) The LVEALYL peptide itself interacts with HI in the presence of hydrophobic surfaces at a substoichiometric concentration in such a way to accelerate aggregation. This peptide has been shown to form antiparallel β-sheets with itself[13] and could therefore help stabilize a conformational change in insulin by binding to intermediate states. (iii) The antagonist effects of the LVEALYL peptide and DnaK binding on HI aggregation reveal the presence of the same aggregation intermediates in the adsorbed HI pool. (iv) DnaK binds to preformed LVEALYL peptide aggregates. We therefore conclude that the buildup of amyloid fibers on the hydrophobic surface is due to HI adsorption and consequent conformational changes, exposing hydrophobic aggregation-prone sites in the protein. This situation occurs for some proteins, but not all of them. BSA, for instance, strongly binds to hydrophobic surfaces but does not accumulate on them and does not aggregate within an entire week in the presence of hydrophobic surfaces.

Perspectives. Our results have interesting potential biochemical and pharmaceutical applications. First, substoichiometric DnaK and DnaJ, in the absence of ATP, could represent a novel and convenient stabilizing additive. Indeed, the low DnaK concentration (0.3 μM), needed to stabilize HI solutions, and its selectivity for exposed hydrophobic peptide domains are characteristics that most traditional stabilizing agents lack. Two recent papers by Rasmussen et al.[31,32] showed that the protein α-crystallin, a member of the small heat shock protein family (sHSP), prevents HI aggregation on hydrophobic surfaces. Molecular chaperones, therefore, represent alternative approaches to guaranteeing the long-term storage of proteins, either in solution or in contact with the container surface. One should nevertheless be aware that DnaK triggers inflammatory responses and thus cannot be injected into patients.[33] DnaK, or better the DnaK–DnaJ combination, could also provide a sensitive in vitro assay to test for protein conformational changes at material surfaces, as shown for HI in this study. By revealing the presence of hydrophobic stretches exposed at the surface of proteins adsorbed on hydrophobic materials, this assay could provide a screening tool for the optimization of protein stability conditions.

AUTHOR INFORMATION

Corresponding Author

*Telephone: ++ 33 4 56 52 93 35. Fax: ++ 33 4 56 52 93 01. E-mail: marianne.weidenhaupt@grenoble-inp.fr.

Present Address

[§]EIFFAGE Travaux Publics, Centre d'Etudes et de Recherches, 8 rue du Dauphiné, 69960 Corbas, France.

Funding

This project was financed by a CNRS "Prise de risques" grant (CHAPROMAT). T.B. is a recipient of a CIFRE fellowship (371/2007). L.N.holds a doctoral fellowship from La Région Rhône-Alpes.

Notes

The authors declare no competing financial interest.

ACKNOWLEDGMENTS

We thank Benoît Duroux, Frédérique Crozet, and Sébastien Janvier for excellent technical assistance in particle size analysis, Laetitia Rapenne and Isabelle Paintrand in EM analysis and Bernd Bukau, Alexander Mogk, and Matthias Mayer for providing chaperone plasmids and protocols. We are grateful for the scientific input of Yves Bréchet (Grenoble-INP). We thank the CIME facility and BBSI laboratory (CEA Grenoble) for access to their equipment.

REFERENCES

(1) Ellis, R. J., and van der Vies, S. M. (1991) Molecular chaperones. *Annu. Rev. Biochem. 60*, 321–347.

(2) Ellis, R. J., van der Vies, S. M., and Hemmingsen, S. M. (1989) The molecular chaperone concept. *Biochem. Soc. Symp. 55*, 145–153.

(3) Ellis, R. J., and Hemmingsen, S. M. (1989) Molecular chaperones: Proteins essential for the biogenesis of some macromolecular structures. *Trends Biochem. Sci. 14*, 339–342.

(4) Mogk, A., Tomoyasu, T., Goloubinoff, P., Rudiger, S., Roder, D., Langen, H., and Bukau, B. (1999) Identification of thermolabile *Escherichia coli* proteins: Prevention and reversion of aggregation by DnaK and ClpB. *EMBO J. 18*, 6934–6949.

(5) Bukau, B., and Horwich, A. L. (1998) The Hsp70 and Hsp60 chaperone machines. *Cell 92*, 351–366.

(6) Goloubinoff, P., Mogk, A., Zvi, A. P., Tomoyasu, T., and Bukau, B. (1999) Sequential mechanism of solubilization and refolding of stable protein aggregates by a bichaperone network. *Proc. Natl. Acad. Sci. U.S.A. 96*, 13732–13737.

(7) Diamant, S., Ben-Zvi, A. P., Bukau, B., and Goloubinoff, P. (2000) Size-dependent disaggregation of stable protein aggregates by the DnaK chaperone machinery. *J. Biol. Chem. 275*, 21107–21113.

(8) Sluzky, V., Tamada, J. A., Klibanov, A. M., and Langer, R. (1991) Kinetics of insulin aggregation in aqueous solutions upon agitation in the presence of hydrophobic surfaces. *Proc. Natl. Acad. Sci. U.S.A. 88*, 9377−9381.
(9) Sluzky, V., Klibanov, A. M., and Langer, R. (1992) Mechanism of insulin aggregation and stabilization in agitated aqueous solutions. *Biotechnol. Bioeng. 40*, 895−903.
(10) Brange, J., Andersen, L., Laursen, E. D., Meyn, G., and Rasmussen, E. (1997) Toward understanding insulin fibrillation. *J. Pharm. Sci. 86*, 517−525.
(11) Sharp, J. S., Forrest, J. A., and Jones, R. A. (2002) Surface denaturation and amyloid fibril formation of insulin at model lipid-water interfaces. *Biochemistry 41*, 15810−15819.
(12) Rüdiger, S., Germeroth, L., Schneider-Mergener, J., and Bukau, B. (1997) Substrate specificity of the DnaK chaperone determined by screening cellulose-bound peptide libraries, *EMBO J 16*, 1507−582.
(13) Ivanova, M. I., Sievers, S. A., Sawaya, M. R., Wall, J. S., and Eisenberg, D. (2009) Molecular basis for insulin fibril assembly. *Proc. Natl. Acad. Sci. U.S.A. 106*, 18990−18995.
(14) Cegielska, A., and Georgopoulos, C. (1989) Functional domains of the *Escherichia coli* dnaK heat shock protein as revealed by mutational analysis. *J. Biol. Chem. 264*, 21122−21130.
(15) McCarty, J. S., and Walker, G. C. (1991) DnaK as a thermometer: Threonine-199 is site of autophosphorylation and is critical for ATPase activity. *Proc. Natl. Acad. Sci. U.S.A. 88*, 9513−9517.
(16) Buchberger, A., Schroder, H., Buttner, M., Valencia, A., and Bukau, B. (1994) A conserved loop in the ATPase domain of the DnaK chaperone is essential for stable binding of GrpE. *Nat. Struct. Biol. 1*, 95−101.
(17) Veinger, L., Diamant, S., Buchner, J., and Goloubinoff, P. (1998) The small heat-shock protein IbpB from *Escherichia coli* stabilizes stress-denatured proteins for subsequent refolding by a multi-chaperone network. *J. Biol. Chem. 273*, 11032−11037.
(18) Olson, B. J., and Markwell, J. (2007) Assays for determination of protein concentration. *Current Protocols in Protein Science*, Chapter 3, Unit 3, 4, Wiley, New York.
(19) Smith, D. A., and Radford, S. E. (2000) Protein folding: Pulling back the frontiers. *Curr. Biol. 10*, R662−R664.
(20) Wiechelman, K. J., Braun, R. D., and Fitzpatrick, J. D. (1988) Investigation of the bicinchoninic acid protein assay: Identification of the groups responsible for color formation. *Anal. Biochem. 175*, 231−237.
(21) Stoscheck, C. M. (1990) Quantitation of protein. *Methods Enzymol. 182*, 50−68.
(22) LeVine, H. III (1999) Quantification of β-sheet amyloid fibril structures with thioflavin T. *Methods Enzymol. 309*, 274−284.
(23) Blundell, T. L., Cutfield, J. F., Dodson, G. G., Dodson, E., Hodgkin, D. C., and Mercola, D. (1971) The structure and biology of insulin. *Biochem. J. 125*, 50P−51P.
(24) Burke, M. J., and Rougvie, M. A. (1972) Cross-β protein structures. I. Insulin fibrils. *Biochemistry 11*, 2435−2439.
(25) Garriques, L. N., Frokjaer, S., Carpenter, J. F., and Brange, J. (2002) The effect of mutations on the structure of insulin fibrils studied by Fourier transform infrared (FTIR) spectroscopy and electron microscopy. *J. Pharm. Sci. 91*, 2473−2480.
(26) Theyssen, H., Schuster, H. P., Packschies, L., Bukau, B., and Reinstein, J. (1996) The second step of ATP binding to DnaK induces peptide release. *J. Mol. Biol. 263*, 657−670.
(27) McCarty, J. S., Buchberger, A., Reinstein, J., and Bukau, B. (1995) The role of ATP in the functional cycle of the DnaK chaperone system. *J. Mol. Biol. 249*, 126−137.
(28) Skowyra, D., and Wickner, S. (1995) GrpE Alters the Affinity of DnaK for ATP and Mg. *J. Biol. Chem. 270*, 26282−26285.
(29) Suh, W.-C., Burkholder, W. F., Lu, C. Z., Zhao, X., Gottesman, M. E., and Gross, C. A. (1998) Interaction of the Hsp70 molecular chaperone, DnaK, with its cochaperone DnaJ. *Proc. Natl. Acad. Sci. U.S.A. 95*, 15223−15228.
(30) Liberek, K., Wall, D., and Georgopoulos, C. (1995) The DnaJ chaperone catalytically activates the DnaK chaperone to preferentially bind the sigma 32 heat shock transcriptional regulator. *Proc. Natl. Acad. Sci. U.S.A. 92*, 6224−6228.
(31) Rasmussen, T., Kasimova, M. R., Jiskoot, W., and van de Weert, M. (2009) The Chaperone-like Protein´-Crystallin Dissociates Insulin Dimers and Hexamers, *Biochemistry 4*893139320.
(32) Rasmussen, T., Tantipolphan, R., van de Weert, M. and Jiskoot, W. (2010) The molecular chaperone alpha-crystallin as an excipient in an insulin formulation. *Pharm Res 2*713371347.
(33) Nolan, A., Weiden, M. D., Hoshino, Y., and Gold, J. A. (2004) Cd40 but not CD154 knockout mice have reduced inflammatory response in polymicrobial sepsis: A potential role for *Escherichia coli* heat shock protein 70 in CD40-mediated inflammation in vivo. *Shock 22*, 538−542.

Acta Biomaterialia 9 (2013) 5070–5079

Contents lists available at SciVerse ScienceDirect

Acta Biomaterialia

journal homepage: www.elsevier.com/locate/actabiomat

Human insulin adsorption kinetics, conformational changes and amyloidal aggregate formation on hydrophobic surfaces

Laurent Nault [a], Perry Guo [a], Bhagyashree Jain [a], Yves Bréchet [b], Franz Bruckert [a], Marianne Weidenhaupt [a,*]

[a] Laboratoire des Matériaux et du Génie Physique, Phelma-Minatec, 3 parvis Louis Néel, BP257, F-38016 Grenoble Cedex, France
[b] Laboratoire de Science et Ingénierie des Matériaux et des Procédés, Phelma-Campus, 1130 rue de la Piscine, BP 75, F-38402 Saint-Martin d'Hères Cedex, France

ARTICLE INFO

Article history:
Received 12 June 2012
Received in revised form 14 September 2012
Accepted 19 September 2012
Available online 25 September 2012

Keywords:
Protein adsorption on material surfaces
Protein aggregation
Insulin
Surface plasmon resonance imaging (SPRi)
Fourier transform infrared spectroscopy (FTIR)

ABSTRACT

The formation of insulin amyloidal aggregates on material surfaces is a well-known phenomenon with important pharmaceutical and medical implications. Using surface plasmon resonance imaging, we monitor insulin adsorption on model hydrophobic surfaces in real time. Insulin adsorbs in two phases: first, a very fast phase (less than 1 min), where a protein monolayer forms, followed by a slower one that can last for at least 1 h, where multilayered protein aggregates are present. The dissociation kinetics reveals the presence of two insulin populations that slowly interconvert: a rapidly dissociating pool and a pool of strongly bound insulin aggregates. After 1 h of contact between the protein solution and the surface, the adsorbed insulin has practically stopped dissociating from the surface. The conformation of adsorbed insulin is probed by attenuated total reflection–Fourier transform infrared spectroscopy. Characteristic shifts in the amide A and amide II′ bands are associated with insulin adsorption. The amide I band is also distinct from that of soluble or aggregated insulin, and it slowly evolves in time. A 1708 cm^{-1} peak is observed, which characterizes insulin adsorbed for times longer than 30 min. Finally, Thioflavin T, a marker of extended β-sheet structures present in amyloid fibers, binds to adsorbed insulin after 30–40 min. Altogether, these results reveal that the conformational change induced in insulin upon binding to hydrophobic surfaces allows further insulin binding from the solution. Adsorbed insulin is thus an intermediate along the α-to-β structural transition that results in the formation of amyloidal fibers on these material surfaces.

1. Introduction

Amyloid fibers are protein aggregates stabilized by intermolecular β-sheets [1]. They are characterized by staining with Congo red and Thioflavin T (ThT), and by a specific cross β X-ray diffraction pattern [2]. Several proteins or polypeptides are able to form amyloids under both natural and artificial conditions [3,4], e.g. islet amyloid polypeptide, which is associated with diabetes II, or the Aβ (1–40) peptide, which fibrillates in Alzheimer's disease [5]. Insulin is a well-known hormone that regulates blood glucose concentration. Its structure in solution is essentially helical [6]. Daily insulin injections are used to treat type I and many type II diabetic patients. It has long been recognized that insulin solutions also form amyloid fibers in the presence of hydrophobic materials [7–9], especially in contact with peristaltic pump tubing [10]. Furthermore, the daily injection of insulin solutions at the same place occasionally induces local amyloidogenesis, characterized by the presence of insulin amyloidal aggregates [11,12]. Similarly, the formation of Aβ (1–40) peptide amyloid fibers is also strongly influenced by material surfaces [13,14], such as Teflon [15], alkanethiol self-assembled monolayers [16] and the air–water interface [17,18]. Understanding the role of material surfaces in protein instability is therefore useful.

Pioneering work by Sluzky et al. [19,20] shows that human insulin (HI) indeed aggregates on hydrophobic material surfaces, at pH 7 and 37 °C under agitation, and that aggregation proceeds in two phases: a nucleation phase or lag time, where no insulin aggregation is observed, followed by an aggregation phase, where most of the insulin aggregates. The length of both phases is influenced by the material hydrophobicity, its surface area compared to the fluid volume, the extent of agitation and the temperature. Ballet et al. [21] further investigated the aggregation mechanism, and showed that the aggregates form on the surface and are later released in the fluid phase. Using DnaK, a bacterial chaperone, as a marker of protein denaturation, they showed that adsorbed HI has a conformation different from soluble and aggregated HI.

* Corresponding author.
E-mail address: marianne.weidenhaupt-blackledge@grenoble-inp.fr (M. Weidenhaupt).

1742-7061/$ - see front matter © 2012 Acta Materialia Inc. Published by Elsevier Ltd. All rights reserved.
http://dx.doi.org/10.1016/j.actbio.2012.09.025

A limitation of these previous studies is that the relatively small amount of adsorbed HI could not be detected with sufficient sensitivity during the nucleation time, with prefibrillar aggregates forming on the material surface. The evidence for the insulin conformational change upon adsorption was also indirect. Finally, in the 96-well plate configuration used in these experiments, ThT binding on adsorbed proteins was detected only after the onset of the aggregation phase. More sensitive methods are therefore required to monitor the adsorption and the interaction of HI molecules on hydrophobic model surfaces in real time.

In this study, we combine three biophysical approaches to study HI adsorption and conformational changes on hydrophobic surfaces (Fig. 1): surface plasmon resonance is sensitive to refractive index changes close to the surface and is used to monitor adsorption kinetics with good temporal resolution; attenuated total reflection–Fourier transform infrared spectroscopy (ATR-FTIR) monitors infrared vibrational bands and is therefore sensitive to conformational changes in surface-adsorbed protein, especially the conversion of α-helices into β-sheets; and ThT binds to amyloidal aggregates and is a sensitive marker of the final insulin state. The common trait of these experiments is that the surface of interest is put into contact with a continuous flow of an HI solution, in contrast with previous experiments, where an HI solution was incubated in a container with a specific surface chemistry. In the configuration presented here, the soluble HI concentration is almost constant throughout the duration of the experiment. A time-resolved sequence of events can thus be defined and studied, from the start of HI adsorption to the formation of amyloidal aggregates on the surface.

2. Materials and methods

2.1. Chemicals

Unless otherwise stated, all chemicals were purchased from Sigma–Aldrich. Experiments were conducted in TBS (25 mM Tris–HCl, pH 7.4, 125 mM NaCl). HI (recombinant, expressed in yeast) solutions were prepared at 0.5 mg ml^{-1} (86 μM). All solutions were filtered (0.22 μm, Millipore Stericup filter unit) before use. For the ATR-FTIR experiments, insulin solutions were prepared at 86 μM in phosphate-buffered saline (10 mM H_3PO_4, 2.7 mM KCl and 137 mM NaCl) in D_2O and filtered at 0.22 μm. The pD was adjusted to 6.89 using a pH-meter, which corresponds to pH 7.30 in H_2O. The refractive index of the solutions was measured with an Abbe refractometer.

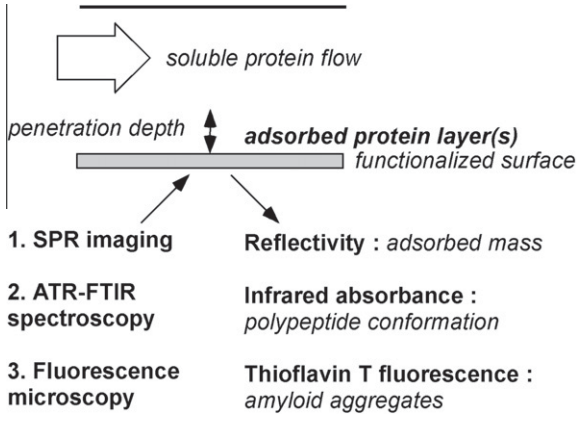

Fig. 1. Scheme of the experimental procedures used in this study. The sensor surface (gray bar) is coated with a hydrophobic self-assembled monolayer and a protein solution is passed over it. Contributions to the signal originate from the adsorbed protein layer and from the soluble protein contained in the penetration depth, which is technique dependent. The different physico-chemical parameters monitored during the studies are summarized below.

2.2. Surface functionalization

Gold-coated prisms (SPRi Biochips) were obtained from Horiba. Prisms were cleaned using oxygen plasma (12 W, 2 min), and half of the gold surface was functionalized with polyethylene glycol thiol (SH-PEG, 8 monomer units, MW = 569.8 g mol^{-1}, from Iris Biotech GmbH) at 1 mg ml^{-1} in water at room temperature to obtain a hydrophilic surface. The other half was then treated with hexadecane thiol (SH-C_{16}) at 1 mg ml^{-1}, diluted in toluene at room temperature to obtain a hydrophobic surface. The water surface contact angle was measured (DSA100 Krüss) and found to be 38 ± 3° and 100 ± 2.5° for the hydrophilic and hydrophobic sides, respectively. After each experiment, the prisms were washed with 1% sodium dodecyl sulfate (SDS) and distilled water to remove insulin aggregates.

Round (35 mm diameter) glass coverslips were cleaned using oxygen plasma (12 W, 2 min), siliconized with dimethyldichlorosilane (DDS) (5% in toluene, 2 h, room temperature), washed in toluene and ethanol, and cured at 110 °C for 2 h. The water surface contact angle was 102.1 ± 1.3°.

For ATR-FTIR measurements, a silicon prism was purchased from Specac Ltd, cleaned using oxygen plasma (12 W, 2 min), functionalized with phenyldimethylmethoxysilane (PDMMS) (5% in toluene, 2 h, room temperature), washed in toluene and ethanol, and cured at 110 °C for 2 h. The water surface contact angle was 103.1 ± 3.7°.

2.3. Surface plasmon resonance sensorgram acquisition and analysis

Buffer and protein solutions were injected in the SPRi chamber using syringe pumps at 100 μl min^{-1} at room temperature (22 °C). Reflectivity images were taken every 3 s. The SPRi instrument (Horiba Scientific SPRi-Lab+™) records reflectivity changes of manually predefined spots on the treated gold surface. Calibration was performed using a 50 mM NaCl solution, to adjust the response of the spots to a known refractive index change (3×10^{-4}). A background image was acquired at the beginning of the experiment, which was then subtracted from the subsequent ones. Three zones of interest were defined on the SH-PEG and SH-C_{16} sides of the prism, and the sensorgrams obtained on each side were averaged. A difference sensorgram $\Delta R(t)$ was finally obtained by subtracting the SH-PEG sensorgram from the SH-C_{16} one.

The adsorption kinetics were analyzed with the following equation:

$$\Delta R(t) = A(1 - \exp(-kt)) + bt \quad (1)$$

where A and k are the amplitude and rate of the fast adsorption component, and b is the rate of the slow protein binding component.

The desorption kinetics were analyzed with the following equation:

$$\Delta R(t) = A_1 \exp(-k_1 t)) + A_2 \exp(-k_2 t) \quad (2)$$

where A_1 and A_2 are the amplitude of the fast and slow desorption components, respectively, and k_1 and k_2 are the rate constants of the fast and slow desorption components, respectively. Data are obtained from several independent experiments, using different functionalized prisms and HI solutions.

The conversion between the ΔR and the adsorbed mass per area is given in pg mm^{-2} by the equation:

$$\text{mass} = 122.25\Delta R - 0.6557 \quad (3)$$

assuming that the signal is in the linear range of the instrument and solution refractive index changes have been corrected (equation provided by Horiba SPRi+). The relationship between ΔR and the refractive index changes, Δn, was determined using NaCl solutions

at different concentrations and was found to be: $\Delta R = 28333\Delta n$. This relation was used to calculate the amplitude of the refractive index change in protein solutions compared to buffer.

Having recorded the dissociation kinetics, the hydrophobic surface was regenerated with SDS (5%, 5 min).

2.4. FTIR recordings

Aggregated HI solutions were prepared in 96-well plates (Greiner Bio-One, contact angle = 85 ± 4.7°) as follows. The plates were covered by plastic sheets, incubated at 37 °C and shaken at 1200 rpm (Heidolph Titramax, 1.5 mm vibration orbit) for 12 h. The aggregated solution was analyzed using a Brucker Vertex 70 FTIR instrument. The liquid cell was a CaF_2 cell from Perkin Elmer Instruments. Using the OPUS software, compensation was applied to filter the contributions of H_2O and CO_2 to the spectra. Smoothing was done using the Savitzky–Golay equation. Baselines were flattened using a linear correction.

2.5. ATR-FTIR recordings

Buffer and protein solutions were prepared in D_2O and injected in the chamber using a peristaltic pump at 10 ml min^{-1} in a closed circuit, at room temperature. A tubing diameter of 5 mm was used to reduce shear stress. No amyloid fibers were formed on the tubing during the time of the experiment. The total volume of the sample was 10 ml. During recording of the spectra (about 2 min), the flow was stopped. Spectra were acquired from 1400 to 4000 cm^{-1}. Baselines were flattened using a linear correction in the range 4000–2800 cm^{-1} and in the range 2000–1400 cm^{-1}. H_2O and CO_2 compensations were done as described for FTIR recordings. Further smoothing was performed using a Savitzky–Golay algorithm. Spectral decomposition of the amide I band (1600–1700 cm^{-1}) was done using the second derivative of the spectra to find peak positions. Then, using the Levenberg–Marquardt algorithm, 3–5 peaks were fitted to the experimental data (residual relative error less than 2.5×10^{-5}).

The spectra $A(t)$ recorded at time t contain two contributions: $A(t) = A_{ads}(t) + A_{sol}$, where $A_{ads}(t)$ is the spectrum of adsorbed HI at time t and A_{sol} is the constant soluble HI contribution. With this notation, the spectrum recorded after 80 min in the presence of HI and 1 min wash with buffer is $A_{ads}(80)$. The spectra of HI adsorbed at time t, $A_{ads}(t)$, can therefore be calculated by the following equation:

$$\begin{aligned} A_{ads}(t) &= A(t) - A(0) + A_{ads}(80) - [A(80) - A(0)] \\ &= A(t) + A_{ads}(80) - A(80) \end{aligned} \quad (4)$$

2.6. Surface fluorescence measurements

A flow chamber was built on a DDS-coated glass coverslip using a Glycotech flow chamber (channel width = 2.5 mm, channel thickness = 0.127 mm). A 20 μl min^{-1} flow rate was applied by a syringe pump. When indicated, ThT was added to the buffer and protein solutions at a 20 μM final concentration. The surface fluorescence was observed by a ×63 objective (NA = 1.4) on an IX-71 Olympus microscope fitted with a DAPI fluorescence cube (λ_{ex} = 435 ± 10 nm, λ_{em} = 485 ± 25 nm) and connected to an Olympus DP30BW camera. The image of the field stop was used to ensure proper focusing on the glass surface. Fluorescence images of the surface were recorded at the indicated times. To avoid photobleaching, each image was recorded at a different position, using a motorized stage. Using the ImageProPlus software, the average fluorescence intensity was calculated on the image of the field stop and the value of the dark background was subtracted.

3. Results

3.1. Insulin adsorption and dissociation kinetics on hydrophobic surfaces

Surface plasmon resonance imaging (SPRi) is a sensitive method to measure the amount of molecules adsorbed on functionalized gold surfaces (see Fig. 1). A gold prism was prepared with half of the surface coated with SH-PEG and the other half with C_{16} alkyl-thiol. SPR is sensitive to refractive index changes within the penetration distance of the evanescent wave. When a solution is bathing the prism, the SPR signal sums up two contributions, one due to the refractive index of the bulk solution, the other due to the mass adsorbed on the gold surface. The response time of the setup was determined by passing a 50 mM NaCl solution over the functionalized prism. In this case, no adsorption is expected. The sensorgrams indeed indicate a fully reversible, fast (<1 min) signal, the amplitude of which minimally depends on the surface functionalization (Fig. 2A and B). This corresponds to the time needed to exchange solutions over the prism surface. The linearity of the technique with respect to the amount of adsorbed material was assessed by adsorbing a polyelectrolyte multilayer film on the prism layer by layer. In this experiment, the prism was not functionalized and a 10 mg ml^{-1} polyethyleneimine (PEI) solution in TBS was passed first to provide an anchoring layer. Solutions of 5 mg ml^{-1} polystyrene sulfonate (PSS, negatively charged) and 5 mg ml^{-1} polyallylaminehydrochloride (PAH, positively charged) in TBS were passed alternately over the surface, separated by washes with TBS (Fig. 2C). Previous work showed that the thickness of these films increased linearly with the number of layers deposited, each polystyrene sulfonate layer forming a 3–5 nm thick layer [22]. Using QCM-D and waveguide spectroscopy, up to 12 layers could be monitored. In contrast, with SPRi, the deposition of the same polyelectrolytes gave signals that rapidly decreased as the number of layers increased (Fig. 2C and D). The amplitude of the signal was plotted as a function of the thickness of the multilayered film, obtained by waveguide spectroscopy [23] and fitted as $S[1 - \exp(-z/d_P)]$, where S represents the maximum reflectivity change and d_P is the penetration distance. From Fig. 2C and D, a penetration distance of 18.7 ± 1 nm and a maximum signal of 26.5 ± 1 RU can be estimated. A single layer of PSS corresponds to 6 RU, which is 0.73 mg m^{-2} according to Eq. (3).

A typical HI adsorption kinetics experiment is shown in Fig. 3A. A 86 μM HI solution (0.5 mg ml^{-1}) was passed over the functionalized prism during 14 min, then the surface was washed with buffer for 45 min. Sensorgrams were recorded on both the hydrophilic SH-PEG-coated side and the hydrophobic C_{16} alkyl-thiol-coated side. On the hydrophilic side, a fast reversible signal was observed, which could be attributed to refractive index changes solely. On the hydrophobic side, a much larger signal was observed, which rose in two phases and decreased much more slowly after the buffer had replaced the protein solution. This signal is due to both the refractive index change and the binding of HI on the hydrophobic surface. After a 5 min wash, the reflectivity remained 0.5 RU higher than on the PEG-coated side.

Subtracting the sensorgram acquired on the PEG-coated surface from the one acquired on the C_{16} alkyl-coated surface allows the common component due to refractive index changes to be eliminated and the HI adsorption and desorption kinetics on the hydrophobic surface to be specifically obtained (Fig. 3B). The association curve consists of two components – a fast signal, rising to 1 RU in

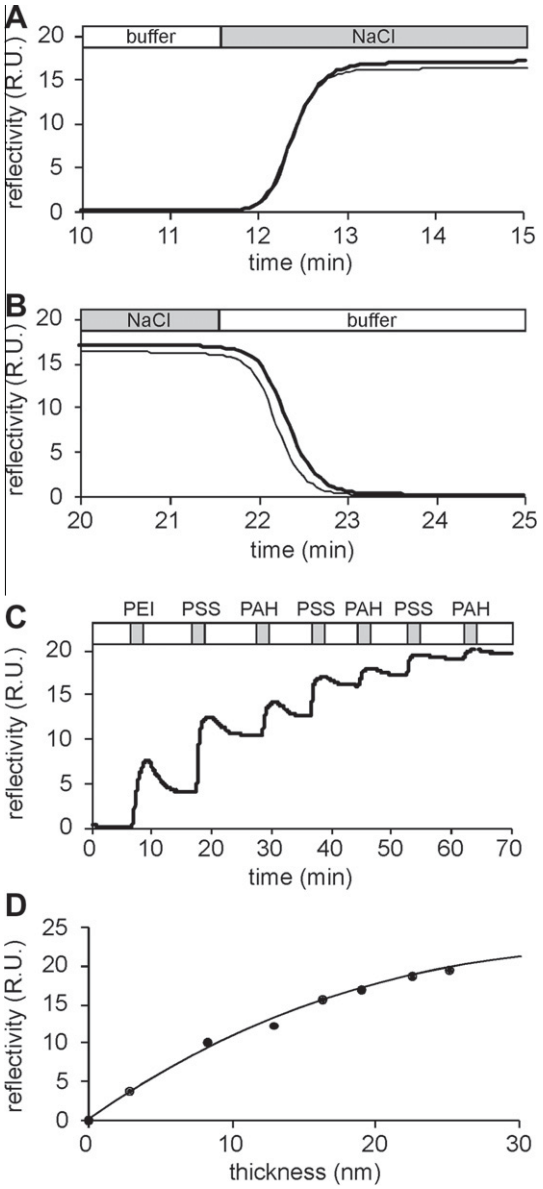

Fig. 2. Calibration of the SPRi apparatus. A and B. Changes in C_{16}-coated (heavy line) and PEG-coated (thin line) gold surface reflectivity were monitored by surface plasmon resonance during injection of 50 mM NaCl (A) and washing in buffer (B). (C) SPRi recording of a PSS and PAH polyelectrolyte layer-by-layer film built on a gold surface. PEI is first deposited as an anchoring layer. (D) The amplitude of the SPRi signal after depositing the successive layers and washing with buffer (data from (C)) is plotted as a function of the adsorbed layer thickness (z) determined by Picart et al. [23]. The solid line is a fit with the equation: $S(z) = S[1 - \exp(-z/d_P)]$, where S (26.5 ± 1 RU) is the maximum reflectivity change and d_P (18.7 ± 1 nm) is the penetration distance.

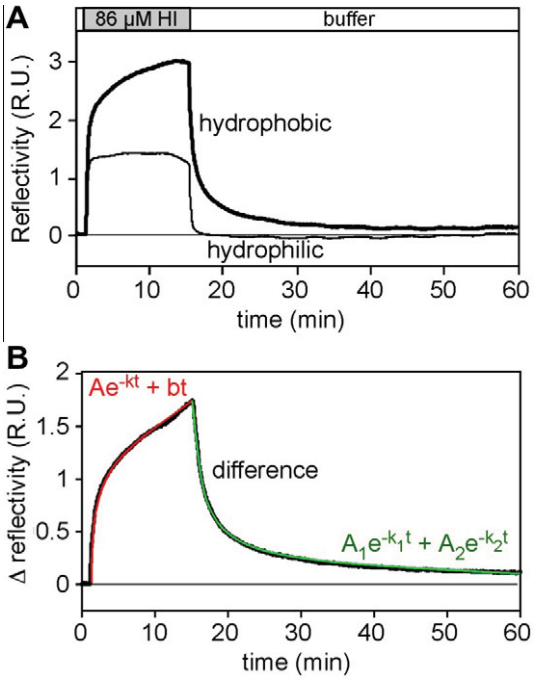

Fig. 3. HI association and dissociation kinetics on hydrophobic surfaces. (A) SPRi signal for 0.5 mg ml^{-1} HI injection and buffer washing on a prism functionalized with C_{16}-thiol (heavy line) or SH-PEG (thin line). (B) The difference signal obtained by subtracting the signals recorded on the SH-PEG and SH-C_{16} sides reveals the HI adsorption and desorption kinetics (black line). The red and green curves represent a mathematical fit of the data with Eqs. (1) and (2), respectively. A = 1.076 ± 0.005; k = 1.32 ± 0.02; b = 0.0545 ± 0.0005. A_1 = 1.153 ± 0.005; k_1 = 0.707 ± 0.007; A_2 = 0.570 ± 0.004; k_2 = 0.0595 ± 0.0007.

about 1 min, followed by a slow, almost linear increase. During the wash, the dissociation curve also consists of two components – a fast signal, going up to 1.3 RU in about 5 min, followed by a much slower decrease that lasted for more than 30 min. The association and dissociation kinetics were adequately fitted by the phenomenological equations 1 and 2 (see Materials and methods), giving seven parameters: A, k, b, A_1, k_1, A_2 and k_2. A and k represent the amplitude and rate constant of the fast association component, and b represents the slope of the slow association component. A_1 and k_1 (and A_2 and k_2) represent the amplitudes and rate constants of the fast (and slow) dissociation components, respectively. These biphasic association and dissociation curves show that HI binding on hydrophobic surfaces is not a reversible process. The slow dissociation component indicates that some HI is strongly bound to the surface, whereas the fast dissociation component suggests that another pool of HI is much more weakly bound to the surface.

In a parallel experiment, the surface concentrations of HI adsorbed on a hydrophilic PEG-coated microwell or on a hydrophobic polystyrene plastic surface (2 cm^2) were directly determined using the bicinchoninic assay [24]. No HI was detectable on the hydrophilic surface, whereas 0.4 mg m^{-2} was quantified on hydrophobic surfaces. Comparing this value to the corresponding SPRi experiments shows that 1 RU = 0.2 mg m^{-2}. This is close to the value obtained with Eq. (3) (0.12 mg m^{-2} per RU). Assuming that the calibration determined for the fast phase of the SPRi association signal holds also for the slow phase, the rate of insulin adsorption would be about 0.013 mg m^{-2} min^{-1}.

Since SPRi is a very sensitive technique, HI adsorption could easily be monitored on hydrophobic surfaces at different concentrations down to 0.1 μM. Fig. 4A shows an SPRi difference sensorgram obtained on the same surface where successive HI concentrations ranging from 0.49 to 86 μM were applied. Each HI concentration was applied for 10 min, after which the surfaces were washed. It is apparent from the difference sensorgram that the slope of the slow association kinetics and the amplitude of the slow dissociation kinetics both increase with HI concentration. In Fig. 4B and C, the effect of increasing HI concentrations on the parameters A, k (Fig 4B) and b (Fig 4C) describing the association kinetics are displayed. The amplitude A of the fast association component increases with HI concentration and saturates at 1 ± 0.05 RU (2.6 mg m^{-2}), with an apparent binding constant of 2.5 ± 0.5 μM, showing that the amount of HI was limited by the available surface. The rate constant of the fast association kinetics k remains constant at 1.3 ± 0.1 min^{-1}. The fast rise of the

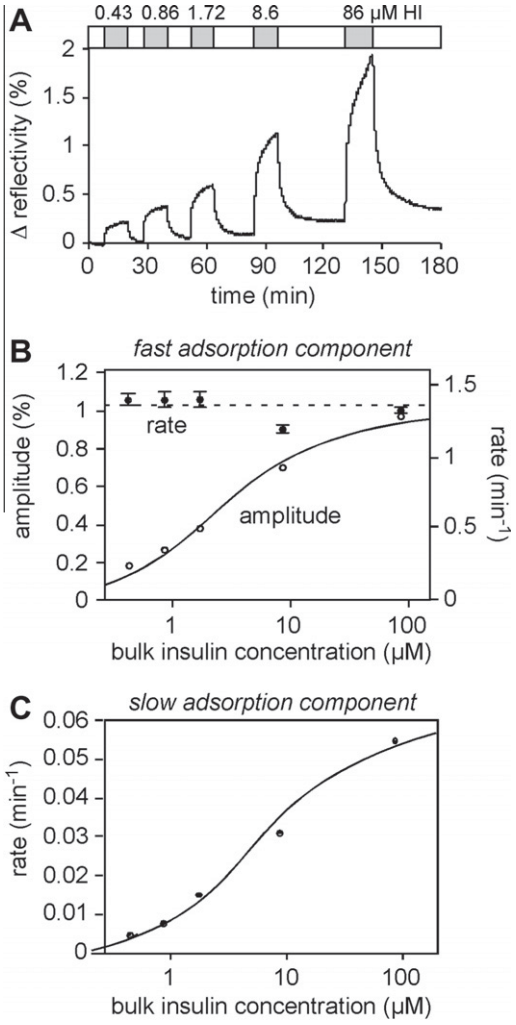

Fig. 4. Effect of HI concentration on HI adsorption and desorption kinetics. (A) Successive HI adsorption and desorption difference SPRi signals recorded at the indicated HI concentrations. (B, C) The adsorption kinetics were fitted with Eq. (1) to calculate the amplitude A and the rate constant k of the fast component and the slope b of the slow component. (B) Parameters A and k are plotted as a function of the HI concentration. The error in A is smaller than the symbol size. The solid curve is a fit with the following relationship: $A = A_{max}[HI]/([HI] + K)$, where A_{max} (1 ± 0.05 RU) is the HI binding site concentration and K (2.5 ± 0.5 μM) is the apparent binding constant. (C) Parameter b is plotted as a function of the HI concentration. The error on b is smaller than the symbol size. The solid curve is a fit with the following relationship: $b = b_{max}[HI]/([HI] + K')$, where b_{max} (0.058 ± 0.002 RU min^{-1}) is the maximum HI association rate and K' (6.1 ± 1 μM) is the apparent binding constant.

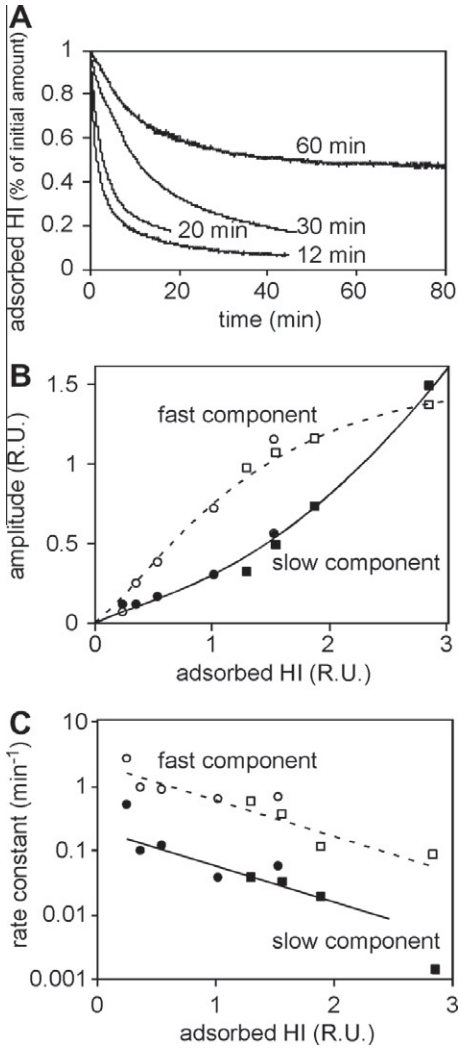

Fig. 5. Effect of incubation time on HI desorption kinetics. (A) SPRi desorption difference sensorgrams obtained after application of 86 μM HI for the indicated time. The SPRi difference signals have been normalized to the values reached at the beginning of the washing with buffer. (B) Amplitudes of the fast (open symbols) and slow (closed symbols) components of the desorption sensorgrams, represented as a function of the SPRi value at the onset of the washing with buffer. They correspond to parameters A_1 and A_2 in Eq. (2). The lines are hand-drawn. (C) Rate constant of the fast (open symbols) and slow (closed symbols) components of the desorption sensorgrams, represented as a function of the SPRi value at the onset of the buffer wash. They correspond to parameters k_1 and k_2 in Eq. (2). The lines are exponential fits of the data. In the case of the slow component, the two extreme points were omitted. In (B) and (C), squares and circles correspond to desorption kinetics obtained after applying either different HI concentrations for the same time or 86 μM HI for different times, respectively. The errors in the determination of the kinetic desorption parameters are smaller than the symbol size.

association kinetics is thus limited by the response time of the SPRi setup. The slope of the slow association component b also increases with HI concentration and saturates at 0.058 ± 0.002 RU min^{-1} (0.023 ± 0.001 mg m^{-2} min^{-1}), with an apparent binding constant of 6.1 ± 1 μM. The growth of HI aggregates on the hydrophobic surface thus occurs at a limited number of specific sites.

In a second set of experiments, we varied the time during which the HI solution was in contact with the prism surface (Fig 5A). As the contact time is increased, the slow association component lasts longer (not shown) and the slow dissociation component becomes more important (Fig 5B) and slower (Fig 5C). This indicates that, as time progresses, insulin binds more strongly to the alkyl surface and an increasing amount of insulin remains adsorbed in a strongly bound form on the hydrophobic surface. The parameters describing the association kinetics are similar to those described in the experiments where the HI concentration was varied. For the dissociation kinetics, both sets of experiments were analyzed together, and the kinetic parameters were plotted as a function of the amount of HI adsorbed on the surface at the beginning of the wash. The relative amplitude of the fast dissociation component A_1 decreased and the amplitude of the slow dissociation component A_2 increased as the amount of adsorbed HI increased. Furthermore, the fast and the slow dissociation rate constants k_1 and k_2 decreased exponentially, in a parallel manner, as the amount of adsorbed HI increased. This shows that the presence of adsorbed HI further stabilizes HI binding. HI adsorption is therefore a cooperative process.

It has been shown that agitation has two opposite effects on HI aggregation induced by hydrophobic surfaces: on the one hand, it prevents the formation of a depleted diffusion layer that slows

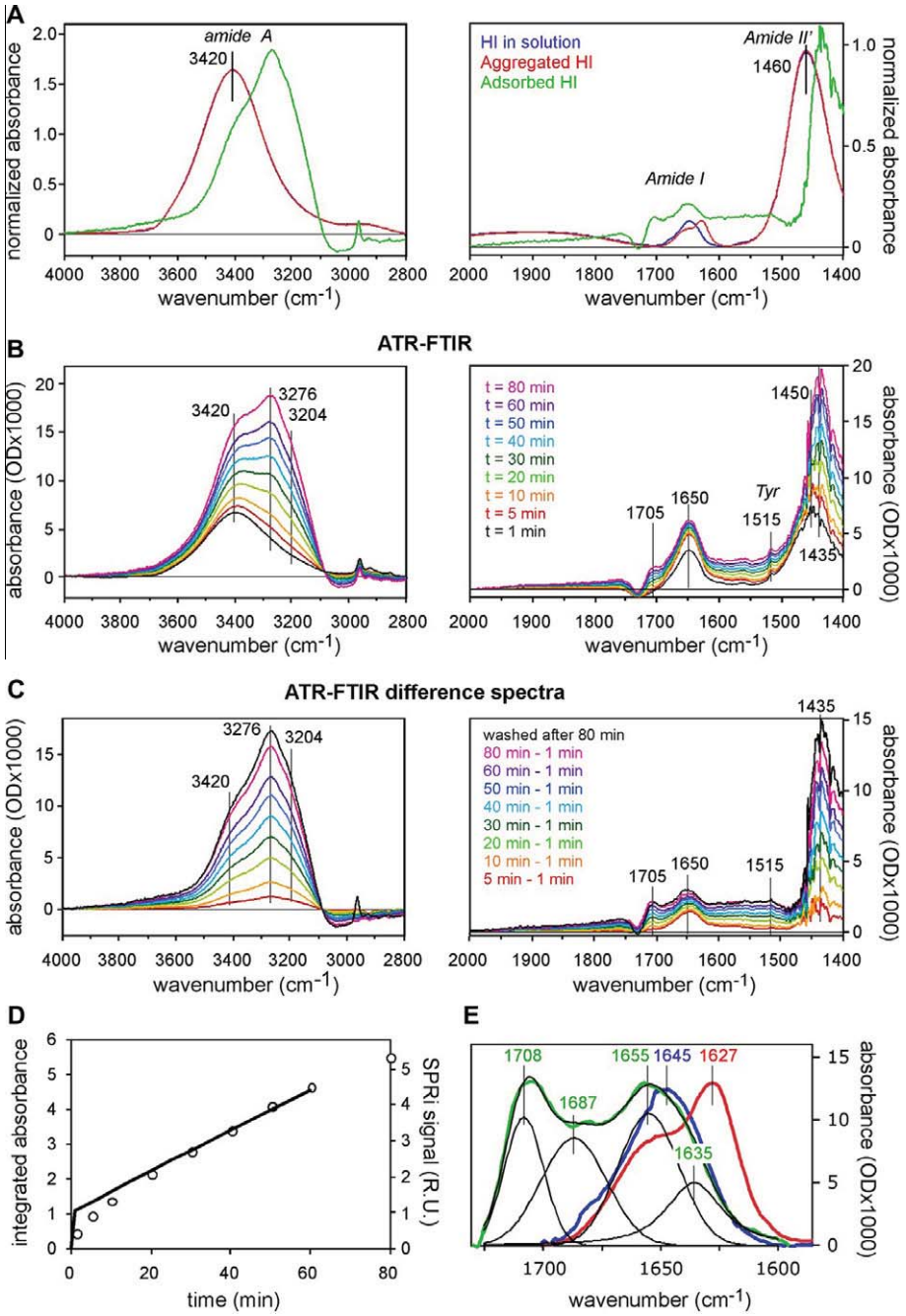

Fig. 6. ATR-FTIR spectra of HI adsorbed on hydrophobic surfaces. In (A), (B) and (C), the left and the right panels display the spectra in the 4000–2800 cm^{-1} or the 2000–1400 cm^{-1} ranges, respectively. In the left and right panels, the baseline was zeroed at 4000 or 2000 cm^{-1}, respectively, except in the right panel of (A), where the zero was set at the minimum. Data are representative of three experiments. (A) Transmission FTIR spectra of soluble (blue) and aggregated (red) HI. ATR-FTIR spectrum of HI adsorbed for 80 min on a hydrophobic surface and washed (green). The spectra have been normalized to the same total area. (B) Successive ATR-FTIR spectra recorded on the same hydrophobic surface while passing an 86 μM HI solution during 80 min. The time is indicated in the right panel. (C) Same data as in (B). The ATR-FTIR spectrum recorded after 1 min has been subtracted from those recorded later to show the increase in adsorbed HI. In addition, the spectrum obtained after 80 min of contact with the HI solution and a 1 min wash is also displayed. (D) Total absorbance of adsorbed HI calculated according to Eq. (3) integrated over the 4000–2800 cm^{-1} and the 2000–1400 cm^{-1} ranges, as a function of time. For comparison, the association SPRi difference signal is represented as a thick line. (E) Amide I band of soluble HI (blue), aggregated HI (red) and HI adsorbed for 80 min on hydrophobic surfaces (green). Data are from (A). The baseline is linearly adjusted between 1700 and 1570 cm^{-1} for soluble HI and aggregated HI spectra, and between 1730 and 1570 cm^{-1} for the adsorbed HI spectrum. In the case of the adsorbed HI spectrum, the decomposition of the band into four peaks is displayed as thin lines that represent the individual peaks and their sum.

down the accumulation of protein on the surface; on the other hand, it helps to detach already formed aggregates. The fluid flow rate was therefore changed to mimic the effect of agitation (data not shown). The rate of HI adsorption was monitored as the fluid flow was stopped. No change was observed, showing that HI diffusion is fast enough to allow HI aggregation at surfaces.

3.2. Insulin conformational changes on hydrophobic surfaces

Insulin conformational changes during its adsorption on hydrophobic surfaces were investigated by ATR-FTIR (Fig. 1). The infrared spectrum of a protein is indeed sensitive to its secondary structure. For this purpose, the top contact surface of an ATR-FTIR

silicon prism was functionalized with phenyldimethylmethoxysilane, which forms a hydrophobic self-assembled monolayer. The baseline spectrum was recorded with the buffer solution. An 86 μM HI solution prepared in ^2H_2O was then passed over the prism and 4000–1400 cm^{-1} infrared spectra were recorded at the times indicated during 80 min at room temperature (20 °C). Since recording a single spectrum takes about 1 min, the infrared spectrum referring to time point 1 corresponds to insulin already adsorbed on the prism for 1–2 min. Infrared spectra were therefore recorded early after the fast initial HI adsorption (time 1) and during the slow phase of the HI adsorption kinetics (subsequent times).

In comparison, Fig. 6A shows the spectra of the initial HI solution and of a suspension of aggregated HI, obtained after agitation in a hydrophobic multi-well plate [21], both recorded by transmission FTIR. The spectra are displayed in two parts, the 4000–2800 cm^{-1} region in the left panel and the 2000–1400 cm^{-1} region in the right one, skipping the intermediate 2800–2000 cm^{-1} region, where the signal is almost flat or does not contain any protein contributions. In proteins, the peptide bond (amide group) is the main contributor to the infrared spectrum, but specific amino acid side chains may also contribute significantly in spectral regions where no other chemical group absorbs, e.g. tyrosines at 1515 cm^{-1}. In the 4000–1400 cm^{-1} range, amide groups contribute to three groups of peaks: the amide A peak, in the 3600–3100 cm^{-1} range, the amide I peaks, in the 1700–1600 cm^{-1} range, and the amide II′ peaks, in the 1500–1400 cm^{-1} range [25]. The prime refers to the fact that in the presence of ^2H_2O, hydrogen is exchanged for deuterium in the amide NH group. The soluble and aggregated HI spectra are similar in the amide A/B and amide II′ bands (3420, 3100 and 1460 cm^{-1}, respectively), but are characteristically different in the amide I band, with one prominent 1650 cm^{-1} band for soluble HI and two bands around 1660 and 1630 cm^{-1} for aggregated HI, as reported previously [26].

The successive ATR-FTIR spectra clearly show the progressive accumulation of protein material on the PDMMS surface (Fig. 6B). The first spectrum (time 1) is very similar to the spectrum of soluble HI and displays the amide A peak at 3420 cm^{-1}, the amide I peak at 1650 cm^{-1}, the tiny tyrosine contribution at 1515 cm^{-1} and the amide II′ peak at 1450 cm^{-1}. At later times, however, specific peaks appear and increase rapidly, especially at 3276 and 3204 cm^{-1} in the amide A band and at 1705 cm^{-1} in the amide I band. Since the penetration distance of the infrared evanescent waves in ATR-FTIR is about 2 μm, the recorded spectra are indeed the sum of the soluble HI contribution and the adsorbed HI contribution. Assuming that the adsorbed HI layer remains negligible compared to the 2 μm penetration depth, the contribution of soluble HI is constant during the association phase. Difference spectra thus reveal the adsorbed HI contribution. In Fig. 6C, the spectrum recorded at $t = 0$ has been subtracted from subsequent spectra. These difference spectra are quite similar in shape, except in the range 1730–1670 cm^{-1} (see below), but are clearly distinct from the spectrum of HI in solution or aggregated (Fig. 6A). Besides the aforementioned amide A and amide I differences, the amide II′ is clearly shifted to 1435 cm^{-1}. Furthermore, these difference spectra are very similar to the ATR-FTIR spectrum recorded at the end of the experiment, once HI had been passed over the prism surface for 80 min and washed with buffer for 1 min (black curve in Fig. 6C). This proves that adsorbed HI has a specific spectrum and that spectra recorded subsequently in time (Fig. 6B) are the sum of a constant soluble HI contribution and increasing adsorbed HI contributions. Curve fitting confirmed this analysis, except in the 1730–1670 cm^{-1} region (see below). After washing with 1% SDS, the flat initial baseline was restored, showing that this detergent is able to remove all adsorbed proteins. The spectrum recorded after buffer wash is therefore due to adsorbed HI. In Fig. 6A, this spectrum has been normalized and displayed along the soluble and aggregated HI ones to facilitate their comparison.

The difference between the spectrum obtained after washing the prism surface (Fig. 6C, black curve) and the last difference spectrum (80 min – 1 min, Fig. 6C, pink curve) corresponds to the HI adsorbed during the first minute. It is therefore possible to calculate the spectrum of adsorbed HI as a function of time from Eq. (3). In Fig. 6D, the absorbance is summed over the 4000–2800 cm^{-1} and 2000–1400 cm^{-1} ranges, and plotted as a function of time. The fact that the integrated absorbance continuously increases over 80 min confirms that HI is indeed able to adsorb not only on the hydrophobic surface, but also on HI molecules already adsorbed on the surface. To compare this plot with the SPRi results, the SPRi association signal was also plotted, and displayed using a scale that allows its comparison to the integrated absorbance signal. The integrated absorbance signal is quite comparable to the SPRi signal: it rises rapidly during the first 10 min (fast component), then increases linearly for about 1 h (slow component). It should nevertheless be noted that the FTIR signal rises less rapidly than the SPRi signal in the first 10 min.

The amide I band of adsorbed HI is strikingly different from that of soluble and aggregated HI. First, the entire band is shifted from the 1700–1600 cm^{-1} range to 1730–1630 cm^{-1}. Second, the substructure of the amide I band exhibits four main peaks, at 1635, 1655, 1687 and 1708 cm^{-1} (Fig. 6E). The relative contributions of these peaks to the amide I band are 18, 33, 29 and 20%, respectively. A detailed analysis of the evolution of the amide I band of adsorbed HI with time reveals that, initially, the 1708 cm^{-1} peak is minimal, but increases over about 30–40 min (Fig. 7A and B). In contrast, the 1655 cm^{-1} peak reaches its maximum level in less than 5 min and remains almost constant thereafter. The evolution of the 1708 cm^{-1} peak parallels that of the relative amplitude of the slow dissociation component of the SPRi signal (Fig. 7B). This documents the complexity of conformational changes and reveals the existence of slow conformational rearrangements within adsorbed HI.

3.3. Insulin aggregate formation on hydrophobic surfaces

Amyloidal aggregates are characterized by the formation of large intermolecular β-sheets, which can be probed by the binding of ThT, resulting in a specific fluorescence signal, distinct from soluble ThT fluorescence. We used a Glycotech flow chamber to pass an HI solution over a surface of interest in the presence of ThT and monitor the fluorescence associated with the surface. The coverslip was functionalized with dimethyldichlorosilane, which forms a hydrophobic self-assembled monolayer on glass. Fig. 8A shows a typical experiment. When a buffer solution containing ThT was introduced in the chamber, a small but significant surface fluorescence signal was detected. Washing the surface with buffer alone resulted in a fast decrease in surface fluorescence down to the background level, showing that the fluorescence signal was due to ThT that was loosely bound to the hydrophobic surface (Fig 8A). When an 86 μM HI solution containing ThT was passed over the coverslip, the fluorescence signal first decreased close to zero, then increased sharply after 40 min and was saturated by about 90 min. No ThT fluorescence signal appeared on a hydrophilic surface (plain glass coverslip, data not shown). Passing a BSA solution over the hydrophobic surface also decreased the surface fluorescence signal, but gave rise to little or no fluorescence recovery. We therefore interpret the surface fluorescence decrease as a strong competitive protein binding, replacing the weakly bound ThT. The fluorescence increase is due to the formation of insulin amyloid aggregates on the surface. BSA indeed does not readily form amyloid aggregates on hydrophobic surfaces (data not shown). Once HI had accumulated on the surface, washing with a

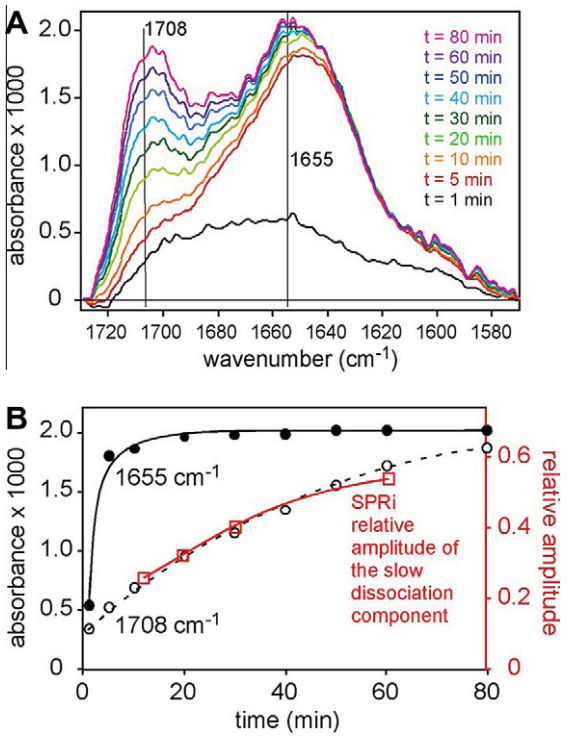

Fig. 7. (A) Evolution of the HI amide I band as a function of the time of contact between an 86 μM HI solution and the hydrophobic surface. Data are from Fig. 6. The adsorbed HI spectra are calculated using Eq. (3). The baselines of the amide I bands are linearly adjusted between 1730 and 1570 cm^{-1}. (B) The infrared absorbances of adsorbed HI at 1655 cm^{-1} (closed circles) and at 1708 cm^{-1} (open circles), and the relative amplitude of the slow component of the SPRi dissociation signal (squares), are plotted as a function of the time of contact between an 86 μM HI solution and the hydrophobic surface. The lines are hand-drawn.

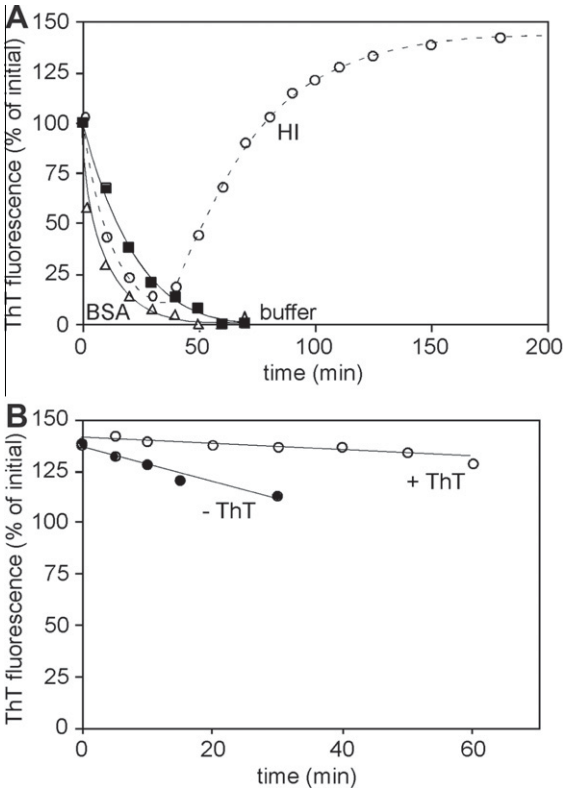

Fig. 8. Formation of HI amyloid fibers on hydrophobic surfaces. The surface fluorescence of a PDMMS-coated coverslip is monitored to detect the presence of bound ThT. The fluorescence levels are normalized to the value obtained after passing a 20 μM ThT solution for 120 min on the surface. The curves displayed are representative of three independent experiments. (A) At $t = 0$, either TBS buffer without ThT (black squares) or TBS buffer containing 0.5 mg ml^{-1} (6.5 μM) BSA and 20 μM ThT (open triangle) or TBS buffer containing 0.5 mg ml^{-1} (86 μM) HI and 20 μM ThT (open circle) are passed over the surface. Surface fluorescence was measured every 10 min. The lines are hand-drawn. (B) After passing a 20 μM ThT solution for 120 min on the surface, the surface is washed at $t = 0$ with either ThT-free TBS buffer (closed circles) or ThT-containing buffer (open circles). The lines represent a linear fit to the data.

buffer solution devoid of ThT resulted in a very slow fluorescence decrease, showing that ThT was now strongly bound to HI adsorbed on the surface (Fig. 8B). Quantitatively, the ThT dissociation kinetics was five times lower from adsorbed HI than from plain hydrophobic surfaces. The surface fluorescence decreased very slowly (typically for 15 h) during washing with a buffer solution containing ThT, confirming that amyloid HI does not easily dissociate from the surface (Fig. 8B). In contrast, washing with SDS allowed a fast and complete disappearance of the surface fluorescence (data not shown). Altogether, these results show that a lag phase of 40 min precedes the appearance of ThT positive aggregates on hydrophobic surfaces, that ThT binds more strongly to adsorbed HI than to hydrophobic surfaces and that ThT-positive aggregates are strongly bound to the surface.

4. Discussion

In this work, we reconstituted the formation of insulin amyloid aggregates on hydrophobic surfaces and delineated in time a series of sequential molecular events that occur on the material surface (Fig. 9). Amyloid aggregates, evidenced by ThT fluorescence, appear about 40 min after the hydrophobic surface is put into contact with an insulin solution. It should be noted that the experimental conditions are slightly different from those used in previous insulin aggregation assays such as in Slutzky et al. [19,20] or Ballet et al. [21]. First, the protein solution flows over the surface of interest, instead of being simply incubated. The bulk protein concentration therefore remains constant, except during ATR-FTIR experiments, where the solution is recirculated. Note that in this case, the total HI content of the setup (5 mg) is in large excess to the HI expected to bind to the tubing and the ATR-FTIR sensor area (4 cm^2; after 1 h, the bound HI is 4×10^{-4} $cm^2 \times (0.2\ mg\ cm^{-2} + 0.013\ mg\ cm^{-2}\ min^{-1} \times 60\ min) = 3.9\ \mu g$, according to Eq. (1)). Second, the experimental temperature, a key parameter in protein unfolding, was 20 °C instead of 37 °C. From the temperature dependence studied by Ballet et al. [24], the lag time before the onset of massive aggregation increases to 5 h at 20 °C compared to 2.5 h at 37 °C. Note that the hydrophobic surface treatment used to treat the SPRi and the ATR-FTIR prisms or the coverslip are not exactly the same. A sixteen-carbon moiety was grafted onto gold, but only a six-carbon one was attached onto silicon or glass. Additional SPRi experiments were performed on a gold prism functionalized with an eight-carbon moiety (octyl-thiol) that gave similar results. We therefore believe that the length of the alkyl molecule used to make the material surface hydrophobic does not play a prominent role in HI adsorption and aggregation as long as the contact angle is close to 100°.

Bovine insulin aggregation at acidic pH and high temperature was studied by Bouchard et al. using FTIR [27]. These authors observe a heat-induced conformational transition characterized by the gradual disappearance of the characteristic α-helix peak (1651 cm^{-1}) concomitantly with the appearance of characteristic β-sheet peaks (1670 and 1627 cm^{-1}). In our study, the final HI aggregates obtained upon contact with hydrophobic surfaces present a very similar FTIR signature (Fig. 6E): a major peak at

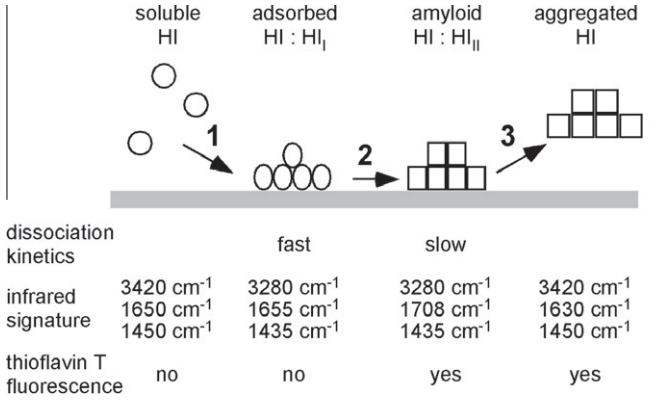

Fig. 9. Intermediates in the formation of HI amyloid fibers on hydrophobic surfaces. The scheme summarizes the different steps in the conversion of soluble HI into amyloidal HI aggregates that takes place on hydrophobic surfaces. (1) Soluble insulin adsorption and accumulation on the surface; it is accompanied by changes in the infrared amide A and II′ bands. (2) Formation of HI amyloid fibers adsorbed on the surface, characterized by the appearance of the 1708 cm^{-1} peak, ThT fluorescence and reinforcement of HI binding to the surface. (3) Dissociation of the HI amyloid fibers.

1628 cm^{-1} (72.1%) and three additional peaks at 1652 cm^{-1} (16.6%), 1662 cm^{-1} (2.4%) and 1669 cm^{-1} (8.9%) (data not shown). The 1628 cm^{-1} peak fits with the observation that characteristic FTIR β-sheet maxima of protein amyloid fibrils extend from 1611 to 1630 cm^{-1} [28]. The final insulin aggregates formed at hydrophobic surfaces are therefore similar to the ones formed in solution at high temperature and acidic pH. Nevertheless, Bouchard and coworkers did not characterize any intermediate conformational state, in contrast to our study. We describe a conformation for adsorbed insulin, which has a different FTIR signature than the final HI aggregates (see below).

A clear accumulation of HI on the surface precedes the onset of ThT-positive fluorescence. This accumulation was reported by Ballet et al. [21], but the limited sensitivity and long processing time of the direct biochemical method prevented their documenting it precisely. SPRi experiments show that HI adsorption proceeds in two phases: first, the very fast binding of an HI monolayer, followed by the slow but steady accumulation of HI on top of the monolayer. Assuming that HI adsorbs uniformly, about two protein layers would be present on the surface at the onset of the ThT fluorescence. This signal pattern illustrates the mechanism of insulin aggregation on hydrophobic surfaces: soluble HI is indeed able to bind to adsorbed HI, increasing the local HI concentration tremendously, which is a prerequisite to the formation of aggregates. The precision of SPRi further allows differentiating two HI populations adsorbed on the material surface, characterized by their dissociation kinetics: one strongly bound to the surface, which dissociates slowly, and another one less strongly bound, which dissociates more easily.

Infrared spectroscopy reveals that adsorbed HI is in a conformational state that is distinct from soluble HI and from suspended HI amyloidal aggregates. The amide A and amide II′ bands are indeed both shifted to lower energy. It is known that the position of the amide A band, which corresponds to NH stretching, is sensitive to hydrogen bonding [29]. Its shift from 3420 cm^{-1} to 3276 and 3204 cm^{-1} thus indicates that adsorbed HI is involved in more hydrogen bonding than soluble HI. The existence of a specific conformation for adsorbed HI is in accordance with Ballet et al. [21], who showed that the bacterial chaperone DnaK recognizes a specific conformation on adsorbed HI. DnaK could bind, though with a diminished affinity, on aggregated HI fibers released in solution, indicating that adsorbed HI and aggregated HI have distinct conformations. In ATR-FTIR, the amide I band in adsorbed HI is also unique. As shown in Fig. 7, it consists of four peaks, at 1635, 1655, 1687 and 1708 cm^{-1}. Assuming that the assignation of the different amide I peaks provided in the literature for soluble proteins [29,30] also holds for adsorbed proteins, we can interpret the 1635 and 1687 cm^{-1} peaks as indicative of the presence of β-sheet, and the 1655 cm^{-1} peak as the residual presence of α-helices. By analogy with the case of cytochrome *c* [31] and fibroin [32], the 1708 cm^{-1} peak could be due to intermolecular β-sheets. Furthermore, its shape slowly evolves as HI accumulates over the surface, showing that some maturation takes place (Fig. 7A). Since the kinetics of the 1708 cm^{-1} peak's appearance roughly matches that of the slow dissociation component evidenced by SPRi, we propose that two states of adsorbed HI are present, corresponding to the fast and slow dissociation components. The first one (HI$_I$), characterized by a prominent peak at 1655 cm^{-1} (Fig. 7A, HI adsorbed after 1 or 5 min), very similar to that of soluble HI, would dissociate fastest. The second one (HI$_{II}$), with a characteristic peak at 1708 cm^{-1} (Fig. 7A, HI adsorbed at 80 min), would dissociate ten times more slowly. Both would be intermediates in the transition from soluble HI to HI amyloid aggregates. Since the HI$_I$ → HI$_{II}$ transition is completed in about 30–40 min (Fig. 7), it is tempting to assume that HI$_{II}$ is ThT-positive whereas HI$_I$ is not. HI$_I$ would thus represent pre-amyloid adsorbed HI and HI$_{II}$ amyloid aggregates (adsorbed HI and amyloid HI in Fig. 9). HI$_{II}$ dissociation from the material surface would allow the formation of mature amyloid fibers in solution. In this state, the infrared signature is different from that of amyloid aggregates bound to the surface, but both are ThT-positive. The mechanical detachment of insulin amyloid fibers has been studied by Ballet et al. [24].

This study underlines the importance of considering the material surface when dealing with protein stability issues. It reveals the complexity of a multi-step adsorption mechanism and the existence of conformationally different protein species that cooperate to form amyloid fibers. Insulin–material interactions are governed by a complex interplay between the hydrophobicity, surface charge and topography of the material. Indeed, it was shown that insulin, although carrying a net negative charge at physiological pH, accumulates in significant amounts on negatively charged, hydrophilic polystyrene sulfonate (water contact angle: 50–60°) [33]. On uncharged poly(ethylene oxide)-coated surfaces (water contact angle: 3.5°), however, no insulin adsorption is measurable [21]. Moreover, Pandey and co-workers have studied the influence of increasing surface hydrophobicity and topography on the nucleation rate using mixed self-assembled monolayers of amine- and octyl-silanes [34]. They show that the lag time of insulin aggregation varies as a function of the amine fraction on the surface and that the morphology of the aggregates depends on the surface chemistry and topography. From these studies we conclude that the conditions that inhibit insulin adsorption on materials and material-induced aggregation, are maximal wettability (water contact angle <5°) and the absence of charges. Further work is clearly needed to examine whether the mechanisms outlined in the case of HI also hold true for other proteins in contact with hydrophobic surfaces, or for HI in contact with other surface chemistries.

Acknowledgements

This work was supported by the ANR grant "Stabilization of Therapeutical Proteins". L.N. was supported by a PhD grant from the Rhone-Alpes Region (Macodev program). B.J. was an exchange student from Delhi University. P.G. was a summer student from Toronto University, supported by a mobility grant from the Rhone-Alpes Region. We thank Catherine Picart and Flora Gilde for access and help with the ATR-FTIR apparatus. The authors acknowledge the "Pôle de Capteurs Thermométriques et

Calorimétrie" of the Institut Néel laboratory for the use of the oxygen plasma etcher.

Appendix A. Figures with essential colour discrimination

Certain figures in this article, particularly Figs. 3, 6 and 7, are difficult to interpret in black and white. The full colour images can be found in the on-line version, at http://dx.doi.org/10.1016/j.actbio.2012.09.025.

References

[1] Westermark P, Benson MD, Buxbaum JN, Cohen AS, Frangione B, Ikeda S, Masters CL, Merlini G, Saraiva MJ, Sipe JD. Amyloid fibril protein nomenclature. J. Amyloid 2002;9:197–200.
[2] Astbury WT, Dickinson S, Bailey K. The X-ray interpretation of denaturation and the structure of the seed globulins. Biochem J 1935;29:2351–2360.1.
[3] Dobson CM. Protein misfolding, evolution and disease. Trends Biochem Sci 1999;24:329–32.
[4] Rudall KM. The proteins of the mammalian epidermis. Adv Protein Chem 1952;7:253–90.
[5] Koo EH, Lansbury PT, Kelly JW. Amyloid diseases: abnormal protein aggregation in neurodegeneration. Proc Natl Acad Sci USA 1999;96:9989–90.
[6] Adams MJ, Blundell TL, Dodson EJ, Dodson GG, Vijayan M, Baker EN, et al. Structure of rhombohedral 2 zinc insulin crystals. Nature 1969;224:491–5.
[7] Feingold V, Jenkins AB, Kraegen EW. Effect of contact material on vibration-induced insulin aggregation. Diabetologia 1984;27:373–8.
[8] Lougheed WD, Albisser AM, Martindale HM, Chow JC, Clement JR. Physical stability of insulin formulations. Diabetes 1983;32:424–32.
[9] Sefton MV, Antonacci GM. Adsorption isotherms of insulin onto various materials. Diabetes 1984;33:674–80.
[10] Lougheed WD, Woulfe-Flanagan H, Clement JR, Albisser AM. Insulin aggregation in artificial delivery systems. Diabetologia 1980;19:1–9.
[11] Dische FE, Wernstedt C, Westermark GT, Westermark P, Pepys MB, Rennie JA, et al. Insulin as an amyloid-fibril protein at sites of repeated insulin injections in a diabetic patient. Diabetologia 1988;31:158–61.
[12] Störkel S, Schneider HM, Müntefering H, Kashiwagi S. Iatrogenic, insulin-dependent, local amyloidosis. Lab Invest 1983;48:108–11.
[13] Moores B, Drolle E, Attwood SJ, Simons J, Leonenko Z. Effect of surfaces on amyloid fibril formation. PLoS One 2011;6:e25954.
[14] Kowalewski T, Holtzman DM. In situ atomic force microscopy study of Alzheimer's beta-amyloid peptide on different substrates: new insights into mechanism of beta-sheet formation. Proc Natl Acad Sci USA 1999;96:3688–93.
[15] Giacomelli CE, Norde W. Influence of hydrophobic Teflon particles on the structure of amyloid beta-peptide. Biomacromolecules 2003;4:1719–26.
[16] McMasters MJ, Hammer RP, McCarley RL. Surface-induced aggregation of beta amyloid peptide by ω-substituted alkanethiol monolayers supported on gold. Langmuir 2005;21:4464–70.
[17] Chi EY, Frey SL, Winans A, Lam KLH, Kjaer K, Majewski J, et al. Amyloid-beta fibrillogenesis seeded by interface-induced peptide misfolding and self-assembly. Biophys J 2010;98:2299–308.
[18] Schladitz C, Vieira EP, Hermel H, Möhwald H. Amyloid-beta-sheet formation at the air–water interface. Biophys J 1999;77:3305–10.
[19] Sluzky V, Tamada J, Klibanov A, Langer R. Kinetics of insulin aggregation in aqueous solutions upon agitation in the presence of hydrophobic surfaces. Proc Natl Acad Sci USA 1991;88:9377–81.
[20] Sluzky V, Klibanov AM, Langer R. Mechanism of insulin aggregation and stabilization in agitated aqueous solutions. Biotechnol Bioeng 1992;40:895–903.
[21] Ballet T, Brukert F, Mangiagalli P, Bureau C, Boulangé L, Nault L, et al. DnaK prevents human insulin amyloid fiber formation on hydrophobic surfaces. Biochemistry 2012;51:2172–80.
[22] Lavalle P, Gergely C, Cuisinier FJG, Decher G, Schaaf P, Voegel JC, et al. Comparison of the structure of polyelectrolyte multilayer films exhibiting a linear and an exponential growth regime: an in situ atomic force microscopy study. Macromolecules 2002;35:4458–65.
[23] Picart C, Ladam G, Senger B, Voegel J-C, Schaaf P, Cuisinier FJG, et al. Determination of structural parameters characterizing thin films by optical methods: a comparison between scanning angle reflectometry and optical waveguide lightmode spectroscopy. J Chem Phys 2001;115:1086.
[24] Ballet T, Nault L, Pandey L, Bruckert F, Bureau C, Boulangé L, et al. Insulin adsorbed on hydrophobic surfaces stimulates the formation and release of insulin amyloid fibers. Submitted for publication.
[25] Barth A, Zscherp C. What vibrations tell us about proteins. Q Rev Biophys 2002;35:369–430.
[26] Dzwolak W, Smirnovas V, Jansen R, Winter R. Insulin forms amyloid in a strain-dependent manner: an FT-IR spectroscopic study. Protein Sci 2004;13:1927–32.
[27] Bouchard M, Zurdo J, Nettleton E, Dobson CM, Robinson CV. Formation of insulin amyloid fibrils followed by FTIR simultaneously with CD and electron microscopy. Protein 2000;9:1960–7.
[28] Zandomeneghi G, Krebs MRH, McCammon MG, Fändrich M. FTIR reveals structural differences between native beta-sheet proteins and amyloid fibrils. Protein Sci 2004;13:3314–21.
[29] Kong J, Yu S. Fourier transform infrared spectroscopic analysis of protein secondary structures. Acta Biochim Biophys Sin 2007;39:549–59.
[30] Mizushima S-I, Tsuboi M, Shimanouchi T, Tsuda Y. Spectroscopic investigation of the strength of hydrogen bonds formed by amides. Spectrochim Acta 1955;7:100–7.
[31] Marboutin L, Boussac A, Berthomieu C. Redox infrared markers of the heme and axial ligands in microperoxidase: bases for the analysis of c-type cytochromes. J Biol Inorg Chem 2006;11:811–23.
[32] Hu X, Kaplan D, Cebe P. Determining beta-sheet crystallinity in fibrous proteins by thermal analysis and infrared spectroscopy. Macromolecules 2006;39:6161–70.
[33] Jeworrek C, Hollmann O, Steitz R, Winter R, Czeslik C. Interaction of IAPP and insulin with model interfaces studied using neutron reflectometry. Biophys J 2009;96:1115–23.
[34] Pandey LM, Le Denmat S, Delabouglise D, Bruckert F, Pattanayek SK, Weidenhaupt M. Surface chemistry at the nanometer scale influences insulin aggregation. Colloids Surf B 2012;100C:69–76.

FEBS Letters 587 (2013) 1281–1286

journal homepage: www.FEBSLetters.org

Peptides that form β-sheets on hydrophobic surfaces accelerate surface-induced insulin amyloidal aggregation

Laurent Nault [a], Charlotte Vendrely [a], Yves Bréchet [b], Franz Bruckert [a], Marianne Weidenhaupt [a,*]

[a] Laboratoire des Matériaux et du Génie Physique, Phelma-Minatec, 3 Parvis Louis Néel CS 50257, F-38016 Grenoble Cedex 1, France
[b] Laboratoire de Science et Ingénierie des Matériaux et des Procédés, Phelma-Campus, 1130 rue de la Piscine, BP 75, F-38402 Saint-Martin d'Hères Cedex, France

ARTICLE INFO

Article history:
Received 12 July 2012
Revised 19 October 2012
Accepted 16 November 2012
Available online 16 March 2013

Edited by Jesus Avila

Keywords:
Material surface
Protein aggregation
Amyloidogenic peptide
Insulin

ABSTRACT

Interactions between proteins and material or cellular surfaces are able to trigger protein aggregation in vitro and in vivo. The human insulin peptide segment LVEALYL is able to accelerate insulin aggregation in the presence of hydrophobic surfaces. We show that this peptide needs to be previously adsorbed on a hydrophobic surface to induce insulin aggregation. Moreover, the study of different mutant peptides proves that its sequence is less important than the secondary structure of the adsorbed peptide on the surface. Indeed, these pro-aggregative peptides act by providing stable β-sheets to incoming insulin molecules, thereby accelerating insulin adsorption locally and facilitating the conformational changes required for insulin aggregation. Conversely, a peptide known to form α-helices on hydrophobic surfaces delays insulin aggregation.

Structured summary of protein interactions:
HI and HI bind by fluorescence technology (View interaction)

1. Introduction

Many protein solutions are prone to aggregation in vitro. This is particularly critical for therapeutic proteins because aggregate formation decreases drug activity and can induce immunogenic reactions when injected in patients. For instance, the most used protein hormone, insulin, can be found in fibrillar form at the site of frequent insulin injections, which causes injection amyloidosis [1]. Moreover, the increasing prevalence of human diseases, characterized by the presence of large amounts of aggregated proteins, like amyloidosis, Alzheimer's, Parkinson's and prion diseases, requires mechanistic studies to understand protein aggregate formation.

The mechanism of protein fibrillation is generally modeled in three steps. (1) Conformational changes, due to defects in the cellular folding processes or due to an abnormal protein environment. (2) Nucleation, during which the misfolded individual proteins are stabilized, mostly by intermolecular interactions, which drives the formation of oligomers. Such oligomers can then evolve into stable nuclei. (3) Growth, during which the nuclei will grow upon binding of other misfolded proteins, leading to the formation of large fibrils. In vivo, the growing step has a major impact on cell survival [2].

Human insulin (HI) has often been used as a model protein in fibrillation studies as it is a non-expensive protein which fibrillates rapidly in vitro, particularly at low pH, high temperature, high ionic strength and on hydrophobic surfaces [3–5]. In a preceding study [6], we have shown that the presence of hydrophobic surfaces is essential for HI fibrillation at pH 7.3 and 37 °C. Such surfaces were assumed to induce the unfolding of HI monomers adsorbed on them, but it appears that all three steps, including nucleation and fibril elongation also take place on the surface, leading eventually to the release of mature fibrils into solution.

Different studies show that the onset of aggregate nucleation can be accelerated by the addition of peptides, which present a pro-aggregative activity [7–10]. Such amyloidogenic peptides are mostly hydrophobic, have beta-sheet conformation and are capable to fibrillate by themselves. They are commonly derived from protein sequences suspected to be involved in fibrillation. In 2009, Ivanova et al. [11] showed that a 7 amino-acid peptide sequence, present in the B chain of native HI (LVEALYL, residues B11–B17), was able, at sub-stoichiometric concentrations, to accelerate the nucleation step of human HI at pH 2.5. On the other hand, it is known that surface hydrophobicity has an important effect on the HI nucleation rate [12] and, given the hydrophobic nature of this peptide, its amyloidogenic properties are likely to rely on its interaction with hydrophobic surfaces. We recently demonstrated that the LVEALYL peptide-driven acceleration of HI aggregation is strictly dependent on the presence of hydrophobic surfaces [6].

In this study, we use mutants of the LVEALYL peptide together with HI to investigate the effects of amino acid changes in this

* Corresponding author.
E-mail address: marianne.weidenhaupt@grenoble-inp.fr (M. Weidenhaupt).

0014-5793/$36.00 © 2013 Federation of European Biochemical Societies. Published by Elsevier B.V. All rights reserved.
http://dx.doi.org/10.1016/j.febslet.2012.11.036

sequence on HI aggregation kinetics, protein adsorption on hydrophobic surfaces and changes in peptide secondary structure. When compared to previous studies measuring the effects of amyloidogenic peptides on HI aggregation kinetics, we have introduced two novel and important parameters: first, the experiments are done at physiological pH and, second, the effect of material surface hydrophobicity is analyzed. Our work suggests that the LVEALYL peptide and mutants thereof induce HI aggregation only if they are previously adsorbed on the material surface. Moreover, it appears that their primary sequence is less important than their ability to stably adsorb in beta-structure on the surface.

2. Materials and methods

2.1. Chemicals

If not otherwise stated, all chemicals were purchased from Sigma–Aldrich. Experiments were conducted in TBS (25 mM Tris–HCl, pH 7.3, 125 mM NaCl and 2 mM $MgCl_2$). HI (recombinant human HI, expressed in yeast) solutions were prepared at 0.5 mg mL^{-1} (86 μM). All solutions were filtered (0.22 μm) before use. Peptides were purchased from Genecust (Luxembourg) and a concentrated stock solution was made at 860 μM in 20 mM NaOH.

2.2. Monitoring of aggregation kinetics

HI aggregation assays were conducted as 8 replicates in plastic 96-well microplates. Polystyrene (Greiner Bio-One, water contact angle = 85° ± 4.7), or PEO-coated, (Corning 3651 microplate, water contact angle = 3.5° ± 5.8) microplates were used. In fluorescence assays, black polystyrene microplates were used (Nunc Nunclon® Δ Surface). The plates were covered by plastic sheets, incubated at 37 °C and shaken at 1200 rpm (Heidolph Titramax, 1.5 mm vibration orbit). Thioflavin T (ThT, 20 μM) fluorescence was directly measured (λ_{ex} = 450 nm, λ_{em} = 482 nm) in the wells [6].

2.3. Kinetic analysis

The aggregation kinetics proceeds in three phases: a lag phase, where the signal is not statistically different from the baseline (mean ± standard deviation), a linear growth phase and a plateau phase. Experimentally, the lag time was defined by the intercept between the linear growth phase and the baseline. The growth rate was defined as the slope of the linear phase and the plateau as the maximum value attained. The parameters were calculated on individual kinetics corresponding to different replicates, and the given statistics represent the average and the standard deviation for each parameter.

2.4. Surface seeding using peptides

96-Well microplates were filled with peptides diluted at 8.6 μM in TBS and incubated at 37 °C, 1200 rpm for 10 min. Wells were then washed once with TBS and filled with HI (86 μM) and incubated at 37 °C, 1200 rpm. HI aggregation kinetics was monitored using ThT as described.

2.5. Quantification of adsorbed protein

HI (86 μM) and/or peptide solutions (8.6 μM) were incubated in 96-well hydrophobic microplates in TBS for 30 min at 37 °C, 1200 rpm. Wells were then washed with TBS and adsorbed peptides and protein were desorbed using Sodium Dodecyl Sulfate (5%) for 30 min at 37 °C and 1200 rpm. The peptide and/or protein concentrations were determined using the Bicinchoninic Assay using Bovine Serum Albumin as a standard.

2.6. Adsorption kinetics and infrared spectroscopy

Peptide and HI association and dissociation kinetics were studied on PEG- and C_{16}-coated surfaces by SPRi as described in Nault et al. [13]. The peptide conformation in solution and adsorbed on hydrophobic surfaces was determined by FTIR transmission or ATR-FTIR experiments, respectively [13].

2.7. Estimation of the hydrophobic contribution to the peptide binding energy to hydrophobic surfaces

The hydrophobic contribution to the binding energy of 7 amino acid long peptides with a hydrophobic surface was calculated for two β-sheet configurations by the following formula:

$$\Delta G_{conf1} = \sum_{1,3,5,7} \Delta G_i - \sum_{2,4,6} \Delta G_i \quad (1)$$

$$\Delta G_{conf2} = \sum_{2,4,6} \Delta G_i - \sum_{1,3,5,7} \Delta G_i \quad (2)$$

$$\Delta G_{sol} = \sum_{1}^{7} \Delta G_i \quad (3)$$

where ΔG_i is the free transfer energy of the ith amino acid side chain [14]. Conformation 1 and 2 correspond to the exposure of even or odd amino acids to solvent, respectively. The third calculation corresponds to the hydrophobic contribution of the peptide transfer energy into solution, with all amino acids exposed to the solvent. This calculation does not consider the contribution of N- and C-termini, which is identical for all peptides and conformations. In the interpretation of the data, peptides are assumed to adopt the conformation having the lowest interaction energy.

3. Results

3.1. The LVEALYL peptide accelerates HI aggregation kinetics when bound to hydrophobic surfaces

As shown before [6], the LVEALYL peptide accelerates HI aggregation kinetics at pH 7.3 and 37 °C, only in the presence of hydrophobic surfaces (polystyrene) but not in the presence of PEG-coated surfaces preventing HI binding. The maximum effect is observed at a peptide concentration of 8.6 μM, and the lag time is reduced by 66% on average (Table 1). We quantified the peptide adsorption on microwells. Table 1 shows that 0.06 μg LVEALYL peptide remains adsorbed on the hydrophobic surface after 30 min, corresponding to 4.5% of the initial peptide amount. These minute amounts have a dramatic effect on HI aggregation, as shown by the following seeding experiment. Hydrophobic surfaces were pre-incubated for 10 min with peptide, washed and exposed to HI. Peptide pre-adsorption decreases the lag-time of HI aggregation by 63% (Table 1). It is noteworthy that preincubating the surface with HI does not decrease the lag time (Table 1, line1). Moreover, supplying the solution with 0.06 μg LVEALYL peptide, does not affect HI aggregation kinetics. The pro-aggregative effect of the peptide is therefore due to the adsorbed fraction on the surface. Upon adsorption, but not in solution, the LVEALYL peptide presents molecular features that strongly accelerate HI binding and aggregation.

3.2. The pro-aggregative peptides LVEALYL and LVAELYL have a strong effect on HI aggregation and adsorption kinetics

The strong effect of the LVEALYL peptide on HI aggregation kinetics prompted us to study different peptide variants (Table 1). All experiments were done at the same peptide (8.6 μM) and HI (86 μM) concentrations. None of the peptides studied here

Table 1
Physico-chemical and pro-aggregative properties of different peptides. The binding energy corresponds to the hydrophobic contribution to the minimum interaction energy of the peptide bound to the surface, calculated by Eqs. (1) or (2) (column 2). For the $(LKKLLKL)_2$ peptide no interaction energy was calculated since this peptide is in α-helical configuration. Lag times were determined from the aggregation kinetics of a 1:10 peptide:protein mixture (column 3) and for a surface first exposed to the indicated peptide (8.6 μM) for 10 min, washed and then incubated with a fresh HI solution (86 μM) (column 4). Adsorption of peptides and peptide plus HI mixtures on hydrophobic surfaces (2 cm^2) was determined as described in Section 2 (column 5 and 6).

Peptide sequence	Interaction energy (kcal mol^{-1})	Lag time of HI aggregation kinetics (h)		Protein adsorbed on the surface after 30 min (μg)	
		8.6 μM peptide mixed with 86 μM HI	After 10 min seeding	8.6 μM peptide alone	8.6 μM peptide mixed with 86 μM HI
No peptide		4.4 ± 0.4	4.3 ± 0.4[a]		0.19 ± 0.01
LVEALYL	−3.3	1.5 ± 0.2	1.7 ± 0.3	0.06 ± 0.01	0.21 ± 0.01
LV**AE**LYL	−16.3	0.4 ± 0.1	2.3 ± 0.3	0.10 ± 0.01	4.28 ± 0.10
L**SAS**L**S**L	−8.2	0.5 ± 0.1	2.5 ± 0.3	0.13 ± 0.01	0.25 ± 0.01
SV**S**A**S**Y**S**	−1.1	2.0 ± 0.1	ND	ND	ND
L**P**EALYL	−0.5	4.1 ± 0.3	ND	ND	ND
LVE**P**LYL	−1.5	4.2 ± 0.2	ND	ND	ND
SV**SPS**Y**S**	−0.7	4.3 ± 0.4	ND	ND	ND
LV**T**ALYL	−6.1	0.5 ± 0.1	2.7 ± 0.3	0.16 ± 0.04	1.6 ± 0.2
LVA**T**LYL	−6.9	0.6 ± 0.1	1.8 ± 0.3	0.15 ± 0.02	0.5 ± 0.2
LV**TP**LYL	−7.9	4.3 ± 0.1	ND	ND	ND
LV**PT**LYL	−5.1	4.6 ± 0.1	ND	ND	ND
ISISISI	−10.6	0.4 ± 0.1	ND	ND	ND
$(LKKLLKL)_2$	ND	>30	ND	ND	ND

[a] Seeding with 86 μM HI.

aggregates on its own, nor triggers HI aggregation in the presence of PEG-coated surfaces, confirming that the kinetic enhancement is dependent on the presence of hydrophobic surfaces. Among the peptides studied, the swapped peptide LVAELYL, where the third and fourth amino acid are exchanged, exhibits a remarkably short lag time (0.4 h). This peptide binds also strongly to hydrophobic surfaces (0.1 μg) and pre-adsorption reduces the lag time of HI aggregation down to 2.3 h (Table 1).

The binding kinetics of both peptides, alone and in combination with HI, were studied by SPRi (Fig. 1A and B). As shown before [13], HI alone binds specifically to hydrophobic surfaces, in a biphasic manner. Fast, reversible binding is followed by a slower increase of HI adsorption, resulting in the formation of a strongly bound HI pool ([13] and Fig. 1). The LVEALYL and LVAELYL peptides alone bind weakly to the hydrophobic surface (Fig. 1A and B). Mixing one of the peptides with HI enhances protein adsorption on the hydrophobic surface but has no effect on HI adsorption on the hydrophilic surface (Fig. 1A and B). More specifically, upon injection of HI with either peptide, there is an increase of the fast association component (first minutes of Fig. 1A and B) and of the slow dissociation component of the SPRi signal (last 10 min of Fig. 1A and last 20 min of Fig. 1B), compared to HI alone. The addition of sub-stoichiometric amounts of both peptides to HI therefore induces the formation of strongly adsorbed HI on the hydrophobic surface. A direct measurement of protein binding to microwell plastic surfaces confirms this result (Table 1). In the presence of the swapped peptide, the total protein bound is larger than in the presence of HI or peptide alone. The wild-type peptide also enhances, but to a lesser extent, protein binding on the surface (Table 1).

3.3. The wild type and the swapped peptides adopt a β-sheet conformation on hydrophobic surfaces

Infrared spectroscopy is sensitive to protein secondary structure in the amide I band and was used to analyze the conformational state of different peptides in solution (FTIR) or adsorbed on hydrophobic surfaces (ATR-FTIR). Decomposing the band into peaks shows that in solution, the wild type and swapped peptides adopt mostly unstructured conformations (Fig. 2A and B, left panels). Indeed, they present a major peak around 1645 cm^{-1}, indicative of random coil conformation, which accounts for 37% and 32% in the wildtype and swapped peptides' solution spectra, respectively (Table 1S). After 30 min adsorption on hydrophobic surfaces,

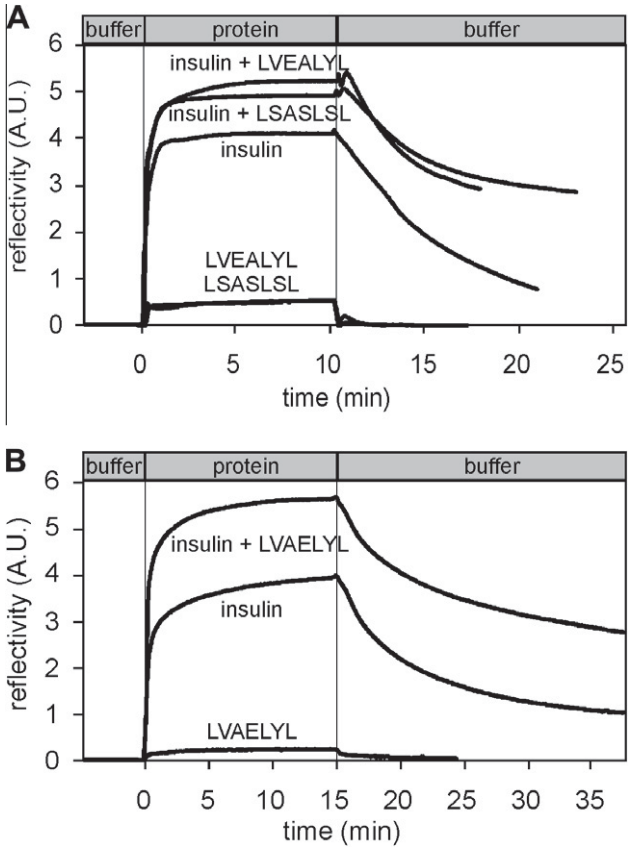

Fig. 1. SPRi sensorgrams of protein adsorption on hydrophobic surfaces. The protein solutions (8.6 μM peptide, 86 μM HI or a mixture of 8.6 μM peptide and 86 μM HI) were injected at $t = 0$ min and the association kinetics were monitored for 10 min (A) or 15 min (B). The surface was then washed with buffer and the protein dissociation kinetics were monitored for 15 min (A) or 20 min (B). The signal represented is the difference between the signal recorded on the C_{16}-coated side and the PEG-coated side of the prism. (A) SPRi curves obtained with peptides LVEALYL and LSASLSL, (B) SPRi curves obtained with peptide LVAELYL.

the amide I band of both peptides changes and reveals prominent peaks around 1694, 1680, 1664, 1648, 1633 and 1622 cm^{-1} (Fig. 2A and B, right panels). This indicates that the conformation of the adsorbed wild type and swapped peptides consists predominantly of

internal and intermolecular β-sheets and β-turns, the residual unstructured coil contribution consisting of 17 and 22%, respectively (Table 1S).

3.4. Characterization of other amyloidogenic peptides: influence of primary and secondary structure

In order to explain the peptide effect on the HI aggregation rate, a simple model was built, assuming that amyloidogenic peptides adopt a β-sheet conformation parallel to the material surface, stabilized by intermolecular hydrogen bonds and side chain interactions with the hydrophobic surface on one side, and the solvent on the other side. Amino acid side chains indeed alternatively point to one side or the other of a β-strand. For a 7 amino acid long peptide, two such conformations exist, with odd or even amino acids exposed to solvent. For each conformation, the hydrophobic contribution of amino acid side chains to the binding energy was summed up using the transfer energies from benzene to water, amino acids exposed to solvent contributing positively, while those in contact with the surface contributing negatively Eqs. (1) and (2). In this way, one can determine the energetically most favorable conformation of a given peptide adsorbed on a hydrophobic surface. For a stable adsorption, this energy should be lower than the one for the peptide in solution Eq. (3). For the LVEALYL peptide, the most stable β-sheet conformation exposes the L–E–L–L amino acids towards the solution, and the –V–A–Y– amino acids towards the surface (interaction energy = -3.3 kcal mol^{-1}). For the LVAELYL peptide, the most stable conformation exposes the –V–E–Y– amino acids towards the solution, and the L–A–L–L amino acids towards the surface (interaction energy = -16.3 kcal mol^{-1}). This justifies the better stability of the swapped peptide.

Two other peptides were studied, SVSASYS and LSASLSL, based on the wild-type and the swapped peptides respectively, where the amino acids supposed to face the surface were conserved and the ones turned to the solvent replaced by serines (S). For both peptides, the most stable conformation exposes hydrophilic S to the solution and hydrophobic amino acids to the surface (interaction energy = -8.2 kcal mol^{-1} for LSASLSL and -1.1 kcal mol^{-1}, for SVSAVYS). In the HI aggregation assay, the SVSASYS and the LSASLSL peptides behaved similarly to their parent peptides (Table 1), showing that the primary sequence exposed to the solvent was not critical. The stronger effect of the LSASLSL peptide, compared to the SVSASYS one, is again justified by its higher stability on hydrophobic surfaces. The LSASLSL peptide also presents a β-sheet rich conformation when adsorbed on hydrophobic surfaces (Fig. 2C and Table 1S), and enhances HI binding on the surface (Fig. 1).

To confirm the importance of peptide conformation on the surface, the $(LKKLLKL)_2$ peptide, known to form α-helices on hydrophobic surfaces [15], was tested. This peptide indeed proved to have completely different FTIR spectra, when compared to the wildtype or swapped peptides (Fig. 2D, left and right panels). Its transmission spectrum indicates that the $(LKKLLKL)_2$ peptide adopts β-sheet, random coil and α-helix conformations in solution (60%, 7% and 33%, respectively; Table 1S). Strikingly, when adsorbed on a hydrophobic surface, its ATR-FTIR signature reveals typical peaks around 1641 and 1655 cm^{-1}, which indicates that this peptide is predominantly in α-helical and random conformation (Table 1S) upon adsorption. At substoichiometric concentrations, $(LKKLLKL)_2$ delays HI aggregation for up to 30 h (Table 1). We therefore conclude that the conformation of the adsorbed $(LKKLLKL)_2$ peptide is not pro-aggregative but rather stabilizes HI.

Furthermore a proline residue (P), was introduced to disrupt the wildtype peptide secondary structure: LPEALYL, LVEPLYL and SVSPSYS. None of these three peptides affect HI aggregation kinetics (Table 1), which consolidates the importance of peptide β-sheet conformation on the surface.

Replacing the negatively charged glutamate residue (E) by a threonine (T) in the wild type or swapped peptide had no effect on the pro-aggregative property of the peptides, showing that electrostatic interactions were not determinant (LVTALYL and LVATLYL in Table 1). Again, the additional A to P mutation abolished the pro-aggregative effect of these peptides (LVTPLYL and LVPTLYL in Table 1).

Finally, we analyzed a peptide, ISISISI, exposing a series of three Ser (S) to the solution and being adsorbed via four Ile (I) to the hydrophobic surface. This peptide has a sequence that is similar to the LKLKLKL peptide, known to form β-sheets on hydrophobic surfaces [15–17], and has no common residues with LVEALYL. The HI aggregation lagtime, obtained using this peptide in seeding experiments, is 0.4 h. This peptide therefore also shows a pro-aggregative effect on HI-surface aggregation and confirms that the primary sequence is not paramount.

4. Discussion

In this study, we show that the LVEALYL peptide, adsorbed on hydrophobic surfaces at sub-stoichiometric concentrations, favors HI binding and the formation of HI amyloidal fibers. We previously showed that HI adsorbed on hydrophobic surfaces exposes a motive containing the LVEALYL peptide, which is recognized by the DnaK/DnaJ bacterial chaperones [6]. Combining these two observations indicates how HI amyloidal aggregates form on hydrophobic surfaces. HI molecules adsorb and change their conformation, exposing the LVEALYL peptide that allows further HI binding in a β-sheet conformation. The conformational change induced on HI directly adsorbed on the surface thus propagates to incoming HI that binds to adsorbed HI. This mechanism is in accordance with the insulin amyloid fiber model proposed by Ivanova et al. [11]. There is some similarity with the prion self-replication mechanism, with soluble and adsorbed HI playing the role of PrP^{C} and PrP^{Sc}, respectively. An important difference is that HI amyloid aggregates released into solution do not seed efficiently fiber growth.

This work confirms the central role played by the LVEALYL peptide, pointed out by Ivanova et al. [11]. We confirm that the SLYQLENY peptide, another HI segment putatively involved in the HI amyloid structure, does not stimulate HI aggregation in contact with hydrophobic material surfaces. This is reasonable since this peptide is globally hydrophilic ($\Delta G_{sol} = -12.3$ kcal mol^{-1}) and therefore not likely to adopt a β-sheet conformation on hydrophobic surfaces. Interestingly, introducing two mutations so that hydrophobic amino acids are placed at even locations (LYQLEAY peptide, $\Delta G_{conf1} = -13.9$ kcal mol^{-1}) has a mild but significant effect on HI aggregation kinetics (lag time = 3.4 h ± 0.1). Our study, although limited to a subset of all possible peptides, strongly suggests that the interaction of HI with the adsorbed peptide is not highly sensitive to the primary structure, as long as the adsorbed peptide provides a stable β-structure on the surface. Furthermore, the effect of the short peptides on insulin aggregation is related to their surface binding energy (minimum -5 kcal mol^{-1}) and requires a β-sheet conformation (Fig. 3). The interaction with the peptide-borne β-structure drives stable HI adsorption by triggering an α to β transition in HI and consequent β-sheet formation between neighboring peptides and incoming HI molecules. This effect is reminiscent of the effect of silver iodide crystals on super-cooled H_2O that induces the formation of ice crystals because of a match between the crystal structures of β-AgI and ice. It is already known that short peptides are able to influence full-length protein amyloid aggregation at iso-stoichiometric concentrations [7–9]. Nevertheless, the impact of container surface chemistry is not systematically taken into account, despite the fact that hydrophobic

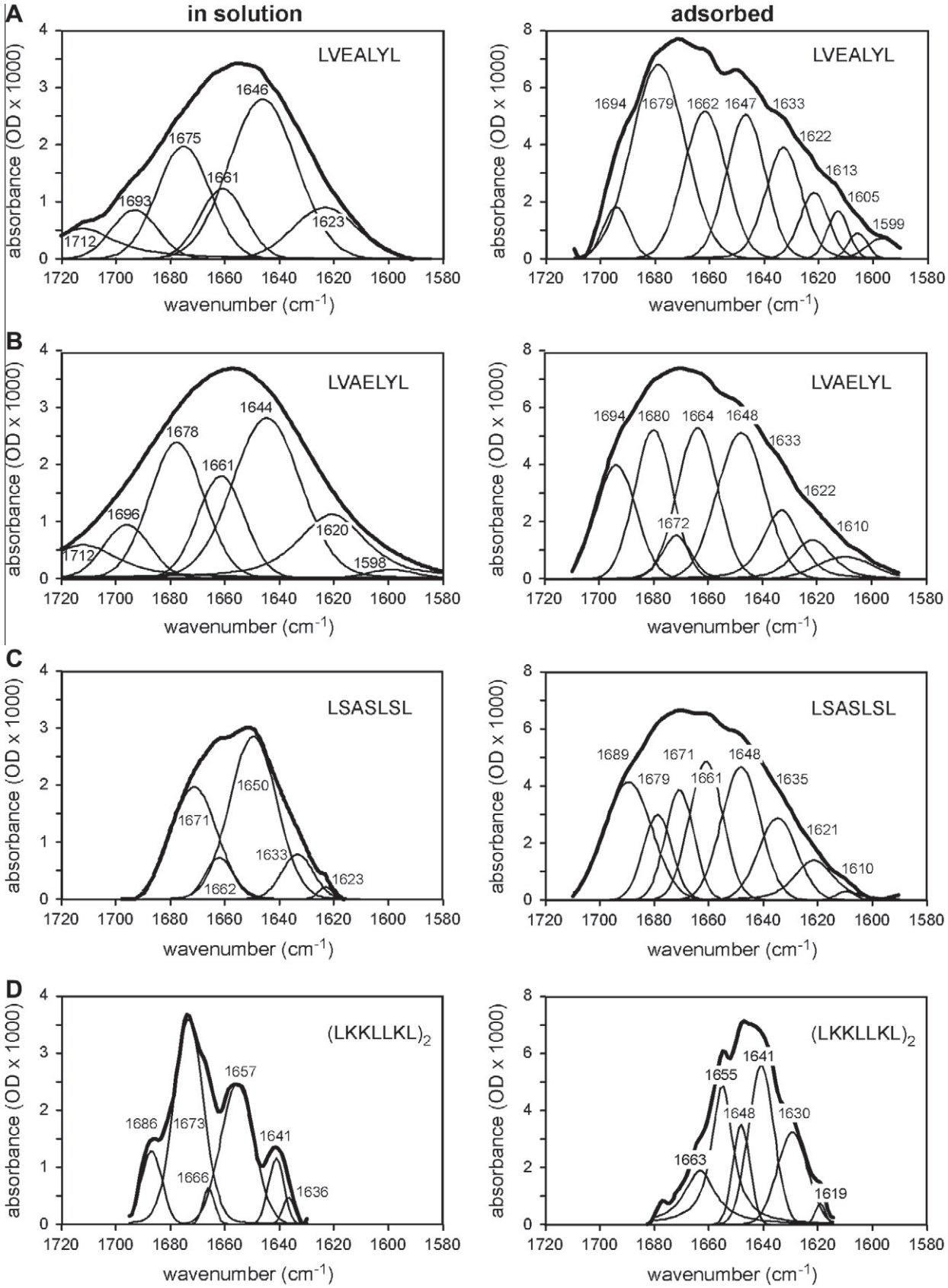

Fig. 2. Amide I band of the LVEALYL (A), LVAELYL (B) and LSASLSL (C) and $(LKKLLKL)_2$ peptides in solution (left) and adsorbed on hydrophobic surfaces (right). Transmission FTIR spectra were recorded with 8.6 μM peptides in deuterated buffer. For ATR-FTIR, peptides were introduced at 8.6 μM in the flow chamber of a hexylmethyl-coated silicon prism. After 30 min, the prism surface was washed with buffer and the infrared spectra were recorded. Thick line: amide I band after linear baseline correction. Thin lines: decomposition of the amide I band into individual peaks.

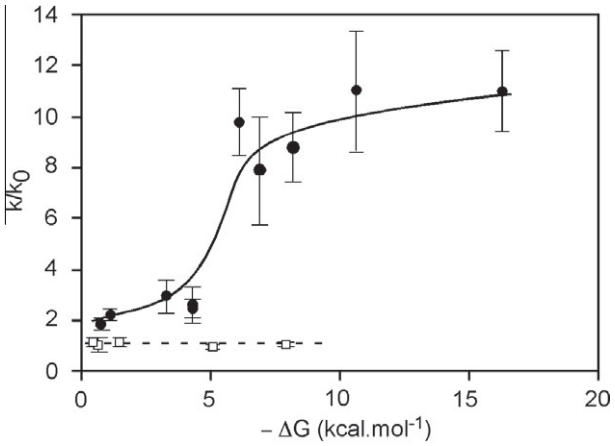

Fig. 3. Effect of different peptides on insulin kinetics. Aggregation kinetics of HI (86 μM) alone or mixed with 8.6 μM peptide were determined. The nucleation rates k (in the presence of peptide) and k_0 (in the absence of peptide) were calculated as the inverse of the lag time. For each peptide, the k/k_0 ratio is plotted as a function of the binding energy of the peptide on hydrophobic surfaces in β-strand conformation Eqs. (1) or (2). Circles: peptides without proline residue. Squares: peptides containing one proline residue. Data are from Table 1. Lines are hand drawn.

interfaces are known to be able to induce the aggregation of different proteins [5,18]. Here we show that peptides present in substoichiometric concentrations, adsorbed on hydrophobic surfaces are able to accelerate or delay HI aggregation.

Acknowledgements

This work was supported by the ANR Grant "Stabilization of Therapeutical Proteins". Laurent Nault held a doctoral fellowship from la Région Rhône-Alpes. We thank Catherine Picart and Flora Gilde for access to and assistance with the ATR-FTIR. The authors acknowledge the "Pôle de Capteurs Thermométriques et Calorimétrie" of the Institut Néel for the use of the oxygen plasma etching equipment.

Appendix A. Supplementary data

Supplementary data associated with this article can be found, in the online version, at http://dx.doi.org/10.1016/j.febslet.2012.11.036.

References

[1] Dische, F.E., Wernstedt, C., Westermark, G.T., Westermark, P., Pepys, M.B., Rennie, J.A., Gilbey, S.G. and Watkins, P.J. (1988) Insulin as an amyloid-fibril protein at sites of repeated insulin injections in a diabetic patient. Diabetologia 31, 158–161.
[2] Wogulis, M., Wright, S., Cunningham, D., Chilcote, T., Powell, K. and Rydel, R.E. (2005) Nucleation-dependent polymerization is an essential component of amyloid-mediated neuronal cell death. J. Neurosci. 25, 1071–1080.
[3] Brange, J., Andersen, L., Laursen, E.D., Meyn, G. and Rasmussen, E. (1997) Toward understanding insulin fibrillation. J. Pharm. Sci. 86, 517–525.
[4] Ahmad, A., Uversky, V.N., Hong, D. and Fink, A.L. (2005) Early events in the fibrillation of monomeric insulin. J. Biol. Chem. 280, 42669–42675.
[5] Sluzky, V., Tamada, J., Klibanov, A. and Langer, R. (1991) Kinetics of insulin aggregation in aqueous solutions upon agitation in the presence of hydrophobic surfaces. Proc. Natl. Acad. Sci. USA 88, 9377–9381.
[6] Ballet, T., Brukert, F., Mangiagalli, P., Bureau, C., Boulangé, L., Nault, L., Perret, T. and Weidenhaupt, M. (2012) DnaK prevents human insulin amyloid fiber formation on hydrophobic surfaces. Biochemistry 51, 2172–2180.
[7] Scrocchi, L.A., Ha, K., Chen, Y., Wu, L., Wang, F. and Fraser, P.E. (2003) Identification of minimal peptide sequences in the (8–20) domain of human islet amyloid polypeptide involved in fibrillogenesis. J. Struct. Biol. 141, 218–227.
[8] Du, H.-N., Li, H.-T., Zhang, F., Lin, X.-J., Shi, J.-H., Shi, Y.-H., Ji, L.-N., Hu, J., Lin, D.-H. and Hu, H.-Y. (2006) Acceleration of alpha-synuclein aggregation by homologous peptides. FEBS Lett. 580, 3657–3664.
[9] Kim, J.R. and Murphy, R.M. (2004) Mechanism of accelerated assembly of beta-amyloid filaments into fibrils by KLVFFK(6). Biophys. J. 86, 3194–3203.
[10] Hong, D.-P. and Fink, A.L. (2005) Independent heterologous fibrillation of insulin and its B-chain peptide. Biochemistry 44, 16701–16709.
[11] Ivanova, M.I., Sievers, S.A., Sawaya, M.R., Wall, J.S. and Eisenberg, D. (2009) Molecular basis for insulin fibril assembly. Proc. Natl. Acad. Sci. USA 106, 18990–18995.
[12] Sluzky, V., Klibanov, A.M. and Langer, R. (1992) Mechanism of insulin aggregation and stabilization in agitated aqueous solutions. Biotechnol. Bioeng. 40, 895–903.
[13] Nault, L., Guo, P., Jain, B., Bréchet, Y., Bruckert, F. and Weidenhaupt, M. (2013) Human insulin adsorption kinetics, conformational changes and amyloidal aggregate formation on hydrophobic surfaces. Acta Biomater. 9, 5070–5079.
[14] Engelman, D.M., Steitz, T.A. and Goldman, A. (1986) Identifying nonpolar transbilayer helices in amino acid sequences of membrane proteins. Annu. Rev. Biophys. Biophys. Chem. 15, 321–353.
[15] DeGrado, W.F. and Lear, J.D. (1985) Induction of peptide conformation at apolar water interfaces. 1. A study with model peptides of defined hydrophobic periodicity. J. Am. Chem. Soc. 107, 7684–7689.
[16] Collier, G., Vellore, N.A., Yancey, J.A., Stuart, S.J. and Latour, R.A. (2012) Comparison between empirical protein force fields for the simulation of the adsorption behavior of structured LK peptides on functionalized surfaces. Biointerphases 7, 24.
[17] Weidner, T., Apte, J.S., Gamble, L.J. and Castner, D.G. (2010) Probing the orientation and conformation of alpha-helix and beta-strand model peptides on self-assembled monolayers using sum frequency generation and NEXAFS spectroscopy. Langmuir 26, 3433–3440.
[18] McMasters, M.J., Hammer, R.P. and McCarley, R.L. (2005) Surface-induced aggregation of beta amyloid peptide by ω-substituted alkanethiol monolayers supported on gold. Langmuir 21, 4464–4470.

THE JOURNAL OF PHYSICAL CHEMISTRY B

Article

pubs.acs.org/JPCB

Dual Effect of (LK)nL Peptides on the Onset of Insulin Amyloid Fiber Formation at Hydrophobic Surfaces

Karim Chouchane, Charlotte Vendrely,[‡] Myriam Amari, Katie Moreaux, Franz Bruckert, and Marianne Weidenhaupt*

[†]University Grenoble Alpes, CNRS, LMGP, F-38000 Grenoble, France

[‡]Cergy Pontoise University, ERRMECe, I-MAT FD4122, F-95302 Cergy Pontoise, France

ABSTRACT: Soluble proteins are constantly in contact with material or cellular surfaces, which can trigger their aggregation and therefore have a serious impact on the development of stable therapeutic proteins. In contact with hydrophobic material surfaces, human insulin aggregates readily into amyloid fibers. The kinetics of this aggregation can be accelerated by small peptides, forming stable beta-sheets on hydrophobic surfaces. Using a series of (LK)nL peptides with varying length, we show that these peptides, at low, substoichiometric concentrations, have a positive, cooperative effect on insulin aggregation. This effect is based on a cooperative adsorption of (LK)nL peptides at hydrophobic surfaces, where they form complexes that help the formation of aggregation nuclei. At higher concentrations, they interfere with the formation of an aggregative nucleus. These effects are strictly dependent on the their adsorption on hydrophobic material surfaces and highlight the importance of the impact of materials on protein stability. (LK)nL peptides prove to be valuable tools to investigate the mechanism of HI aggregation nuclei formation on hydrophobic surfaces.

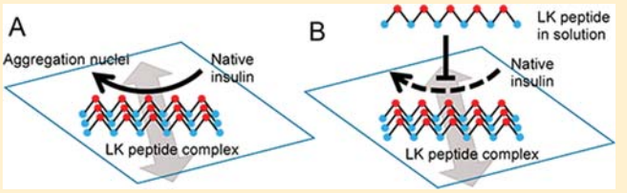

INTRODUCTION

Protein stability is a crucial parameter, foremost because it is a prerequisite for cellular function but also for safety and economic reasons in the production, storage, and delivery of therapeutics. Alteration of the protein structure usually entails the formation of aggregates, among which the amyloid fiber is widely studied. Amyloid aggregation of proteins in vivo is linked to major diseases, like Alzheimer's or Parkinson's.[1] Insulin, the most produced therapeutic protein, is known for decades for its propensity to aggregate into fibers, which is a serious drawback for the development of novel diabetes therapies.[2] Understanding the mechanisms involved in protein fibrillation is therefore essential to be able to control protein stability.

The transition from the soluble protein to the aggregated amyloid fiber is generally described in three successive steps: (1) a conformational change triggered by improper folding or environmental conditions, (2) stabilization of partly unfolded protein monomers by intermolecular interactions to form nucleation sites, and (3) association of successive unfolded monomers with the nuclei to promote fiber growth. Accordingly, a lag phase (steps 1 and 2) and a growth phase (step 3) are characteristically defined to describe protein fibrillation. For human insulin (HI), fibrillation can be triggered in vitro by low pH, high temperature, high ionic strength, and hydrophobic surfaces.[3−5] We have shown that at pH 7 and 37 °C, all three steps of the fibrillation process are strictly dependent on the presence of hydrophobic surfaces.[6] This finding highlights an aspect that is generally overseen in protein aggregation studies: the impact of the container material used for the experiments. In most cases, plastic containers are used and their hydrophobic surface represents both the site and trigger for insulin aggregation. In the following, we define nuclei as the surface-bound structures, able to trigger fibril growth (seeds). All complexes present during the maturation of these nuclei are termed prenuclei.

In an attempt to understand protein aggregation into amyloid fibers, multiple studies have been aimed at identifying minimal peptide sequences, inhibiting, or accelerating the aggregation kinetics of the parent protein. For example, an 8 amino-acid prion peptide segment (residues 113−120: AGAAAAGA), a 6 amino-acid modified peptide from Aβ (residues 16−20: KLVFF) and a 5 amino-acid segment from IAPP (residues 22−27: NFGAIL) can delay fibril formation of their respective full-length protein.[7−10] Such peptides are often hydrophobic, adopt a beta-sheet conformation, and fibrillate by themselves. The inhibitory effect is generally obtained at high concentrations, ranging from equimolar to concentrations exceeding ten times the protein concentration. On the other hand, amyloidogenic peptides, accelerating the aggregation lag phase, were also discovered.[11−13] They are often effective at low concentrations compared to the protein. Interestingly, many peptides have both accelerating and inhibiting effects on protein aggregation, depending on their relative concentrations. Ivanova et al. have shown that the HI B-chain peptide LVEALYL (residues B11 to B17) is able, at substoichiometric

Received: July 30, 2015
Revised: August 1, 2015
Published: August 1, 2015

DOI: 10.1021/acs.jpcb.5b07365
J. Phys. Chem. B 2015, 119, 10543−10553

concentrations to reduce the HI aggregation lag-time significantly and, at higher concentrations, to inhibit fibril growth.[12]

Using the same LVEALYL peptide and mutants thereof, we could demonstrate that the amyloidogenic effect described by Ivanova et al.[12] depends on the adsorption of the peptide in beta-sheet conformation on a hydrophobic surface.[14] Moreover, we could show that the secondary structure and not the sequence of the adsorbed peptide was crucial.[14,15]

Amyloidogenic peptides thus represent a tool to elucidate how a hydrophobic surface can trigger the formation of aggregation nuclei and hence amyloid fiber growth. They can be customized in sequence and chemical properties (functional groups, fluorescent labels). In this way, they are at the same time amyloid aggregation inducers and tools to investigate the aggregates they trigger. In order to get insight into the underlying molecular phenomena, we decided to use peptides adopting well-defined beta-sheet structures on hydrophobic surfaces. Such peptides were described by De Grado and Lear[16] and consist of alternating leucine (L) and lysine (K) residues to create a hydrophobic repeat, matching a beta-sheet. Using circular dichroism (CD) and Fourier-transform infrared spectroscopy (FTIR), they demonstrated that the synthetic peptide LKLKLKL adopted beta-sheet-stabilized monolayers at apolar interfaces, the hydrophobic leucine residues segregating toward the hydrophobic surface, and the lysine residues toward the water. On the basis of these findings, we reasoned that LK-repeat peptides of variable length were ideal tools to investigate the formation of nuclei, presenting an aggregation-triggering, surface-adsorbed beta-sheet structure to incoming HI molecules.

Here we present a thorough study of the mechanism of formation of HI aggregation nuclei on hydrophobic surfaces, using a series of (LK)nL peptides with varying length and a fluorescent tag. We investigate the dual concentration-dependent effect that these peptides have on HI aggregation kinetics. We demonstrate that their accelerating effect is based on their cooperative and stable adsorption properties, increasing the efficiency of formation of surface-bound prenuclei and that their inhibitory effect is due to an excess of peptide in solution.

EXPERIMENTAL AND THEORETICAL METHODS

Human Insulin. Recombinant human insulin (HI) produced in *Saccharomyces cerevisiae* was purchased from Sigma-Aldrich (ref: I2643). HI solutions TMN buffer (NaCl 125 mM, $MgCl_2$ 2 mM, Tris-HCl 25 mM, pH 7.4). In order to solubilize insulin, the pH of the solution was lowered to 3.2 using 1 M HCl then adjusted to pH 7.4 with 1 M NaOH using a pH electrode. The HI concentration was then precisely adjusted to 86 μM, measuring the 280 nm absorbance [ε_{280}(HI) = 5.53 mM^{-1} cm^{-1})]. The resistivity of the pure water used was 18 MOhm cm at 25 °C. Once adjusted at the proper concentration, the solution was filtered through a 0.22 μm Millex-GV filter unit (ref: SLGV033SS). The solutions were stored at T = 4 °C for less than 2 weeks and refiltered (if not fresh) before use.

Thioflavin T. When linked to amyloid fibers, Thioflavin T (ThT) undergoes a fluorescence shift from (λ_{ex} = 342 nm; λ_{em} = 430 nm) to (λ_{ex} = 450 nm; λ_{em} = 482 nm). This property allows the direct quantification of amyloid fibers by fluorescence since the fluorescence of linked ThT is proportional to the amount of amyloid fibers. Thioflavin T (from Sigma-Aldrich, ref: T3516) was solubilized in TMN buffer. Then the ThT concentration was adjusted to 1 mM by absorbance measurement (in ethanol ε_{416}(ThT) = 26.6 mM^{-1} cm^{-1}). Finally, solutions were filtered through a 0.22 μm Millex-GV filter (ref: SLGV033SS) and conserved protected from light at T = 4 °C for several months.

Peptides. Chemically synthesized (LK)nL peptides as well as the tetramethyl rhodamine-labeled (LK)5L peptide (TAMRA-LK11) (Table 1) were ordered from Genecust (Luxembourg), solubilized in 10 mM NaOH to a concentration between 75 and 115 μM then filtered through a 0.22 μm filter (Millex-GV ref: SLGV033SS) and stored at T = −20 °C. The concentration of unlabeled peptides was determined using the Quanti Pro Bicinchoninic acid assay (Sigma-Aldrich ref QPBCA). The concentration of TAMRA-LK11 was determined using the molar extinction coefficient of tetramethyl rhodamine, ε = 65 200 M^{-1} cm^{-1}.[17] A linear correlation curve linking fluorescence at 585 nm to the amount of TAMRA-LK11 peptide was established (data not shown).

Table 1. (LK)nL Peptides

peptide name	peptide sequence
LK5	LKLKL
LK7	LKLKLKL
LK9	LKLKLKLKL
LK11	LKLKLKLKLKL
TAMRA-LK11	^{TAMRA}LKLKLKLKLKL

Quantification of TAMRA-LK11 Adsorption on Hydrophobic Surfaces. TAMRA-LK11 was incubated at different concentrations (up to 2.8 μM) in hydrophobic 96-well plates (in triplicate) and shaken at 1200 rpm for 10 min. The solution was then discarded and the well washed with 200 μL of filtered TMN buffer. After discarding the buffer, the adsorbed peptide was desorbed using 0.5% SDS in TMN buffer (1 min at 1200 rpm and 37 °C). The peptide TAMRA-LK11 was then quantified using a calibration curve (see above).

Measurement of Insulin Aggregation Kinetics. Aggregation kinetics were done in a 200 μL reaction volume in hydrophobic black 96-well plates (Nunc TM ref: 237105). In each well, aggregation assays were performed in the following conditions: [HI] = 86 μM, [ThT] = 20 μM, [LK peptide] = 0−5 μM, at T = 37 °C and agitation of 1200 rpm on a plate agitator (Heidolph instrument, Titramax 100). The amount of amyloid fibers has been monitored by fluorescence measurement of ThT bound to amyloid fibers (λ_{ex} = 450 nm, λ_{em} = 482 nm). The plates were removed from the incubator/agitator in order to read their fluorescence in a Tecan infinite M1000 plate reader, every 15 min. The bandwidth of the monochromators at the excitation and emission wavelengths was 5 nm. Data were obtained with three independent experiments using five replicates for each experimental condition. Lag times and growth rates were obtained by fitting data points of individual replicates.[14] These were then used to calculate mean values and standard deviations.

Cooperativity Calculations. To calculate the Hill coefficient of the cooperative effect of the peptides on the lag time, the experimental data points of the lag times (τ) as a function of peptide concentration (see also Figure 1) were fitted to the following equation:

$$\tau = \tau_{max} - (\tau_{max} - \tau_{min}) * \frac{[LK]^n}{[LK]^n + [LK]_c^n} \quad (1)$$

DOI: 10.1021/acs.jpcb.5b07365
J. Phys. Chem. B 2015, 119, 10543−10553

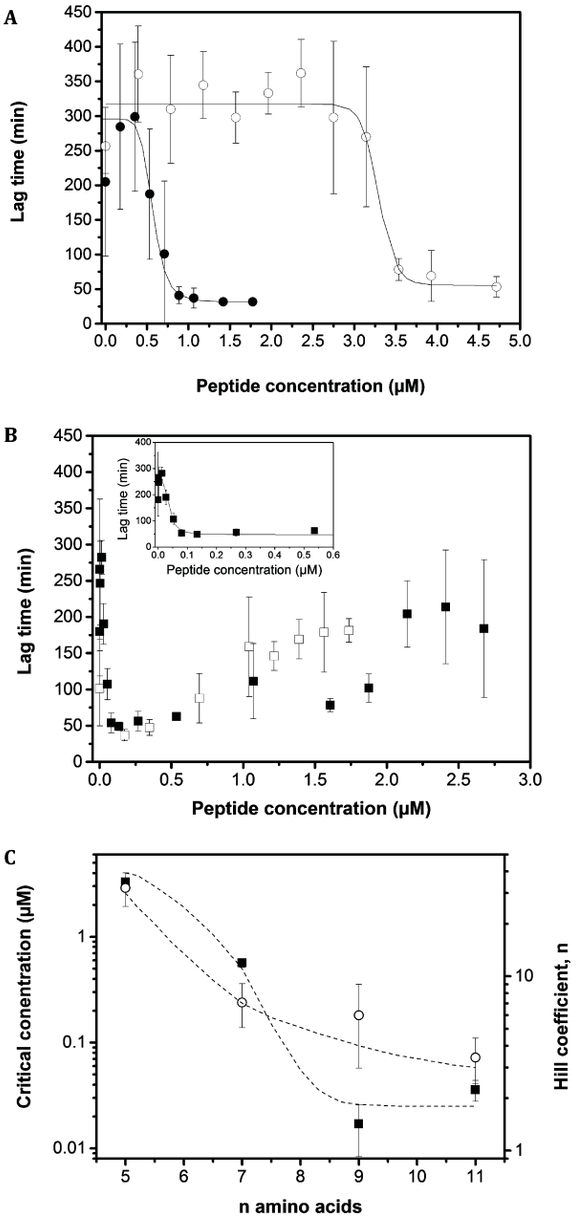

Figure 1. Different effects of LK peptides on the lag time of fibrillation. HI and ThT have been mixed with LK5 (A, ○), LK7 (A, ●), LK9 (B, □) and LK11 (B, ■) peptides at different concentrations and HI fibrillation has been monitored by ThT fluorescence. The solid line represents the fit of the experimental data with the Hill equation (see Experimental and Theoretical Methods). (C) The Hill coefficient (circles) and the critical concentration (squares), corresponding to the one at which 50% of the reduction of the maximal lag time was obtained, are plotted versus the number of LK amino acids. For easier reading, symbols are joined by a hand-drawn dashed line.

where τ_{max} represents the lag time (min) without peptide, τ_{min} the minimal lag time (min) obtained for a given peptide, [LK] the peptide concentration (μM), $[LK]_c$ the critical peptide concentration, corresponding to the concentration at which the lag time is half maximal and n the Hill coefficient. The fit was obtained by minimizing the quadratic error between experimental and calculated τ, weighted by the standard deviation of the lag time.

For the cooperative adsorption of TAMRA-LK11 on the hydrophobic surface of 96-well plates, the following equation was used to fit the experimental data:

$$[LK11]_{ad} = [LK11]_{max} * \frac{[LK11]_{sol}^{n}}{[LK11]_{sol}^{n} + [LK11]_{c}^{n}} \quad (2)$$

where $[LK11]_{ad}$ represents the concentration (in μM) of the TAMRA-LK11 peptide adsorbed on the well walls, $[LK11]_{sol}$ represents the concentration (in μM) of the TAMRA-LK11 peptide remaining in solution (i.e., $[LK11]_{sol} = [LK11]_{initial} - [LK11]_{ad}$), and $[LK11]_{max}$ represents the equivalent maximum concentration (in μM) of TAMRA-LK11 peptide adsorbed on the well surface for a given initial TAMRA-LK11 concentration, $[LK11]_{initial}$. $[LK11]_c$ represents the critical [LK11] concentration (in μM), corresponding to the half-maximal concentration of adsorbed TAMRA-LK11, and n represents the Hill coefficient of cooperative peptide surface adsorption. The fit was obtained by minimizing the quadratic error between experimental and calculated peptide concentration, weighted by the standard deviation of the measured concentrations.

Atomic Force Microscopy. *Glass Functionalization.* Borosilicate coverslip glasses (ϕ = 32 mm, from VWR international ref: 631-0162) were washed successively in SDS, ethanol, water, dried, and then activated in oxygen plasma for 4 min, and treated (t = 2 h) with dimethyldichlorosilane 5% (v/v) in toluene. This process covalently couples the silane to the glass by reacting with exposed Si−OH groups on the glass. The coverslips were then washed in toluene and absolute ethanol, and incubated at T = 100 °C (2 h) (curing) in order to cross-link silane oxides. Functionalization of the glass was controlled by water contact angle analysis (20 μL droplets of pure H_2O). The resulting glass presented a contact angle of 100° ± 5°, indicating a significant hydrophobicity.

Sample Preparation for the Observation of Insulin Aggregation Nuclei by AFM. Functionalized borosilicate coverslips were incubated in 6-well Nuclon Delta surface plates (Thermo scientific, ref: 140675) under the following conditions: T = 37 °C, 1200 rpm, [HI] = 43 μM, [LK9] = 0 or 0.2 μM, [ThT] = 20 μM in TN (NaCl 125 mM, Tris-HCl 25 mM, pH 7.4). The aggregation state was monitored using fluorescence measurements with a Tecan infinite M1000 apparatus (λ_{ex} = 450 nm; λ_{em} = 482 nm for bound ThT). Before AFM imaging, the samples were washed briefly by dipping in 0.1 μm-filtered TN buffer and dried. Mg was omitted from the buffer to avoid crystal formation during drying.

Visualization of Insulin Amyloid Aggregation Nuclei by Atomic Force Microscopy. Samples were imaged in TN buffer using a Dimension Icon (Bruker SAS, Palaiseau, France), equipped with a 150 μm scanner in the intermittent-contact mode. We used a Scanasyst-air Si_3N_4 cantilever (Bruker) with a resonance frequency of 70 kHz and a spring constant of 0.4 N m^{-1}. Images were obtained in the center of the coverslips, where nuclei density was highest. We show representative 2 × 2 μm^2 topology images. The analysis of the topologies was performed using the NanoScope Analysis software (Bruker).

Fluorescence Microscopy. *Sample Preparation for the Observation of Insulin Amyloid Aggregates by Fluorescence Microscopy.* Fluorescence microscopy observations of HI aggregates were conducted in transparent polystyrene flat-bottom 96 well plates (Greiner bio-one, ref: 655101). The aggregation procedure was the same as for the kinetic measurements. At selected time points, the plate was removed

DOI: 10.1021/acs.jpcb.5b07365
J. Phys. Chem. B 2015, 119, 10543−10553

from agitation, and the wells were imaged using an Olympus IX71 fluorescence microscope equipped with an Olympus U-CMAD3 camera, with an objective magnification of 20×.

Particle Analysis. Particle counting and measurement of particle area (in pixels) from 16 images (covering 0.53 mm^2) at each time point were performed with ImageJ, using a fluorescence intensity threshold adjusted to the background for each image set. The selection of the particles was done using the particle analysis command and defining 10 pixels as the minimal particle area. The areas were then converted into μm^2 using the rate of 0.023 μm^2 $pixel^{-1}$.

RESULTS

LK Peptides Show Concentration-Dependent Effects on the Lag Time of HI Fibrillation but Have No Influence on the Fibril Growth Rate. As described in our previous work, HI fibrillation was monitored using ThT fluorescence emission at 482 nm in polystyrene 96 well plates at 37 °C with an orbital agitation of 1200 rpm.[14] In order to study the effect of LK peptides on HI amyloid formation, the peptides, at concentrations between 0.01 and 4.7 μM, were mixed with the HI solution, and the fibrillation kinetics were recorded defining the lag time, elongation, and plateau phases. As a control, no ThT fluorescence increase was observed in wells containing 2.6 μM of peptide alone without HI, showing that the LK peptides do not assemble into amyloid fibers by themselves.

Our results show that, upon incubation with LK5, the shorter peptide, at concentrations up to 3 μM, the lag times of HI fiber formation were not modified and remained similar to those obtained in the absence of peptide (i.e., about 300 min) (Figure 1A, ○). By mixing HI with LK5 at concentrations equal or higher than 3.5 μM, the lag times of HI self-aggregation were decreased about six times to around 75−50 min. The LK7 peptide also shortens the lag times for peptide concentrations higher than 0.7 μM (Figure 1A, ●). For LK7 concentrations from 0.9 to 1.7 μM, the lag times were about 6 times decreased. No effect of the peptide is observed for LK7 concentrations lower than 0.7 μM. Using peptides of longer sequences, LK9 and LK11, the accelerating effect occurs at very low peptide concentrations, lower than 0.3 μM (Figure 1B). The lag time decrease became evident for LK11 concentrations of 0.03 μM, and the minimum lag time, equal to 50 min, was reached for 0.1 μM of LK11 (Figure 1B, inset). Moreover, for LK9 and LK11, a second effect was seen at concentrations higher than 0.3 μM: the lag times increased and reached a value similar to the one obtained without peptide. At 1.5 to 3 μM, LK9 and LK11 seemed to delay the nucleation, as the lag times were higher than the one observed without peptide (see also Figures 3 and 5, white bars). HI fibrillation kinetics is known to be highly variable, and this phenomenon is reflected by the large standard deviations obtained at high peptide concentrations (Figure 1B). In contrast, in the presence of LK peptides in accelerating conditions, the variability is strongly reduced.

For each peptide, the variations of the lag times with their concentration showed a sigmoidal shape suggesting a cooperative effect of the peptides on the acceleration of the nucleation step. Indeed, a critical concentration, corresponding to the one with which the accelerating effect obtained was 50% of the maximum, could be determined. For longer LK peptides, lower concentrations were enough to shorten the lag phase, suggesting that the accelerating effect of the LK peptides is more efficient with increasing peptide length. To assess this point, we plotted the correlation between the length of the peptides and the logarithm of their critical concentration (Figure 1C). This plot shows that the critical concentration decreases sharply with the length of the LK peptide until 9 amino acids. For LK11 a Hill coefficient of 2.5 and a critical concentration of 0.035 μM are observed (Figure 1C).

In order to check if LK peptides could influence the growth of HI fibrils (elongation phase), the variations of the growth rates in function of the peptide concentration have been investigated (Figure 2). At the different peptide concentrations tested, the growth rates of HI fibrillation remained stable at a value similar to the rate observed without peptide (i.e., about 60 AU min^{-1}), suggesting that the four peptides LK5, LK7, LK9, and LK11 have no significant effect on the elongation step of HI fibrillation. The plateau values recorded during fibrillation experiments remained also unchanged in the presence of LK peptides. Hence LK peptides play a critical role only in the nucleation step. The length of the LKnL peptides in amino acids is important for this process.

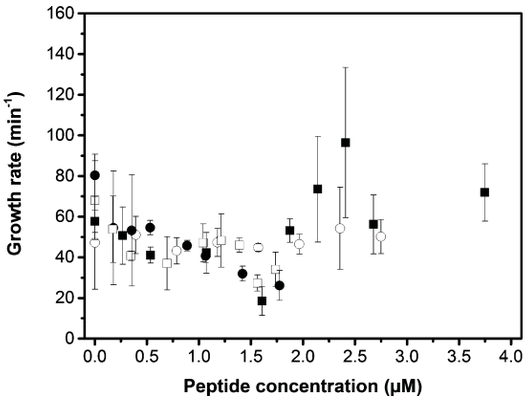

Figure 2. No influence of LK peptides on the growth rate of HI fibrillation. HI and ThT were mixed with LK5 (○), LK7 (●), LK9 (□), and LK11 (■) peptides at different concentrations, and HI fibrillation was monitored by ThT fluorescence.

Accelerating HI Fibrillation: LK Peptides Form Complexes Facilitating the Formation of Seeds on the Hydrophobic Surface. In order to gain insight into the role of the peptides on the hydrophobic surface, we investigated the effect of preadsorption of the peptides on the surface, on the formation of HI aggregation nuclei.

The LK11 peptide was preadsorbed onto hydrophobic surfaces by incubation at 37 °C with rotation at 1200 rpm during 10 min. After the incubation, nonadsorbed peptides were removed by a buffer wash. Then HI solution (86 μM) containing ThT (20 μM) was added to the wells and incubated at 37 °C and 1200 rpm. The lag times of the fibrillation curves, obtained in the presence of preadsorbed peptides, have been compared to the lag times obtained by mixing HI and LK11 simultaneously in the hydrophobic wells. Three concentrations of peptide, 0.01, 0.3, and 3 μM, correlated to three different effects seen on Figure 1B, were compared.

No shortening of the lag time was observed at a peptide concentration of 0.01 μM in comparison with the condition without peptide (Figure 3). In contrast, when mixed with HI, 0.3 μM of LK11 decreased the lag time, and this effect was inversed with a 3 μM concentration of peptide (Figure 3, white bars). These results confirmed the concentration dependency

DOI: 10.1021/acs.jpcb.5b07365
J. Phys. Chem. B 2015, 119, 10543−10553

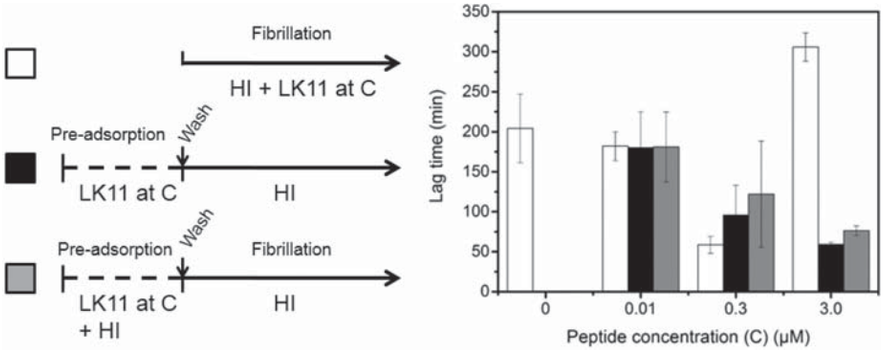

Figure 3. Preadsorption of LK11 peptide onto hydrophobic surfaces is enough to decrease the lag time of HI fibrillation. The peptide was incubated with the surface and rinsed before adding HI with ThT to monitor the aggregation kinetics by ThT fluorescence. The influence of different peptide concentrations on the lag time is shown. The effect of the peptide directly mixed with HI (white bars) is compared with the preadsorbed peptide (black bars) and with the preadsorbed peptide in the presence of an HI solution (gray bars).

of the effect of the peptide when mixed with HI as previously shown on Figure 1B.

The preincubation of the peptide at a concentration of 0.01 μM did not influence the HI aggregation kinetics (Figure 3, black column). In contrast, the lag time was greatly shortened when 0.3 or 3 μM of peptide were preadsorbed on the surface before triggering HI fibrillation, when compared to the experiment without peptide (Figure 3, black columns). Indeed, preadsorption of LK11 at 0.3 μM leads to a lag time of about 100 min, while preadsorption of LK11 at 3 μM resulted in a very similar lag time to the one obtained by directly mixing 0.3 μM of LK11 with HI (about 50 min). These results suggest that the accelerating effect of the peptide depends on the amount of adsorbed peptide remaining on the hydrophobic surface and not on the peptide in solution.

Thanks to their high adsorption energy, the peptides could form stable complexes on the surface favoring the growth of amyloid nuclei. This could be achieved in two possible ways: the aggregative complexes could (1) be made of peptides alone and form seeds for HI fibrillation or (2) consist in assemblies of peptides together with HI molecules. In order to assess this point, the influence of HI on the preadsorption of the peptides has been investigated. By adding HI to the peptide solution during the preadsorption step, the decrease of the lag times of fibrillation observed at the peptide concentrations of 0.3 and 3 μM was less pronounced (Figure 3, gray columns). Indeed, for 0.3 μM of preadsorbed LK11, the lag time obtained was about 125 min when HI was added during preadsorption, instead of 100 min for preadsorption of the peptide alone. Similarly, a lag time of about 125 min was also observed, when HI alone was preadsorbed then washed before triggering the formation of the fibrils by adding the peptide at 0.3 μM with HI. These results show that the peptide and HI have no synergistic effect in assembling aggregative prenuclei on the surface in these conditions and that both species, HI and LK peptides, compete for adsorption at the surface.

LK Peptides Adsorb in a Cooperative Manner on Hydrophobic Surfaces and Remain Stably Adsorbed. Because the accelerating effect of LKnL peptides on HI aggregation kinetics is linked to their preadsorption on hydrophobic surfaces, we investigated the adsorption properties of the LK11 peptide in more detail using a fluorescently tagged TAMRA-LK11 peptide (see Experimental and Theoretical Methods). As represented in Figure 4A, this peptide shows a similar accelerating effect on the HI aggregation lagtime at low concentrations (0.07−0.28 μM). Likewise, at high concentrations (>0.7 μM) TAMRA-LK11 strongly inhibits HI aggregation.

To obtain a closer insight into the binding of the TAMRA-LK11 peptide on hydrophobic surfaces, we plotted the concentration of adsorbed peptide after 10 min of incubation as a function of the total peptide concentration (Figure 4B) and the peptide concentration remaining in solution (Figure 4B inset). The results indicate that the TAMRA-LK11 peptide cooperatively adsorbs to the hydrophobic surface and reaches a maximum adsorption after 10 min incubation at 0.07 nMol (eq 0.35 μM in a 200 μL well). Using the Hill equation, described in Experimental and Theoretical Methods, we have determined a Hill coefficient of 2.1 and a critical concentration of 0.14 μM for the TAMRA-LK11 peptide adsorption.

We then used this peptide to analyze the stability of its adsorption on hydrophobic surfaces in the presence of HI. TAMRA-LK11 was incubated at 1.4 μM in hydrophobic 96-well plates and shaken at 1200 rpm for 10 min. The solution was then discarded, the well washed with TMN buffer and incubated with 86 μM HI. After the indicated times, the well was rinsed and the adsorbed peptide was desorbed in TMN buffer containing 0.5% SDS before quantification as described in Experimental and Theoretical Methods. As can be seen in Figure 4C, the amount of adsorbed peptide decreases slowly over 120 min. Indeed fitting the data points to an exponential function shows that the TAMRA-LK11 peptide has a $t_{1/2}$ of 99 min on the hydrophobic well surface. We can therefore assume that less than 30% of the peptide desorbs from the surface during the lag time.

These results strongly indicate that the cooperative accelerating effect of LK peptides at low concentrations on the lag time of HI aggregation kinetics is driven by a cooperative adsorption mechanism of these peptides on the hydrophobic surface and sustained by the stability of their surface-binding over time.

Inhibiting HI Fibrillation: LK Peptides in Excess in Solution Block Fibril Formation. In solution, LK peptides showed inhibitory effects at high concentrations. Indeed, when an excess of LK11 peptide remained in solution, it delayed the fibrillation kinetics (Figure 3, white bar at 3 μM, Figure 1B for LK11 > 2 μM, and Figure 4A for TAMRA-LK11 > 0.7 μM).

To gain insight into the effect of the peptide in solution, LK11 has been preadsorbed on the hydrophobic surface at three relevant concentrations C (0.01, 0.3, and 3 μM) and

DOI: 10.1021/acs.jpcb.5b07365
J. Phys. Chem. B 2015, 119, 10543−10553

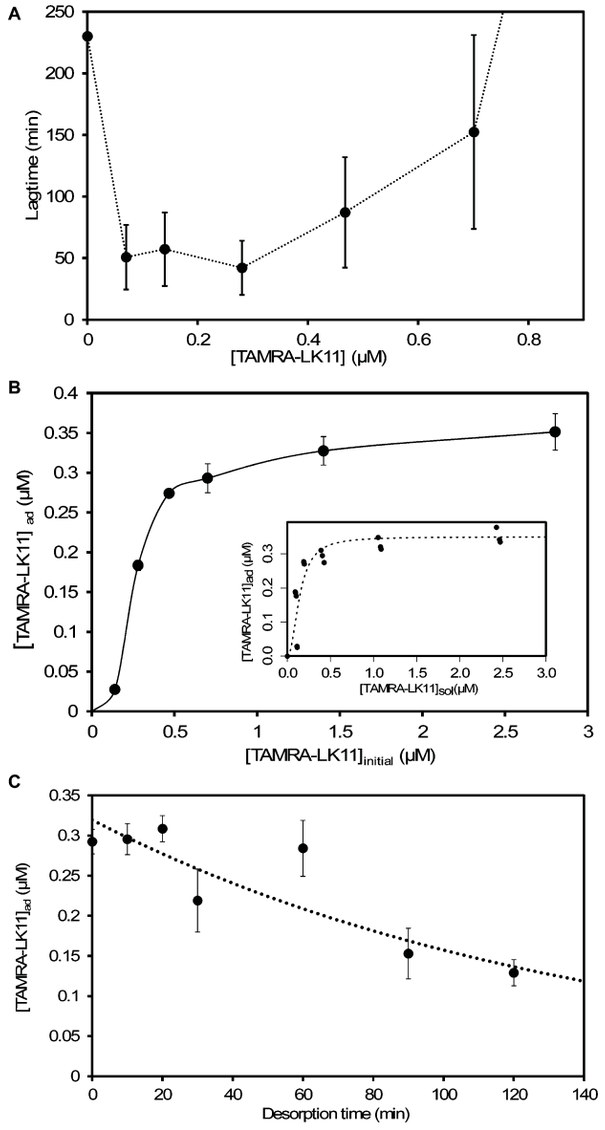

Figure 4. Stable and cooperative adsorption of TAMRA-LK11 on hydrophobic surfaces drives insulin amyloid aggregation. (A) Evolution of the lag time (circles) of HI aggregation as a function of the TAMRA-LK11 concentration. For easier reading, data points are joined by a hand-drawn dashed line. At 1.4 μM TAMRA-LK11, the lagtime is longer than 24 h. (B) Cooperative adsorption of TAMRA-LK11 on hydrophobic surfaces. The evolution of the amount of adsorbed peptide after 10 min incubation is shown as a function of the initial TAMRA-LK11 peptide concentration. The inset shows a fit using the Hill equation (dotted line) of the adsorbed TAMRA-LK11 peptide as a function of the peptide remaining in solution. (C) Desorption kinetics of TAMRA-LK11. TAMRA-LK11 (1.4 μM) was preadsorbed in TMN buffer (10 min, 1200 rpm, 37 °C), and the concentration of the peptide remaining adsorbed was measured by fluorescence as a function of time. Data were obtained with three replicates.

rinsed. Indeed, as shown in Figure 4B, at 0.3 μM, most LK11 is adsorbed in oligomers on the surface, while at 3 μM, an excess of peptide remains in solution. Then, the fibrillation has been monitored after adding HI and the peptide at the same concentration C in solution as used for the preadsorption (Figure 5, black bars) or after adding HI and LK11 in excess at 3 μM (Figure 5, gray bars). The lag times obtained were compared to those observed by directly mixing HI with LK11 at concentrations C.

Figure 5 shows that LK11 preadsorbed at 0.3 μM and added at the same concentration in solution can accelerate HI fibrillation. In that case, the lag times obtained are similar to those observed when directly mixing LK11 and HI (Figure 5, white and black bars at 0.3 μM). It suggests that, although insufficient amounts of peptide remain adsorbed on the surface during preadsorption (see Figure 3), the nucleation phase can be accelerated later thanks to the continued presence of the peptide in solution. In contrast, when the peptide is added in excess at 3 μM consecutively to the preadsorption at 0.3 μM, the accelerating effect of LK11 is abolished (Figure 5, gray bar at 0.3 μM).

Figure 5 confirms that, the accelerating effect, obtained by preadsorption of 0.3 μM LK11 peptide, can be blocked by inhibiting peptide concentrations in solution (3 μM). This clearly demonstrates that the peptide can interact with insulin and prevent it from aggregating into growing fibrils. This effect is strongly dependent on the free concentration of peptide in solution (≥3 μM, Figure 5). The inhibitory effect of the LK11 peptide on HI aggregation is probably driven by electrostatic interactions between the positively charged K side chains and HI (negatively charged at pH 7.4). Indeed, high NaCl concentrations (500 mM) reduce this effect drastically but do not affect the acceleration behavior at 0.3 μM (Figure 6).

Rotation is Not Necessary for the Preadsorption of the Peptide but for the Nucleation Step. In order to gain insight into the mechanism of LK seed formation, the influence of the rotation during the preadsorption of the peptide has been investigated.

Figure 7 shows that, at LK11 concentrations of 0.3 and 3 μM, agitation was not necessary to obtain the pro-amyloidogenic effect of LK11. Peptides thus efficiently adsorb on the hydrophobic surface by diffusion and form stable complexes. In contrast, rotation is necessary for the nucleation step: no aggregation was observed when the plates were not agitated after the preadsorption step. Moreover, incubation of LK11 at 0.3 μM in the presence of HI for several hours without agitation is not sufficient to create seeds as essayed with a fresh insulin solution. Thus, the transformation of HI and peptide complexes into active nuclei requires agitation.

Amyloid Prenuclei Can Be Observed by Microscopy. The nucleation and elongation phases of HI fibrillation can be monitored by different microscopy techniques. We used atomic force microscopy (AFM) to image amyloidogenic prenuclei in situ in the dry state. Glass coverslips were silanized to obtain hydrophobic surfaces and were subsequently incubated at 37 °C under rotation with HI solutions containing LK9 peptide or not (Figure 8).

Using AFM, no aggregates can be observed for the LK9 peptide alone after 2 h of incubation (Figure 8A) or HI alone after 1 h of incubation (Figure 8B). At this same time point, heterogeneous prenuclei can be observed on coverslips incubated with an HI solution mixed with LK9 peptide at 0.2 μM (Figure 8C). These complexes were diverse in shape and size, ranging from 10 nm to at least 35 nm in height and up to several hundred nanometers in width. Their distribution was rather dense after 1 h of incubation, when compared to the coverslips incubated with HI or peptide alone (Figure 8, panels A and B). After HI incubation, the surface rugosity varies from 0.5 nm without peptide to 6 nm in the presence of LK9. The

DOI: 10.1021/acs.jpcb.5b07365
J. Phys. Chem. B 2015, 119, 10543−10553

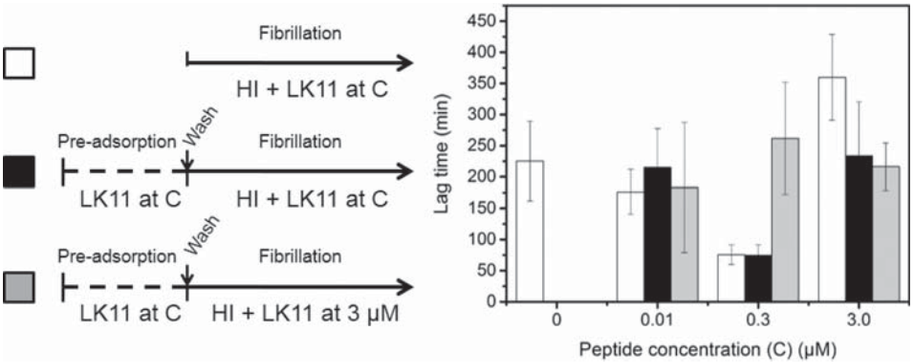

Figure 5. Excess of peptide LK11 in solution delays HI fibrillation. The peptide was incubated at concentrations C = 0.01, 0.3, or 3 μM with the hydrophobic surface and rinsed. Then, HI was added together with the peptide at the same concentration C to monitor the aggregation kinetics by ThT fluorescence (black columns). For comparison, HI was also supplemented with LK11 at C = 3 μM and ThT fluorescence was recorded (gray columns). The results have been compared with the effect of the peptide directly mixed with HI (white columns).

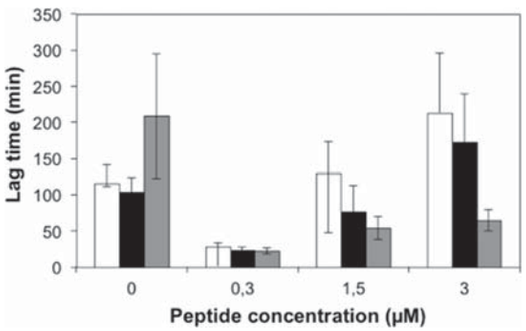

Figure 6. Effect of NaCl concentration on the lag time of HI aggregation. HI and ThT have been mixed with LK11 peptide at different concentrations in Tris buffer containing NaCl at 125 mM (white column), 250 mM (black column), or 500 mM (gray column). HI fibrillation was monitored by ThT fluorescence.

observed prenuclei in Figure 8C highly reduce the lag time of HI aggregation but do not abolish it, relative to the sample shown in Figure 8B.

ThT allows the labeling of amyloid structures and their observation by fluorescence microscopy (Figure 9). No specific fluorescence could be detected in the well incubated with HI and ThT for 120 min (Figure 9A). However, in wells incubated in the presence of LK9 at 0.2 μM, multiple small fluorescent objects, with different sizes up to 40 μm in diameter, could be observed at 120 min (Figure 9, panels B, C, and D).

Image analysis allows the determination of the size of the particles at the surface of the well with time. Fluorescent particles (up to 15 μm^2) were already identified after 30 min of incubation of HI mixed with LK9 (Figure 9C). The amount of such small particles increased dramatically after 120 min incubation (Figure 9D), and concomitantly bigger particles, up to 40 μm^2, were observed.

Together, the AFM and fluorescence microscopy observations confirm that LK peptides enhance the formation of surface-bound aggregative prenuclei that promote fibril growth.

DISCUSSION

In this paper, we use a series of (LK)nL peptides of various lengths as tools to investigate the mechanism of HI aggregation on hydrophobic surfaces. The results discussed here shed light on how amyloidogenic peptides cooperate with HI to either form stable aggregation nuclei on material surfaces, or, at higher concentration, block efficient fibril growth at the aggregation nucleus.

Cooperative Acceleration of Nuclei Formation at Low LK Peptide Concentration. Peptides (LK)nL, at low substoichiometric concentrations, accelerate the lag time of HI aggregation on hydrophobic surfaces and hence permit faster creation and maturation of amyloidogenic, surface-bound

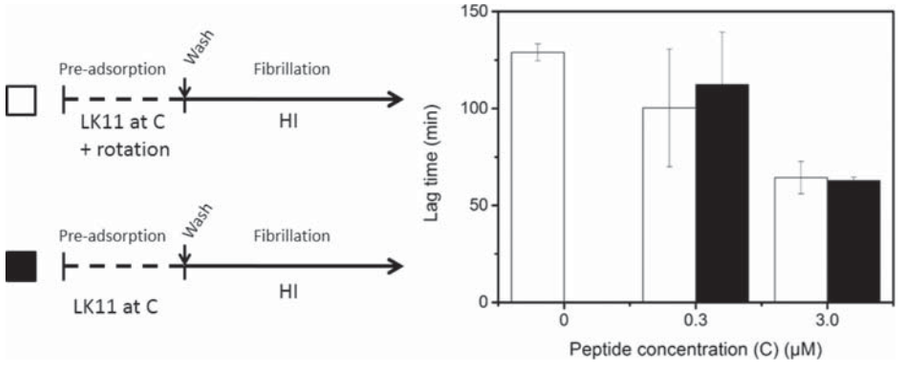

Figure 7. The agitation is not an important parameter for the preadsorption of the peptide. The LK11 peptide has been preadsorbed with (white bar) or without (black bar) agitation (1200 rpm) at a concentration of 0.3 or 3 μM and rinsed. HI and ThT were then added to monitor the aggregation kinetics by fluorescence measurements.

DOI: 10.1021/acs.jpcb.5b07365
J. Phys. Chem. B 2015, 119, 10543−10553

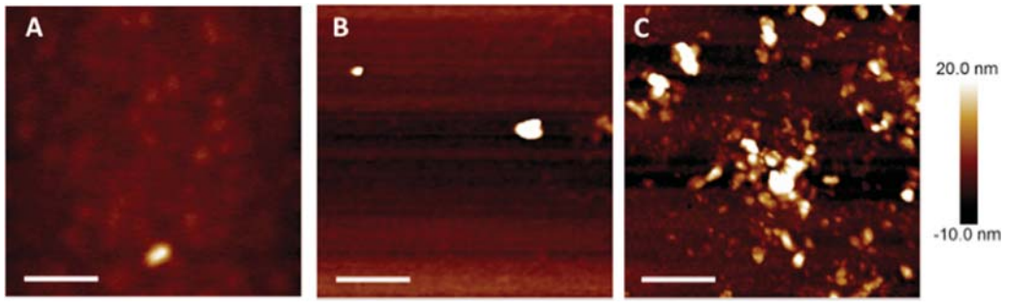

Figure 8. Observation of amyloid prenuclei. AFM (tapping mode) images of silanized glass coverslips incubated at 37 °C, 1200 rpm for 2 h with (A) LK9 peptide alone (0.2 μM), for 1 h with (B) HI solution without peptide, or with (C) HI solution containing 0.2 μM of LK9 peptide. Note that these time points correspond to the lag phase under these experimental conditions. The scale bar represents 500 nm. Images are representative of about 20 independent samples.

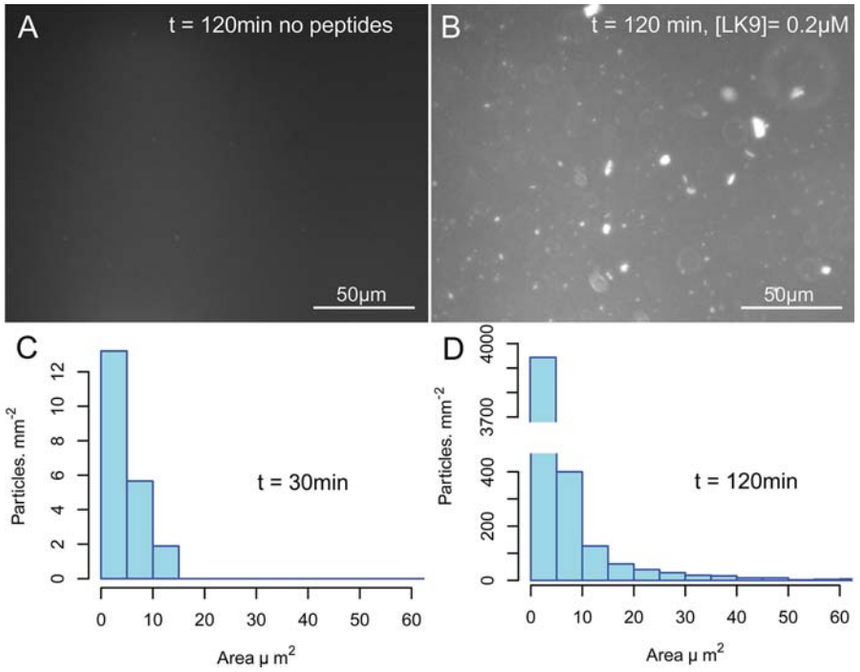

Figure 9. Fluorescence microscopy observation of insulin aggregates. HI was incubated at 37 °C and 1200 rpm and observed by fluorescence microscopy (DAPI filter) every 30 min. Images of the hydrophobic surface at 120 min are shown for (A) HI alone and for (B) HI in the presence of 0.2 μM LK9. The distribution of the particle size over a surface of 0.53 mm^2 is shown for HI + LK9 (0.2 μM) at (C) t = 30 min and (D) t = 120 min. Most particles are in focus and firmly adsorbed to the surface, some appear blurred and are not attached to the surface.

prenuclei (Figures 1 and 4A). This effect is most prominent with longer peptides (Figure 1 C), the fastest lag time (40−50 min) being recorded for LK11 and TAMRA-LK11 (Figures 1B and 4A). The increase of the accelerating effect with the length of the peptide is likely to be caused by stronger adsorption of long peptides onto hydrophobic surfaces. Indeed, the hydrophobic contribution to the adsorption energy increases with the number of hydrophobic amino acids. For LK5, which has the smallest hydrophobic contribution to its adsorption energy in the (LK)nL series tested here, higher peptide concentrations are needed to observe an acceleration of the nucleation step (Figure 1A). In line with the assumption that strong LK adsorption promotes faster aggregation, one expects that, for a peptide at a given concentration, the lag time decreases with longer surface contact times. This can be seen for example for LK11, for which the lag time is around 100 min if preadsorbed during 10 min but decreases to 50 min for longer contact times (Figure 3 black bar at 0.3 μM and Figure 1B). Furthermore, the results of Figures 3 and 4 demonstrate that, to obtain an accelerating effect, it is sufficient that peptides are stably adsorbed on the surface. After their surface adsorption, their presence in solution is no longer required to accelerate HI aggregation. This is due to the stability of their surface adsorption, as demonstrated with the fluorescently labeled TAMRA-LK11 (Figure 4C). This result confirms and strengthens the importance of a stable surface adsorption for peptides/proteins in order to promote the conformational changes that induce nuclei formation and fibrillation (Figure 10).

Plotting the lag time accelerating effect as a function of the LK peptide concentration, shows a sigmoidal behavior indicative of a cooperative effect of the peptides (Figure 1). Using the Hill equation (see Experimental and Theoretical Methods), we could determine a critical concentration and the

DOI: 10.1021/acs.jpcb.5b07365
J. Phys. Chem. B 2015, 119, 10543−10553

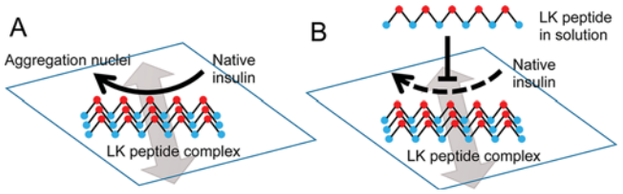

Figure 10. Dual effect of LK peptides on HI aggregation kinetics. (A) LK peptide complexes (represented with blue leucine and red lysine residues) cooperatively and stably adsorb on the hydrophobic surface (square) in β-sheet conformation. The hydrogen-bonding axis is represented by a gray transparent double-headed arrow. Upon integration of native insulin, they accelerate the formation of aggregation nuclei. (B) LK peptides in solution inhibit the formation of active aggregation nuclei.

Hill coefficient of each LK peptide concerning its effect on the lag time and for TAMRA-LK11 concerning its surface adsorption (Figure 1C and 4B). All peptides show a positive cooperative behavior and both critical concentrations and Hill coefficients decrease with peptide length (Figure 1C). This holds true for LK peptides that have less than 9 amino acids, and strongly indicates that stable complex formation relies on the local assembly of a defined number of peptides in time. The speed at which such complexes can be created depends on how quickly individual peptides can assemble at a given density on the surface. Using the fluorescently labeled TAMRA-LK11 peptide, we show that the peptide adsorption on the hydrophobic surface itself is positively cooperative (Figure 4B). Together with the demonstrated stability of their surface adsorption (Figure 4C), the cooperative binding of LKnL peptides to the surface is the driving force, accelerating the formation of surface-bound aggregation nuclei. Peptide length, and therefore occupied surface area, and the stability with which they adsorb on the surface determine their cooperative efficiency. For longer peptides less molecules are necessary because they reach higher surface coverage and/or bind more stably than smaller ones. The LK11 peptide shows slightly higher values for the Hill coefficient and the critical concentration than LK9 (Figure 1C), indicating that an optimal peptide length can be defined for efficient aggregation nuclei formation. The cooperative behavior demonstrates the strong potential of aggregative peptides to control aggregation kinetics on material surfaces.

Beyond stable surface adsorption, the conformation and spatial organization of LK peptides on a hydrophobic surface is paramount. DeGrado and Lear[16] have shown by circular dichroism and infrared spectroscopy that LK7 is structurally organized in antiparallel beta sheets in solution and at hydrophobic interfaces for micromolar concentrations and at neutral pH. Matthes et al.[18] determined the conformation of the HI B-chain-derived peptide LVEALYL and showed that it is organized in antiparallel beta sheets and the determination of the crystal structure of the same peptide (PDB: 2OMQ[19]) confirms this. The LVEALYL peptide is known to form the spine of the HI fibril[12] and to have accelerating effects similar to those of LK peptides when adsorbed in substoichiometric concentrations on hydrophobic surfaces.[14] We showed that beta-sheet conformation of peptides is essential to obtain accelerating effects, α helix conformations delaying aggregation.[14] Altogether these data strongly support the idea that the establishment of peptide complexes on hydrophobic surfaces effectively triggering nucleation requires the presence of antiparallel beta sheets (Figure 10). These are either formed by HI upon surface adsorption[15] or provided by adsorbed peptides or a combination of both. It is tempting to speculate that the lag time can be shortened because adsorbed peptides facilitate conformational changes on incoming HI for its incorporation into prenuclei (Figure 10). Electrostatic interactions between HI and solution-exposed K residues probably play only a minimal role. Indeed, in a previous study,[14] we have used a mutant of the B-chain LVEALYL peptide, in which we replaced the negative charge of the glutamate residue (E) by the neutral side chain of threonine (T). When adsorbed to a hydrophobic surface, the resulting LVTALYL peptide exhibits the side chains of amino acids L-T-L-L to the solution, instead of L-E-L-L for the wildtype peptide. Both peptides show similar, accelerated lag times in HI aggregation kinetics, indicating that charges are not the principle driving force for the accelerating effect of these adsorbed peptides. Also, we have used $(IS)_2I$ and $(IS)_3I$ peptides, which adsorb with their hydrophobic isoleucine side chain to the hydrophobic surface and expose a neutral serine side chain to the solution. Both $(IS)_2I$ and $(IS)_3I$ peptides show an accelerating effect,[14] and this effect is cooperative, similar to (LK)nL peptides (data not shown). Moreover high salt concentrations do not affect the accelerating effect of LK peptides (Figure 6).

Our results show that, in order to obtain an accelerating effect on the lag time of HI aggregation, LK peptides do not need to cover the entire material surface but are probably adsorbed in small discrete "islands" scattered over the hydrophobic surface. Indeed, at 0.2 μM, when LK11 reduces the lag time considerably (Figure 1B), there are not enough LK11 molecules in solution to cover the well surface uniformly. Assuming the peptide is a rectangle of width 2.5 Å and length 2 Å per amino acid, one LK11 molecule occupies approximately 55 Å^2. In order to cover the entire surface of a reaction well filled with 200 μL solution (0.02 dm^2) by a monolayer of peptides, 3.6×10^{14} LK11 molecules are needed. However, at 0.1 nMol (see Figure 4B), the number of LK11 peptide molecules adsorbed is 6×10^{13}, covering 17% of the surface. Therefore, LK peptides must be adsorbed in a discrete manner on hydrophobic surfaces, at the time when they accelerate nuclei formation. This is also documented by our microscopy results (Figures 8 and 9). In this context, it is relevant to note that DeGrado and Lear demonstrated that the LK7 peptide is organized in aggregates of 31 molecules at the water−air interface.[16] Nayak et al. have measured the kinetics of the formation of insulin aggregation nuclei in solution using small angle neutron scattering and proposed that aggregation nuclei are composed of 3 insulin dimers (6 monomers).[20] On a surface, however, this might be different, as peptide/protein adsorption increases their local concentration, and their interaction with surfaces is likely to stabilize the nucleation multimer. The stoichiometry of peptide/HI molecules in surface-bound aggregation nuclei is hitherto unknown, but amyloidogenic peptides are a valuable tool to investigate it.

Inhibition of HI Aggregation at High LK Peptide Concentration. The lag time decrease, observed for LK peptides at low concentrations, is reversed at higher peptide concentrations, albeit still substoichiometric (Figures 1 and 4A). For example, LK9 and LK11 lose their accelerating effect gradually when present in concentrations higher than 0.5 μM (Figure 1B). Moreover, we show that the delay in HI aggregation comes from an excess of peptide in solution (Figures 3 and 5). Our results presented in Figure 2 further

DOI: 10.1021/acs.jpcb.5b07365
J. Phys. Chem. B 2015, 119, 10543−10553

show that none of the LK peptides have an effect on the fibrillation growth rate. It is therefore likely that nonadsorbed LK peptides remaining in solution interfere with efficient HI integration at growing prenuclei, either by interacting with preformed nuclei per se or by blocking the conformational changes that HI undergoes when incorporated into an aggregation nucleus (Figure 10). Because this inhibitory effect is observed at peptide concentrations in solution that are largely substoichiometric compared to the concentration of HI (86 μM), it is unlikely that the peptide interacts stably with HI before it reaches an aggregation nucleus. The mechanism of interaction of LK peptides with HI is unknown but probably based on hydrophobic or electrostatic interactions, given the nature of these peptides. Indeed, high ionic concentrations dampen the inhibitory effect (Figure 6), showing that the positively charged K residues and the negatively charged HI (pI = 5.3) could be electrostatically attracted.

The affinity of LK peptides for HI interaction at a growing nucleus is unknown, but the inhibitory effect is predominantly seen with longer peptides LK9 and LK11, suggesting a threshold for the size of the peptide. It is also possible that steric constraints present beyond a certain peptide size interfere with efficient incorporation of HI into a preformed surface-bound prenucleus. Along this line, the TAMRA tag, which is bulky, dramatically enhances the inhibitory effect of the TAMRA-LK11 (Figure 4A) at concentrations >0.7 μM. Finally LK peptides could also interfere with a domain in HI, exposed when HI is being integrated into the prenucleus, thereby hindering HI conformational changes. A comparative shielding mechanism has been shown to be efficient in preventing islet amyloid polypeptide (IAPP) aggregation during expression in *E. coli*.[21] Indeed, a recombinant protein tag using the HI18-binding domain, known to interact with a hydrophobic sequence in IAAP involved in aggregation, was used to sequester soluble IAAP monomers, thus preventing its aggregation. It is possible that LK peptides interact with partially unfolded HI thereby blocking further transition into the beta-sheet conformation found in the mature amyloid fiber.

CONCLUSIONS

In this paper, we demonstrate that small peptides consisting of alternate leucine and lysine amino acids of the type (LK)nL are capable to dramatically accelerate HI aggregation but also to inhibit it depending on their concentration. These effects are strictly dependent on the presence of hydrophobic material surfaces and highlight the importance of the impact of materials on protein stability. Indeed, we demonstrate that the cooperative effect on the acceleration of HI aggregation is based on a cooperative binding of the peptides to the surface. Beyond the results presented here, (LK)nL peptides clearly represent a versatile tool to study early stages of material-bound surface aggregation of proteins. As they are incorporated into aggregation nuclei, they are at the same time amyloid aggregation inducers and tools to investigate the aggregates they trigger.

AUTHOR INFORMATION

Corresponding Author

*Address: LMGP, Phelma Minatec, 3 parvis Louis Néel, CS50257, F-38016 Grenoble cedex1, France. Tel: ++ 33 4 56529335. Fax: ++ 33 4 56529301. E-mail: marianne.weidenhaupt@grenoble-inp.fr.

Notes

The authors declare no competing financial interest.

ACKNOWLEDGMENTS

This work was supported by a Ph.D. fellowship from the MENRT to K.C. We thank the CNRS for funding C.V. as a visiting researcher and acknowledge the Nanomonde facility of the CIME Nanotech and Sidali Bessa for assistance with the AFM experiments.

REFERENCES

(1) Eisenberg, D.; Jucker, M. The Amyloid State of Proteins in Human Diseases. *Cell* **2012**, *148* (6), 1188−203.
(2) Lougheed, W. D.; Albisser, A. M.; Martindale, H. M.; Chow, J. C.; Clement, J. R. Physical Stability of Insulin Formulations. *Diabetes* **1983**, *32* (5), 424−432.
(3) Ahmad, A.; Uversky, V. N.; Hong, D.; Fink, A. L. Early Events in the Fibrillation of Monomeric Insulin. *J. Biol. Chem.* **2005**, *280* (52), 42669−75.
(4) Brange, J.; Andersen, L.; Laursen, E. D.; Meyn, G.; Rasmussen, E. Toward Understanding Insulin Fibrillation. *J. Pharm. Sci.* **1997**, *86* (5), 517−25.
(5) Sluzky, V.; Tamada, J. A.; Klibanov, A. M.; Langer, R. Kinetics of Insulin Aggregation in Aqueous Solutions upon Agitation in the Presence of Hydrophobic Surfaces. *Proc. Natl. Acad. Sci. U. S. A.* **1991**, *88* (21), 9377−81.
(6) Ballet, T.; Brukert, F.; Mangiagalli, P.; Bureau, C.; Boulange, L.; Nault, L.; Perret, T.; Weidenhaupt, M. Dnak Prevents Human Insulin Amyloid Fiber Formation on Hydrophobic Surfaces. *Biochemistry* **2012**, *51* (11), 2172−80.
(7) Chabry, J.; Caughey, B.; Chesebro, B. Specific Inhibition of In Vitro Formation of Protease-Resistant Prion Protein by Synthetic Peptides. *J. Biol. Chem.* **1998**, *273* (21), 13203−7.
(8) Findeis, M. A.; Musso, G. M.; Arico-Muendel, C. C.; Benjamin, H. W.; Hundal, A. M.; Lee, J. J.; Chin, J.; Kelley, M.; Wakefield, J.; Hayward, N. J.; et al. Modified-Peptide Inhibitors of Amyloid Beta-Peptide Polymerization. *Biochemistry* **1999**, *38* (21), 6791−800.
(9) Kapurniotu, A.; Schmauder, A.; Tenidis, K. Structure-Based Design and Study of Non-Amyloidogenic, Double N-Methylated IAPP Amyloid Core Sequences as Inhibitors of IAPP Amyloid Formation and Cytotoxicity. *J. Mol. Biol.* **2002**, *315* (3), 339−50.
(10) Tjernberg, L. O.; Naslund, J.; Lindqvist, F.; Johansson, J.; Karlstrom, A. R.; Thyberg, J.; Terenius, L.; Nordstedt, C. Arrest of Beta-Amyloid Fibril Formation by a Pentapeptide Ligand. *J. Biol. Chem.* **1996**, *271* (15), 8545−8.
(11) Du, H. N.; Li, H. T.; Zhang, F.; Lin, X. J.; Shi, J. H.; Shi, Y. H.; Ji, L. N.; Hu, J.; Lin, D. H.; Hu, H. Y. Acceleration of Alpha-Synuclein Aggregation by Homologous Peptides. *FEBS Lett.* **2006**, *580* (15), 3657−64.
(12) Ivanova, M. I.; Sievers, S. A.; Sawaya, M. R.; Wall, J. S.; Eisenberg, D. Molecular Basis for Insulin Fibril Assembly. *Proc. Natl. Acad. Sci. U. S. A.* **2009**, *106* (45), 18990−5.
(13) Kim, J. R.; Murphy, R. M. Mechanism of Accelerated Assembly of Beta-Amyloid Filaments Into Fibrils by KLVFFK(6). *Biophys. J.* **2004**, *86* (5), 3194−203.
(14) Nault, L.; Vendrely, C.; Brechet, Y.; Bruckert, F.; Weidenhaupt, M. Peptides that Form Beta-Sheets on Hydrophobic Surfaces Accelerate Surface-Induced Insulin Amyloidal Aggregation. *FEBS Lett.* **2013**, *587* (9), 1281−6.
(15) Nault, L.; Guo, P.; Jain, B.; Brechet, Y.; Bruckert, F.; Weidenhaupt, M. Human Insulin Adsorption Kinetics, Conformational Changes and Amyloidal Aggregate Formation on Hydrophobic Surfaces. *Acta Biomater.* **2013**, *9* (2), 5070−9.
(16) DeGrado, W.; Lear, J. D. Induction of Peptide Conformation at Apolar/Water Interfaces. 1. A Study with Model Peptides of Defined Hydrophobic Periodicity. *J. Am. Chem. Soc.* **1985**, *107*, 7684−7689.

DOI: 10.1021/acs.jpcb.5b07365
J. Phys. Chem. B 2015, 119, 10543−10553

(17) Meadows, D. L.; Shafer, J. S.; Schultz, J. S. Determining the Extent of Labeling for Tetramethylrhodamine Protein Conjugates. *J. Immunol. Methods* **1991**, *143* (2), 263−72.
(18) Matthes, D.; Daebel, V.; Meyenberg, K.; Riedel, D.; Heim, G.; Diederichsen, U.; Lange, A.; de Groot, B. L. Spontaneous Aggregation of The Insulin-Derived Steric Zipper Peptide VEALYL Results In Different Aggregation Forms with Common Features. *J. Mol. Biol.* **2014**, *426* (2), 362−76.
(19) Sawaya, M. R.; Sambashivan, S.; Nelson, R.; Ivanova, M. I.; Sievers, S. A.; Apostol, M. I.; Thompson, M. J.; Balbirnie, M.; Wiltzius, J. J.; McFarlane, H. T.; et al. Atomic Structures of Amyloid Cross-Beta Spines Reveal Varied Steric Zippers. *Nature* **2007**, *447* (7143), 453−7.
(20) Nayak, A.; Sorci, M.; Krueger, S.; Belfort, G. A Universal Pathway for Amyloid Nucleus and Precursor Formation for Insulin. *Proteins: Struct., Funct., Genet.* **2009**, *74* (3), 556−65.
(21) Mirecka, E. A.; Gremer, L.; Schiefer, S.; Oesterhelt, F.; Stoldt, M.; Willbold, D.; Hoyer, W. Engineered Aggregation Inhibitor Fusion For Production of Highly Amyloidogenic Human Islet Amyloid Polypeptide. *J. Biotechnol.* **2014**, *191*, 221−7.

DOI: 10.1021/acs.jpcb.5b07365
J. Phys. Chem. B 2015, 119, 10543−10553

LANGMUIR

Article

pubs.acs.org/Langmuir

Insulin Aggregation at a Dynamic Solid−Liquid−Air Triple Interface

Thibaut Frachon,[†,‡] Franz Bruckert,[†] Quentin Le Masne,[‡] Emmanuel Monnin,[‡] and Marianne Weidenhaupt*[,†]

[†]LMGP, University Grenoble Alpes, CNRS, F-38000 Grenoble, France

[‡]Eveon S.A.S., Inovallée, F-38330 Montbonnot Saint Martin, France

Supporting Information

ABSTRACT: Therapeutic proteins are privileged in drug development because of their exquisite specificity, which is due to their three-dimensional conformation in solution. During their manufacture, storage, and delivery, interactions with material surfaces and air interfaces are known to affect their stability. The growing use of automated devices for handling and injection of therapeutics increases their exposure to protocols involving intermittent wetting, during which the solid−liquid and liquid−air interfaces meet at a triple contact line, which is often dynamic. Using a microfluidic setup, we analyze the effect of a moving triple interface on insulin aggregation in real time over a hydrophobic surface. We combine thioflavin T fluorescence and reflection interference microscopy to concomitantly monitor insulin aggregation and the morphology of the liquid as it dewets the surface. We demonstrate that insulin aggregates in the region of a moving triple interface and not in regions submitted to hydrodynamic shear stress alone, induced by the moving liquid. During dewetting, liquid droplets form on the surface anchored by adsorbed proteins, and the accumulation of amyloid aggregates is observed exclusively as fluorescent rings growing eccentrically around these droplets. The fluorescent rings expand until the entire channel surface sweeped by the triple interface is covered by amyloid fibers. On the basis of our experimental results, we propose a model describing the growth mechanism of insulin amyloid fibers at a moving triple contact line, where proteins adsorbed at a hydrophobic surface are exposed to the liquid−air interface.

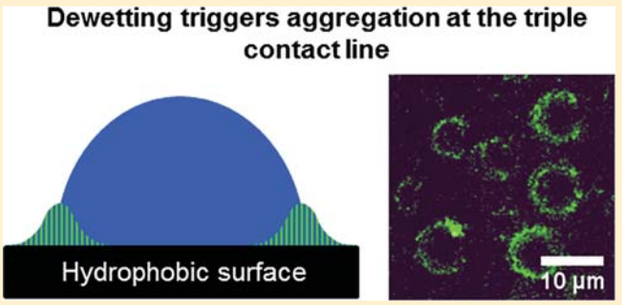

INTRODUCTION

Therapeutic proteins have opened new avenues in disease treatment because their unequaled specific interactions allow drug targeting with unprecedented molecular precision. This property comes at the price of guaranteeing their native conformation, which is inherently far more complex and less stable for proteins than for chemically synthesized drugs. Insulin and monoclonal antibodies (mAbs) are the most produced and administered therapeutic proteins, and their structural stability is determining not only their therapeutic value but also the economic viability of their production.

Besides the multiple environmental factors affecting protein stability (temperature, pH, ionic strength, and so forth), protein aggregation triggered by adsorption at material surfaces or air interfaces is emerging as a crucial parameter commanding conformational stability.[1−4] Indeed, during their fabrication, storage, transport, and until their delivery, therapeutic protein solutions are constantly in contact with different material surfaces and are very often exposed to air, which can be considered as a smooth and flexible hydrophobic interface. Moreover, in medical devices used for reconstitution or injection, protocols involving intermittent wetting expose the protein solutions to a triple solid−liquid−air interface, which is often dynamic (pump cavitation, agitation, air bubbles in tubing, and headspace in perfusion bags).

It is well-documented that insulin adsorption at material surfaces, in particular hydrophobic ones, and at the liquid−air interface is detrimental for its stability and leads to accelerated amyloid aggregation. Sluzky and colleagues[5] pinpointed in a pioneering study that insulin aggregates only in the presence of hydrophobic surfaces when agitated. Since then numerous studies have shed light on kinetic, structural, and nucleation aspects of interfacial insulin aggregate formation, and it is widely accepted that interfacial effects play an important role in insulin stability (for recent examples, see refs 6−9). For antibodies, usually formulated at very high therapeutic concentrations, interface adsorption is one of the parameters guiding formulation strategies. Among many examples, Couston and colleagues[10] have examined the structural organization and surface loading of a mAb under relevant pH and surfactant conditions on silica. A repetitive rupture of the air−liquid interface has been shown to induce the aggregation of mAbs,[11] and the effect of a liquid−air interfacial mAb layer

Received: September 8, 2016
Revised: November 14, 2016
Published: November 16, 2016

DOI: 10.1021/acs.langmuir.6b03314
Langmuir 2016, 32, 13009−13019

on the rheological properties of mAb solutions has been examined.[12]

The above-selected studies underline that a detailed mechanistic understanding on how therapeutic proteins organize at interfaces is a timely subject, which takes all of its importance in the context of today's drug development. In this study, we focus on insulin adsorption and aggregation at a dynamic triple solid−liquid−air interface, mimicking intermittent wetting phenomena encountered in numerous industrial protocols. Although some recent studies are analyzing the effect of a moving air−liquid interface in the context of therapeutic protein aggregation,[12−14] a detailed real-time assessment of the protein fate at a moving triple contact line is still missing.

It is commonly accepted that proteins have surfactant-like properties and adsorb on hydrophobic interfaces by displacing weakly bound water molecules.[2,15,16] Secondary structure rearrangements allowing the establishment of hydrophobic interactions with the material or air interface stabilize their adsorption, counterbalancing the surface dehydration with an entropy gain. Subsequently, an interfacial protein layer organizes, in which packing density, lateral interactions, cooperative effects, and aggregation are known to operate at different rates, depending on the nature of the protein.[2] At a moving triple interface, several interfacial phenomena co-occur, likely potentiating the above effects. Indeed, proteins adsorbed at the solid−liquid and air−liquid interfaces collide at this point inducing higher local concentrations and therefore intensifying intermolecular interactions. Moreover, a moving liquid−air interface submits the locally concentrated proteins to partial dehydration, enhancing conformational instability due to the loss of an integer hydration shell that proteins tend to retain.[17] This is especially true when protein adsorption is strong enough to prevent their dissociation from the surface as the liquid is removed.

We therefore developed a microfluidic setup allowing the movement of an insulin solution back and forth over a hydrophobic surface, thereby displacing the triple solid−liquid−air interface locally and continuously in a controlled way (Scheme 1). Insulin is known to aggregate and form amyloid fibers at hydrophobic surfaces and at the liquid−air interface, following nucleation-based aggregation kinetics.[9] The α-helix-rich native conformation of the insulin monomer unfolds upon adsorption to form a β-sheet. The stacking of β-sheets between adjacent monomers leads to the rapid formation of amyloid fibers, which can be detected by thioflavin T (THT) fluorescence.[18] Combining reflection interference contrast and fluorescence microscopy, we monitor, in real time and concomitantly, the morphology of the liquid film and the formation of insulin amyloid deposits on the material surface, respectively. We demonstrate that insulin fibers exclusively form in the region of intermittent wetting but not in the region exposed to hydrodynamic shear stress alone, remaining always wet. We show that the triple contact line is the place where the first aggregates are created, and we measure the growth kinetics of insulin amyloid aggregation at the edge of the liquid droplets. Finally, we propose a simple physicomathematical model describing the forces driving these phenomena.

EXPERIMENTAL SECTION

Chemicals. Recombinant human insulin (HI) produced in yeast, bovine serum albumin (BSA), and thioflavin T were purchased from Sigma-Aldrich (ref: I2643, P0914, and T3516, respectively). HI stock solutions were prepared at a concentration of 0.5 mg/mL (86 μM) in TN buffer (Tris-HCl 25 mM, NaCl 125 mM, pH 7.4). HCl (1 M) was added to completely dissolve HI in the buffer at pH 3.2, and then 1 M NaOH was added to adjust the final pH to 7.4. The concentration was adjusted by UV absorbance at 280 nm using an extinction coefficient of 5.53 mM^{-1} cm^{-1}. BSA solutions were diluted in pure water to reach a concentration of 0.5 mg/mL. THT stock solutions were prepared in TN buffer at a concentration of 1 mM, adjusted by absorbance measurement (1% THT solution in ethanol, ε_{416} (THT) = 26.6 mM^{-1} cm^{-1}). Tween 20 and Tween 80 were purchased from Sigma-Aldrich (ref: P1379, MW: 1228 g/mol and P1754, MW: 1310 g/mol, respectively). A polysorbate stock solution was prepared with 10% (v/v) Tween in water, the working concentration was 200 ppm in a standard HI solution (0.5 mL HI at 86 μM + 1 μL Tween 10%). All solutions were stored at 4 °C, conserved less than 2 weeks and filtered through a 0.22 μm Millex-GV filter unit from Merck Millipore (ref: SLGV033SS) before use.

Scheme 1. Experimental Setup[a]

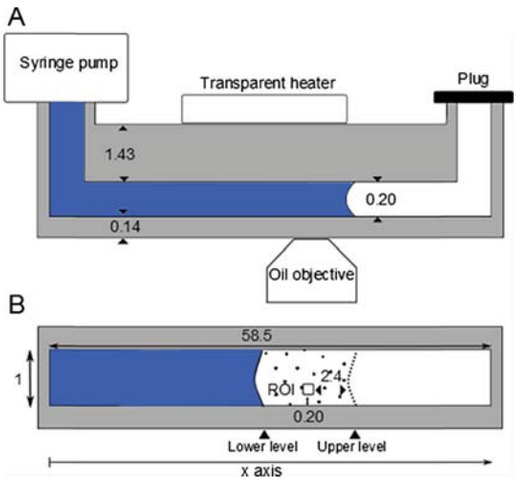

[a](A) Side view. (B) Top view. Blue represents the protein solution, white represents the air, and gray represents the chip material. Dimensions are in millimeters. The *x*-axis represents the length of the channel and defines the position at which the images are taken. The upper and lower levels correspond to the far left and far right meniscus positions during a cycle. The displaced liquid volume during each cycle is defined by the pump parameters and equals 2 μL. The cycle duration corresponds to the time that the liquid takes to reach the upper level and to come back to the lower level and equals 15 s. ROI represents the microscope objective position and the field of view during a time-lapse acquisition.

Experimental Setup. *Microscopy Setup Specifications.* An Olympus IX71 inverted microscope equipped with an Olympus DP30BW camera, a 60× magnification oil objective with a numerical aperture of 1.25 (ref: UPLanFLN), and a 100 W Hg lamp (U-LH100HG and HBO103W/2) were used for fluorescence and reflection interference contrast microscopy (RICM). The camera field of view was 200 by 150 μm. The size of the observed pixels was 150 nm resulting in a lateral resolution of 300 nm. A motorized stage (with a resolution of 0.05 μm and an accuracy of ±3 μm), purchased from Märzhäuser Wetzlar, was used for image acquisitions along the channel. A shutter, purchased from Vincent Associates (ref: Uniblitz VS35S2ZM1R3-NL-24), was used to avoid bleaching during time-lapse fluorescence acquisitions. The camera, the shutter, and the motorized stage were all synchronized and automated with Image Pro Plus 5 (Media Cybernetics) and home-made short programs.

Fluorescence Microscopy. The THT dye was used to monitor the amount of amyloid fibers formed at the channel surface. When incorporated into amyloid fibers, THT undergoes a fluorescence shift from (λ_{ex} = 342 nm; λ_{em} = 430 nm) to (λ_{ex} = 450 nm; λ_{em} = 482 nm).[19] This property allows the direct quantification of amyloid fibers

DOI: 10.1021/acs.langmuir.6b03314
Langmuir 2016, 32, 13009−13019

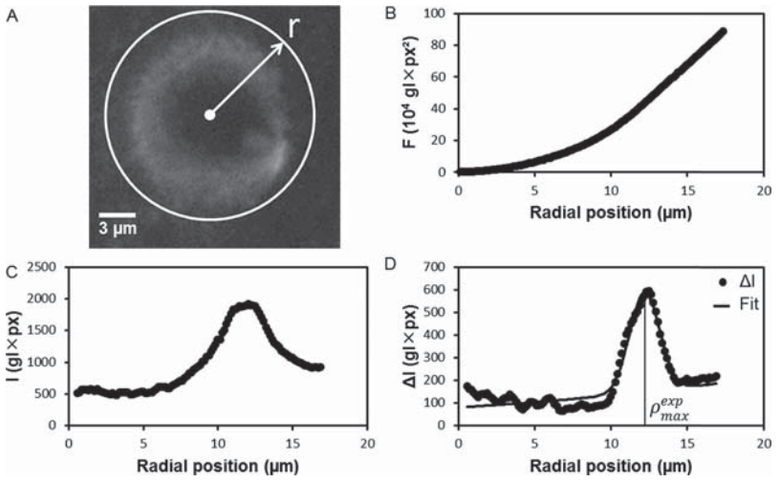

Figure 1. Image processing of the evolution of a THT-positive ring observed by fluorescence microscopy. (A) Example of a concentric circle drawn around the center of the droplet (white dot). *r* represents the radial distance to the center. Units: gl = gray level. (B) *Integrated fluorescence intensity profile* (*F*, gl × pixel^2) as a function of radius *r*. (C) *Radial fluorescence intensity profile* (*I*, gl × pixel) as a function of radius *r*. (D) *Differential fluorescence increase distribution* (ΔI, gl × pixel) over a 10 cycle interval as a function of the radius *r*. Continuous line: fit of $\Delta I(r)$ by two Gaussian functions (see eq 4). ρ_{max}^{exp} represents the *radial position of the maximal fluorescence increase*.

by fluorescence recordings at 482 nm. Fluorescence images were acquired with the microscope described above using a DEAC fluorescence cube (λ_{ex} = 436 ± 10 nm, λ_{em} = 480 ± 15 nm). Two neutral density filters (Olympus, 32ND6 and 32ND12) were used to reduce the light intensity of the Hg lamp by 92.8%.

RICM. For RICM, a green filter selected the 546 nm Hg emission peak of the lamp, and a semireflecting plate was set at 45° of the optical axis to illuminate the sample.[20] A neutral density filter (Olympus, 32ND12) was used to reduce the light intensity of the Hg lamp by 88%.

Microfluidic Setup. Straight microfluidic channel chips were purchased from microfluidic ChipShop (ref: 01-0175-0138-02). The channel dimensions were 200 μm deep, 58.5 mm long, and 1 mm large, with a 140 μm thick cover lid compatible with microscope oil objectives. They were equipped with a female mini luer fluidic interface for tubing connections. The chips were made in glass or in cyclo-olefin copolymer (COC, grade: mcs-Topas-03 mcs foil 011), a nonpolar, amorphous, and hydrophobic thermoplastic polymer.

A syringe pump was purchased from World Precision Instruments (ref: AL-6000) and adapted to be used with a 125 μL Distritips syringe body purchased from Socimed (ref: SOC-F164100). Tubing was purchased from Masterflex (ref: Tygon Lab E-3603 L/S 14). Male mini luer fluid connectors and male mini luer plugs were purchased from microfluidic ChipShop (ref: 09-0545-0333-09 and 09-0550-0334-09). A home-made conductive transparent heater was used to uniformly heat the channel at 37 °C, consisting of a silver nanowire network directly deposited on the top of the microchannel and connected to a power generator. Thanks to the Joule effect, when an electrical current is applied through the network, heat is released and transferred to the substrate.[21] A calibration curve was obtained using a thin Pt500 platinum resistor placed underneath the microchannel to relate the steady-state temperature difference relative to the room temperature to the applied voltage. The room temperature was controlled, and the temperature variation during the entire experiment did not exceed 1 °C.

Wetting/Dewetting Cycles in a Micro Channel. The COC microchannels were washed before the experiments with 10 mL of 5% sodium dodecyl sulfate, then with 10 mL of deionized water, 10 mL of 96% ethanol, and finally 10 mL of deionized water. The glass microchannels were washed with 14 M NaOH for 5 min and rinsed with 10 mL of deionized water. A new channel was used for each experiment. The 125 μL syringe was filled with a solution containing HI at 86 μM and THT at 20 μM, previously degased for 10 min. The syringe was fixed on the syringe pump and connected to the microchannel with tubing using a male mini luer fluid connector. All connections were sealed with parafilm. The chip was firmly clamped on the motorized microscope stage. The channel was completely filled up to the outlet. Then, a plug was introduced in the outlet that made the liquid move back to the upper level (Scheme 1). The plug sealed the device and insured the repeatability of the liquid levels during the cycles by avoiding evaporation. The transparent heater was then placed over the chip to cover the triple interface zone, and the adjacent zone remaining always wet. The syringe pump flow rate was set to 16 μL/min and programmed to repeatedly withdraw and push 2 μL of HI/THT solution, thus moving the liquid−air interface between the upper and the lower levels (see Scheme 1). A complete cycle of wetting−dewetting thus lasted 15 s.

Image Acquisition. *Time-Lapse Acquisition.* Before starting the pump, the microscope objective was focused on the cover lid, at 2.4 mm from the upper level and 200 μm from the channel wall (Scheme 1). The pump was programmed to stop for 1 s, every 10 cycles (150 s). The shutter and the camera were synchronized to acquire one image each time the pump stopped. This procedure resulted in a time-lapse image sequence acquisition of one image every 150 s for the entire experiment. Fluorescence or RICM microscope images were acquired as the liquid meniscus was at the upper level or the lower level, respectively. With our microscope setup, it is not possible to simultaneously acquire both fluorescence and RICM time-lapse image series. Consequently, the results based on different imaging mode time-lapse series come from different experiments (such as shown in Figures 5 and 7). Nevertheless, at specific time points, the imaging mode can be switched manually, allowing a fluorescence and RICM image acquisition during the same liquid cycle (see Figures 4 and 6). The gain and acquisition time of the camera were chosen to prevent saturation during the recordings.

End-Point Fluorescence Distribution. At the end of the experiment, the protein solution was withdrawn, and the channel was filled with 1 mL of TN buffer supplemented with 20 μM THT. The microscope objective was placed at 200 μm from the channel wall. Fluorescence images were then acquired along the *x*-axis, every 200 μm, using the motorized stage, allowing a total surface coverage along the *x*-axis. The three regions, always dry, triple interface, and always wet, were covered by the image sequence.

RICM Movie. RICM movies were acquired at different times during the experiment in order to determine droplet growth kinetics. The shutter was kept open because there is no photobleaching in RICM recordings. A movie was acquired over several consecutive wetting−

DOI: 10.1021/acs.langmuir.6b03314
Langmuir 2016, 32, 13009−13019

dewetting cycles with the DP Controller software (Olympus) at 15 frames per second.

Image Analysis. All image treatments and analyses were performed with ImageJ.

Fluorescence Quantification of Insulin Aggregation Kinetics and End-Point Distribution of Amyloid Aggregates in Microfluidic Channels. At any given time point, THT fluorescence was quantified by calculating the mean gray level intensity of the corresponding fluorescence image. Error bars represent the standard deviation of the measured intensities. The same procedure was applied to quantify the THT fluorescence distribution along the microchannel at the end of an aggregation experiment.

Detailed Growth Kinetics of Amyloid Aggregates around Liquid Droplets Remaining in the Microchannel after Dewetting. The following image treatment protocol was used to determine the radial distribution of the THT fluorescence increase around the droplets, remaining on the microchannel surface, using fluorescence images recorded every 10 cycles. At each time point, the *radial fluorescence intensity profile* ($I(r)$) was determined as a function of the distance to the center of the fluorescent ring (Figure 1A–C); then, the *differential fluorescence intensity distribution* ($\Delta I(r)$) over 10 cycles was calculated and analyzed to obtain the *net fluorescence increase* (Σ_{exp}) and the *radial position of the maximum fluorescence increase* (ρ_{max}^{exp}) (Figure 1D).

For each fluorescent image, a circle around the outlines of the fluorescent ring was first drawn (Figure 1A), and the center of this circle was used as the center of the droplet (white dot). Concentric circles of pixel-wise increasing radii were then defined, until they reached another fluorescent ring or the border of the image. The integrated fluorescence intensity profile was calculated by integrating the total fluorescence inside of each circle defined by its radius r (Figure 1B). At every time point t, expressed in cycles (1 cycle = 15 s), the integrated fluorescence intensity profile can be analytically expressed as

$$F(r, t) = \int\int_{0,0}^{r,2\pi} I(u, \theta, t)u \, du \, d\theta = \int_0^r 2\pi I(u, t)u \, du \quad (1)$$

where $I(u, t)$ corresponds to the average fluorescence intensity along the perimeter of the segmentation circle or radius u at a time point t.

The *radial fluorescence intensity profile* $I(r, t)$ at any time point t was obtained by deriving $F(r, t)$ from eq 1 (Figure 1C)

$$I(r, t) = \frac{1}{2\pi r}\frac{dF(r, t)}{dr} \quad (2)$$

The $F(r, t)$ derivative was calculated with the Savitzky and Golay algorithm, using seven points (coefficients used: −3, −2, −1, 0, 1, 2, and 3 normalized by dividing by 28).[22]

Then, consecutive *radial fluorescence intensity profiles* were subtracted to define the *differential fluorescence intensity distribution* over a 10 cycle interval, ΔI (Figure 1D).

$$\Delta I(r, t) = I(r, t) - I(r, t - 1) \quad (3)$$

The *net fluorescence increase* over a 10 cycle interval, Σ_{exp}, is obtained by integration of the ΔI differential profile along r.

Finally, each differential profile was fitted with two Gaussian functions and six parameters (Figure 1D)

$$\Delta I(r, t) = A_1 e^{-(r-\rho_{max}^{exp})^2/2\sigma_1^2} + A_2 e^{-(r-r_2)^2/2\sigma_2^2} \quad (4)$$

where A_1 and A_2 represent the amplitudes, ρ_{max}^{exp} and r_2 represent the peak positions, and σ_1 and σ_2 represent the widths of the two Gaussian functions. The first Gaussian function was used to fit the main peak of the profile, and the second Gaussian function was used to fit the baseline (Figure 1D). The *radial position of the maximal fluorescence increase* is thus determined by the center of the first Gaussian peak, ρ_{max}^{exp} (Figure 1D).

Droplet Superimposition Index. At each time point, the *superimposition index* was determined from two RICM images of droplets obtained after dewetting (Figure 2A), separated by 10 cycles (150 s). For each RICM image, a binary image was created by manually defining a threshold so as to select the dark disk inside of the droplets and colored in red for the first image and in green for the second one, obtained 10 cycles later (Figure 2B). Afterward, the 10 cycle-separated colored images were superimposed, resulting in a red, green, and blue (RGB) image (Figure 2C). The superimposition index is calculated from the three RGB images by the ratio of the yellow pixels (red AND green) to the sum of the red and green pixels minus the yellow pixels (red OR green).

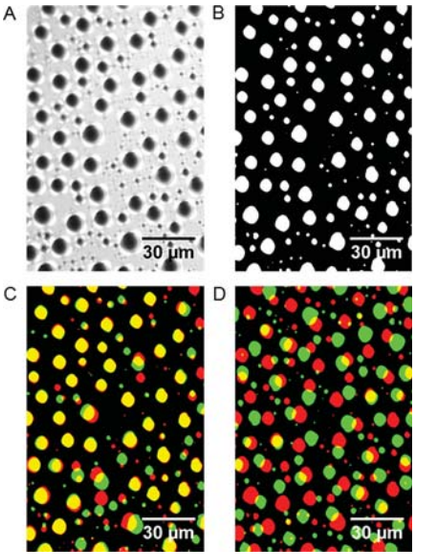

Figure 2. RICM image processing and superimposition index calculation. An RICM time-lapse image (A) is used to create a binary image (B) of the dark disks inside of the droplets. Binary images separated by 10 cycles are then superimposed to form an RGB image (C) from which the superimposition index is calculated (see text). (C) Superimposition index equals 0.58 (calculated at 49 min of experiment). A control is shown in (D), representing the superposition of (B) with itself rotated by 180 °. The superimposition index of (D) equals 0.09.

$$\text{Superimposition index} = \frac{\text{overlapping droplet area}}{\text{total droplet area}} = \frac{Y}{R + G - Y} \quad (5)$$

The error bars were calculated as the maximal error that could originate from alternative threshold choices.

In order to estimate the probability that droplets overlap randomly, another RGB image was created (Figure 2D), where one image was superimposed with itself, flipped by 180°. The superimposition index is 0.09 in this case. We therefore consider that superimposition indices >0.15 indicate nonrandomness.

Droplet Reformation Kinetics. At different time points, the droplet reformation kinetics was determined by analyzing an RICM movie (Movie S1).

First, the first and last frames obtained in the dewetted time interval at ROI were selected. Then, five droplets were selected and their initial and final size was determined using binary images of these two images, as shown in Figure 2B. The reformation kinetics of each droplet was finally calculated as the droplet size difference between the two images divided by the dry time interval. A mean value was obtained by averaging the reformation kinetics of the five droplets and has been calculated at 10, 50, 75, 90, and 120 min of the experiment. Error bars represent the standard deviation of the growth kinetic values.

RESULTS AND DISCUSSION

We designed a model experiment to be able to observe insulin aggregation at a dynamic triple solid–liquid–air interface. In a microchannel (Scheme 1), an insulin solution is repetitively moved back and forth between two positions (lower and upper

DOI: 10.1021/acs.langmuir.6b03314
Langmuir 2016, 32, 13009–13019

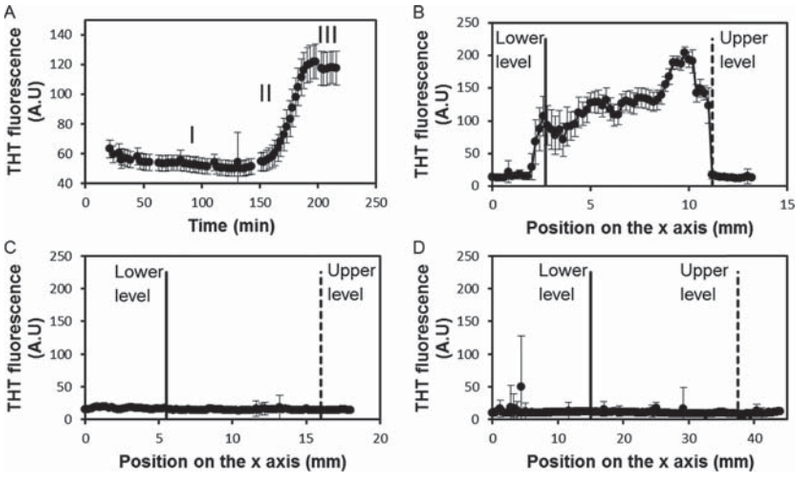

Figure 3. Insulin aggregation is caused by a moving triple interface on a hydrophobic surface. (A) HI aggregation kinetics. 0.5 g/L of HI is cyclically moved between the lower and the upper levels (15 s per cycle), at 37 °C. The mean THT fluorescence at ROI (Scheme 1) is plotted as a function of time. I, II, and III represent the different phases of insulin aggregation kinetics. (B–D) Aggregate distribution along the *x*-axis (Scheme 1) of the microchannel after 6 h of cycling at 37 °C, measured by THT fluorescence after washing for 0.5 g/L of HI in a COC microchannel (B), 0.5 g/L of BSA in a COC microchannel (C), and 0.5 g/L of HI in a glass microchannel (D). Vertical bars represent the upper (dashed line) and lower levels (solid line). Error bars represent the standard deviation of the average pixel gray value for each image. The results of panels A and B are representative of eight independent experiments.

levels) such that the channel comprises three different regions: a region that is always wet (blue in Scheme 1), a region that is intermittently wet (dotted in Scheme 1), and a region that is always dry (white in Scheme 1). This setup allows a direct in situ analysis of the effect of a moving triple solid–liquid–air interface on protein aggregation. Moreover, a direct comparison between insulin aggregation kinetics at the triple solid–liquid–air interface and at the solid–liquid interface is possible within the same experiment. THT fluorescence is used to monitor the formation of amyloid deposits and RICM to monitor the morphology of the liquid film after liquid receding in real time. A constant 37 °C temperature is maintained in the setup by a transparent heater.

Insulin Amyloid Aggregates Grow Only in the Intermittently Wet Region Where Triple Interfaces Are Created on a Hydrophobic Surface. Insulin aggregation kinetics was recorded using THT fluorescence images acquired every 10 cycles (150 s) at the ROI (Scheme 1) during the experiment, when the liquid reached the upper level in the channel. The mean gray level of the images, representing the amount of fibrils created on the surface of the microchannel, is reported in Figure 3A as a function of time. The recorded fluorescence signal follows a standard, nucleation-dependent behavior with three distinct phases: a lag phase (I in Figure 3A), where the fluorescence remains very low, a growth phase (II in Figure 3A), where the fluorescence increases strongly with time and amyloid fibers are forming on the surface, and a plateau phase (III in Figure 3A), where the fluorescence stabilizes indicating that no more fibers are created. The duration of the lag phase varies between 60 and 180 min, as commonly observed for nucleation-dependent insulin aggregation.[5,23] When the same experiment was performed at room temperature, amyloid fibers were also formed but on a much longer time scale (6–8 h). Insulin aggregation kinetics is therefore thermally activated, as expected.

When the plateau phase was reached, the HI aggregate distribution was determined using a sequence of consecutive THT images along the *x*-axis covering the dry, the intermittently wet, and the constantly immersed regions (Scheme 1). The mean gray level of each image, indicative of the amount of HI fibrils created at each position, is shown in Figure 3B. The fluorescence signal remains very low both in the constantly wet and dry regions, documenting the absence of amyloid aggregates in these areas. Thus, no HI aggregates are desorbed from the surface and deposited randomly during the experiment. On the contrary, in the intermittently wet region, the THT fluorescence is drastically increased, the highest signal being observed at the upper level, in the region remaining dry for the longest time between immersion cycles. Amyloid aggregates are thus only created on the surface in the intermittently wet region, where they remain strongly attached, delimitating this aggregation-prone region sharply from adjacent wet and dry zones. The difference in the fluorescence signal between the always wet and intermittently wet regions shows that the presence of a triple interface is critical to induce HI surface aggregation. At this low flow rate, the shear rate corresponds approximately to 60 s^{-1}, and shear stress alone (due to the liquid movement on the surface) is well below values sufficient to trigger the aggregation of cytochrome *c*.[24] However, the presence of a moving triple interface potentiates the effects of a local shear stress that is enough to trigger HI amyloid aggregation. This observation is in accordance with the literature, where it is well-established that shear stress alone is not detrimental for protein aggregation or inactivation, but the combination of shear stress with interfacial adsorption phenomena is affecting protein stability.[25] For mAbs, for example, Biddlecombe and colleagues have demonstrated and quantified in a thorough analysis that mAb monomer depletion is sizeable above shear rates of 5000 s^{-1} at a solid–liquid interface.[26] This indicates that in the triple interface zone, forces that exceed shear stress alone are present and are sufficient to denature proteins.[27]

The control experiments using BSA (Figure 3C) or insulin in a glass channel (Figure 3D) show that there is no amyloid fiber formation inside of the microchannel in these cases. The mechanism triggering the observed HI aggregation is thus

DOI: 10.1021/acs.langmuir.6b03314
Langmuir 2016, 32, 13009–13019

dependent on the concomitant presence of a hydrophobic surface and a moving air−liquid interface and is not observed for BSA.

HI Amyloid Aggregates Are Observed Concomitantly with Droplets Left on the Surface after the Liquid Has Receded. RICM was used to observe and characterize the hydrophobic surface at the ROI when the meniscus of the solution is at the lower level position in the channel (Scheme 1). Characteristic RICM images of the surface at three time points chosen in the lag phase (I in Figure 3A), the growth phase (II in Figure 3A), and the plateau phase (III in Figure 3A) during the HI aggregation kinetics are shown in parallel with THT fluorescence images at the same time points (Figure 4). The black disks surrounded by a white ring seen on RICM images (Figure 4B, D, and F) correspond to the liquid droplets left on the surface when the liquid has receded. The cross shape on the droplets is a camera artifact and is not visible by direct observation in the microscope objective. Fluorescence corresponding to surface-adsorbed HI amyloid aggregates is observed in Figure 4A, C, and E.

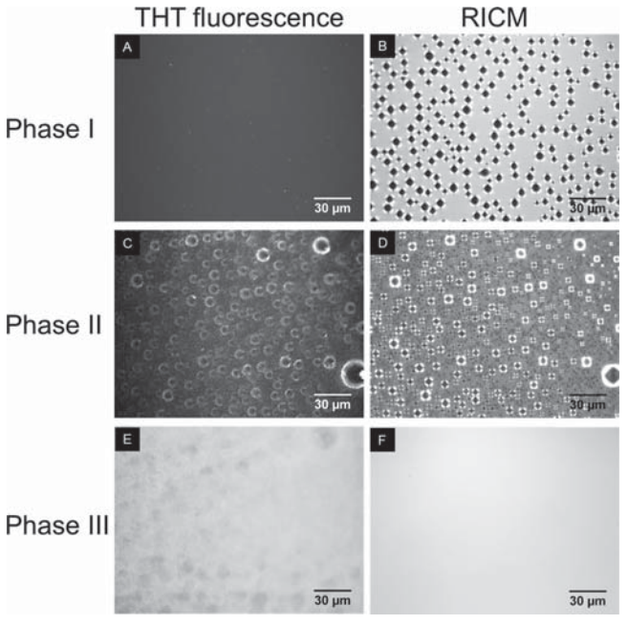

Figure 4. Position of THT-positive insulin aggregates correlates with the position of droplets on the dewetted surface. Microscopic images at ROI showing THT-positive amyloid aggregates (THT fluorescence, left panels, A, C, and E) and liquid droplets (dark circles surrounded by a bright ring, observed in RICM, right panels, B, D, and F) at the different phases of insulin aggregation (I, II, and III). RICM images are taken when the liquid is at the lower level (channel-dewetted), and fluorescence images are taken when the liquid is at the upper level (channel-filled). The field of view corresponds to 200 × 150 μm^2. The results shown are representative of eight independent experiments.

Right from the start of the first cycles, liquid droplets appear on the surface (Figure 4B). However, during the whole lag phase, no THT-positive aggregates are observed on the fluorescence images (Figure 4A). When the growth phase is reached, liquid droplets are still visible on the RICM images (Figure 4D), and amyloid aggregates start to appear as circles (Figure 4C). The fluorescent rings extend until the entire channel surface is covered by the amyloid fibers (Figure 4E). At this time, the plateau phase is reached, no more droplets form on the surface (Figure 4F), but a continuous liquid film remains above the fibers after liquid withdrawal. These observations demonstrate that HI amyloid aggregate growth is intimately correlated with the presence of droplets and that the creation of an aggregate layer modifies the water-retaining properties of the initially hydrophobic material surface.

Liquid Droplets Are Anchored by Proteins Adsorbed on the Microchannel Surface and Reform at the Same Location Cycle after Cycle. It should be noted that when a buffer solution was used instead of the protein solution, more and smaller droplets were observed during the dewetting period, at 37 °C (Figure S1A). The presence of insulin therefore has a strong effect on liquid film dewetting. Moreover, we noticed that the liquid droplets remain at the same position during most of the experiment with HI. RICM time-lapse images are used to calculate a droplet superimposition index (see Experimental Section), which represents the percentage of droplets that reform at the same location after 10 wetting−dewetting cycles. For the experiment shown in Figure 5, the lag phase is estimated to extend from 0 to 60 min, the growth phase is estimated to extend from 60 to 100 min, and the plateau phase is situated beyond 100 min (based on fluorescence images taken from time to time during the entire experiment). Plotting the superimposition index as a function of time (Figure 5A) reveals a rapid increase during the first 30 min and then stabilization until 90 min before a sharp decrease. Droplets appear immediately after the first liquid withdrawal. Long before any THT fluorescence is detectable, droplets are anchored to the surface and remain at the same place for much of the growth phase, before disappearing at the end of the growth phase. The same droplet anchorage is also observed when a BSA solution is used in the experiment, indicating that amyloid fibers are not necessary to anchor droplets. In the absence of protein, however, droplets reformed randomly on the surface, and the superimposition index remained below 0.15 (Figure S1B). Droplet anchorage can, thus, be explained by a progressive modification of the surface hydrophobicity during

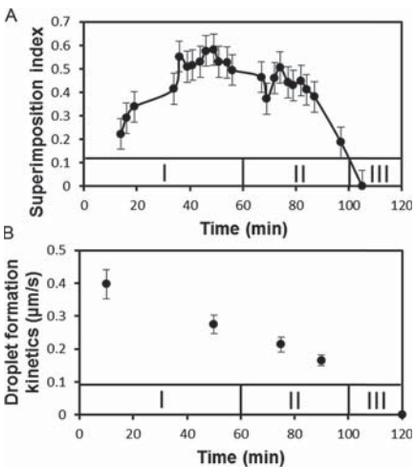

Figure 5. Droplet anchorage and droplet formation kinetics. (A) Droplet superimposition index at ROI, represented as a function of time. (B) Droplet formation kinetics is calculated on a set of representative droplets and is shown as a function of time. I, II, and III indicate the lag phase, growth phase, and plateau phase of insulin aggregation kinetics, respectively. The results shown are representative of three independent experiments.

DOI: 10.1021/acs.langmuir.6b03314
Langmuir 2016, 32, 13009−13019

the lag phase. Indeed, during the initial wetting−dewetting cycles, the gradual adsorption of proteins most likely modifies the nature of the surface locally from hydrophobic to hydrophilic, thus creating energetically favorable wetting zones, where water is preferentially retained.

The adsorbed proteins thus anchor the droplets, which in turn supply further proteins and thereby initiate the aggregation process at their very edge, where the solid material, liquid, and air meet, as is demonstrated hereafter.

A closer observation of the droplet reformation has been performed with the acquisition of RICM movies at the ROI during several cycles (see Movie S1), covering the entire aggregation process. After the liquid recedes, droplets reform by gathering the liquid that remains as a thin film on the microchannel surface around them. Their diameter therefore increases rapidly (Movie S1). An average speed for the reformation of a droplet can thus be calculated by the difference in the droplet radii at the beginning and end of the dry phase during the aggregation kinetics (Figure 5B). The results show a linear decrease in this speed until a complete liquid film is formed on the surface.

All of these observations fit with the idea that amyloid fibers grow at the microchannel surface. As they grow, a porous, proteinaceous zone is created, retaining the liquid and decelerating its movement during the droplet formation. This is reminiscent of the effect of anchored polymers on the dewetting velocity of a liquid thin film.[28]

HI Amyloid Aggregates Grow Eccentrically around Droplets at the Triple Contact Line. The superimposition of RICM and fluorescence images, separated by 10 cycles (Figure 6A), shows that the amyloid aggregates form only around the droplets. Overlaying consecutive fluorescence images, separated by 20 cycles (Figure 6B), shows that amyloid fibers form exclusively at the outer edge of the existing fluorescent ring. No fibers grow on the surface inside of the droplets or on the one devoid of droplets.

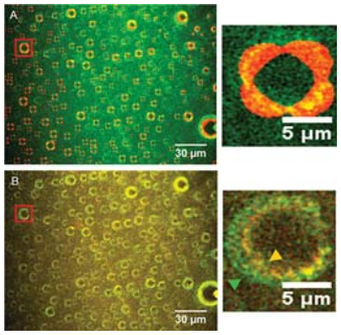

Figure 6. Progressive accumulation of insulin amyloid aggregates at the edge of the droplet. (A) Superimposition of an RICM image (droplets represented as red circles) and a THT fluorescence image (THT-positive amyloid aggregates in green) taken 10 cycles later at ROI. The right panel shows the magnified view of the region highlighted in A (red square). (B) Superimposition of two THT fluorescence images taken at a 20 cycle interval. THT-positive amyloid aggregates are represented in red for the first image and in green for the following one. Overlapping fluorescent pixels between both images appear in yellow (see yellow arrowhead in the magnified image at the right). The right panel shows a magnified view of the region highlighted in B (red square). The newly formed THT-positive aggregates appear in green (see green arrowhead in the magnified image at the right) at the outer border of the already formed fluorescent aggregate ring.

These results demonstrate that the triple contact line, where a droplet edge meets the microchannel surface, is a local trigger for HI aggregation. The presence of a growing amyloid fiber ring around the droplets explains the gradual slowdown of droplet formation kinetics and their stable anchoring at the same place.

Kinetics of the Formation of HI Amyloid Fibers at a Moving Solid−Liquid−Air Interface. To study the growth kinetics of HI amyloid fibers near the triple interface, four droplets with different sizes were selected in a time-lapse fluorescence movie corresponding to the experimental results in Figure 3. By quantitative image analysis, the radial distribution of newly formed aggregates was determined (see Experimental Section) during the time course of the aggregation kinetics, from which the total amount of aggregates created over a 10 cycle interval (Σ_{exp}) and the radial distance at which most of these newly formed aggregates appear (ρ_{max}^{exp}) were calculated.

Figure 7A,B represents the evolution of Σ_{exp} and ρ_{max}^{exp} with time. During phase II (growth phase, 150−180 min, 120 cycles), Σ_{exp} increases quasiexponentially, with an experimental growth rate of $\alpha_{exp} = 0.0226 \pm 0.0009$ cycle^{-1}. During the same time interval, ρ_{max}^{exp} increases quasilinearly with time defining an experimental velocity for the amyloid fiber formation $v_{exp} = 0.0282 \pm 0.0061$ µm·cycle^{-1}, confirming that new aggregates accumulate on the outer edge of the ring of previously formed ones. As time goes on, the position of the triple interface moves away from the center of the droplet, driven by the formation of new aggregate fiber layers on the material surface, and the droplets progressively flatten until no more droplets form.

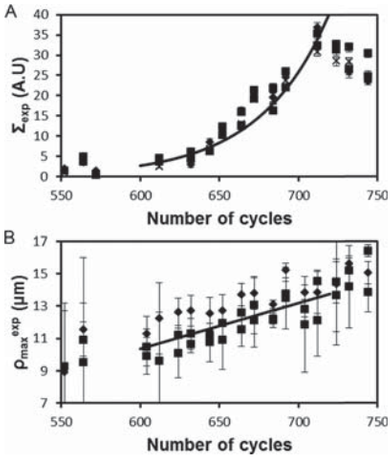

Figure 7. Detailed growth kinetics of the aggregate ring formed around droplets. Results from four different droplets are represented with square, circle, diamond, and cross symbols. An overall fit of the results is displayed with a continuous line. (A) Net fluorescence increase over a 10 cycle interval, Σ_{exp}, as a function of the number of cycles. Data are fitted by an exponential function with an amplitude of 915 ± 273 at 600 cycles and an experimental growth rate of $\alpha_{exp} = 0.0226 \pm 0.009$ cycle^{-1}. (B) Radial position of the maximal fluorescence increase, ρ_{max}^{exp}, as a function of the number of cycles. Data are fitted by a linear function with a y-intercept of 9.00 ± 1.15 µm at 600 cycles and a linear coefficient of $v_{exp} = 0.0282 \pm 0.0061$ µm·cycle^{-1}. Results are representative of three independent experiments.

DOI: 10.1021/acs.langmuir.6b03314
Langmuir 2016, 32, 13009−13019

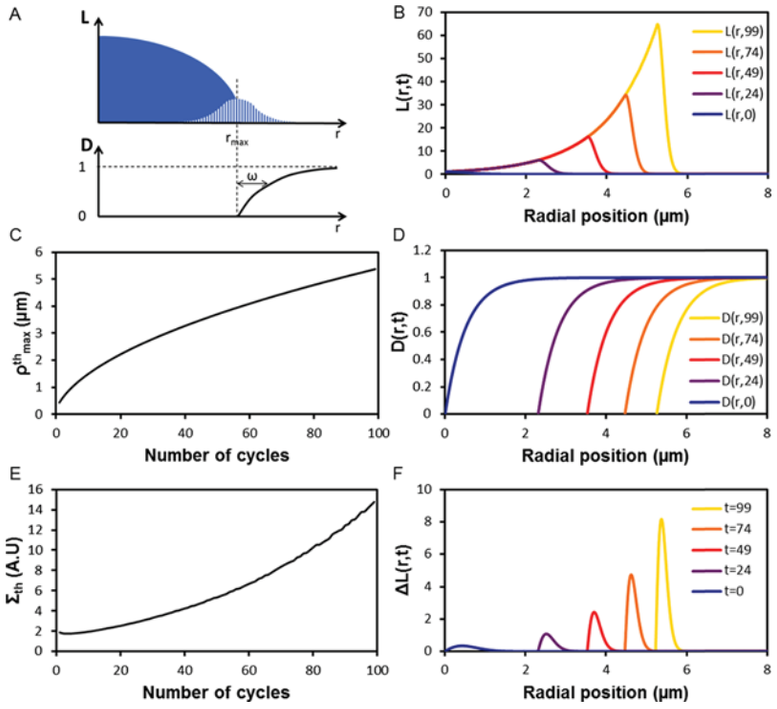

Figure 8. Physicomathematical model of the amyloid fiber formation at the triple interface. (A) Top: schematic view of the triple interface at the edge of a droplet anchored on an aggregate ring. Bottom: the associated dehydration function. The droplet is represented in blue, and the distribution of amyloid fibers is represented as white bars. The fiber length or density, $L(r)$, depends on r, the radial distance to the center of the droplet. The liquid droplet anchors at the radius where the aggregate distribution is maximal (r_{max}). The aggregates outside of the droplet are partially wet. ω represents the characteristic length of the dehydration function. (B–F) Results from a Scilab simulation with $k = 0.81$, $\omega = 0.54$ μm, and $\sigma = 0.76$ μm. Time (t) is expressed in wetting–dewetting cycles (1 cycle = 15 s) with respect to the onset of aggregation. The radial position is expressed in micrometers with respect to $r_{max}(0)$. The simulation is performed for 100 cycles. The results are shown at $t = 0$ (blue line), 24 (purple line), 49 (red line), 74 (orange line), and 99 (yellow line) cycles. (B) Amyloid fiber length distribution $L(r, t)$ as a function of radius r. (C) Evolution of ρ^{th}_{max}, the distance at which most of the amyloid fibers grow with respect to the number of cycles. (D) Dehydration function $D(r, t)$ as a function of radius r. (E) Evolution of Σ_{th}, the amount of new insulin aggregates grown per cycle with respect to the number of cycles. (F) Distribution of new fibers $\Delta L(r, t)$ between cycle t and $t + 1$ as a function of radius r.

The formation of protein aggregates at the edge of the droplets during phase II can be explained as follows. The region surrounding the droplet contains surface-bound amyloid fibrils, which (i) anchor the liquid droplet and (ii) act as a porous reservoir of the liquid, bringing further insulin in contact with the aggregated insulin. Insulin from the air–liquid interface is brought into close proximity to the adsorbed fibers during dewetting. Adsorption of these insulin molecules on insulin fibers leads to their incorporation into the fiber. The partial dehydration induced by the receding liquid film favors intermolecular interactions between the adsorbed proteins and the protein fibrils, leading to amyloidal fiber growth. The driving force for the conformational change could in part be provided by the release of solvation water around the insulin molecules concomitant with the formation of intermolecular hydrogen bonds. An induced decrease in the protein hydration layer is well-known to accompany adsorption and aggregation phenomena at hydrophobic interfaces.[16] Our results imply that amyloid aggregates grow at the surface around the droplets rather than being formed elsewhere (e.g., at the liquid–air interface) and being deposited there. Indeed, we observe that during the growth phase, the gain in the THT fluorescence intensity increases by a factor 6 (Figure 7A, between 620 and 700 cycles), whereas the radius of the fluorescence ring (and hence the droplet) increases only about 1.2 times (Figure 7B, between 620 and 700 cycles). It is therefore unlikely that protein aggregates originate from the air–liquid interface because the amount deposited should only marginally increase with time. By contrast, this strong fluorescence increase better fits with the idea that new insulin fibers grow in contact with the existing ones. The fact that in the presence of nonionic surfactants (Tween 20 or 80), no THT-positive HI aggregates are observed in our system, stresses the importance of interfacial adsorption in HI amyloid aggregation (Figure S2). Indeed polysorbates are added to most of the therapeutic protein formulations in order to prevent interfacial stresses, as these amphiphilic molecules preferentially adsorb at hydrophobic interfaces, thus keeping the proteins in solution.[29]

Physicomathematical Model of Insulin Amyloid Fiber Growth at a Moving Triple Interface. From the above consideration, a simplified model of insulin aggregation is presented below that takes into account the key observations: (i) amyloid fibers form at the surface, (ii) they prevent a full dewetting of the surface, (iii) they allow amyloid fiber growth at the periphery of the droplets, and (iv) no amyloid fiber growth is observed inside of the droplets.

Figure 8A illustrates schematically the growth of insulin amyloid aggregates at the triple interface, located at the edge of a droplet. The distribution of amyloid fibers attached to the surface at a distance r to the center of the droplet after cycle t is called $L(r, t)$. L may represent the size and/or the density of the fibers. We hypothesize that at a given cycle t, the droplet

DOI: 10.1021/acs.langmuir.6b03314
Langmuir 2016, 32, 13009–13019

margin anchors at the position r where $L(r, t)$ is maximal, which is called $r_{max}(t)$. We assume (i) that, after a given number of cycles t, the formation of new aggregates takes place in the dewetted zone only, for $r > r_{max}(t)$ and (ii) that the growth is governed by a combination of two factors: the hydration of the deposited proteins, and the amount of fibrils already present. Existing fibrils thus play two roles: they constitute a reservoir for insulin solution and a collection of binding sites for incoming insulin molecules.

The growth of amyloid fibrils, $\Delta L(r, t)$, after each wetting−dewetting cycle is thus represented by the following equation

$$\Delta L(r, t) = k \times D(r - r_{max}(t)) \times L(r, t) \quad (6)$$

where k is a rate constant and $D(r)$ is a nondimensional dehydration function (Figure 8A). The fiber length distribution after a wetting−dewetting cycle, $L(r, t + 1)$ is thus iteratively calculated by

$$L(r, t + 1) = L(r, t) + \Delta L(r, t) \quad (7)$$

for $r \geq 0$, $t \geq 0$. At each cycle, $r_{max}(t + 1)$ is recalculated and used in the next iteration step. The initial distribution of amyloid aggregates at the edge of a droplet, at $t = 0$, is modeled by a Gaussian function $L(r, 0)$, centered at $r_{max}(0) = 0$, where σ is the width of this initial aggregate distribution

$$L(r, 0) = e^{-\left(\frac{r}{\sigma}\right)^2} \quad (8)$$

The dehydration function, $D(r)$ represents the degree of hydration of the protein layer as a function of the distance to $r_{max}(t)$. Because no new amyloid aggregates are created in the wet region ($r < r_{max}$), we assume that for $r < 0$, $D(r) = 0$. We then assume that the dehydration function progressively increases around the droplet to reach one in the fully dehydrated region, with a characteristic distance ω. A simple expression is thus

$$\text{for } r > 0 \quad D(r) = 1 - e^{-r/\omega} \quad (9)$$

The behavior of this system of coupled differential equations depends on three parameters, k, σ, and ω. For a fixed set of parameters, a numerical simulation is conducted over 100 wetting−dewetting cycles using Scilab. At each cycle, Σ_{th}, the amount of new protein aggregates created per cycle, is calculated using

$$\Sigma_{th} = \int_0^{+\infty} \Delta L(r, t) dr \quad (10)$$

and ρ^{th}_{max}, the distance at which the amyloid fiber growth is maximal, is defined as the radial position r where $\Delta L(r, t)$ is maximal. We also calculate $w(t)$, the width of the zone of newly grown amyloid fibers, defined by the interval where $\Delta L(r, t) > 0.25$.

A wide range of parameters is studied: $0.5 < k < 2$, $0.074 < \omega < 0.74$, and $0.3 < \sigma < 3$. Figure 8 shows a representative example of such a simulation, with $k = 0.81$, $\omega = 0.54$, and $\sigma = 0.76$ μm. After a short transitory period (about 30 cycles), new amyloid material grows at each cycle in the form of an annulus that moves at a constant velocity and increases in amplitude (Figure 8C, E, and F). During this stable period, the width of the zone of fiber formation, w, remains constant (Figure S3), whereas ρ^{th}_{max} and Σ_{th} increase linearly and exponentially with the number of cycles, respectively, in accordance with the experimental observations. A theoretical aggregation velocity v_{th} is determined by a linear fit of ρ^{th}_{max}, and a theoretical characteristic rate α_{th} is obtained from an exponential fit of Σ_{th} between 30 and 99 cycles. The constant growth width, w, of the fiber formation zone is defined as w at $t = 99$ cycles. In Figure S4, we represent the effect of σ, k, and ω on v_{th}, α_{th}, and w. v_{th} is proportional to σ and $\ln(k)$ and independent of ω (Figure S4). α_{th} linearly increases with k and σ and exponentially decreases with ω (Figure S4). w increases as a function of $\ln(k)$, and σ decreases as a function of ω (Figure S4). The rate constant k increases the width of the fiber growth zone, which explains the increased theoretical aggregation velocity v_{th} and the theoretical aggregation rate α_{th}. At high ω, fibers that are close to the droplet edge are submitted to a smaller dehydration function and therefore grow less. Nevertheless, ρ^{th}_{max} is attained at the same distance from the droplet edge, which explains the constant value of v_{th}.

Using these simulations, it is possible to determine, for each studied droplet, a specific set of parameters (σ, ω, and k) that matches our experimentally determined values for v_{exp} and α_{exp} (results shown in Table S1). First, σ is experimentally determined from the first fluorescence image in the movie, where a fluorescent ring is visible around the droplet. The radial fluorescence intensity profile is extracted and fitted with two Gaussian functions to determine the fluorescence ring and the background (see Experimental Section). σ is equal to the standard deviation of the Gaussian function that fits the fluorescent peak. Second, k is calculated from v_{exp} and the linear relationship between v_{th} and $\ln(k)$, using the value of σ already determined because v_{th} is independent of ω (Figure S4). Third, ω is determined from α_{exp} and the exponential relationship between α_{th} and ω (Figure S4), using the values of σ and k previously determined.

Comparing the results obtained for each droplet, the value of the dehydration characteristic distance ω is remarkably constant, whereas σ and k display more variability. The fact that k is close to one indicates that the amount of fibers at the triple interface, most exposed to dehydration, could potentially double at each cycle.

Alternatively, a unique set of parameters can be determined similarly from the fits of Σ_{exp} and ρ^{exp}_{max} described in Figure 7 by pooling all data. An average σ (0.53 ± 0.16 μm) is used as an input to calculate values of k (1.07 with a 60% confidence interval between 0.59 and 1.92) and ω (0.50 ± 0.01 μm) that fit all data. The theoretical values of v_{th} and α_{th} are estimated to be 0.0280 μm·cycle^{-1} and 0.0222 cycle^{-1}, which is close to the experimental values $v_{exp} = 0.0282 \pm 0.0061$ μm·cycle^{-1} and $\alpha_{exp} = 0.0226 \pm 0.0009$. Using this set of parameters, we calculate the width of the fiber formation ring at each cycle, after the transitory period, which equals 0.397 ± 0.006 μm (Figure S3). This confirms that the new amyloid fiber growth is restricted to the close proximity of the droplet, in the region where the solid−liquid and liquid−air interfaces meet.

CONCLUSIONS

In this study, we present the first in situ, real-time analysis of insulin amyloid aggregation at a dynamic triple contact line. Although insulin is likely to adsorb at all of the interfaces present in our setup, the conformational changes and intermolecular interactions necessary to form THT-positive aggregates are triggered preferentially by the forces acting at the triple contact line. Our study reveals a new mechanism for protein aggregation driven by the partial dehydration of surface-adsorbed proteins at the edge of droplets, where the solid−liquid and liquid−air interfaces meet. HI is known to bind THT

DOI: 10.1021/acs.langmuir.6b03314
Langmuir 2016, 32, 13009−13019

when adsorbed at hydrophobic surfaces.[5,7] It has been shown to be monomeric at the air−liquid interface at pH 2.[6,30] Moreover, it is well-established that the insulin monomer is the most aggregation-prone form at hydrophobic interfaces.[5,31] Therefore, at the triple contact line, three crucial parameters come together: high and possibly monomeric insulin concentration at the air−liquid interface, adsorbed and possibly denatured proteins at the solid−liquid interface, and partial dehydration that favor amyloid fiber growth. Moreover, air−liquid interfaces, in contrast to solid−liquid interfaces, allow for the interfacial diffusion of adsorbed proteins and therefore can contribute to favorable local protein orientations, which combined with the stabilization of adsorption-induced conformational changes, can lead to aggregation nuclei formation and amyloid fiber growth. In addition, mechanical efforts exerted at the droplet edge, where capillary forces are important, may also contribute to de novo fiber formation, by fragmenting existing fibers and therefore creating more elongation sites. A relationship between amyloid fiber fragmentation propensity and growth rate has indeed been documented for yeast Sup35 prion.[32]

The role of interfaces in the amyloid aggregation of other proteins has been studied. Jean and colleagues[33] have shown, for islet amyloid polypeptide and amyloid β peptide (Aβ), that their surface-active properties lead to a local protein enrichment at the air−liquid interface above the critical fibrillar concentration, thus enhancing amyloid fibrillation in the presence of an air−liquid interface. Similarly, Morinaga and colleagues[34] have demonstrated that, at low concentrations (5 μM), the presence of an air−water interface triggers the fibrillation of Aβ, which does not occur in the absence of such an interface, at this concentration after 3 weeks. For α-synuclein, an air−water interface has been shown to induce surface-catalyzed nucleation and/or branching.[35] Altogether these studies highlight the importance of the local protein enrichment as a determining factor in the amyloid aggregation process at air−liquid interfaces. However, in these studies, the presence of solid surfaces, where proteins could adsorb, is not considered.

The role of solid surfaces is evidenced by the fact that agitation strongly enhances aggregation kinetics, which is not explained by the concentration effect at the interfaces alone. Morinaga and colleagues,[34] for instance, highlight the effect of agitation on Aβ amyloid aggregation at the air−liquid interface. Although not discussed in their study, it is likely that Aβ amyloids originate at the well border, where the air−liquid interface transiently meets the solid−liquid interface before spreading over the entire air−liquid interface by diffusion.

Compression or rupture of the air−liquid interface strongly enhances mAb aggregate accumulation.[11,13] In these studies, an intermittently wet surface was created either on a rotating needle or on the walls of a tilted vial but the authors did not analyze the presence of protein aggregates at this place. Similarly, the aggregation of recombinant human growth hormone is strongly enhanced at dynamically renewed air−liquid interfaces by bubble aeration.[14] For the production of air bubbles and for the stirring of the solution, hydrophobic surfaces were also present in this study. The adsorption of proteins at such hydrophobic solid surfaces is therefore likely to create a similar situation of intermittent wetting than the one mimicked in our setup, accelerating protein aggregation by partial dehydration of proteins and by capillary forces acting at the triple contact line.

Despite the accumulating evidence of interfacial effects on protein stability, many solid−liquid or liquid−air interface studies do not observe protein aggregation in real time and do not consider the triple contact line, although it is generally present in most of the conventional setups. Concerning practical applications, our study explains why agitation can be detrimental to protein stability in pharmaceutical containers, where an air headspace or bubbles are often unavoidable. The possible formation of wetting−dewetting zones at interfaces, where proteins strongly adsorb, should thus be carefully examined in industrial processes, as they can be the trigger for aggregate formation.

■ ASSOCIATED CONTENT

Supporting Information

The Supporting Information is available free of charge on the ACS Publications website at DOI: 10.1021/acs.langmuir.6b03314.

RICM visualization of droplet reformation at the microchannel surface (AVI)

RICM image and RGB superimposition image of liquid droplets using the TN buffer with 20 μM THT. Effect of Tween 20 and 80 on HI aggregation kinetics. Distribution of new fibers and width of the newly amyloid fiber growth zone between 30 and 99 cycles. Effect of the initial distribution width, the dehydration characteristic distance and the rate constant on the theoretical aggregation velocity, the theoretical characteristic rate, and the constant growth width. Summary of the experimentally determined parameters and the deduced values of k, ω, v_{th}, and α_{th} for four droplets according to the model (PDF)

■ AUTHOR INFORMATION

Corresponding Author

*E-mail: marianne.weidenhaupt@grenoble-inp.fr. Phone: +33 4 56529335. Fax: +33 4 56529301.

ORCID

Marianne Weidenhaupt: 0000-0001-5180-6758

Notes

The authors declare no competing financial interest.

■ ACKNOWLEDGMENTS

The authors thank Daniel Bellet and Mélanie Lagrange for their contribution concerning the electric heating system and Mikhail Anikin for his dedicated technical assistance. T.F. is supported by ANRT CIFRE PhD grant.

■ REFERENCES

(1) Vogler, E. A. Protein adsorption in three dimensions. *Biomaterials* **2012**, *33*, 1201−1237.

(2) Rabe, M.; Verdes, D.; Seeger, S. Understanding protein adsorption phenomena at solid surfaces. *Adv. Colloid Interface Sci.* **2011**, *162*, 87−106.

(3) Pinholt, C.; Hartvig, R. A.; Medlicott, N. J.; Jorgensen, L. The importance of interfaces in protein drug delivery—why is protein adsorption of interest in pharmaceutical formulations? *Expert Opin. Drug Delivery* **2011**, *8*, 949−964.

(4) Norde, W. My voyage of discovery to proteins in flatland ... and beyond. *Colloids Surf., B* **2008**, *61*, 1−9.

(5) Sluzky, V.; Klibanov, A. M.; Langer, R. Mechanism of insulin aggregation and stabilization in agitated aqueous solutions. *Biotechnol. Bioeng.* **1992**, *40*, 895−903.

DOI: 10.1021/acs.langmuir.6b03314
Langmuir 2016, 32, 13009−13019

(6) Johnson, S.; Liu, W.; Thakur, G.; Dadlani, A.; Patel, R.; Orbulescu, J.; Whyte, J. D.; Micic, M.; Leblanc, R. M. Surface chemistry and spectroscopy of human insulin Langmuir monolayer. *J. Phys. Chem. B* **2012**, *116*, 10205−10212.
(7) Nault, L.; Guo, P.; Jain, B.; Bréchet, Y.; Bruckert, F.; Weidenhaupt, M. Human insulin adsorption kinetics, conformational changes and amyloidal aggregate formation on hydrophobic surfaces. *Acta Biomater.* **2013**, *9*, 5070−5079.
(8) Mauri, S.; Volk, M.; Byard, S.; Berchtold, H.; Arnolds, H. Stabilization of Insulin by Adsorption on a Hydrophobic Silane Self-Assembled Monolayer. *Langmuir* **2015**, *31*, 8892−8900.
(9) Li, S.; Leblanc, R. M. Aggregation of insulin at the interface. *J. Phys. Chem. B* **2014**, *118*, 1181−1188.
(10) Couston, R. G.; Skoda, M. W.; Uddin, S.; van der Walle, C. F. Adsorption behavior of a human monoclonal antibody at hydrophilic and hydrophobic surfaces. *mAbs* **2013**, *5*, 126−139.
(11) Rudiuk, S.; Cohen-Tannoudji, L.; Huille, S.; Tribet, C. Importance of the dynamics of adsorption and of a transient interfacial stress on the formation of aggregates of IgG antibodies. *Soft Matter* **2012**, *8*, 2651−2661.
(12) Gleason, C.; Yee, C.; Masatani, P.; Middaugh, C. R.; Vance, A. Probing Shear Thinning Behaviors of IgG Molecules at the Air−Water Interface via Rheological Methods. *Langmuir* **2016**, *32*, 496−504.
(13) Bee, J. S.; Schwartz, D. K.; Trabelsi, S.; Freund, E.; Stevenson, J. L.; Carpenter, J. F.; Randolph, T. W. Production of particles of therapeutic proteins at the air−water interface during compression/dilation cycles. *Soft Matter* **2012**, *8*, 10329−10335.
(14) Wiesbauer, J.; Prassl, R.; Nidetzky, B. Renewal of the air−water interface as a critical system parameter of protein stability: Aggregation of the human growth hormone and its prevention by surface-active compounds. *Langmuir* **2013**, *29*, 15240−15250.
(15) Arai, T.; Norde, W. The behaviour of some model proteins at the solid-liquid interface 1. Adsorption from single protein solutions. *Colloids Surf.* **1990**, *51*, 1−15.
(16) Krishnan, A.; Liu, Y.-H.; Cha, P.; Allara, D.; Vogler, E. A. Scaled interfacial activity of proteins at a hydrophobic solid/aqueous-buffer interface. *J. Biomed. Mater. Res., Part A* **2005**, *75*, 445−457.
(17) Biedermannová, L.; Schneider, B. Hydration of proteins and nucleic acids: Advances in experiment and theory. A review. *Biochim. Biophys. Acta, Gen. Subj.* **2016**, *1860*, 1821−1835.
(18) Nielsen, L.; Khurana, R.; Coats, A.; Frokjaer, S.; Brange, J.; Vyas, S.; Uversky, V. N.; Fink, A. L. Effect of environmental factors on the kinetics of insulin fibril formation: Elucidation of the molecular mechanism. *Biochemistry* **2001**, *40*, 6036−6046.
(19) LeVine, H. Quantification of β-sheet amyloid fibril structures with thioflavin T. *Methods Enzymol.* **1999**, *309*, 274−284.
(20) Limozin, L.; Sengupta, K. Quantitative reflection interference contrast microscopy (RICM) in soft matter and cell adhesion. *ChemPhysChem* **2009**, *10*, 2752−2768.
(21) Sorel, S.; Bellet, D.; Coleman, J. N. Relationship between material properties and transparent heater performance for both bulk-like and percolative nanostructured networks. *ACS Nano* **2014**, *8*, 4805−4814.
(22) Savitzky, A.; Golay, M. J. E. Smoothing and differentiation of data by simplified least squares procedures. *Anal. Chem.* **1964**, *36*, 1627−1639.
(23) Ballet, T.; Brukert, F.; Mangiagalli, P.; Bureau, C.; Boulangé, L.; Nault, L.; Perret, T.; Weidenhaupt, M. DnaK prevents human insulin amyloid fiber formation on hydrophobic surfaces. *Biochemistry* **2012**, *51*, 2172−2180.
(24) Jaspe, J.; Hagen, S. J. Do protein molecules unfold in a simple shear flow? *Biophys. J.* **2006**, *91*, 3415−3424.
(25) Thomas, C. R.; Geer, D. Effects of shear on proteins in solution. *Biotechnol. Lett.* **2011**, *33*, 443−456.
(26) Biddlecombe, J. G.; Craig, A. V.; Zhang, H.; Uddin, S.; Mulot, S.; Fish, B. C.; Bracewell, D. G. Determining antibody stability: Creation of solid−liquid interfacial effects within a high shear environment. *Biotechnol. Prog.* **2007**, *23*, 1218−1222.
(27) Bee, J. S.; Stevenson, J. L.; Mehta, B.; Svitel, J.; Pollastrini, J.; Platz, R.; Freund, E.; Carpenter, J. F.; Randolph, T. W. Response of a concentrated monoclonal antibody formulation to high shear. *Biotechnol. Bioeng.* **2009**, *103*, 936−943.
(28) Reiter, G.; Schultz, J.; Auroy, P.; Auvray, L. Improving adhesion via connector polymers to stabilize non-wetting liquid films. *Europhys. Lett.* **1996**, *33*, 29−34.
(29) Khan, T. A.; Mahler, H.-C.; Kishore, R. S. K. Key interactions of surfactants in therapeutic protein formulations: A review. *Eur. J. Pharm. Biopharm.* **2015**, *97*, 60−67.
(30) Mauri, S.; Weidner, T.; Arnolds, H. The structure of insulin at the air/water interface: Monomers or dimers? *Phys. Chem. Chem. Phys.* **2014**, *16*, 26722−26724.
(31) Nielsen, L.; Frokjaer, S.; Carpenter, J. F.; Brange, J. Studies of the Structure of Insulin Fibrils by Fourier Transform Infrared (FTIR) Spectroscopy and Electron Microscopy. *J. Pharm. Sci.* **2001**, *90*, 29−37.
(32) Knowles, T. P. J.; Buehler, M. J. Nanomechanics of functional and pathological amyloid materials. *Nat. Nanotechnol.* **2011**, *6*, 469−479.
(33) Jean, L.; Lee, C. F.; Vaux, D. J. Enrichment of amyloidogenesis at an air−water interface. *Biophys. J.* **2012**, *102*, 1154−1162.
(34) Morinaga, A.; Hasegawa, K.; Nomura, R.; Ookoshi, T.; Ozawa, D.; Goto, Y.; Yamada, M.; Naiki, H. Critical role of interfaces and agitation on the nucleation of Aβ amyloid fibrils at low concentrations of Aβ monomers. *Biochim. Biophys. Acta, Proteins Proteomics* **2010**, *1804*, 986−995.
(35) Campioni, S.; Carret, G.; Jordens, S.; Nicoud, L.; Mezzenga, R.; Riek, R. The presence of an air−water interface affects formation and elongation of α-Synuclein fibrils. *J. Am. Chem. Soc.* **2014**, *136*, 2866−2875.

DOI: 10.1021/acs.langmuir.6b03314
Langmuir 2016, 32, 13009−13019